HIGH VOLTAGE DEVELOPMENT AND LASER SPECTROSCOPY FOR THE SEARCH
OF THE PERMANENT ATOMIC ELECTRIC DIPOLE MOMENT OF RADIUM-225

By

Roy Anthony Ready

A DISSERTATION

Submitted to
Michigan State University
in partial fulfillment of the requirements
for the degree of

Physics – Doctor of Philosophy

2021

ABSTRACT

HIGH VOLTAGE DEVELOPMENT AND LASER SPECTROSCOPY FOR THE SEARCH
OF THE PERMANENT ATOMIC ELECTRIC DIPOLE MOMENT OF RADIUM-225

By

Roy Anthony Ready

Permanent electric dipole moments (EDMs) violate parity (P), time reversal (T), and combined charge-conjugation and parity transformation (CP) assuming CPT symmetry. Radium-225 is expected to have an enhanced atomic EDM because its nucleus is octupole-deformed. In the Ra EDM experiment, ^{225}Ra atoms are vaporized in an effusive oven, slowed and collimated by cooling lasers, and trapped between two high voltage electrodes. We measure the spin precession frequency of the trapped radium in uniform, applied electric and magnetic fields and search for a frequency shift correlated with the electric field, the signature of a nonzero EDM.

There are two first generation radium EDM measurements. The most recent measurement reduced the upper limit to 1.4×10^{-23} e cm. In the upcoming second generation measurements, we will implement key upgrades to improve our EDM sensitivity by up to three orders of magnitude. This thesis focuses on my work improving the electric field strength and laser cooling efficiency for the second generation measurements.

Additionally, The Facility of Rare Isotope Beams is expected to produce Radium-225 that can be harvested for EDM measurements. We are developing a laser induced fluorescence experiment that will measure the absolute flux of a directed beam of atoms emitted from an effusive oven. The flux measurement will use stable surrogate isotopes to characterize radium harvesting efficiency. I will report the results of our initial efforts modeling and measuring the atomic beam fluorescence of multiple atom sources.

I was at while guiding me with well-timed support, advice, and humorous anecdotes. Jaideep taught me an inestimable amount about being a good scientist and I'm excited to bring it to bear in my future endeavors.

Lastly, I'm grateful for the love and support of my family: my sisters, Kristen and Brianna; my parents, Charisa and John; our dog, Summer; my grandparents, Joy and John; and my great-grandmother, Barbara. You always believed in me and helped me build the confidence to follow through with my education. Twenty year-old Roy did not know he was going to study physics! It seemed to turn out okay though, and through it all I took solace knowing that you were rooting for me from afar.

Thank you!

TABLE OF CONTENTS

LIST OF TABLES

KEY TO ABBREVIATIONS

ANL .... Argonne National Lab

AOM .... acousto-optical modulator

APD .... avalanche photodiode

AWG .... American wire gauge

BAU .... baryon asymmetry of the Universe

BCP .... buffered chemical polish

BEGe .... broad energy germanium

BR .... branching ratio

BSM .... Beyond the Standard Model

C .... charge conjugation symmetry

CARIBU ...... Californium Rare Isotope Breeder Upgrade

CEDM .... quark chromo-electric dipole moment

CKM .... Cabibbo-Kobayashi-Maskawa

CL .... confidence level

CMB .... Cosmic Microwave Background

CP .... combined charge conjugation and parity symmetry

CPT .... combined charge conjugation, parity, and time reversal symmetry

CSS .... colloidal silica suspension machine polish

DAQ .... data acquisition card

dph .... discharges per hour

DPP .... diamond paste polish

EDM .... permanent electric dipole moment

EP .... electropolish

FRIB .... Facility for Rare Isotope Beams

FWHM .... full width at half maximum

SAM .... Single Atom Microscope

SiC .... silicon carbide machine polish

SM .... Standard Model

STIRAP .... Stimulated Raman Adiabatic Passage

SUS .... specially refined stainless steel ("Clean-Z")

T .... time reversal symmetry

TEC .... thermoelectric temperature controller

Ti:Saph .... titanium sapphire

TMP .... turbomolecular pump

TUM .... Technical University of Munich

UCN .... ultracold neutron

UHV .... ultrahigh vacuum

UPW .... ultrapure water

USR .... ultrasonic rinse

USTC .... University of Science and Technology of China

VB .... vacuum outgas bake

WB .... water bake

WD .... working distance

SYMMETRY VIOLATION AND PERMANENT ELECTRIC DIPOLE MOMENTS

1.1 The Standard Model

The Standard Model (SM) explains the interactions between all quarks, which make up baryons such as protons and neutrons, and leptons, such as electrons. The interactions are characterized by the exchange of force-mediating particles: gluons for the strong force, photons for the electromagnetic force, and W and Z bosons for the weak force. Quarks, leptons, and their associated antiparticles undergo interactions in accordance with fundamental symmetry rules established by the Standard Model.

There is more matter than antimatter in the universe due to a minute degree of violation of fundamental discrete symmetries that otherwise treat particles and antiparticles equally. To date, the Standard Model is consistent with all experimentally observed symmetry-breaking processes.

1.1.1 Predictive power

Particles with intrinsic angular momentum will precess about an external magnetic field with a frequency that is characterized by its gyromagnetic ratio g. An electron is a point-like particle with intrinsic spin $J = 1/2$. In an empty vacuum, the expectation value of the electron's gyromagnetic ratio is $g = 2$.

In reality, space is permeated by virtual particles that are spontaneously created and annihilated. The deviations from the empty vacuum expectation value of g caused by these particle pairs can be calculated with quantum electrodynamics. The electron's gyromagnetic ratio has been measured to a precision of less than one part in a trillion (10^{12}) [1, 2]. This is one of the most sensitive tests of the SM and turns out to be in complete agreement with theory.

The Standard Model has also predicted the existence of particles, including the top quark and the Higgs boson.

1.1.2 Unsolved puzzles

While unifying the electromagnetic, strong, and weak forces, the SM fails to describe dynamics involving the gravitational force. It also cannot account for matter that does not interact through the three unified forces. Observable, radiative matter makes up only 5% of the total mass needed to explain the observed kinematics of galaxies and the expansion of the universe. The missing mass is thought to be balanced by 75% dark energy and 20% dark matter.

1.2 Fundamental Symmetries

1.2.1 Time reversal

There are three fundamental discrete symmetries: parity transformation (P), charge conjugation (C), and time reversal (T). Fields, particles, and particle properties behave differently under application of any one or any composite of these transformations. Their behavior is characterized by "even-ness" or "odd-ness" under a transformation. For example, under time reversal the electric field is even and the magnetic field is odd:

$$\mathcal{T}\vec{\mathbf{E}}(\vec{\mathbf{r}}, t) = \vec{\mathbf{E}}(\vec{\mathbf{r}}, -t) = \vec{\mathbf{E}}(\vec{\mathbf{r}}, t) \quad \text{``even''}$$

$$\mathcal{T}\vec{\mathbf{B}}(\vec{\mathbf{r}}, t) = \vec{\mathbf{B}}(\vec{\mathbf{r}}, -t) = -\vec{\mathbf{B}}(\vec{\mathbf{r}}, t) \quad \text{``odd''}$$

Here t is time, $\vec{\mathbf{r}}$ is the position vector, $\mathcal{T}$ is the time reversal operator, $\vec{\mathbf{E}}(t)$ is the electric field, and $\vec{\mathbf{B}}(t)$ is the magnetic field. The P and T transformations of $\vec{\mathbf{E}}, \vec{\mathbf{B}}$, intrinsic angular momentum $\vec{\mathbf{J}}$, and their dot products are given in Table 1.1.

This can be generalized to any quantum system. We can write the time reversal trans-

formation of any state characterized by the wave function $\psi_i(\vec{\mathbf{r}}, t)$ $\left[\mathrm{m}^{-3/2}\right]$:

$$\mathcal{T}\psi_1(\vec{\mathbf{r}}, t) = \psi_1(\vec{\mathbf{r}}, t) \quad \text{``even''}$$

$$\mathcal{T}\psi_2(\vec{\mathbf{r}}, t) = -\psi_2(\vec{\mathbf{r}}, t) \quad \text{``odd''}$$

1.2.2 Parity transformation

Parity transformation, or space inversion, inverts the coordinates of the state. In a Cartesian coordinate system ($\vec{\mathbf{r}} = x\hat{\mathbf{x}} + y\hat{\mathbf{y}} + z\hat{\mathbf{z}}$), a parity transformation can be written as:

$$\pi\psi(\vec{\mathbf{r}}, t) = \psi(-\vec{\mathbf{r}}, t) = \begin{cases} +\psi(\vec{\mathbf{r}}, t)\,, & \text{``even''} \\ -\psi(\vec{\mathbf{r}}, t)\,, & \text{``odd''} \end{cases}$$

where π is the parity operator. Polar vectors such as the electric field $\vec{\mathbf{E}}$ are odd, while pseudovectors (cross product of two polar vectors) such as the magnetic field $\vec{\mathbf{B}}$ are even.

Parity violation was first measured in 1957 by Wu et. al [3], following the proposal of Lee and Yang [4], in the beta-decay of cobalt-60 (1925-day half-life) to nickel-60:

$$^{60}_{27}\mathrm{Co} \rightarrow\ ^{60}_{28}\mathrm{Ni} + e^- + \overline{\nu_e}\,,$$
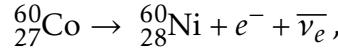
where e^- is an electron (beta particle) and $\overline{\nu_e}$ is an antineutrino. They polarized a sample of $^{60}\mathrm{Co}$ in a magnetic field and measured the beta particle intensity at an angle θ and $\theta - 180°$ with respect to the polarization axis. In the first field orientation, the nuclei tended to emit beta particles opposite the direction of nuclear spin. Wu then inverted the nuclear spin of the sample by switching the polarizing field direction, simulating the parity transformation, and repeated the measurement. Again, the beta particles preferentially emitted opposite the nuclear spin. This test demonstrated parity violation through the observation of the correlation between the beta decay direction and the nuclear spin.

Table 1.1: Even/odd-ness of the electric field ($\vec{\mathbf{E}}$), magnetic field ($\vec{\mathbf{B}}$), intrinsic angular momentum ($\vec{\mathbf{J}}$), and their dot products under time reversal and parity transformations.

	$\vec{\mathbf{J}}$	$\vec{\mathbf{B}}$	$\vec{\mathbf{E}}$	$\vec{\mathbf{J}}\cdot\vec{\mathbf{B}}$	$\vec{\mathbf{J}}\cdot\vec{\mathbf{E}}$
P	$+1$	$+1$	-1	$+1$	-1
T	-1	-1	$+1$	$+1$	-1

1.2.3 Charge conjugation

Charge conjugation changes a particle to its antiparticle and vice versa, for example an electron to a positron. This transformation can be written in ket notation as follows:

$$\mathcal{C}\,|e^-\rangle \rightarrow |e^+\rangle \,,$$

where $\mathcal{C}$ is the charge conjugation operator. Unlike P and T symmetry, the state is changed unless the particle is its own antiparticle, e.g. the photon.

1.2.4 CP transformation

The CKM matrix characterizes the approximate preservation of quark generation number (up/down, charm/strange, top/bottom). Quark interactions involve a small amount "mixing" where, for example, an up quark may undergo an interaction and convert to a strange quark a very small percentage of the time. Violation of combined charge conjugation (C) and parity (P) symmetry, or CP, is a necessary ingredient of the observed dominance of matter over antimatter, or baryon asymmetry of the universe (BAU) [5]. CP violation is encoded in the Standard Model (SM) by a complex phase δ in the Cabibbo-Kobayashi-Maskawa (CKM) quark mixing matrix [6].

To date, CP violation has been measured in two systems. The first is from the indirect observation of the CP-forbidden 2π decay of the long-lived K meson mixed state in 1964 [7]. The effect is small, a few parts in a thousand, but this decay process is quite common. This was later directly observed (i.e. no state mixing) [8].

Table 1.2: Standard Model estimates of electric dipole moments of different particles.

label	EDM system	SM prediction $\left(\times 10^{-32}\, e\,\mathrm{cm}\right)$	
d_e	electron	0.000 000 000 001	[14]
d_q	quark	0.01	[15]
d_n	neutron	1	[16]
d_p	proton	1	[16]
$d_A\left(^{129}\mathrm{Xe}\right)$	xenon atomic	0.005	[6]
$d_A\left(^{199}\mathrm{Hg}\right)$	mercury atomic	0.04	[6]

The second measured CP-violating process is the decay of neutral B meson pairs B^0 and $\bar{B}^0$ in 2001 [9, 10]. Two collaborations (the "B-factory" measurements) independently measured asymmetric branching ratios in one of the baryon-antibaryon decay channels. The measurements were initially indirect observations of CP violation. The experiment was repeated by both groups and direct CP violation was observed in 2004 [11, 12].

Experimental input from the B-factory and other measurements yield SM-consistent CP-violation calculations with the single CP-violating phase parameterization of the CKM matrix [13].

CP violation has also been searched for in measurements of the permanent electric dipole moments (EDMs) of leptons, nucleons, atoms, and molecules. The Standard Model predictions for EDMs are far smaller than current best measurements, as shown in Table 1.2. We will discuss CP violation in the context of EDMs in Section 1.5.

CP-violating interactions in quantum chromodynamics arise from the "theta term" $\overline{\theta}$ [dimensionless] (also called θ_{QCD}) described by quark flavor mixing [17]. As we will see in Section 1.4, quark and lepton EDMs scale linearly with $\overline{\theta}$. SM estimates of EDMs of electrons, neutrons, and atoms are listed in Table 1.2.

1.2.5 *CPT* transformation

The *CPT* theorem rose to notoriety after *P* violation was observed in the Wu experiment and *CP* violation was observed in the Cronin & Fitch measurement.

The *CPT* theorem arises from quantum field theory and states that the combined discrete symmetry transformation of charge, parity, and time reversal is conserved ($CPT = +1$) in all interactions. From this it follows that each particle and its antiparticle, for example an electron and a positron, must have exactly the same mass. *CPT* conservation also means that any violation of *CP* is compensated by an equal violation of *T*.

To date, there is no known interaction that violates *CPT*. The most stringent experimental test is that of the mass difference $m_{K^0} - m_{\overline{K}^0}$ [GeV] between the neutral kaon pair K^0 and $\overline{K}^0$ [18, 19, 20, 21, 22, 13]:

$$m_{K^0} - m_{\overline{K}^0} < 4.0 \times 10^{-19} \text{ GeV} \quad 95\% \text{ confidence level}$$

The neutral kaon mass is 497.6 MeV, so the precision of this test is eight parts in 10^{-19}.

1.3 Baryon asymmetry of the Universe

The baryon asymmetry of the Universe (BAU) is the extremely high abundance of baryons, for example protons and neutrons, relative to antibaryons. Baryon dominance allows matter to stick around. If fundamental processes weighted baryon generation and antibaryon generation equally, then theses and the keyboards needed write them wouldn't exist because the baryons needed to make those things would annihilate with an equal number of antibaryons.

Antimatter abundance can be directly searched for in cosmic rays (atoms traveling near the speed of light) and in the Faraday rotation of light passing through the interstellar medium, as well as indirectly in the decay products of annihilation pairs [23]. Recent measurements of antiproton/proton and positron/electron ratios in cosmic rays place increasingly stringent constraints on antimatter abundance [24, 25, 26, 27].

One way the BAU could have been established is through baryogenesis. Baryogenesis proposes that at some time after the early, "particle soup" phase of the Universe, the Universe reached a critical temperature that allowed some CP-violating mechanism switched on, allowing a net generation of baryons [5]. As the Universe cooled further, the net baryon-generating process ramped down, preserving the asymmetry [28].

In electroweak baryogenesis, CP-violating processes drive baryon generation at a critical electroweak phase transition temperature of approximately 100 GeV. However, Standard Model calculations of the phase transition cannot reproduce the observed BAU. This is primarily due to the heaviness of the Higgs boson (125 GeV) and the small-ness of the CKM matrix-induced CP-violation [29].

This CP-violating phase is related to the observed baryon-to-photon to ratio η [dimensionless]:

$$\eta = \frac{n_B - n_{\bar{B}}}{n_\gamma}$$
$$\propto \sin(\delta),$$
(1.1)

where

$n_B \left[\mathrm{m}^{-3}\right]$ is the baryon density,

$\bar{n}_B \left[\mathrm{m}^{-3}\right]$ is the antibaryon density, and

$n_\gamma \left[\mathrm{m}^{-3}\right]$ is the early universe photon density.

Nuclear physics models and astronomical observations are used to determine the mass fractions of light elements such as Helium-4. These mass fractions are used to constrain η. The net baryon density is also inferred from measurements of the cosmic microwave background (CMB). Both the mass fractions and CMB measurements are in concordance, resulting in $\eta \approx 10^{-9}$ [30].

The CP-violating phase in the Standard Model yields a baryon-to-photon ratio of $\eta \approx 10^{-26}$ [31]. This discrepancy strongly motivates the search for new sources of CP violation.
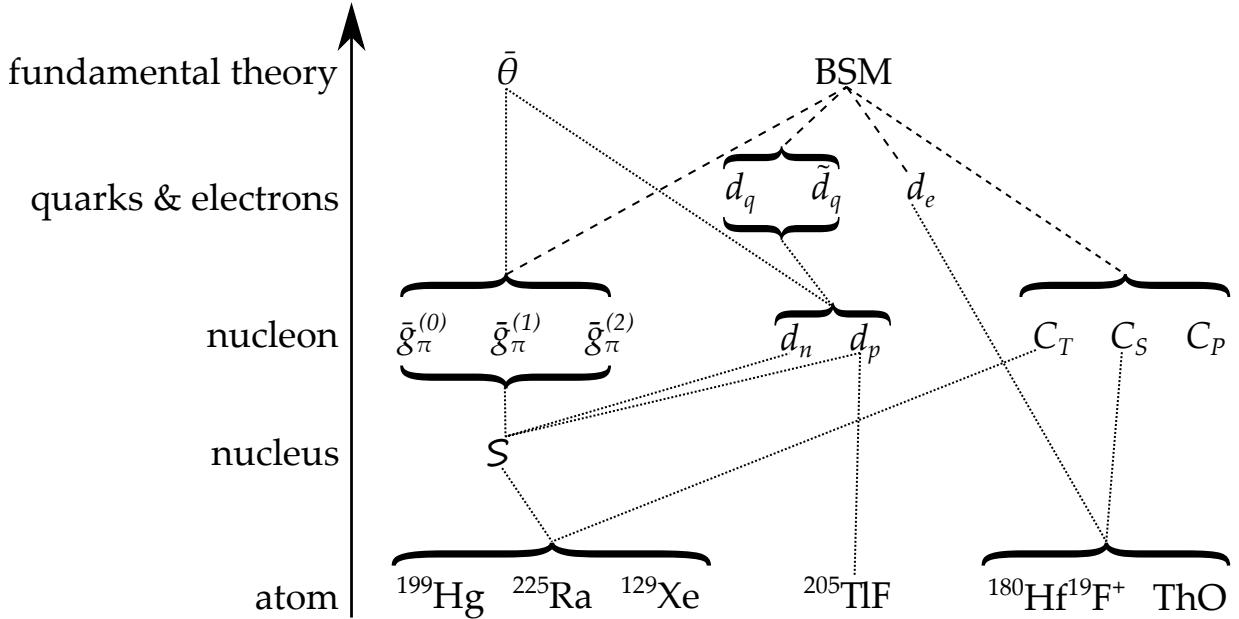
Figure 1.1: A hierarchical diagram depicting the relationships between *CP*-violating phenomena at the low-energy (atomic) scale up to the high-energy (theory) scale. Dotted lines connect parameters with the highest coupling strength. Dashed lines represent potential *CP*-violating provided by BSM physics.

1.4 *CP* Violation Beyond the Standard Model

Figure 1.1 shows a simplified hierarchy of the relation between subatomic EDMs and *CP*-violating interactions to atomic and molecular EDMs. Strong couplings between terms are highlighted with connecting lines. The path for nonzero EDMs in the Standard Model is through the CKM matrix and $\overline{\theta}$. BSM theories provide potential additional *CP*-violating channels that significantly increase predicted EDM magnitudes.

Supersymmetry (SUSY) is one extension to the Standard Model that proposes that every particle has its own "super" particle, doubling the number of particles in the Standard Model. The minimal supersymmetric Standard Model (MSSM) is one version of SUSY where all supersymmetric masses are equivalent to M_{SUSY} [TeV] [32].

In the search for a theory unifying the electromagnetic, weak, and strong forces ("grand unification"), particles possessing both quark quantum numbers and lepton quantum

numbers have been proposed. These leptoquarks are thought to be very heavy bosons that can interact with both quarks and leptons [32]. If observed, leptoquarks would be a clean source of new physics and provide an additional contribution to the tensor electron-nucleon interaction C_T (discussed in Section 1.6.3).

SUSY provides a contribution to the neutron EDM through the quark EDMs d_q and quark chromo-EDMs $\tilde{d}_q$ [33, 34, 17]:

$$d_n = \frac{4}{3}\, d_d - \frac{1}{3}\, d_u - \frac{m_\pi^2}{m_N}\frac{e}{\overline{m}}\left(\frac{2}{3}\, \tilde{d}_d + \frac{1}{3}\, \tilde{d}_u\right) \tag{1.2}$$

$$\overline{m} = \frac{m_u + m_d}{2}, \tag{1.3}$$

where

$m_u = 2.32 \pm 0.10$ MeV is the up quark mass,

$m_d = 4.71 \pm 0.09$ MeV is the down quark mass,

m_N [eV] is the nucleon mass, and

m_π [eV] is the pion mass.

The EDM of the neutron and proton d_n, d_p depends most strongly on $\overline{\theta}$ and the isoscalar pion-nucleon coupling parameter $\overline{g}_\pi^{(0)}$. The nucleon EDMs have very similar expressions, so for brevity I'll show just the neutron EDM dependence [35]:

$$d_n = d_n^{sr} - \frac{e\, g_A\, \overline{g}_\pi^{(0)}}{8\pi^2\, F_\pi}\left(\log\frac{m_\pi^2}{m_N^2} - \frac{\pi\, m_\pi}{2m_N}\right), \tag{1.4}$$

where

$e > 0$ is the elementary charge,

d_n^{sr} [e cm] is the short-range neutron EDM,

$g_A \approx 1.27$ [dimensionless] is the strong pion-nucleon coupling constant, and

$F_\pi \approx 92.4$ [MeV][1] is the pion decay constant.

---

[1] I have also seen reported values of $F_\pi \approx 186$ MeV [36] and ≈ 130.2 MeV [37], where these values differ from the main text value by factors of 2 and $\sqrt{2}$, respectively.

Recently, the dependence of d_n on $\overline{\theta}$ and $\overline{g}_\pi^{(0)}$ has been calculated using Lattice QCD [35]:

$$d_n = -(1.52 \pm 0.71) \times 10^{-16}\, \overline{\theta}\, e\, \text{cm}\,, \tag{1.5}$$

$$\overline{g}_\pi^{(0)} = -(12.8 \pm 6.4) \times 10^{-3}\, \overline{\theta} \tag{1.6}$$

The isovector pion-nucleon coupling constant $\overline{g}_\pi^{(1)}$ is related to the up and down quark chromo-EDMs (CEDMs) by the following expression [34]:

$$\overline{g}_\pi^{(1)} = 3 \times 10^{-12}\, \frac{\tilde{d}_u - \tilde{d}_d}{10^{-26}\ \text{cm}}\, \frac{|<\overline{q}q>|}{(225\ \text{MeV})^3}\, \frac{\left| m_0^2 \right|}{0.8\ \text{GeV}^2}\,, \tag{1.7}$$

where $|<\overline{q}q>| = |\langle 0|\, \overline{q}q\, |0\rangle|\, \left[\text{MeV}^3\right]$ is the quark gluon condensate and $m_0^2 \approx -m_N^2\, \left[\text{MeV}^2\right]$ is the strength coefficient of $|<\overline{q}q>|$.

The pion-nucleon coupling constants are related to $\overline{\theta}$ by the following expression [38, 39]:

$$|\overline{g}| \approx 0.027\overline{\theta}\,, \tag{1.8}$$

$$\overline{g} = \overline{g}_\pi^{(0)} + \overline{g}_\pi^{(1)} - 2\overline{g}_\pi^{(2)} \tag{1.9}$$

The pion-nucleon coupling constants are related to the CEDMs by [40, 39]:

$$\overline{g}_\pi^{(0)} + \overline{g}_\pi^{(1)} - 2\overline{g}_\pi^{(2)} = \frac{\tilde{d}_u - \tilde{d}_d}{10^{-14}\ \text{cm}} \tag{1.10}$$

The electron EDM is a lepton, does not participate in strong interactions, and therefore is not expressed in terms of $\overline{\theta}$ or the pion-nucleon coupling constants. As shown in Figure 1.1, d_e couples strongly to paramagnetic systems, which I'll discuss in Section 1.6.2. In the MSSM extension, the electron EDM d_e and the quark EDM d_q are given by [34, 32]:

$$d_e \approx \frac{e\, m_f}{16\pi^2\, M_{\text{SUSY}}^2} \left(\frac{5g_2^2 + g_1^2}{24}\, \sin\theta_\mu \tan\beta + \frac{g_1^2}{12}\, \sin\theta_A \right)\,, \tag{1.11}$$

$$d_q \approx \frac{Q_q e\, m_f}{16\pi^2\, M_{\text{SUSY}}^2}\, \frac{2g_s^2}{9} \left(\sin\theta_\mu\, [\tan\beta]^{-2Q_q+1/3} - \sin\theta_A \right)\,, \tag{1.12}$$

$$\tan\beta = v_d\, /\, v_u\,, \tag{1.13}$$

where

> Q_q [e] is the electric charge of the quark,
>
> g_1 [dimensionless] is the $U(1)_Y$ gauge theory coupling,
>
> g_1 [dimensionless] is the $SU(2)_L$ gauge theory coupling,
>
> g_s [dimensionless] is the QCD coupling,
>
> θ_A [rad] is a CP-violating phase, and
>
> v_u / v_d [dimensionless] is the ratio of the vacuum expectation values of the up and
> down Higgs fields.

There is a similar expression for CEDMs. With reasonable assumptions, one can estimate the electron EDM $d_e \approx 10^{-27}$ e cm, quark EDM $d_q \approx 10^{-25}$ e cm, and quark chromo-EDM $\tilde{d}_q \approx 10^{-25}$ cm in the MSSM framework [32].

1.5   Electric dipole moment searches as a probe of CP violation

An electric dipole moment is the distribution of charge along the position vector pointing from negative to positive charge. A permanent electric dipole moment $\vec{\mathbf{d}}$ [e cm] is aligned with the intrinsic angular momentum of the particle, $\vec{J}$ [6]:

$$\vec{\mathbf{d}} = \int \vec{\mathbf{r}} \, \rho_Q d\mathcal{V} = d \, \frac{\vec{J}}{J} \, , \tag{1.14}$$

where $\vec{\mathbf{r}}$ [cm] is the position of the charge, ρ $\left[e \text{ m}^{-3} \right]$ is the electric charge distribution, and $\mathcal{V} = \int d\mathcal{V}$ $\left[\text{m}^3 \right]$ is the volume of the particle.

A nonzero permanent electric dipole moment violates time-reversal (T) and P symmetry. To see this, we consider the Hamiltonian $\mathcal{H}$ [J] of a system with intrinsic spin in the presence of an electric and magnetic field:

$$\mathcal{H} = -\mu \, \frac{\vec{J} \cdot \vec{\mathbf{B}}}{J} - d \, \frac{\vec{J} \cdot \vec{\mathbf{E}}}{J} \, , \tag{1.15}$$

where $\vec{\mu} = \mu \left(\vec{J}/J \right)$ [J/T] is the magnetic moment.

The first term in Equation 1.15 is proportional to the magnetic moment. As we can see from Table 1.1, $\vec{J} \cdot \vec{\mathbf{B}}$ is even under both P and T transformation. The second term, $\vec{J} \cdot \vec{\mathbf{E}}$,

Table 1.3: EDM measurements of different systems. UCN = ultracold neutron. CL = confidence level. PSI = Paul Scherrer Institute. JILA = Joint Institute for Laboratory Astrophysics. Boulder = University of Colorado, Boulder. PTB = Physikalisch Techische Bundesanstalt. ANL = Argonne National Lab. ILL = Institut Laue-Langevin.

particle	sensitivity	90% CL [e cm]	95% CL [e cm]	Ref.
UCN	d_n	1.8×10^{-26}	.	PSI [41]
UCN	d_n	3.0×10^{-26}	3.6×10^{-26}	ILL[42, 43]
^{180}Hf^{19}F$^+$	C_S , d_e	1.3×10^{-28}	.	JILA/Boulder [44]
ThO	C_S , d_e	1.1×10^{-29}	.	ACME [45]
^{199}Hg	C_T , $\mathcal{S}$	.	7.4×10^{-30}	Seattle [46]
^{129}Xe	C_T , $\mathcal{S}$	.	1.4×10^{-27}	HeXeEDM PTB[47]
^{225}Ra	C_T , $\mathcal{S}$	.	1.4×10^{-23}	RaEDM ANL [48]
proton ^{205}TlF$^{\text{b}}$	d_p	.	$6.5 \times 10^{-23\text{c}}$	Yale [49, 50]

[a] EDM limit interpreted by setting $C_S = 0$ (sole source).
[b] ^{199}EDM currently gives a stronger limit on d_p than TlF. The reported limit for TlF interprets the CP-violating frequency shift as an effective proton EDM (sole source).
[c] Calculated from symmetric Gaussian statistics.

is proportional to the EDM and is odd under P and T. A nonzero EDM therefore violates both P and T symmetry.

Assuming CPT conservation, EDMs also violate CP. Neutron, electron, molecular, and atomic EDM experiments have been carried out over the last seven decades in an effort to measure a nonzero EDM magnitude. A nonzero EDM has not been measured yet, but the precision of EDM experiments continues to improve. Observing a nonzero EDM near sensitivities of today's leading experiments would provide a clean signature of Beyond the Standard Model physics [6].

A Table of EDM limits for neutron, proton, electron, and atomic EDMs is given in Table 1.3. The world's most sensitive atomic EDM measurement uses ^{199}Hg.

1.5.1 Neutron electric dipole moment

Neutrons EDMs are primarily sensitive to the short-range neutron EDM d_n^{sr} and pion-nucleon coupling constants $\bar{g}_\pi^{(0)}$, $\bar{g}_\pi^{(1)}$.

The first EDM experiment was a beamline neutron measurement at Oak Ridge National Lab (ORNL) [51]. They sent a collimated beam of neutrons traveling at a Maxwellian velocity of approximately 2870 m/s through a uniform DC magnetic field and a tuneable radiofrequency (RF) magnetic field. The spin precession frequency was determined by measuring the neutron intensity with a counter as a function of the RF frequency.

To measure spin precession frequencies correlated with an electric field, the neutrons also passed between two nickel-plated copper electrodes 135 cm long. The static electric field was 25 kV / 3.49 mm = 7.2 kV/mm and parallel to the DC magnetic field. By measuring the spin precession frequency under parallel and antiparallel DC fields, they measured the upper limit of the neutron EDM to be 5×10^{-20} e cm.

In 1980 the first ultracold neutron (UCN) EDM measurement was demonstrated [52] at the Leningrad Nuclear Physics Institute. A beam of thermal neutrons was impinged on a beryllium target cooled to 30 K with helium gas. The neutrons were guided to a precession chamber with a reduced speed of approximately 7 m/s. The UCN approach allowed for longer spin precession times and reduced the systematic source of uncertainty due to motional magnetic fields, or the "$\vec{E} \times \vec{v}$" effect [6].

The current most sensitive neutron EDM measurement was performed in 2020 at the Paul Scherrer Institute [41]. They use a ^{199}Hg vapor as a comagnetometer dispersed with the UCNs to track systematic drifts in the uniform magnetic field. They report a neutron EDM upper limit of 1.8×10^{-26} e cm (90% confidence).

1.6 CP Violation in Atoms and Molecules

1.6.1 The shielding of the nucleus from external fields

The nucleus of a neutral atom is shielded from external electric fields by the surrounding electron cloud, which polarizes to cancel the field. The shielding is exact and the net field is zero at the location of a classical point-like nucleus [53]. Finite-sized nuclei break this perfect shielding. The spin of the nucleus interacts with a fraction of the external field. Large, octupole-deformed nuclei are less shielded than smaller, more spherical nuclei, enhancing the nuclear Schiff moment [54, 55] .

1.6.2 Sensitivity to the electron electric dipole moment

In the presence of a static electric field, the atomic EDM causes a linear Stark shift. The measurement of the upper limit of the Stark shift is interpreted as an atomic EDM.

Paramagnetic atoms and molecules, which have an unpaired valence electron, have an enhanced sensitivity to the electron electric dipole moment d_e. The enhancement comes from imperfect Schiff shielding due to relativistic effects of the unpaired electron and scales with the size of the nucleus [56, 57]:

$$\frac{d_a}{d_e} \approx 10Z^3\alpha^2\,,$$

where d_a is the atomic EDM, Z is the proton number of the atom, and $\alpha = 7.29735257 \times 10^{-3}$ is the fine-structure constant.

1.6.3 The electron-nucleon interaction

An atomic EDM can arise from CP-violating interactions between the nucleons and electrons. These couplings are characterized by the scalar, pseudoscalar, and tensor electron-nucleon couplings C_S, C_P, and C_T [dimensionless].

The atomic Hamiltonian can be written in terms of the electron-nucleon couplings [17]:

$$\mathcal{H}_{\mathrm{TVPV}} = \mathcal{H}_S + \mathcal{H}_P + \mathcal{H}_T \tag{1.16}$$

The Hamiltonians follow similar forms, although $\mathcal{H}_P$ is suppressed by a factor of m_N. Focusing on C_T, $\mathcal{H}_T$ shows how the P-violating and T-violating interaction between electrons and nucleons generates an atomic EDM that diamagnetic systems are primarily sensitive to [58]:

$$\mathcal{H}_T = \frac{1}{\sqrt{2}} C_T \, i \, G_\mathrm{F} \sum_{n,e} \left(\overline{\psi}_n \, \gamma_5 \, \sigma_{\mu\nu} \, \psi_n \right)\left(\overline{\psi}_e \, \sigma^{\mu\nu} \, \psi_e \right), \tag{1.17}$$

where

$G_\mathrm{F}/(\hbar c)^3 = 1.16638 \times 10^{-5} \, \mathrm{GeV}^{-2}$ is the Fermi coupling constant,

ψ_n, ψ_e are the nucleon and electron wavefunctions,

$\gamma^5 \equiv i\gamma^0\gamma^1\gamma^2\gamma^3 = \begin{pmatrix} \mathbb{O} & \mathbb{I} \\ \mathbb{I} & \mathbb{O} \end{pmatrix}$ is the 4×4 Dirac gamma matrix, and

$\sigma^{\mu\nu}$ are the Dirac matrices generated from the Pauli matrices σ_i in 3+1 dimensional notation.

$\mathcal{H}_T$ includes contributions from every nucleon, so diamagnetic atoms such as ^{129}Xe, ^{171}Yb, ^{199}Hg, and ^{225}Ra are its most sensitive probes. Sensitivity to C_T depends both on the nuclear and atomic structure of the atom.

The atomic permanent electric dipole moment d_A [e cm] can be explicitly written as a linear combination of CP-violating parameters [17]:

$$d_\mathrm{A} = \frac{\partial d_\mathrm{A}}{\partial d_e} \, d_e + \frac{\partial d_\mathrm{A}}{\partial \overline{d}_n^{sr}} \, \overline{d}_n^{sr} + \frac{\partial d_\mathrm{A}}{\partial \overline{d}_p^{sr}} \, \overline{d}_p^{sr} + \frac{\partial d_\mathrm{A}}{\partial C_S} \, C_S + \frac{\partial d_\mathrm{A}}{\partial C_P} \, C_P + \frac{\partial d_\mathrm{A}}{\partial C_T} \, C_T + \ldots$$
$$+ \frac{\partial d_\mathrm{A}}{\partial \overline{g}_\pi^{(0)}} \, \overline{g}_\pi^{(0)} + \frac{\partial d_\mathrm{A}}{\partial \overline{g}_\pi^{(1)}} \, \overline{g}_\pi^{(1)} + \frac{\partial d_\mathrm{A}}{\partial \overline{g}_\pi^{(2)}} \, \overline{g}_\pi^{(2)}, \tag{1.18}$$

where the coefficients $\partial d_\mathrm{A} / \partial C_j$ indicate the sensitivity of the atomic EDM to parameters

Table 1.4: 95% confidence level upper limit calculations of low-energy CP-violating parameters based on experimental measurements using a global approach [59, 6]. C_S and d_e calculated from measurements by paramagnetic systems [60, 61, 62, 63]. $\overline{g}_\pi^{(0)}$, $\overline{g}_\pi^{(1)}$, C_T, and d_n^{sr} calculated from measurements in diamagnetic systems and nuclear theory as of 2019 [64, 65, 43, 66, 67, 68].

label	description	primary sensitivity	global upper limit
d_e	electron EDM	paramagnetic	$8.4 \times 10^{-28}\ e$ cm
C_S	scalar electron-nucleon interaction	paramagnetic	7.5×10^{-8}
$\overline{g}_\pi^{(0)}$	isoscalar pion-nucleon coupling	diamagnetic	1.5×10^{-8}
$\overline{g}_\pi^{(1)}$	isovector pion-nucleon coupling	diamagnetic	2.4×10^{-9}
C_T	tensor electron-nucleon interaction	diamagnetic	1.1×10^{-6}
d_n^{sr}	short-range neutron EDM	neutron	$2.4 \times 10^{-22}\ e$ cm

C_j. Some of the coefficients are often written in a more compact notation:

$$\partial d / \partial d_e \to \eta_e \qquad \partial d / \partial C_T \to \alpha_{C_T}{}^{\text{b}} \qquad \partial d \big/ \partial \overline{g}_\pi^{(0)} \to a_0 \qquad \partial d \big/ \partial \overline{g}_\pi^{(1)} \to a_1$$

$$\partial d \big/ \partial \overline{g}_\pi^{(2)} \to a_2 \qquad \partial d / \partial C_S \to k_S \qquad \partial d / \partial C_P \to \quad k_P$$

These parameters couple fundamental theory properties such as the CKM matrix, BSM physics, or the strong interaction parameter $\overline{\theta}$ to low-energy, potentially measurable EDMs.

To set the stage for the key parameters that I'll discuss in the following sections, I will rewrite Equation 1.18 in terms of the Schiff moment, scalar and tensor electron-nucleon interactions, and electron EDM [6]:

$$d_A = \eta_e\, d_e + k_S\, C_S + \alpha_{C_T}\, C_T + \kappa_S\, S \,, \tag{1.19}$$

where I've omitted terms with weaker coupling to paramagnetic and diamagnetic systems.

Paramagnetic systems are most sensitive to d_e and C_S. For example, in ^{205}Tl, the tensor electron-nucleon interaction is a higher-order effect, and $C_S\left(^{205}\text{Tl}\right) \gg C_T\left(^{205}\text{Tl}\right)$.

$^{\text{b}}k_T$ is sometimes used as well.

In the past ten years, strides in measurement sensitivity have been made by forming paramagnetic systems from diatomic molecules [69]. The most stringent limit on d_e and C_S comes from a global analysis from recent EDM measurements of ThO and ^{180}Hf^{19}F$^+$, as shown in Table 1.4.

I've listed global-source calculations of the low-energy CP-violating parameters from measurements made in paramagnetic and diamagnetic systems in Table 1.4. Several parameters are not included in the global analysis. The sole-source calculation of the isotensor pion-nucleon coupling $\overline{g}_\pi^{(2)} < 1.1 \times 10^{-12}$ and short-range proton EDM $d_p^{sr} < 2.0 \times 10^{-25}$ e cm are found from the ^{199}Hg measurement [46, 6]. The pseudoscalar electron-nucleon interaction C_P is not listed because it is a higher-order effect that is suppressed by an additional factor of $1/m_N$ (the nucleon mass), giving $\alpha_{C_T} \gg k_P$ [17, 70].

The leading order term of the isoscalar pion-nucleon coupling $\overline{g}_\pi^{(0)}$ is given by [71]:

$$2F_\pi \, \overline{g}_\pi^{(0)} = \delta^{(0)} m_N \, \frac{m_* \, \overline{\theta}}{\overline{m} \, \epsilon} \, , \tag{1.20}$$

$$\delta^{(0)} m_N = m_d - m_u \, , \tag{1.21}$$

$$\epsilon = \frac{m_d - m_u}{m_d + m_u} \, , \tag{1.22}$$

$$m_* = \frac{m_u m_d m_s}{m_s(m_u + m_d) + m_u m_d} = \frac{\overline{m} \, (1 - \epsilon^2)}{2 + \overline{m} \, m_s^{-1}(1 - \epsilon^2)} \, , \tag{1.23}$$

where $\delta^{(0)} m_N$ [MeV] is the neutron-proton mass difference and $m_s = 92.9 \pm 0.7$ MeV is the strange quark mass.

Using the values from the literature for $\overline{m} = 3.39 \pm 0.04$ MeV [30], $m_s/\overline{m} = 27.37 \pm 0.10$ MeV [30], $\delta^{(0)} m_N = 2.39 \pm 0.13$ MeV [71], and the quark masses and Equation 1.22 and Equation 1.23 for $\epsilon = 0.352 \pm 0.020$, $m_* = 1.695 \pm 0.066$ MeV, I calculate $\overline{g}_\pi^{(0)} \approx (0.019 \pm 0.003)\overline{\theta}$.

Nuclear forces in diamagnetic atoms and molecules induce nuclear moments that can be several orders of magnitude larger than the constituent neutron and proton EDMs [70]. Therefore, diamagnetic atomic and molecular EDMs are written in terms of the nuclear

Table 1.5: A collection of calculations of nuclear Schiff moment coefficients for Radium-225 and Mercury-199. Ranges are listed in brackets.

System	κ_S $\left(\text{cm fm}^{-3} \right)$	α_{C_T} $(e\,\text{cm})$	$a_0 \left(e\,\text{fm}^3 \right)$	$a_1 \left(e\,\text{fm}^3 \right)$	Ref.
^{225}Ra			$+0.2 \pm 0.6$	-5 ± 3	[72]
^{225}Ra	-8.5×10^{-17}	$+5.3 \times 10^{-20}$	$[-6, -1]$	$[+4, +24]$	[55, 73, 74, 17, 59]
^{199}Hg	-2.8×10^{-17}	$+3.0 \times 10^{-20}$	$[0.005, 0.05]$	$[-0.03, +0.09]$	[75, 76, 59]
^{199}Hg^a			$+0.087$	$+0.087$	[75, 17]
^{199}Hg^b			$+0.010$	$+0.074$	[77]

  ^{a} Schematic method.
  ^{b} Skyrme SkO' QRPA.

Schiff moment $\mathcal{S}$ $\left[e\,\text{fm}^3 \right]$:

$$d_A = \kappa_S\,\mathcal{S} - k_{C_T}\,C_T{}^c \,, \tag{1.24}$$

$$\mathcal{S} = s_N\,d_N + \frac{m_N\,g_A}{F_\pi} \left[a_0\,\bar{g}_\pi^{(0)} + a_1\,\bar{g}_\pi^{(1)} + a_2\,\bar{g}_\pi^{(2)} \right] \,, \tag{1.25}$$

where κ_S $\left[\text{cm fm}^{-3} \right]$ is the Schiff moment sensitivity and k_{C_T} $[e\,\text{cm}]$ is the electron-quark tensor interaction sensitivity. We've dropped the higher-order terms η_e, $\partial d_A / \partial \bar{d}_n^{sr}$, $\partial d_A / \partial \bar{d}_p^{sr}$, $\partial d_A / \partial C_S$, $\partial d_A / \partial C_P$. The isotensor pion-nucleon coupling $\bar{g}_\pi^{(2)}$ may also be neglected, as it is suppressed by a factor of [78, 6, 71, 17]:

$$\bar{g}_\pi^{(2)} / \bar{g}_\pi^{(1)} = \epsilon m_\pi^2 / M_{\text{QCD}}^2 \approx 0.007 \,,$$

where $m_\pi = 139.57$ MeV is the mass of the charged pion [13] and $M_{\text{QCD}} \approx 1$ GeV is the hadronic energy scale [78].

I've listed estimates of the Schiff coupling parameters of radium and mercury in Table 1.5. Note that in the top row, recent calculations of radium aided by correlated octupole moment measurements have significantly reduced uncertainties of a_i [72].

  $^c k_{C_T}$ has an isoscalar and isovector component which I've simplified for clarity.

1.7 *CP* Violation in Diamagnetic Systems

The atomic EDM is directly proportional to the Schiff moment, as shown in Equation 1.19. The Schiff moment $\mathcal{S}\ [e\ \text{fm}^3]$ is given by [73]:

$$\mathcal{S} = \left\langle \Psi_0 \left| \hat{S}_z \right| \Psi_0 \right\rangle \tag{1.26}$$

$$= \sum_{i \neq 0} \frac{\left\langle \Psi_0 \left| \hat{S}_z \right| \Psi_i \right\rangle \left\langle \Psi_i \left| \hat{V}_{\text{PT}} \right| \Psi_0 \right\rangle}{E_0 - E_i}, \tag{1.27}$$

$$\hat{S}_z = \frac{e}{10} \sum_p \left(r_p^2 - \frac{5}{3} \bar{r}_{\text{ch}}^2 \right) z_p, \tag{1.28}$$

where

$\Psi_0\ \left[\text{m}^{-3/2}\right]$ is the ground state wavefunction,

$\hat{S}_z\ \left[e\ \text{fm}^3\right]$ is the component of the Schiff moment along the axis of the nuclear spin,

$E_0\ [e\text{V}]$ is the energy of the ground state

$\hat{V}_{\text{PT}}\ [e\text{V}]$ is the P and T-violating interaction,

$\bar{r}_{\text{ch}}^2\ \left[\text{m}^2\right]$ is the mean square charge radius,

$r_p\ [\text{m}]$ is the proton distance, and

$z_p\ [\text{m}]$ is the z-component of the proton position.

Nuclear Schiff moment-induced atomic EDM searches are carried out in the diamagnetic atoms Mercury-199, Xenon-129, and Radium-225.

The nuclear Schiff moment is enhanced by octupole deformation (pear shape) of the nucleus. The deformation is characterized by the octupole deformation parameter β_3 [dimensionless]. The Schiff moment can be rewritten as [6]:

$$\mathcal{S} = \eta\ e\ \frac{\beta_2\ \beta_3^2\ Z\ A^{2/3}\ r_0^3}{\Delta E}, \tag{1.29}$$

where

$\eta\ [e\text{V}]$ is the strength coefficient of the P and T-odd interaction,

Table 1.6: Experimental (even-even) and calculated (odd-even beta deformation parameters for a selection of isotopes.

isotope	β_2	β_3	$\mathcal{S}\left(\eta \times 10^8\ e\,\mathrm{fm}^3\right)$	ΔE	Ref.
^{129}Xe	·	·	+1.75	·	[54]
^{199}Hg	·	·	−1.4	·	[54]
^{223}Ra	0.125	0.100	+500	50.2	[55, 54]
^{224}Ra	0.154	0.097	·	·	[79]
^{225}Ra	0.143	0.099	+1100	55.2	[55, 54]
^{229}Pa	0.176	0.082	+300000	0.22	[55, 54]

ᵃ Calculated using one-tailed Gaussian statistics.

e is the elementary charge,

β_2 [dimensionless] is quadrupole moment deformation parameter,

Z [dimensionless] is the number of protons in the nucleus,

A [dimensionless] is the number of protons + neutrons in the nucleus,

$r_0 = 1.2$ fm is the internucleon distance, and

ΔE [eV] is energy difference between the parity doublet states of the nucleus.

The deformation parameters are found by Coulomb excitation experiments with isotopes with even numbers of neutrons and protons ("even-even"). The deformation parameters of even-odd isotopes such as ^{225}Ra are inferred from these measurements or calculated. A selection of deformation parameters for several isotopes is given in Table 1.6.

1.8 Thesis outline

This thesis details my work on high voltage development and precision spectroscopy. So far, I've discussed electric dipole moments and discrete symmetry violation in general. In Chapter 2, I will describe the radium experiment and associated systematic effects. Chapter 3 is about my work in developing a new pair high voltage electrodes to use in the radium experiment. I discuss my efforts using laser induced fluorescence (LIF) to measure the branching ratios of a cycling transition for an improved laser-cooling scheme

for the radium experiment in Chapter 4. In Chapter 5, I will detail isotope harvesting studies at the Facility for Rare Isotope Beams (FRIB) for harvesting radium for EDM measurements in the future. I take a detour in Chapter 6 to describe my computational and experimental work in precision gamma-ray intensity measurements for nuclear security applications. Finally, I offer concluding thoughts and explicitly list my personal contributions to the experiments described in this thesis in Chapter 7.

CHAPTER 2

INTRODUCTION TO THE RA EDM EXPERIMENT

2.1 Motivation

The atomic EDM of ^{225}Ra (nuclear spin $I = 1/2$) is enhanced by the octupole deformation ("pear shape") of its nucleus. Radium-225 has a 55 keV parity doublet ground state structure, compared to approximately 1 MeV in spherically symmetric nuclei [80]. The nuclear Schiff moment of ^{225}Ra is predicted to be up to three orders of magnitude larger than that of diamagnetic atoms with spherically symmetric nuclei [54, 73, 74, 76]. These effects greatly enhance experimental sensitivity to the atomic EDM.

2.1.1 Laser-cooled electric dipole moment searches

In the ^{199}Hg and ^{129}Xe EDM experiments, the atoms are contained within vapor cells. This technique allows the spin precession frequency of a large sample of atoms to be repeatably measured. The sample size N, spin precession time τ, and integration time T are large. The leading systematic uncertainty for both the mercury and xenon experiments is related to high voltage-correlated motion of the vapor cells [46, 47].

The vapor pressure of ^{225}Ra is too low for a radium vapor cell. Instead, atoms are heated up in an oven to generate an atomic beam, and a system of laser cooling and trapping is needed to place the atoms in an optical dipole trap between two high voltage electrodes in a background-shielded "science chamber". The ODT is a linearly polarized 1550 nm laser detuned far below the atom resonant transition frequency. Detuning the laser far below the transition frequency attracts the atoms to the ODT intensity maximum and reduces atom heating from scattered laser photons [81].

The Ra EDM laser trap confines the atoms to a 100 μm diameter cloud [48]. The small atom volume is advantageous for maintaining a highly uniform electric and magnetic

field throughout the cloud. Vapor cells, by contrast, can be tens of millimeters in diameter, and atoms may experience significantly different fields at different locations in the cell volume. A new EDM measurement of ^{171}Yb at the University of Technology and Science of China (USTC) will use a cooling and trapping setup similar to the Ra EDM experiment.

The laser trapping approach faces the challenge of efficiently collecting atoms exiting the oven. The efficiency of trapping ^{225}Ra atoms is on the order of parts per million [82], resulting in an ODT population of only several hundred atoms. The ODT trap lifetime limits each spin precession frequency measurement to approximately twenty seconds [48].

There are three ODT systematic effects that must be considered. First, circularly-polarized light from the ODT laser causes Zeeman splitting of the atoms, causing a vector light shift [81]. The vector light shift $\Delta \nu_V$ [Hz] is given by the following:

$$\Delta \nu_V = \nu_V(P) \times \left(m_f \, P_h \, \hat{k} \cdot \hat{B} \right), \tag{2.1}$$

where

$\nu_V(P)$ [Hz] is the vector light shift scale factor at laser power P [W],

m_F [dimensionless] is the projection of the intrinsic angular momentum along the DC magnetic field axis,

P_h [dimensionless] $\in [0,1]$ is the fraction of circular polarization,

$\hat{k}$ [dimensionless] is the ODT axis, and

$\hat{B}$ [dimensionless] is the DC magnetic field axis.

We try to minimize this effect by suppressing residual circular polarization in the ODT beam and by aligning the ODT perpendicular to the magnetic field. The upper bound of this effect on the Ra EDM experiment is calculated to be $< 10^{-25}$ e cm [48].

Second, the DC electric field can cause significant mixing of opposite-parity atomic

states, or Stark mixing. This effect is called the Stark light shift $\Delta\nu_{\mathrm{S}}$ [Hz]:

$$\Delta\nu_{\mathrm{S}} = \nu_1\left(\hat{b}\cdot\hat{\sigma}\right)\left(\hat{\epsilon}\cdot\hat{E}\right) + \nu_2\left(\hat{b}\cdot\hat{E}\right)(\hat{\epsilon}\cdot\hat{\sigma}) ,\tag{2.2}$$

where

ν_1, ν_2 [Hz] are the Stark interference scale factors,

$\hat{b} = \hat{k}\times\hat{\epsilon}$ [dimensionless] is the AC magnetic field of the ODT,

$\hat{\sigma} = \hat{B}$ [dimensionless] is the spin quantization axis, equivalent to the DC magnetic field axis,

$\hat{\epsilon}$ [dimensionless] is the laser polarization direction, and

$\hat{E}$ [dimensionless] is the DC electric field axis.

This effect is similar to the vector light shift in that it is suppressed by appropriately oriented ODT and DC magnetic field axes and by using a linearly-polarized ODT laser. As I will discuss in Section 2.4, we align $\vec{E}$ parallel or antiparallel to the DC magnetic field. The Ra EDM Stark shift systematic uncertainty is calculated to be $< 10^{-25}$ e cm [48].

The Stark mixing systematic is sensitive to the alignment of the DC electric field. In Section 2.5 I will use finite element modeling to demonstrate the effect of the electric field for a range of electrode misalignments.

Atoms with nuclear spin $I \geq 1$ undergo a quadratic Stark shift proportional to the square of the applied electric field [81, 83]. ^{225}Ra is spin-1/2, so it does not experience a quadratic Stark shift.

However, radium atoms may be repelled from the center of the ODT by E^2-proportional effects other than the quadratic Stark shift. The field gradient would cause different spin precession frequencies. Under an asymmetric electric field reversal, this will introduce a systematic mimicking an EDM signal. In the most recent ^{225}Ra measurement, the field reversal asymmetry was 0.7%, resulting in a systematic uncertainty of 10^{-25} e cm [48]. This systematic scales with the statistical sensitivity, for example improving the sensitivity of the measurement by a factor X also reduces the E^2 effect by factor X. The systematic
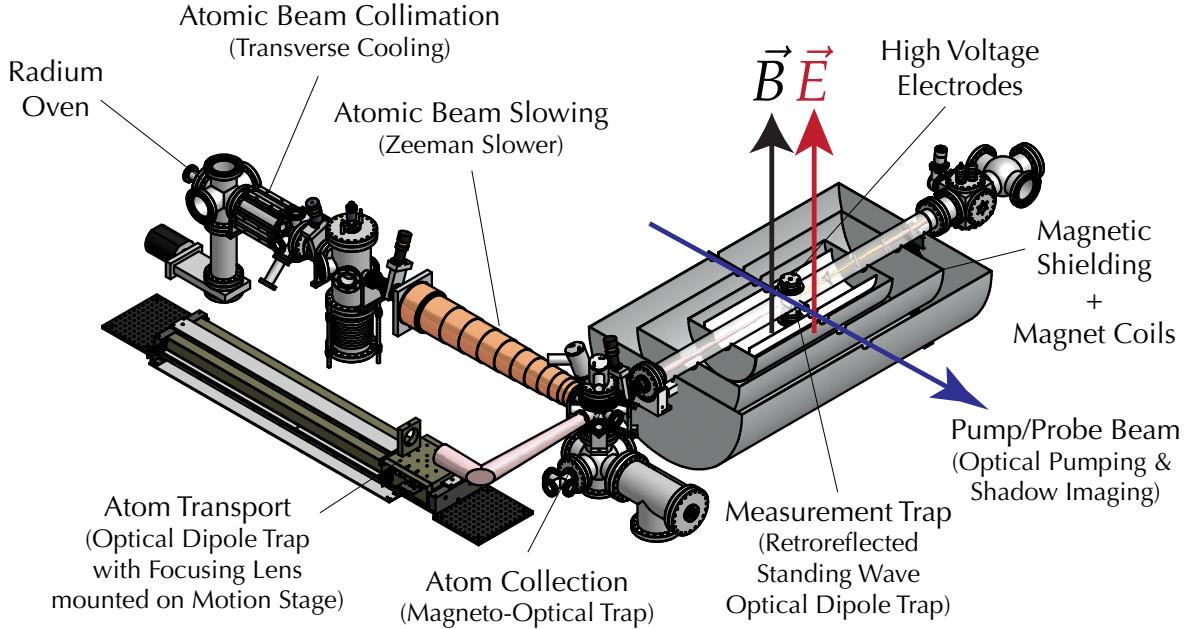
Figure 2.1: The Ra EDM experimental apparatus.

will be suppressed even further as the ODT is improved to confine the atoms to a smaller volume.

2.1.2 Sensitivity to experimental parameters

The Ra EDM experiment (Argonne National Lab, Michigan State University) searches for the EDM of ^{225}Ra by measuring the spin precession frequency of ^{225}Ra in a controlled, uniform magnetic and electric field between two high voltage electrodes in an optical dipole trap. EDM searches are performed at Argonne National Lab (ANL). Offline upgrades such as the high voltage development discussed in this thesis are carried out at Michigan State University (MSU). In the proof of principle measurement, the EDM upper limit was measured to 5.0×10^{-22} e cm at the 95% confidence level (CL) [65]. This was reduced to 1.4×10^{-23} e cm in the subsequent run [48]. Hereafter we will refer to these as the 'first generation' measurements.

The statistical sensitivity of our measurement is estimated by the quantum projection

noise-limited EDM standard error σ_{EDM} [e cm]:

$$\sigma_{\text{EDM}} = \frac{\hbar}{2E\sqrt{\epsilon N T \tau}}\,, \tag{2.3}$$

where

E [V/cm] is the external electric field,

$\hbar$ [eV s] is the reduced Planck constant,

ϵ [unitless] is the atom detection efficiency,

N [unitless] is the number of atoms per sample,

T [s] is the total measurement time, and

τ [s] is the measurement time per cycle.

As seen in Equation 2.3, the EDM statistical sensitivity scales linearly with the electric field strength. The Ra EDM experiment will be significantly improved with targeted upgrades to the experimental apparatus over the next several 'second generation' measurements. In particular, we will use a new atom detection method to increase ϵ and new electrodes to increase E.

We will surpass the 10^{-25} e cm sensitivity level during this phase and the ^{225}Ra EDM limit will constrain hadronic CP-violating parameters alongside other EDM experiments. For example, a radium EDM measurement of 10^{-25} e cm will improve the constraint on the tensor electron-nucleon interaction C_T by more than an order of magnitude within the framework of a global EDM analysis [59, 6].

2.2   Overview of experimental apparatus

A schematic of the Ra EDM experimental apparatus is shown in Figure 2.1. Radium is packaged as nitrate salt and loaded into the oven with metallic barium chips. The oven is heated to 350–500 °C to emit an atomic beam from the oven nozzle. The nozzle has a length of 83 mm and a diameter of 2 mm, or a nozzle ratio of $\gamma = 2/83 = 0.024$ [82].

2.2.1 Laser cooling and the Zeeman Slower

The atomic beam is collimated in the chamber adjacent to the oven by laser light from a titanium sapphire (Ti:Saph) laser, oriented transverse to the beam and tuned to the $^1S_0 \rightarrow {}^3P_1^o$ transition at 714 nm.

Then the atoms enter the Zeeman Slower section, where they are slowed ("cooled") along the atomic beam axis by a counterpropagating laser beam. In the current "red" slower configuration, atoms are slowed over a length of one meter by lasers resonant with the $^3P_1^o$ transition ($\lambda = 714$ nm, $\tau = 420$ ns). The Doppler shift of the atom excitation frequency is compensated by a Zeeman shift from a calibrated magnetic field gradient that is generated by a tapered solenoid.

For the following discussion we will work in the dipole approximation limit $\lambda \gg a_0$, where $a_0 = 5.292 \times 10^{-11}$ m is the Bohr radius. When a two-level atom with states $|1\rangle$ and $|2\rangle$ interacts with light in an electric field $\vec{E}$ that is resonant with the transition frequency between the two states, it will excite and deexcite between the levels. The excitation rate occurs at the Rabi frequency Ω [rad/s] [84]:

$$\Omega = \frac{\langle 1|e\vec{r}\cdot\vec{E_0}|2\rangle}{\hbar} = \frac{e\mathcal{X}_{12}\left|\vec{E_0}\right|}{\hbar} \, , \tag{2.4}$$

$$\mathcal{X}_{12} = \langle 1|x|2\rangle \, , \tag{2.5}$$

$$\vec{E} = \vec{E_0}\cos(\omega t) \, , \tag{2.6}$$

where

e [C] is the electron charge,

$\vec{r}$ [m] is the position of the electron with respect to the nucleus,

ω [rad/s] is the angular frequency of the photon, and

$\vec{E_0}$ [V/m] is the electric field amplitude.

The matrix element $\mathcal{X}_{12}$ can be expressed in terms of the likelihood of exciting an

Table 2.1: Radium Zeeman slower properties for the current red cycling transition and the planned blue cycling transition.

transition	wavenumber $\overline{\nu}$ (cm^{-1})	wavelength λ (nm)	lifetime τ (ns)	recoil v_r (cm/s)	scatter R (s^{-1})	saturation I_0 (mW/cm^2)
$^1S_0 \to {}^3P_1^o$	13999.38	714	420	0.25	1.2×10^6	0.136
$^1S_0 \to {}^1P_1^o$	20715.71	483	5.5	0.37	9.1×10^7	33.6

atom from $|1\rangle$ to $|2\rangle$, or Einstein B-coefficient:

$$B_{12} = \frac{\pi e^2 |\mathcal{X}_{12}|^2}{\epsilon_0 \hbar^2} \tag{2.7}$$

The rate that atoms absorb and re-emit resonant laser photons, or the scattering rate R, is given by:

$$R = \frac{\Gamma}{2} \frac{\Omega^2}{\delta^2 + \Omega^2/2 + \Gamma^2/4}, \tag{2.8}$$

where $\Gamma = 1/\tau \left[s^{-1}\right]$ is the decay rate of the transition. The Rabi frequency is related to the saturation intensity $I_s(\omega) \left[\text{W/m}^2\right]$:

$$I_s(\omega) = \frac{\hbar \omega A_{21}}{2\sigma(\omega)} = I_0 \frac{2\Omega^2}{\Gamma^2}, \tag{2.9}$$

$$I_0 = I_s(\omega_0) \tag{2.10}$$

$$= \frac{\pi}{3} \frac{hc}{\lambda^3 \tau}, \tag{2.11}$$

where

$A_{21} \left[s^{-1}\right]$ is the spontaneous emission rate (Einstein A-coefficient) from $|\,2\,\rangle \to |\,1\,\rangle$,

$\sigma(\omega) \left[\text{m}^2\right]$ is the absorption cross section at angular frequency ω,

λ [m] is the wavelength of the transition, and

$\tau = 1/A_{21}$ [s] is the lifetime of the transition.

Now R can be expressed in terms of the laser intensity. The force F [N] exerted on an atom by a counterpropagating laser photon with momentum $\hbar k$ [kg m/s] is given by the following:

$$F = \hbar k \times R = \hbar k \frac{\Gamma}{2} \frac{I/I_0}{1 + I/I_0 + 4\delta^2/\Gamma^2} \tag{2.12}$$

28
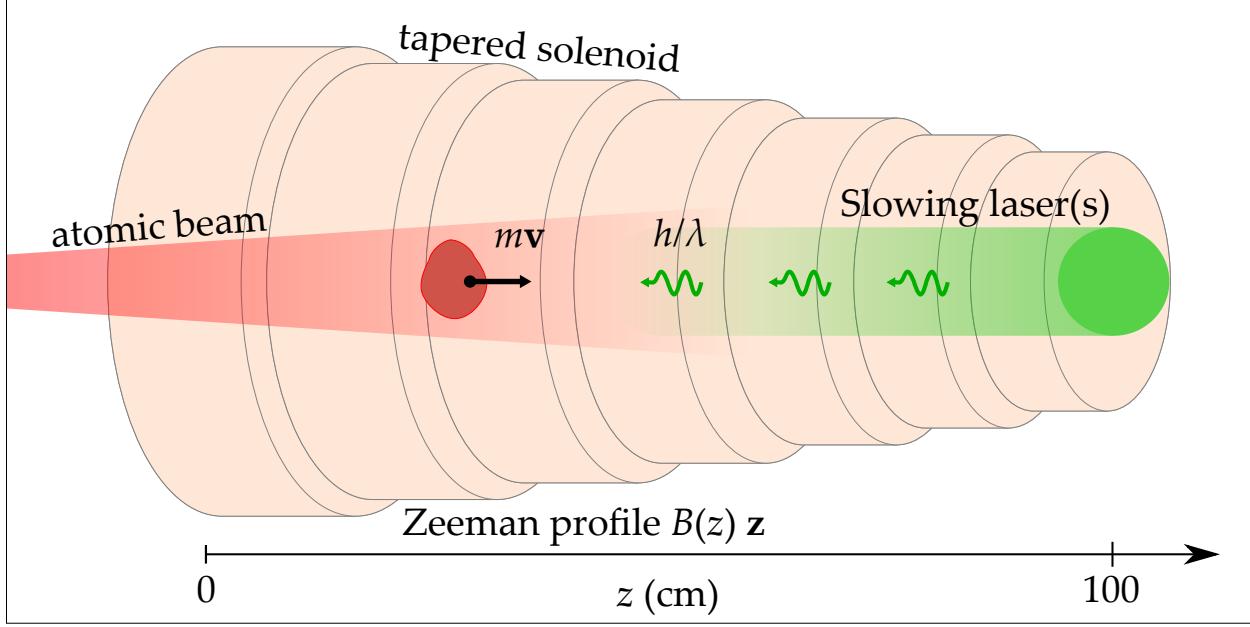
Figure 2.2: A cartoon of the radium Zeeman slower. $\vec{\mathbf{p}} = m\vec{\mathbf{v}}$ is the momentum of a radium atom with mass m and velocity $\vec{\mathbf{v}}$ and $\vec{\mathbf{p}}_\gamma = -h/\lambda \, \hat{z}$ is the momentum of a slowing laser photon with wavelength λ.

When an atom emits an absorbed photon, it experiences a "momentum kick" characterized by the recoil velocity v_r [m/s]:

$$\frac{v_r}{2\tau} = a_{\max} = \frac{F_0}{m} = \frac{\hbar k}{m} \frac{\Gamma}{2},\tag{2.13}$$

where $a_{\max}$ $\left[\text{m s}^{-2}\right]$ is the maximum acceleration and F_0 [N] is the maximum force exerted on the atom. From Newtonian kinematics we can estimate the length scale L_0 [m] over which an atom with initial speed v_0 [m/s] can be stopped by the laser beam:

$$L_0 = \frac{v_0^2}{a_{\max}}\tag{2.14}$$

The atoms are exposed to a counterpropagating, circularly-polarized laser as they move through the solenoid, as shown in Figure 2.2. The solenoid magnetic field is tuned to compensate for both the atom Doppler shifts (velocity-related) and the Zeeman shifts (quantum number related). The atoms absorb and emit the laser photons at a rate determined by the lifetime of the optical cycling transition [85]. Each photon absorption-emission cycle gives a small momentum kick to the atom, slowing it down.

The Ra EDM Zeeman slower uses the $^1S_0 \longleftrightarrow {}^3P_1^o$ optical cycling transition to trap atoms with initial speeds up to 55 m/s. A one meter-long, tapered solenoid generates a magnetic field gradient along the atomic beam axis. The magnetic field causes a Zeeman shift E_z [J] in the energy of the atom:

$$E_z = g_F \, m_F \, \mu_B \, B_z \,, \tag{2.15}$$

$$g_F = \frac{F(F+1) + J(J+1) - I(I+1)}{2F(F+1)} \, g_J \,, \tag{2.16}$$

$$g_J = \frac{3}{2} + \frac{S(S+1) - L(L+1)}{2J(J+1)} \,, \tag{2.17}$$

where

g_F, g_J [unitless] are the Landé g-factors,

μ_B [J/T] is the Bohr magneton,

$F = I + J$ [unitless] is the total angular momentum,

$J = L + S$ [unitless] is the electron total angular momentum,

L, S [unitless] is the electron orbital angular momentum and spin, and

B_z [T] is the Zeeman slower magnetic field.

In general, the total Zeeman-shifted energy ΔE_z must account for the energy shift of the excited state and the ground state. For our case of an optical cycling transition with $^1S_0$ atoms, the Zeeman shift is dominated by the excited state contribution and I make the approximation $\Delta E_z \approx E_z$.

The excitation angular frequency ω of the atom is modified by a Doppler and Zeeman contribution, shifting it from the unperturbed angular frequency ω_0:

$$\omega + kv = \omega_0 + \Delta E_z / \hbar \tag{2.18}$$

To keep the atom resonant with the laser, the magnetic field profile is given by:

$$B(z) = B_0 \left(1 - \frac{z}{L_0} \right)^{1/2} + B_{\text{bias}} \,, \tag{2.19}$$

$$B_0 = \frac{hv_0}{\lambda \mu_B} \tag{2.20}$$
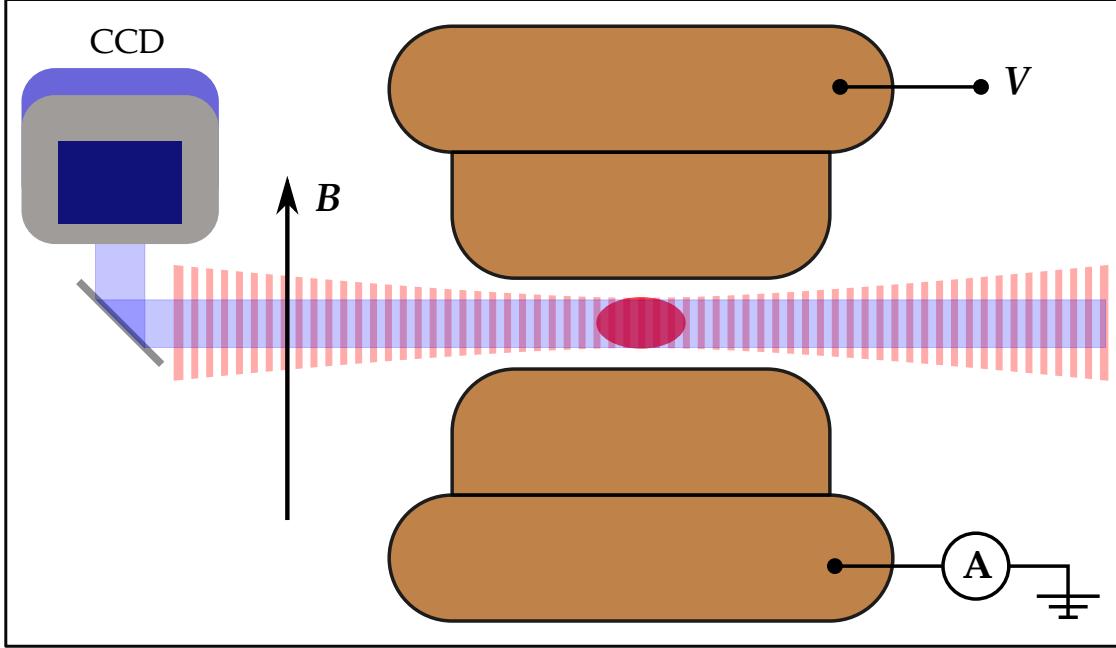
Figure 2.3: Cloud of radium atoms trapped between high voltage electrodes in optical dipole trap.

For the $^3P_1^o$ transition, $B_0 = 5.5\,\text{mT} = 55\,\text{G}$. This produces a Zeeman shift $\nu = E_z/h \approx 80\,\text{MHz}$.

2.2.2 Laser trapping

The Zeeman slower cools a small fraction of the atom beam to sufficiently low speeds. These are trapped by a three-dimensional magneto-optical trap (3D MOT) downstream of the Zeeman Slower (bottom-center of Figure 2.1). The MOT is formed by three lasers slightly detuned from the $^3P_1$ transition. The lasers are mutually perpendicular and intersect. The laser paths are immersed within a magnetic field gradient of approximately 0.5 Gauss / cm [86]. The trapping efficiency is a few parts per million [82].

A 1550 nm laser is overlapped with the center of the MOT. The MOT lasers and field are switched off and the atoms are now attracted to the focus of the 1550 nm laser. This laser is an optical dipole trap with a 500 μK trapping depth. The location of the beam focus is controlled by a lens on a translation stage.

The "Bus" ODT transports the atoms from the MOT into a nonmagnetic, borosilicate glass tube chamber called the "science chamber." The tube is surrounded by concentric nickel-alloy "mu" metal, so-named for its high relative permeability $\mu_r \approx 20000$. There are three layers of mu-metal surrounding the tube. The mu-metal is de-Gaussed by running a 10 Hz AC current through wires coiled around the mu-metal. The de-Gaussed shield suppresses low-frequency external fields by a factor of $\approx 10^4$. This reduces Earth's magnetic field from 500 mGauss to 50 μGauss inside the science chamber.

The atoms are transported to the center of the science chamber between two metal high voltage electrodes. The electrodes are mounted in a Macor holder within the tube, separated by a distance on the order of millimeters. The electrodes are discussed in detail in Chapter 3. Inside the science chamber, we apply a uniform 10 mGauss field in the vertical direction.

The Bus ODT is overlapped with a second, perpendicular "Holding" ODT in the electrode gap. The Holding ODT is a 1550 nm laser with a 100 μm diameter at the focus. The Bus ODT is shuttered at this point and the atom cloud is in position for spin precession frequency measurements.

Figure 2.3 shows a schematic of the EDM measurement. The atoms are polarized along the axis of the Holding ODT with a pulse from the collinear "Pump/Probe" beam tuned to the $^1S_0 \rightarrow {}^1P_1^o$ (483 nm) transition. The atomic spins precess at a frequency of ≈ 20 Hz in the Holding ODT. A uniform electric field is generated parallel to the applied magnetic field by charging one of the electrodes with a bipolar high voltage power supply. The field direction is reversed by reversing the polarity of the power supply. The Ra EDM measurement aims to detect a frequency difference in the atom spin precession when the electric field is aligned and anti-aligned with the magnetic field.

Systematic effects related to laser trapping and the EDM apparatus were studied by previous Ra EDM graduate students Mukut Kalita, Richard Parker, and Ibrahim Sulai. Their findings are discussed in great detail in their theses [86, 87, 88].

2.2.3   The 2015 Radium-225 measurement

The second and most recent ^{225}Ra EDM measurement was performed in the summer of 2015. The high voltage electrodes supplied an electric field of 15 kV/ 2.3 mm = 6.5 kV/mm [48]. A single radium oven load of 9 mCi was used, simplifying the previous experiment which used separate oven loads of 3 mCi and 6 mCi [65].

The result of the most recent measurement, an EDM upper limit of $d(^{225}\text{Ra}) = 1.4 \times 10^{-23}$ e cm), improves the constraint of the former limit by a factor of 36 [48]. General refinements in laser stability, data acquisition, analysis, and the apparatus between the first and second experiment contribute to the improvement. The largest source of improvement was a factor of 10 increase in the atom trap lifetime of the atoms (τ in Equation 2.3). This was achieved by improving the stability of the Holding ODT and significantly reducing the science chamber vacuum pressure.

I'll highlight targeted upgrades to the EDM experimental apparatus for the next measurement in Section 2.3. Then I'll describe the EDM measurement scheme in Section 2.4.

2.3   Targeted upgrades for an improved electric dipole moment measurement

2.3.1   Atom cooling with an improved Zeeman slower

We used the $^1\text{S}_0 \rightarrow {}^3\text{P}_1^o$ transition to slow the atoms in the first generation measurements. This cycling transition only requires a single repump laser tuned to the $^3\text{D}_1 \rightarrow {}^1\text{P}_1^o$ transition. The drawback is that less than 1% of the atoms exiting the oven are sufficiently slowed to be captured. The details of the operation of a Zeeman slower are discussed in Section 2.2.1.

We will improve the Zeeman slower by using the faster-cycling $^1\text{S}_0 \rightarrow {}^1\text{P}_1^o$ transition to slow more than half of all the atoms exiting the oven. This will increase the number of atoms that we can measure in the science chamber (N in Equation 2.3). The improved "blue" slower will operate simultaneously with the current "red" slower. The blue slower

optical cycling scheme requires three repump lasers.

I built a fluoroscopy setup to measure the additional repump channels to verify the feasibility of the blue slower scheme. The branching ratios to these additional D states were predicted to be favorable [89]. Prior to my work, the D state branching ratios were not yet experimentally verified [89]. I'm the third author of our publication describing the branching ratio measurement and results [90]. My contribution to the radium branching ratio measurement is further discussed in Chapter 4.

2.3.2 Atom detection efficiency with Stimulated Raman Adiabatic Passage

For the first generation EDM experiments, we measured the atom spin precession by pulsing the atoms with circularly polarized (σ^+) laser light tuned to the $^1S_0$ ($F = 1/2$) $\rightarrow$ $^1P_1^o$ ($F' = 1/2$) transition, where $F = I + J$ is the total angular momentum summing nuclear spin I and total electronic angular momentum J. The atoms scatter an average of three photons before decaying from the excited state to a ground state that we cannot utilize for spin precession frequency detection, *i.e.* a dark state.[i]

To increase the number of photon scatters per atom, and thus the detection efficiency in Equation 2.3, we will use a hyperfine magnetic sublevel-selective measurement scheme with the $^1S_0$ ($F = 1/2$) $\rightarrow$ $^1P_1^o$ ($F' = 3/2$) transition. With this method, the atoms are expected to scatter an average of one thousand photons.

Our strategy to measure the spin-selective $F' = 3/2$ transition is to use the technique of Stimulated Raman Adiabatic Passage (STIRAP). This technique uses two lasers: one tuned to the transition $| 1 \rangle \rightarrow | 2 \rangle$, and one tuned to $| 2 \rangle \rightarrow | 3 \rangle$. By pulsing the atom cloud with the two lasers separated by the time interval δ [μs], we can transfer the population of state $| 1 \rangle$ directly to state $| 3 \rangle$.

---

[i]Atoms may also decay to the equally unusable metastable $^3D_1$ state $\approx 0.1\%$ of the time.

These are the proposed ^{225}Ra detection scheme states:

$$| \, 1 \, \rangle = {}^{1}\!S_{0} \ (F = 1/2; \ m_{F} = -1/2)$$

$$| \, 2 \, \rangle = {}^{1}\!P_{1}^{o} \ (F = 1/2; \ m_{F} = +1/2)$$

$$| \, 3 \, \rangle = {}^{3}\!D_{1} \ (F = 1/2; \ m_{F} = -1/2) \, ,$$

The spin-selective atom detection is then carried out by probing the $^{1}\!S_{0} \ (F = 1/2; \ m_{F} = +1/2) \rightarrow \ {}^{1}\!P_{1}^{o} \ (F' = 3/2; \ m_{F'} = +3/2)$ transition with σ^{+} circularly-polarized light.

Tenzin Rabga led the recent effort resulting in significant progress towards achieving spin-selective STIRAP with radium. This work is discussed in great detail in his thesis [91].

2.3.3 Higher electric field strength

The first generation experiments used an electric field of 6.7 kV/mm and 6.5 kV/mm. We used a pair of oxygen-free, electropolished copper electrodes. The copper electrodes were tested (conditioned) to fields as high as 10 kV/mm in a test apparatus at ANL. However, they were unstable at those fields when they were installed in the EDM apparatus. The installation procedure is invasive and requires a teardown of the vacuum equipment on the opposite side of the MOT chamber in Figure 2.1.

After the most recent EDM measurement, four pairs of niobium electrodes and two pairs of titanium electrodes were prepared at Jefferson Lab and sent to MSU. I built a high voltage test station and conditioned new titanium and niobium electrode pairs at MSU. I improved the conditioning procedure and developed analysis code that can be run concurrently with conditioning to inform the testing. To store, transport, and install the electrodes in high voltage setups, I designed clean rooms, storage containers, and installation procedures.

I transported a pair of conditioned niobium electrodes to the EDM apparatus. The electrodes were conditioned to 20 kV/mm at MSU. I built a clean room around the teardown section of the EDM apparatus and installed the electrodes in the EDM apparatus and revalidated them to 20 kV/mm. This will more than triple the electric field strength (E in Equation 2.3). Since the EDM sensitivity is linearly proportional to the electric field strength, it should also triple the sensitivity of the next EDM measurement. The details of this work is discussed in Chapter 3.

2.3.4 Increasing Radium-225 availability

^{225}Ra was procured from Oak Ridge National Lab (ORNL) for the first two EDM experiments. The new Facility for Rare Isotope Beams (FRIB) linear accelerator at MSU is approaching full operation. Isotope production was recently benchmarked at the NSCL for ^{47}Ca to inform future isotope harvesting at FRIB [92]. When fully operational, FRIB is expected to be capable of supplying at least 4.9 mCi of ^{225}Ra per week [93], and significantly more for a dedicated radium harvesting campaign.

FRIB-harvested radium will allow us to perform an EDM measurement with larger source loads more frequently. First we will develop the extraction and sample preparation procedure, starting with stable calcium as a radium surrogate. Calcium, like radium, has a strong $^1\mathrm{P}_1^o$ cycling transition and can be used in atomic beam studies.

We're developing an atomic beam fluorescence (ABF) study at MSU that will calibrate the harvesting procedure. Our goal is to compare the initial harvested atom source size to the atom rate it produces in an effusive oven that will be measured with laser induced fluorescence (LIF). The details of my ABF measurements and analysis are in Chapter 5.

2.4 Experimental requirements

2.4.1 Measurement technique

The EDM couples to an external electric field analogously to the coupling of the magnetic dipole moment to an external magnetic field. The Hamiltonian $\mathcal{H}$ [eV] of an atom in the presence of a perfectly uniform electric and magnetic field is given by:

$$\mathcal{H} = -\mu\left(\frac{\vec{\mathbf{I}} \cdot \vec{\mathbf{B}}}{I}\right) - d\left(\frac{\vec{\mathbf{I}} \cdot \vec{\mathbf{E}}}{I}\right), \tag{2.21}$$

where

$\mu = -2.3 \times 10^{-8}$ eV/T is the nuclear magnetic moment of ^{225}Ra [94],

$\vec{\mathbf{I}}$ is the nuclear spin,

$\vec{\mathbf{B}}$ [T] is the applied magnetic field,

d [e cm] is the atomic EDM, and

$\vec{\mathbf{E}}$ [V/cm] is the applied electric field.

The ^{225}Ra atomic spins will precess with frequency ω_+ (ω_-) when $\vec{\mathbf{E}}$ is parallel (antiparallel) to $\vec{\mathbf{B}}$:

$$\omega_\pm = \frac{2}{\hbar}(\mu B \pm dE), \tag{2.22}$$

In the most recent Ra EDM experiment we applied a 2.6 μT magnetic field and measured a spin precession frequency of 181.1 ± 1.6 rad/s [48].

We use a pair of identical plane-parallel electrodes to produce a stable, uniform, and symmetric electric field. The spin precession frequency of the atoms is measured in three configurations: with the electric field parallel to the magnetic field, with the electric field antiparallel to the magnetic field, and with no applied electric field. The "field-off" setting is used to control for a systematic effect generated by an imperfect reversal of the electric field. We measure the accumulated spin precession phase for each field configuration. The extracted EDM is proportional to the accumulated phase difference

Table 2.2: Ra EDM systematic requirements at the $10^{-26}\,e$ cm sensitivity level. Detailed systematic limit evaluations for these parameters can be found in previous work [48, 95]. ΔB is determined by Equation 2.29.

description	systematic limit		Section
$\vec{E}$, $\vec{B}$ alignment	θ_E	≤ 2 mrad	2.4.4
polarity imbalance	$\dfrac{\|\Delta E\|}{E}$	$\leq 0.7\%$	2.4.5
electrode magnetic impurity	ΔB	≤ 100 fT[a]	2.4.3
steady-state leakage current	$\bar{I}$	≤ 100 pA[a]	2.4.4
magnetic Johnson noise	$\sqrt{\dfrac{dB_n^2}{d\nu}}$	$\leq 15\ \dfrac{\text{pT}^{\text{a}}}{\sqrt{\text{Hz}}}$	2.4.2

[a] per measurement cycle

between the parallel and antiparallel configurations, $\Delta\phi$ [rad]:

$$d = \frac{\hbar\Delta\phi}{4E\tau} \tag{2.23}$$

With a perfectly uniform and static magnetic field under all configurations, the phase difference between the parallel and antiparallel field configurations is purely due to the EDM interaction with the electric field. A higher electric field will result in a larger accumulated phase and will increase our EDM sensitivity.

During each measurement cycle, one electrode is charged to $\leq +30$ kV (positive polarity) while the other is grounded. The atom trap lifetime is currently about twenty seconds. We expect to increase the trap lifetime to one hundred seconds [81] as improvements are made to the ODT. The charged electrode is then ramped to zero voltage and remains grounded for a period of 60 s while a new sample of atoms is prepared. The cycle restarts and the electrode is charged to the same voltage magnitude at negative polarity. We repeat this process until the atomic oven is depleted after approximately two weeks.

Now we'll discuss EDM measurement systematics related to the high voltage system. Our requirements for each systematic are given in Table 2.2.

The electric field between the electrodes must be symmetric, uniform, and reversible
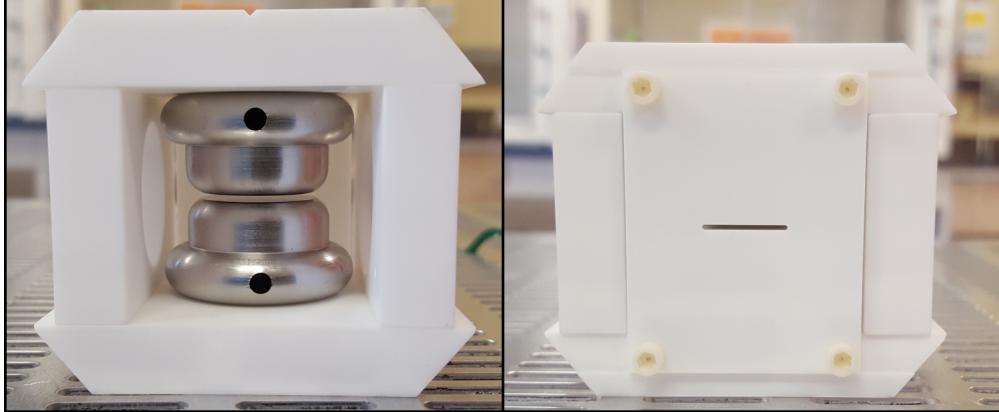
Figure 2.4: Left: assembly of the niobium pair Nb_{56} at 1 mm gap in Macor holder. Right: a slit centered on the gap shields the electrode surfaces from heating by the atom trapping and polarizing lasers.

to minimize systematic effects. The alignment between $\vec{E}$ and $\vec{B}$ is fixed after mounting the electrodes to the Macor holder, as shown in Figure 2.4. In the experimental apparatus, the holder and electrodes rest within a borosilicate glass tube (see Figure 2.1). We will use vector fluxgates with a system of autocollimators to optically determine the field uniformity and alignment for the second generation EDM measurements [96]. The field reversibility is measured with a calibrated high voltage divider (Ross Engineering V30-8.3-A).

2.4.2 Magnetic Johnson noise calculations

Magnetic field fluctuations caused by random thermally-induced currents in the electrodes, or magnetic Johnson noise (MJN), limits the choice of electrode materials and geometries that are suitable for an EDM measurement [97, 98].

In the next two years, we are aiming for a statistical sensitivity of $d \approx 10^{-25}$ e cm or better as improvements in the external electric field and atom detection efficiency are implemented in the second generation measurements. The Ra EDM roadmap includes upgrades over the next five years that will enable an EDM sensitivity as high as $d \approx 10^{-28}$ e cm.

In the presence of perfectly uniform magnetic and electric fields, the atom spin precesses with a frequency given by Equation 2.22. With an applied electric field of 30 kV/mm, I find the following frequency due to an EDM magnitude $d \approx 10^{-25}$ e cm:

$$f(\text{upper limit}) = \frac{4dE}{h} = \frac{4 \times 10^{-25} e \text{ cm} \times 30 \times 10^4 \text{ V/cm}}{4.135 \times 10^{-15} \text{ } eV/\text{Hz}} \approx 2.9 \times 10^{-5} \text{ Hz}$$

The atomic spins precess with a Larmor frequency of approximately 20 Hz in a 10 mGauss laboratory magnetic field. The fractional change in the spin precession frequency due to the EDM is $2.9 \times 10^{-5}/20 \approx 1.5$ ppm. Therefore systematics affecting the spin precession frequency signal should be suppressed to below 150 ppb.

The thermal or Johnson noise in a conductor at position $\vec{r}$ is given by the following:

$$\frac{dB_{n,q}^2}{d\nu} = \frac{\mu_0^2 k_{\text{B}} T}{4\pi^2 \rho} \mathcal{V}_u ,$$
(2.24)

$$\mathcal{V}_u = \int \left| \frac{(\vec{r} - \vec{u}) \times \hat{\mathbf{q}}}{|\vec{r} - \vec{u}|^3} \right|^2 d^3 u ,$$
(2.25)

where

$dB_{n,q}^2/d\nu$ $\left[\text{T}^2 \text{ Hz}^{-1} \right]$ is the magnetic field noise density in direction $\hat{\mathbf{q}}$,

μ_0 $\left[\text{N A}^{-2} \right]$ is the vacuum magnetic permeability,

k_{B} [J/K] is the Boltzmann constant,

T [K] is the temperature,

ρ [Ω m] is the resistivity of the conductor, and

$\vec{u}$ [m] is the location of the infinitesimal conductor volume element.

The resistivities of copper, niobium, and titanium are shown in Table 3.2. For the Ra EDM electrode geometry (Figure 3.1), $\mathcal{V}_x = \mathcal{V}_y = 93.1$ cm^{-1} and $\mathcal{V}_z = 57.2$ cm^{-1} in the vertical direction [99].

With improvements to the thermal stability of the transport beam, we expect to achieve an atom trap lifetime of $\tau = 100$ s. At room temperature ($T = 298$ K), I find the corre-

sponding rms magnetic field noise $\sqrt{B_{n,q}^2}$ [T]:

$$\sqrt{B_{n,q}^2} = \sqrt{\frac{dB_{n,q}^2}{d\nu}} \times \tau^{-1/2} = \sqrt{\frac{\mathcal{V} \times 1.647}{\tau \rho'}} \times 10^{-12} \text{ T}, \tag{2.26}$$

where $\rho' = \rho/(10^{-8}\ \Omega\ \text{m})$. For a pair of niobium electrodes, the magnitude of the magnetic field noise in the vertical direction is:

$$\sqrt{\frac{dB_{n,z}^2}{d\nu}} \text{ (niobium)} = 2.48 \frac{\text{pT}}{\sqrt{\text{Hz}}}$$

With a trap lifetime of 100 s, this gives the following rms magnetic field:

$$\sqrt{B_{n,z}^2} \text{ (niobium)} = \sqrt{\frac{dB_{n,z}^2}{d\nu}} \cdot \frac{1}{\sqrt{100\ \text{s}}} = 2.48 \times 10^{-13} \text{ T} = 2.48 \times 10^{-9} \text{ G}$$

From the rms field and the laboratory magnetic field, I can estimate the per-shot frequency sensitivity δ_f [Hz]:

$$\delta_f \text{ (niobium)} = \frac{2.48 \times 10^{-9} \text{ G}}{10^{-2} \text{ G}} \approx 250 \text{ ppb}$$

The spin precession frequency measurement is repeated many times over the course of the EDM experiment. The total number of spin precession frequency measurements N reduces δ_f to the integrated frequency sensitivity σ_f [Hz]:

$$\sigma_f = \frac{\delta f}{\sqrt{N}} \tag{2.27}$$

For a 15-day EDM measurement, I calculate the following number of spin precession frequency measurements:

$$N = 15 \text{ days} \times \frac{24 \text{ hours}}{\text{day}} \times \frac{60 \text{ minutes}}{\text{hour}} \times \frac{1 \text{ measurement}}{2 \text{ minutes}} \approx 10^4 \text{ measurements.}$$

Our integrated frequency sensitivity must be better than the fractional change in the spin precession frequency due to the EDM, which we found to be ≈ 150 ppb. Therefore the per-shot frequency sensitivity must be better than $150 \text{ ppb} \times \sqrt{10^4} = 15$ ppm. This corresponds to a per-measurement noise of:

$$15 \text{ ppm} \times \left(10^{-2}\ \text{G}\right) \times \sqrt{100\ \text{s}} \times \frac{10^{12}\ \text{pT}}{10^4\ \text{G}} = 150 \frac{\text{pT}}{\sqrt{\text{Hz}}} \tag{2.28}$$
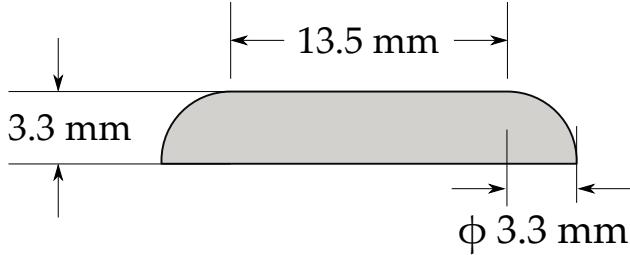
Figure 2.5: One possible electrode design whose volume is a factor of ten smaller than the standard Ra EDM electrode.

Earlier, we saw that the per-shot frequency sensitivity of niobium is $250 \text{ ppb} = 2.48 \text{ pT}/\sqrt{\text{Hz}}$. The magnetic field noise scales as $\rho^{-1/2}$, from which we estimate the per-shot frequency sensitivity of copper and titanium to be $(250 \text{ ppb}) \times \sqrt{15.2/1.543} \approx 780 \text{ ppb}$ and $(250 \text{ ppb}) \times \sqrt{15.2/39} \approx 160 \text{ ppb}$, respectively.

Given these estimates, I expect that MJN will remain a minor source of systematic uncertainty for EDM measurements at the $d \approx 10^{-25} \ e$ cm level. As we approach our long-term goal of $10^{-28}e$ cm, we'll need to modify the electrodes to reduce magnetic noise. For example, Figure 2.5 shows a possible design where the volume of the electrode has been reduced by an order of magnitude, reducing the field noise by approximately a factor of $\sqrt{10}$.

A new electrode geometry could be optimized by rigorous modeling of the field uniformity under a variety of potential electrode misalignments. I discuss this type of analysis I performed for the current Ra EDM electrode geometry in Section 2.5.

2.4.3 Paramagnetic impurities

We consider a potential systematic in which the magnetization of a fraction of the impurities in the electrodes depends on the polarity of the charging current. A sufficiently high concentration of paramagnetic impurities near an electrode primary surface could perturb the magnetic field in the radium cloud region. This would induce a polarity-dependent spin precession frequency mimicking an EDM signal, or "false" EDM

$d_{\Delta B}$ [e cm]:

$$d_{\Delta B} = \frac{\mu \Delta B}{E} \, , \tag{2.29}$$

where

μ is the nuclear magnetic moment,

E is the magnitude of the applied electric field, and

ΔB is the change in local magnetic field under reversal of E.

Impurities in the electrode material are minimized by using high-grade materials, using machine shop tooling that does not embed impurities on the surface, and using polishing and cleaning techniques that remove surface-level contaminants. In the scenario of an applied electric field of 30 kV/mm and a magnetic field change of 100 fT under reversal, I find the following false EDM magnitude:

$$d_{\Delta B} = \frac{2.3 \times 10^{-8} \text{ eV/T} \times 100 \times 10^{-15} \text{ T}}{30 \times 10^{4} \text{ V/cm}} = 7.7 \times 10^{-27} e \text{ cm}$$

Other EDM high voltage systematic requirements are given in Table 2.2. Table 3.1 and Table 3.2 list the material properties and processing techniques that we use. I'll discuss electrode material selection and surface processing in detail in Section 3.1.

2.4.4 Leakage current and field angle

I define leakage current as any current flowing between the electrodes. This includes current flowing through the insulating mount and "field emission" between the two primary surfaces across the electrode gap. An electrode gap of 1 mm is shown in Figure 2.4. Leakage current induces magnetic fields whose properties depend on the magnitude, path, and dynamic properties of the current.

I define an electrode discharge as a transient surge in field emission between the electrode surfaces. Discharges are discussed in detail in Section 3.4.4. In the event of a

E, B alignment requirement for 10^{-26} e cm
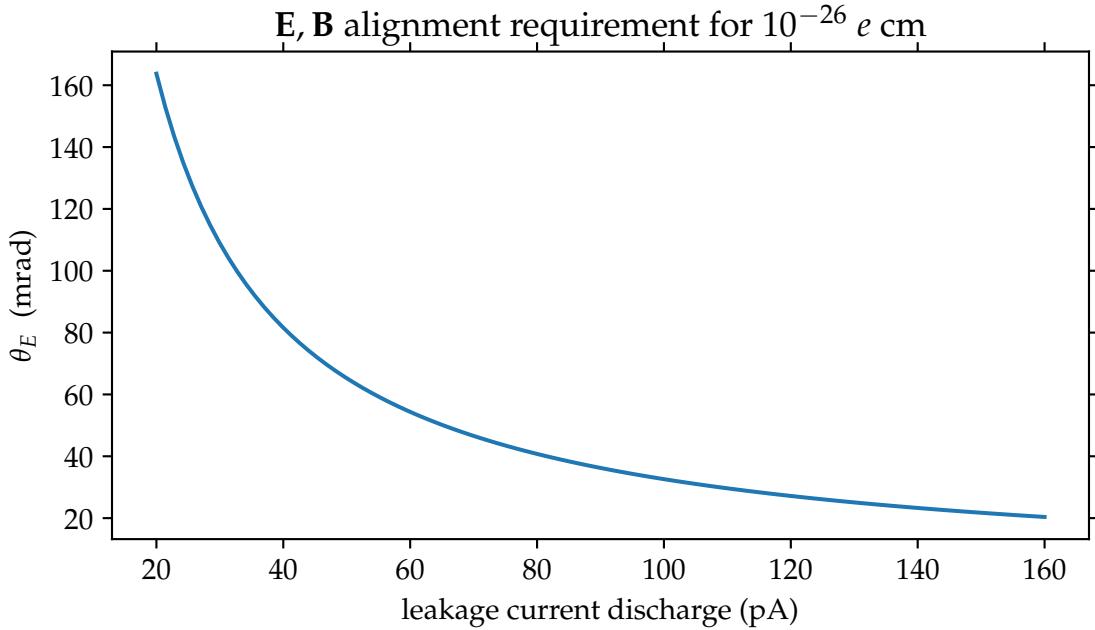
Figure 2.6: A plot of the maximum allowed field misalignment over a range of leakage currents for a targeted 10^{-26} e cm sensitivity.

discharge close to the location of the atom cloud, the atoms will interact with the induced magnetic field. The interaction will manifest as a change in the spin precession frequency of the atoms. If the discharge rate is correlated with the polarity of the electrodes, it will introduce a systematic shift in the EDM signal.

To study the effect of leakage current on the spin precession frequency, we model the discharge as a thin wire of current traveling a distance r [m] from the cloud. This consequent "false" EDM signal $d_{\bar{I}}$ [e cm] is given by [48]:

$$d_{\bar{I}} = \frac{\mu \vec{\mathbf{B}}}{E} \cdot \hat{\mathbf{B}} = \frac{\mu}{E} \frac{\mu_0 \bar{I}}{2\pi r} \sin \theta_E \,, \tag{2.30}$$

where

$\mu = -2.3 \times 10^{-8}$ [eV/T] is the nuclear magnetic moment of ^{225}Ra,

$\bar{I}$ [A] is the steady-state leakage current, and

θ_E [rad] is the angle between the applied electric and magnetic fields.

The field alignment tolerance for an EDM sensitivity of 10^{-26} e cm is plotted as a func-

tion of the leakage current in Figure 2.6. With an applied electric field of $E = 30$ kV/mm, a discharge-atom distance of $r = 50$ μm, $d_{\overline{I}} = 10^{-27}$ e cm, and a leakage current $\overline{I} = 100$ pA, I find a maximum misalignment of 30 mrad.

2.4.5 Polarity imbalance in the electric field

Any change in the EDM spin precession frequency arising from a difference in the strength of the electric field between negative and polarity is proportional to the square of the electric field [48, 46]. This is a property of the high voltage system. In the Ra EDM measurement, the polarity imbalance is symmetric to within 0.7%.

2.5 Effect of Electrode Misalignments

We use identical, plane-parallel electrodes so that the reversible field is uniform and symmetric as the electrodes alternate roles as cathode and anode every EDM measurement cycle. The primary surface, seen as the top surface in Figure 3.1, is flat and 16 mm in diameter. The rounded edges have 4 mm circular radial curvatures.

The Ra EDM experiment requires an applied electric field that is symmetric, uniform, and reversible in the center of the electrode gap where the spin precession frequency of the 50 μm diameter radium cloud is measured. Our electrode geometry reliably meets these requirements at field strengths of 12–30 kV/mm.

Systematic effects arising from asymmetric field reversal must continue to be reduced as the experimental sensitivity improves. In the current measurement scheme, one electrode is permanently grounded and the other electrode is charged by a bipolar power supply. We will design a more symmetric apparatus that allows us to alternate the charged and grounded electrodes using high voltage switches and a unipolar 50 kV power supply in the next phase of high voltage development.

I demonstrated the effect of steady-state leakage current on the spin precession frequency with a simple wire model in Section 2.4.4. In Section 2.5.1 I will show that the
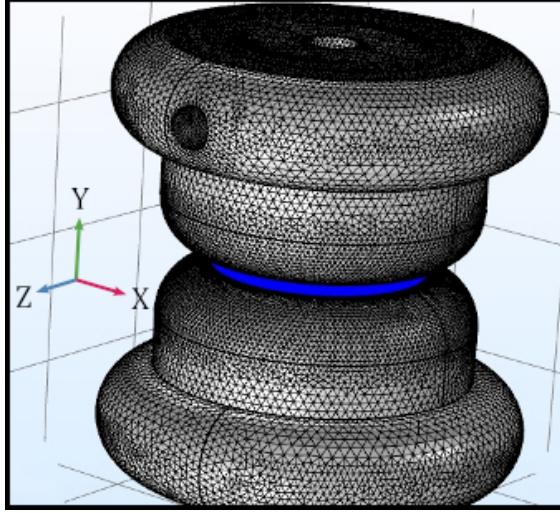
Figure 2.7: A software meshed model of the electrode pair and coordinate system. The finer-meshed electrode gap region is shaded blue.

electrode electric field matches that of the ideal infinite-plane capacitor in the atom cloud region using finite element modeling. We will use the methods developed here to optimize electrode geometries as the experiment sensitivity improves.

2.5.1 Description of the electric field finite element analysis

I modeled the high voltage electrodes in the finite element analysis software COMSOL Multiphysics (version 5.3) to study the electrostatic field uniformity under a range of potential electrode misalignments. In the model, the electrodes are surrounded by a perfect vacuum. The electrode gap size is set to a 1 mm gap size and the top electrode is charged to -30 kV for a nominal electric field of $E_0 = 30$ kV/mm.

My simulations use the Extremely Fine settings with Size Expression increased to 4×10^{-4} in the gap region and Resolution increased to 200 along the upper curved electrode surface. One can see the higher mesh element density in Figure 2.7. The minimum mesh element size is set to 20 μm, where I found that the electric field dependence on the mesh size converges to negligibly small fluctuations.

The coordinate system of the electrostatic model of the electrodes is shown in Fig-

Field angle response to different angular misalignments
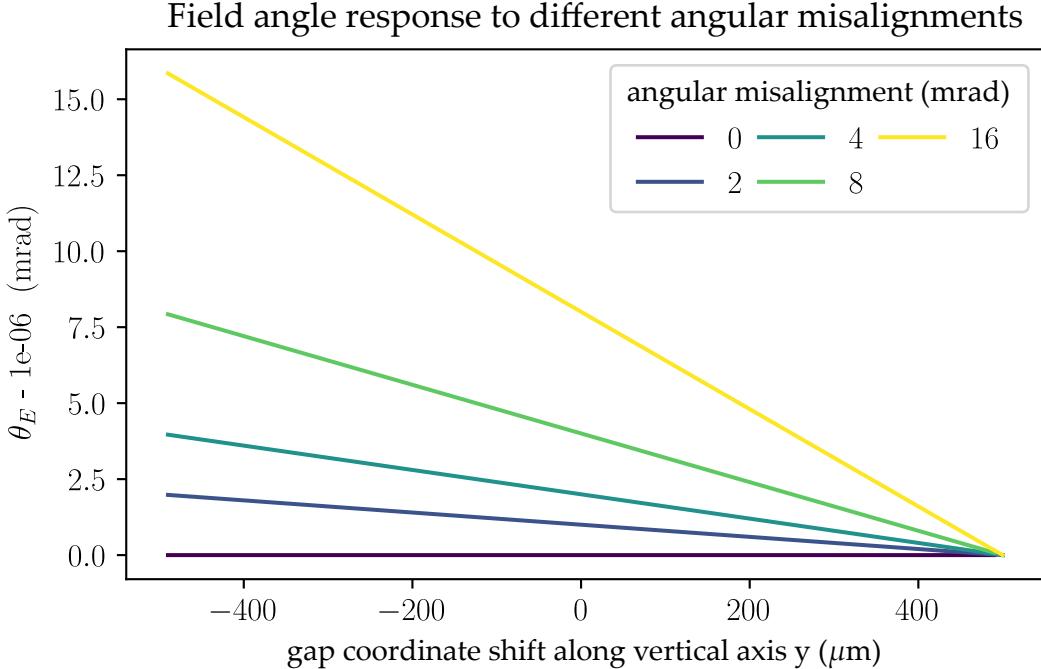
Figure 2.8: A plot of the electric field angle as a function of the vertical position y. In this plot, the electrodes are axially aligned and the angular misalignment is varied from 0–16 mrad. The center of the gap, 0.5 mm below the top electrode, corresponds to $y = 0$.

ure 2.7, with the origin defined as the midpoint between the two electrodes along their vertical axis of the top electrode. I find that the vertical field strength E_y changes by less than 6 ppb per 100 μm when the electrodes are perfectly aligned. The horizontal field magnitude $E_\perp = \sqrt{E_x^2 + E_z^2}$ changes by less than 5 ppb per 100 μm with respect to E_0 within 0.5 mm of the origin. In practice, we align our electrodes to better than 4 mrad in the high voltage test stand described in Section 3.4.1.

The mesh density was optimized in the volume between the electrode primary surfaces. We refined the maximum and minimum element size to minimize field calculation dependence on mesh settings. This was done by convergence analysis, decreasing the minimum element size from 120 μm to 18.5 μm and recording the change in the maximum electric field with a gap size of 1 mm and an applied voltage of -30 kV. The lower bound of the mesh size is limited by the RAM of our workstation PC (32 GB). I fixed the maximum element size to be a factor of 4 larger than the minimum element size.
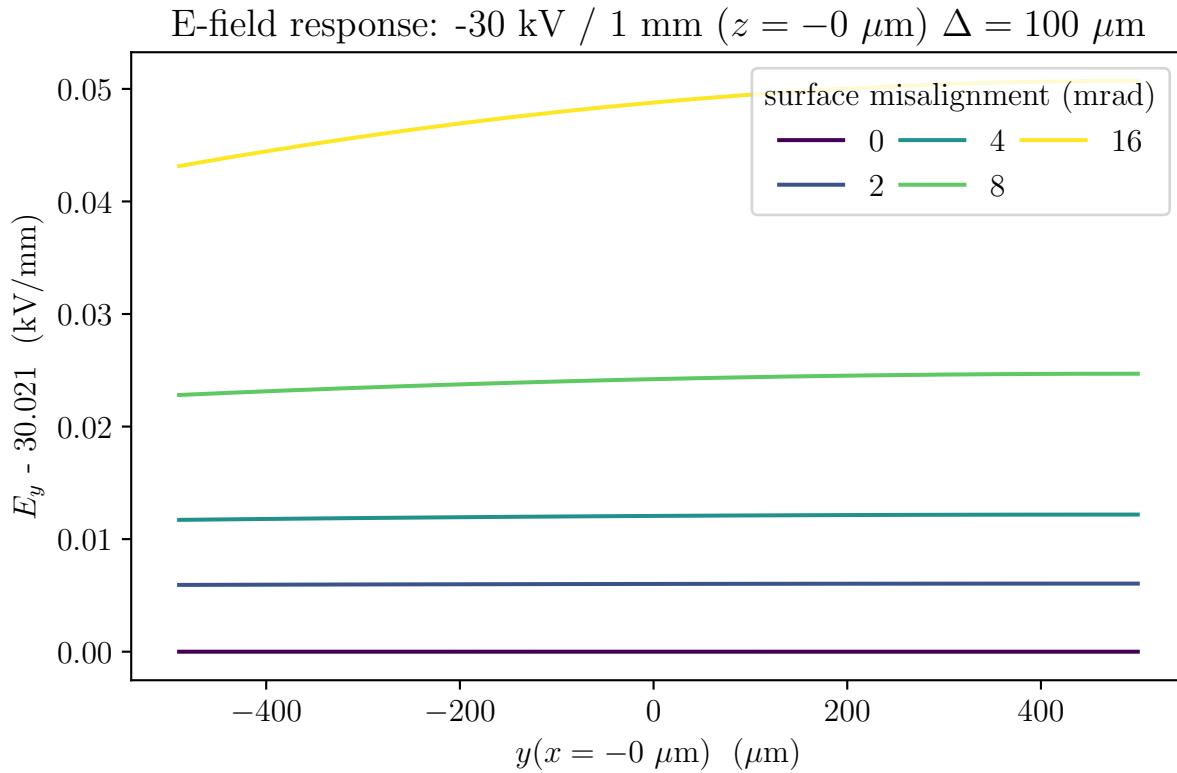
Figure 2.9: A plot of the vertical electric field for angular alignments in the range 0–16 mrad. The axial misalignment is 100 μm. The center of the gap, 0.5 mm below the top electrode, corresponds to $y = 0$.

I set the maximum and minimum element sizes in the gap between the electrodes to be 80 μm and 20 μm, respectively, where the maximum vertical component of the electric field changes by less than 0.03% (about 10 V/mm) when changing the mesh size by 10%. However, these deviations are based on field points very close to the mesh border and electrode surfaces. When we perform an identical convergence analysis while restricting the maximum field value to the horizontal plane bisecting the electrode gap, the field changes by less than 4 parts per billion.

2.5.2 Electric field response to electrode misalignment near the center of the gap

I investigated the effect of misalignments between the electrodes on the electric field angle, defined as $\theta_E = \arctan\left(E_\perp / E_y\right)$. There are two types of misalignments we consider.

Angular misalignments, or tilts, are introduced by rotating the bottom electrode about the z axis in the range 0–16 mrad. Axial misalignments, or shifts, translates the bottom electrode along the x axis and offsets the electrode centers. Shifts of up to 1 mm displacements are considered in this work. When the tilt and shift are zero, the electrodes are perfectly aligned and $\theta_E = 0$ near the center of the gap, corresponding to a uniform vertical field. When the electrodes are perfectly aligned ($\theta_E = 0, \Delta = 0$) $E_\perp$ fluctuates by ≈ 6 ppb and $\delta(E_y) \approx 10$ ppb from the nominal applied field of -30 kV/mm for $x \cap z \leq 100$ μm.

I've plotted the electric field angle θ_E for a range of electrode tilts in Figure 2.8. From my definition of the coordinate system, θ_E is zero at $\vec{r} = +0.5\hat{y}$ mm, the surface of the top electrode. For a tilt of 0 mrad, the electric field angle is perfectly aligned ($\theta_E = 0$) across the electrode gap. For nonzero tilts, θ_E scales linearly with distance y from the top electrode surface to the value of the electrode tilt angle at the surface of the bottom electrode, $\vec{r} = -0.5\hat{y}$ mm. Even for the largest angular misalignment of 16 mrad, the electric field angle θ_E is linear and appears insensitive to the effects from the electrode edge.

I also studied the effect of shifting the bottom electrode along $\hat{x}$ with respect to the top electrode's vertical axis in the range 0–1000 μm. In Figure 2.9, I show the vertical component of the electric field response for a 100 μm shift. The bottom electrode is offset along $-\hat{x}$ to maximize the convolution of angular and spatial misalignment. Even for large tilts, axial misalignments introduce a constant offset in E_y that appears to be independent of the tilt. In this worst-case scenario, the magnitude of the constant depends on both the tilt and the horizontal misalignment, which brings one side of the bottom electrode closer to the surface of the top electrode.

The constant term in E_y can be found by considering the electrodes at a reduced gap size of $\Delta \times \tan\theta$, where Δ is the spatial displacement. For a tilt of 16 mrad and a spatial misalignment of 1 mm (the largest misalignment simulated), this results in a shift of $+0.5$ kV/mm along the vertical axis. The shift value will be negative if we move along $-\hat{x}$ a distance greater than the offset because the electrode surfaces will be angled away from
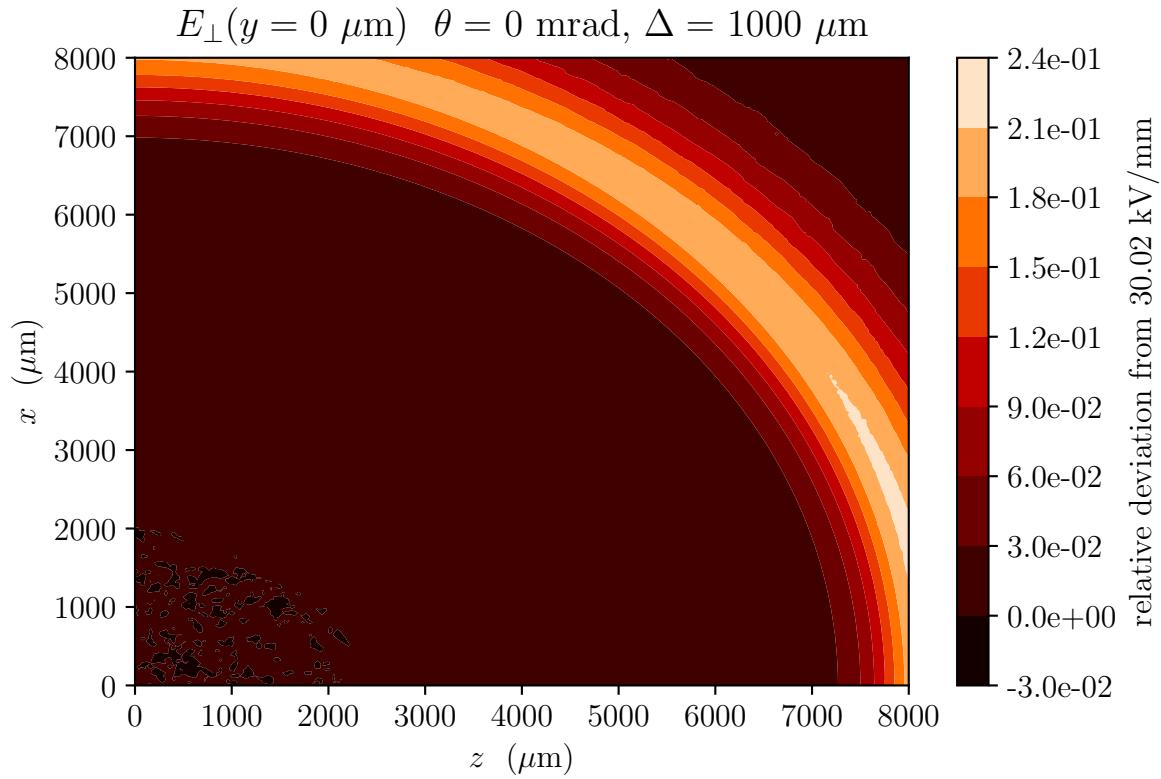
Figure 2.10: A contour of the horizontal electric field magnitude for misaligned electrodes close to the 8 mm edge region.

each other. In all configurations shown in Figure 2.9, the contributions to changes in the electric field due to angular and spatial misalignments are independent of each other for horizontal displacements $x \cap z \leq 1$ mm.

2.5.3 Electric field behavior in the electrode edge region

The first curved edge region of the (Figure 2.7) is 8 mm from the electrode center axis. A contour of the perpendicular component of the electric field $E_\perp$ is shown in Figure 2.10. The nominal field of this simulation, like all the others I discuss in this section, is $E_0 = V/d = 30$ kV/mm. With perfectly parallel surfaces (tilt $\theta_E = 0$ mrad) and an axial misalignment of 1 mm (shift $\Delta = 1000$ μm), there is approximately a 3.5% gradient in $E_\perp$ about 0.5 mm from the edge of the top electrode. The horizontal field is as high as
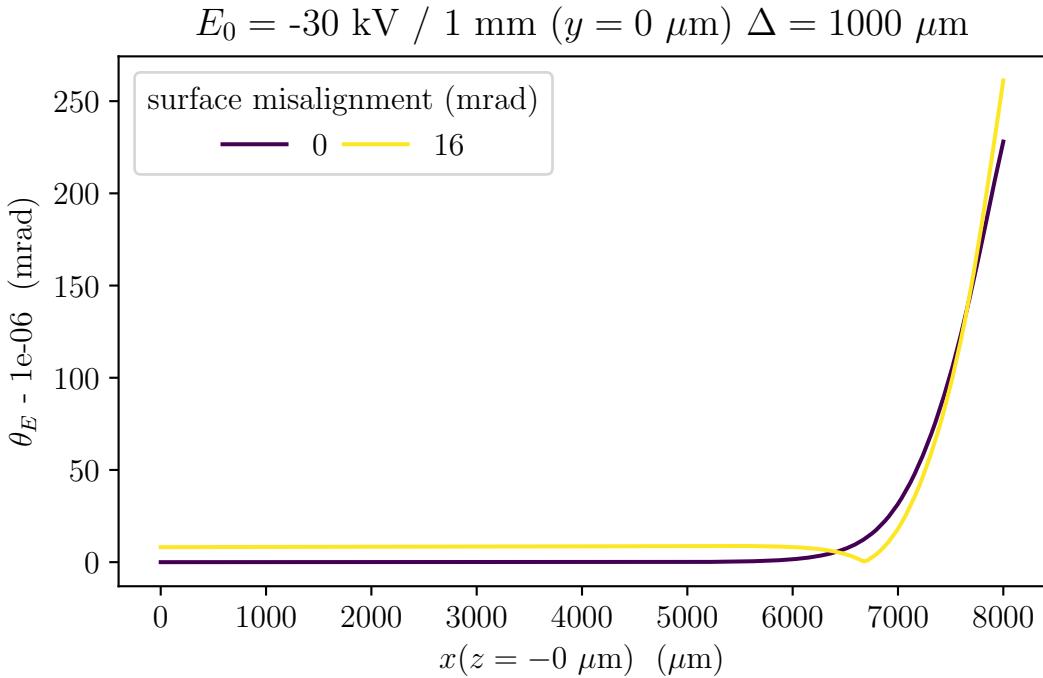
Figure 2.11: A plot of the electric field angle as we scan horizontally across the electrode surface (8 mm radius) from the center to the edge region.

7 kV/mm as the edge rounds off to the side of the electrode. Within 7 mm of the center of the electrode, $E_\perp$ varies by less than 3%.

To further illustrate the edge behavior, a plot of the field angle θ_E is shown for perfectly parallel electrodes and for a tilt of 16 mrad with a 1 mm shift in Figure 2.11. The field angle starts to change significantly at a horizontal distance $x = 6000$ μm from the origin. Interestingly, the field angle exponentially increases for the parallel line series but there is a dip in the field angle in the 16 mrad series, leading to a crossing between the two. At $x > 7000$ μm, the field angle of the 16 mrad line increases more rapidly than the parallel line.

Finally we look at the vertical component of the field behavior near the edge region in Figure 2.12. Since we're interested specifically in the edge behavior, we start from $\vec{r}(\mu m) = 4000\hat{x} + 0\hat{y} + 4000\hat{z}$ and scan horizontally along $\hat{x}$. E_y decreases by approximately 0.9 kV/mm over both curved surfaces of the electrodes, from 8 mm to 12 mm and 12 mm
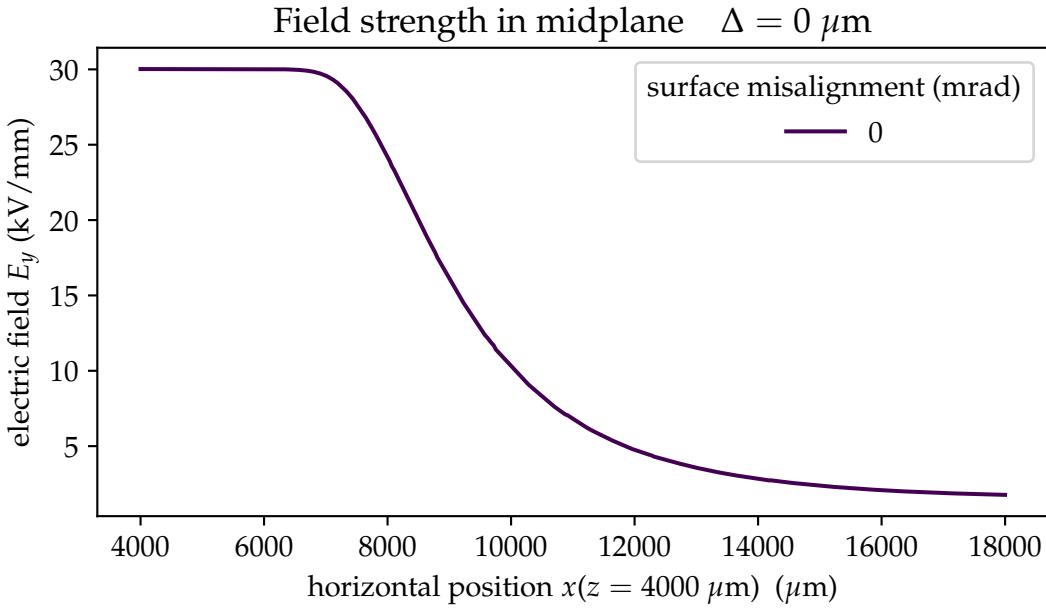
Figure 2.12: A plot of the vertical component of the electric field as we scan horizontally across the electrode surface in the edge region (radius of 8 mm).

to 16 mm. In this region, the horizontal field strength is on the same order of magnitude as the vertical field strength.

2.5.4 Modeling the electric field behavior near the center of the electrode gap

The electric field angle θ_E scales linearly with the angular misalignments, as shown in Figure 2.8. I modeled the change in θ_E as a linear function of the position in both the xy plane and the xz plane. The linear change in E_y along the horizontal xz plane is very weak. I show the fit to E_y for the more interesting case of the vertical xy plane in Figure 2.13. The linear model reproduces the change in the electric field angle to an accuracy of better than 1 μrad in both planes up to 1 mm from the center of the gap, even for large angular and axial misalignments.

I also modeled the change in the horizontal component of the electric field $E_\perp$ as the fraction of the maximum angle. Like the fit to θ_E in Figure 2.13, $E_\perp$ scales linearly with the distance from the origin. For a 16 mrad tilt and $E_0 = 30$ kV/mm, I find the following
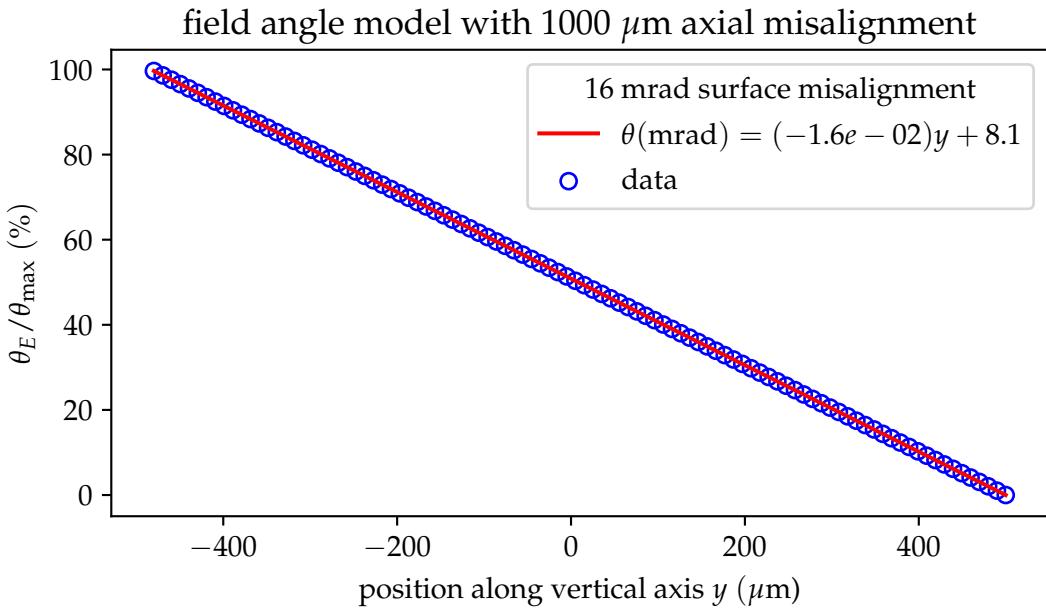
Figure 2.13: A straight line fit to the simulated polar angle of the electric field for an angular misalignment of 16 mrad and an axial misalignment of 1 mm. The center of the gap, 0.5 mm below the top electrode, corresponds to $y = 0$.

fractional linear change:

$$\frac{E_\perp/E_0}{\theta} \approx 0.1\% \,/\, \text{mrad}$$

I modeled the behavior of the vertical electric field E_y using the same misalignment settings as the θ_E model in Figure 2.14. The misalignment causes a 1.6% reduction in the field strength and the change in E_y along $\hat{y}$ is nonlinear. I compared the behavior with a $\cos(\theta_E)$ model, which assumes that the change in E_y is purely due to the changing field direction.

The reduction in E_y is larger than the amount reproduced by the cosine model. For a 16 mrad tilt, the cosine model accounts for a change of $\Delta E_y/E_0 \approx 100$ ppm per 500 μm from the origin while the total effect is 230 ppm / 500 μm.
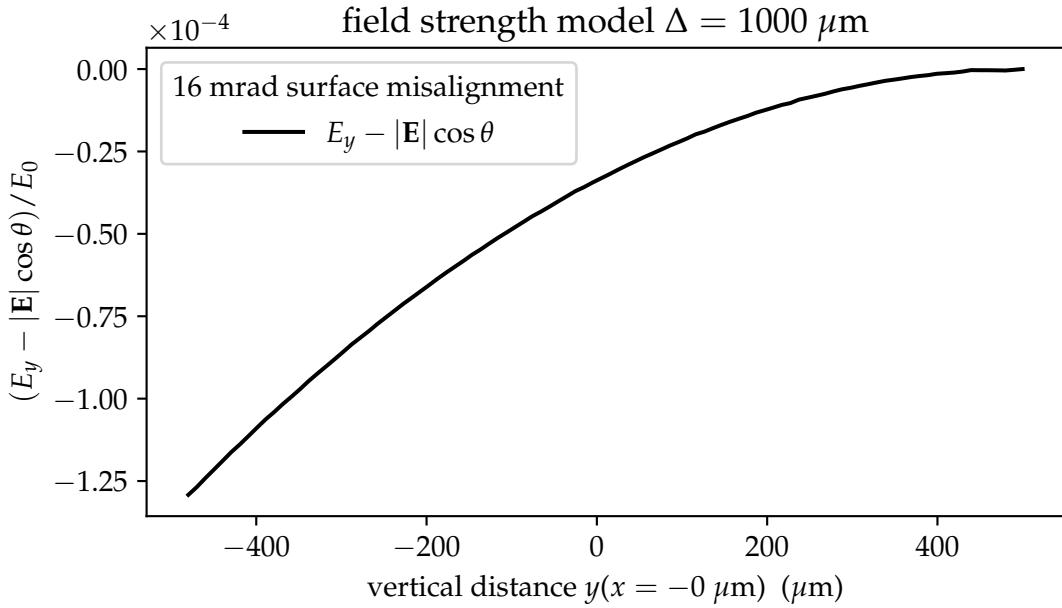
Figure 2.14: A residual plot of a model of the vertical electric field for a 16 mrad angular misalignment and 1 mm axial misalignment. The model assumes that the field is a function of the angle of the electric field.

2.5.5 Estimating effects for realistic misalignments in the high voltage apparatus

A contour of the vertical component of the electric field for a 2 mrad tilt is shown in Figure 2.15. The total change in E_y across a 1000 μm range in x is 2.1%. Even for large horizontal radial displacements ($x \cap z > 100$ μm), the electric field is uniform. This can be seen in the left panel, where the change in the electric field depends on x and is insensitive to displacement along the axis of rotation ($\hat{z}$).

For a larger 4 mrad tilt, the electric field gradient becomes $(\Delta E_y/E_y)/25$ μm ≈ 100 ppm. This gradient would cause an EDM systematic on the order of $10^{-29}e$ cm across a 100 μm radium cloud. The behavior of $E_\perp$ is identical but the strength of the gradient is more than two orders of magnitude weaker.

In the more realistic case of a 2 mrad tilt, we find that θ_E changes by 0.2 μrad per 100 μm in the vertical plane and 0.02 μrad per 100 μm in the midplane. EDM systematic effects arising from field angle changes of this magnitude are far below our current statistical
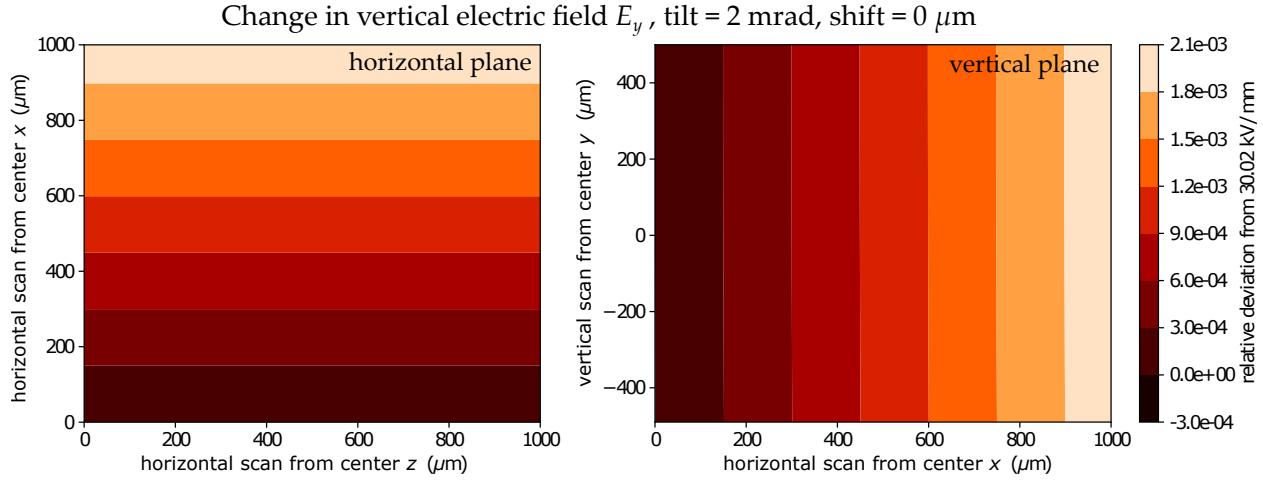
Figure 2.15: Contour plots of the vertical component of the electric field in the xz (left) and xy (right) plane and with a 2 mrad tilt.

sensitivity.

2.6   Electrode Upgrade Strategy and Results

2.6.1   High voltage discharge-conditioning

We define discharge-conditioning as the process of applying iteratively higher voltages to the electrodes to suppress steady-state leakage current and discharge rates between them. Leakage current refers to any current flowing between the electrodes and is measured by a picoammeter in series with one of the electrodes, as shown in Figure 3.11.

Figure 2.16 shows several forty-minute snapshots of a subset of shifts over the lifetime of conditioning and validating a pair of niobium electrodes. I started with manually controlled voltage steps before using a periodic, polarity-alternating voltage to simulate EDM measurement conditions for the electrodes.

A schematic of one full period of the conditioning voltage waveform is shown in Figure 2.17. The period is 280 seconds (60 seconds positive polarity, 80 seconds no voltage, 60 seconds negative polarity, 80 seconds no voltage). This period is chosen to reflect the measurement technique discussed in Section 2.4.1.

We differentiate our method from the standard "current-conditioning" method [100]
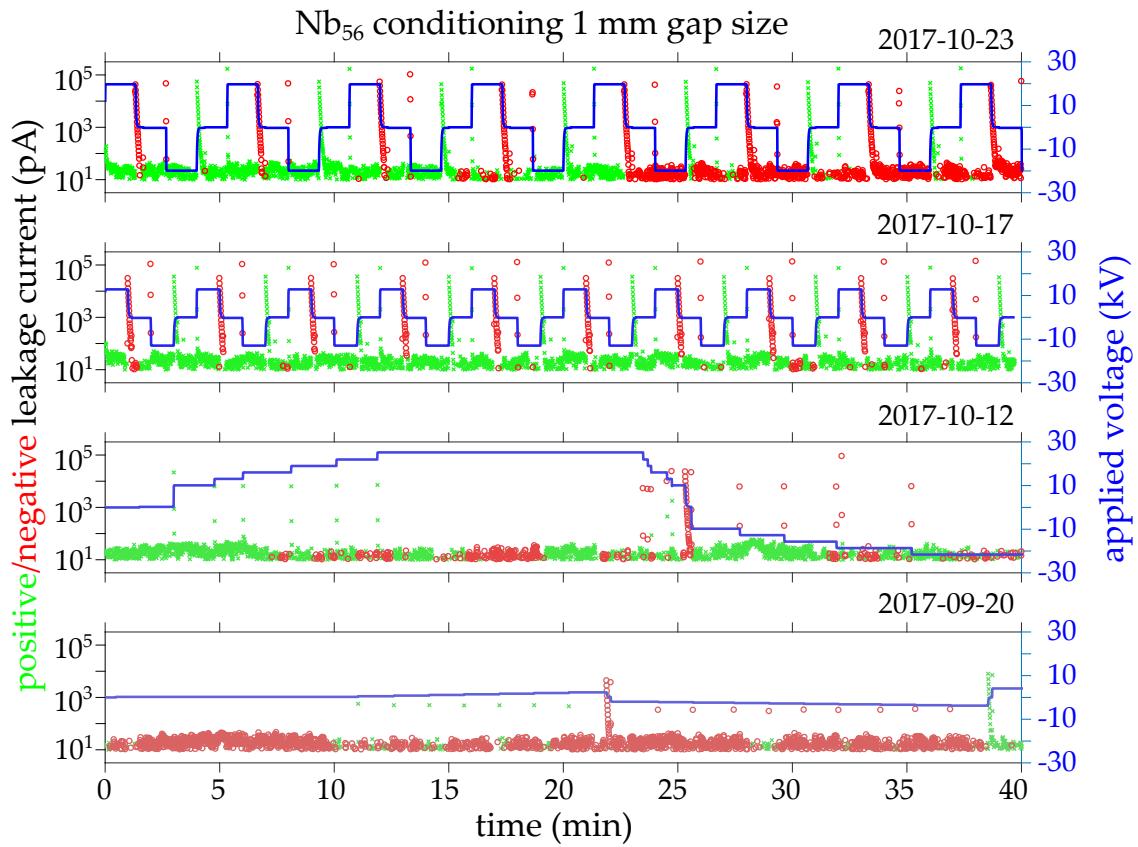
Figure 2.16: Forty-minute snapshots of the conditioning process in early, middle, and final stages. Positive and negative current is plotted with green crosses and red circles on a logarithmic scale. Leakage current less than 10 pA is omitted for clarity. The right vertical axis is the applied voltage and is plotted as a blue line.

because we characterize electrode performance by counting discrete discharges over time and we use a periodic voltage waveform. I will interchangeably use the shorthand term "conditioning" when referring to discharge-conditioning.

In the absence of surface particulate contamination, electrode discharges are caused by charge buildup on microprotrusions on the electrode surfaces [101], which we will refer to as charge emitters. We process and handle our electrodes in Class 100 or better environments to minimize particulate contamination. The height of charge emitters have been measured on the order of 1 μm in buffer chemical-polished large-grain niobium electrodes prepared similarly to our electrodes [102]. If the charge emitter is near the edge of the electrode, we expect the higher gradients will increase the likelihood of a
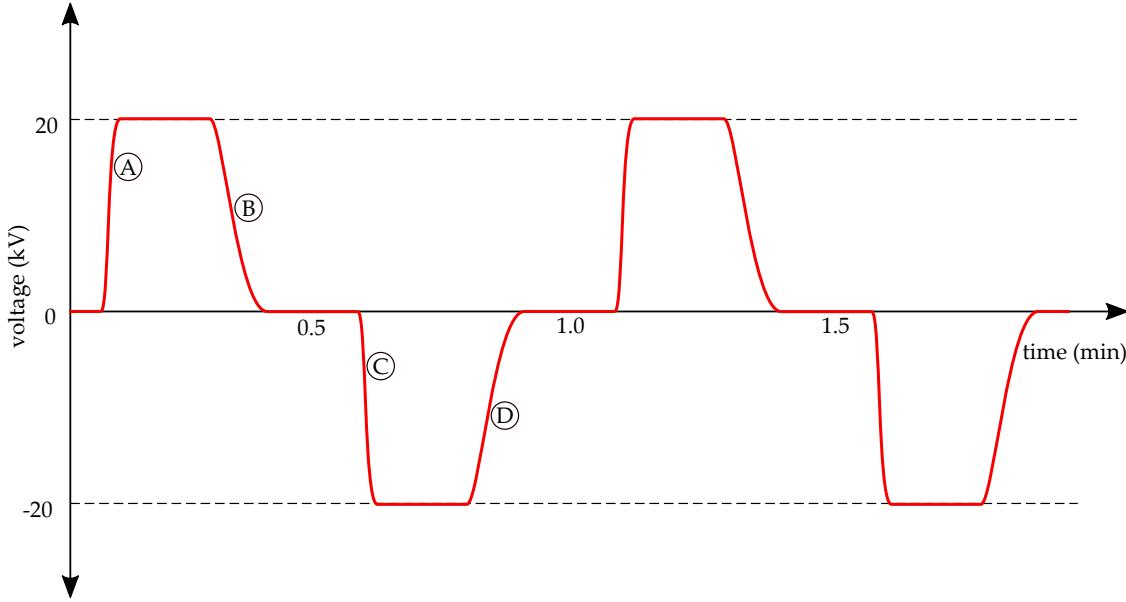
Figure 2.17: A schematic of the periodic EDM high voltage waveform. (A) positive charging up ramp. (B) positive charging down ramp. (C) negative charging up ramp. (D) negative charging down ramp.

discharge.

Controlled discharges electrically polish away, or ablate charge emitters over time, allowing the electrodes to perform reliably at higher voltages [100]. As shown in Section 3.4, it may take tens to more than one hundred hours of discharge-conditioning to suppress charge emitters. We expect the required conditioning duration may take longer if the surface is insufficiently polished or contaminated. Bulk properties, such as the work function, resistivity, or hardness of the electrode may also play a role in the conditioning time. These bulk properties are listed for a selection of commonly used electrode materials in Table 3.2.

2.6.2 Typical size of discharges

The electrode geometry is shown in Figure 3.1. We'll consider the main high-gradient surfaces of the electrodes as the only surfaces where discharges occur. For a pair of circular, parallel plate capacitors whose diameter $2R$ is much greater than the electrode gap

57

d, the electrode capacitance C [F] is given by the following:

$$C = \frac{Q}{V} = \epsilon_o \frac{\pi R^2}{d}, \tag{2.31}$$

where Q [C] is the charge on each electrode, V [V] is the electric potential between the two electrodes, and ϵ_o $\left[\text{F m}^{-1}\right]$ is the vacuum electric permittivity constant.

For an electrode gap of $d = 1 \times 10^{-3}$ m, a plate radius $R = 8 \times 10^{-3}$ m, and an applied voltage of $V = 30$ kV, we get a capacitance of 1.78 pF. However, from the model of the electrodes in COMSOL, I get a capacitance of 3.3728 pF. This gives a total charge of $Q = 3.3728$ pF $\times$ 30 kV $= 1.01 \times 10^{-7}$ C.

I integrate the discharge current $I(t)$ [A] to estimate the amount of charge ejected from an electrode surface in a discharge, Q_{dc} [C]:

$$Q_{dc} = \int_{-\infty}^{+\infty} I(t) dt \tag{2.32}$$

The discharge current waveform varies in duration and amplitude, but a reasonable estimate is an amplitude of 100 nA over a 1 ms timescale. I'll approximate the waveform as Gaussian:

$$Q_{dc} = \int_{-\infty}^{+\infty} (100 \text{ nA}) \exp\left\{-\left(\frac{t^2}{2\sigma^2}\right)\right\} dt, \tag{2.33}$$

$$\sigma = 1 \text{ ms} \tag{2.34}$$

In such a discharge we would expect to see $\approx 2.51 \times 10^{-10}$ C or 1.56×10^9 electrons. This is $\approx Q_{dc}/Q \times 100 \% = 0.25 \%$ of the total charge stored on each electrode.

2.6.3   Results

Four pairs of niobium electrodes and two pairs of titanium electrodes were surface processed as described in Table 3.1. After high-pressure rinsing they are preserved in clean room environments of Class 100 (ISO 5) or better. I conditioned pairs of electrodes in a custom, Class 100-rated high voltage test station at MSU by applying DC voltages as high

as ±30 kV at gap sizes in the range 0.4–2.5 mm. Maximum fields of +52.5 kV/mm and −51.5 kV/mm were tested and are discussed in Section 3.4.7.

One pair of large-grain niobium electrodes was validated to operate reliably at 20 kV/mm at MSU. I mounted the electrodes in a stainless steel container and sealed the container with tubing. The container was backfilled with particle-filtered, dry nitrogen and transported to ANL. Then I constructed and validated a Class 100 clean room that covered the electrode entry point to the Ra EDM experimental apparatus. The electrodes were removed from their packaging and installed in the experimental apparatus in May 2018, where I revalidated them to 20 kV/mm.

CHAPTER 3

HIGH VOLTAGE ELECTRODE DEVELOPMENT

In Section 3.1 I will describe past and present considerations in electrode material and surface processing. We start with the preparation of the previous electrode pair used for the first generation EDM measurements in Section 3.1.1. Material selection, surface processing, and electrode decontamination for the new electrodes tested in this work are detailed in Sections 3.1.2 and 3.3.1. I will present our method of benchmarking the performance of the electrodes in Section 3.4. Finally, we'll compare the performance of all the tested pairs in Section 3.4.10.
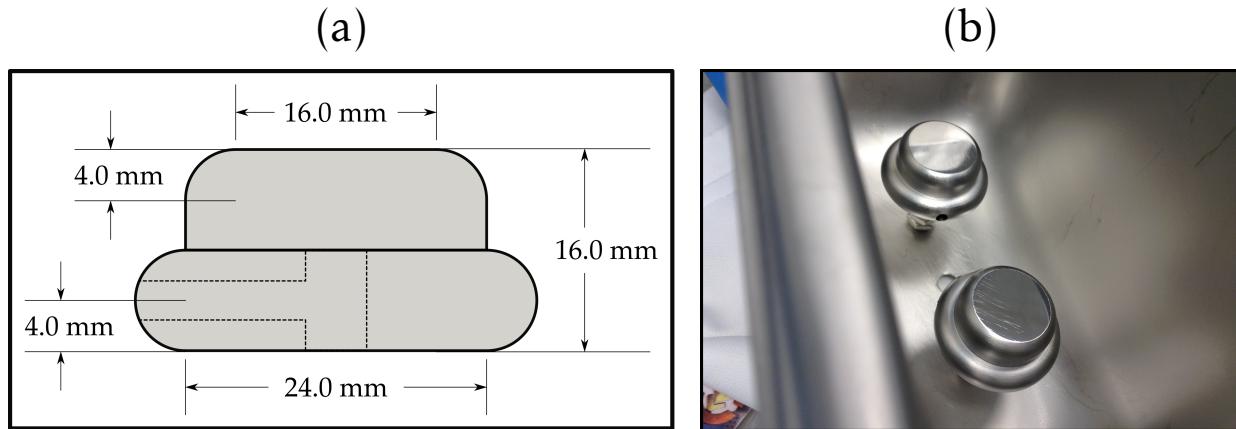
Figure 3.1: (a) Cross-sectional electrode schematic. Surfaces have a flatness tolerance of 25.4 μm and a parallelism of 50.8 μm. The top surface is polished to an average roughness of 0.127 μm. The base is mounted by a 10-32 tapped hole. Copper rods are used to connect to the electrodes' 3.2 mm diameter side bore to high voltage feedthroughs. (b) A pair of large-grain Niobium electrodes in a clean room stainless steel container.

Figure 3.2: From left to right: a copper, niobium, and titanium electrode.

3.1 Electrode Properties and Preparation

3.1.1 Legacy electrode preparation

The first generation EDM measurements used a pair of electropolished oxygen-free copper electrodes [65, 48]. Their geometry is identical to the new electrodes discussed in this work (Figure 3.1). Surface processing of these electrodes, labeled Cu_{12}, is detailed in Table 3.1.

The legacy electrodes were conditioned at ANL with a unipolar -30 kV power supply (Glassman PS/WH-30N15-LR) in a Macor holder at a 2 mm gap size in 2008 [103]. The electric field was reversed by turning the system off and manually switching the power supply terminations at the high voltage feedthroughs. Voltage was increased from 1–20 kV in 1 kV steps while monitoring the steady-state leakage current. Conditioning was declared complete if the electrodes could hold 20 kV with a steady-state leakage current of < 100 pA for ten hours.

Four pairs of electrodes total were tested in this manner, including two pairs of tita-

Table 3.1: Electrode inventory. Large-grain (LG) niobium electrode residual resistance ratio (RRR) > 250. OF = oxygen free. G2 = grade-2. Simichrome polish by hand. Diamond paste polish (DPP) by hand. LPR = low pressure rinse. HPR = high pressure rinse. HF = hydrofluoric chemical polish. EP = electropolish. BCP= buffered chemical polish. SiC = silicon carbide machine polish. CSS = colloidal silica suspension machine polish. VB = 420–450 °C vacuum outgas bake. WB = 150–160 °C water bake. USR = ultrasonic rinse after detergent bath.

batch	material	pair	surface processing recipe			
1	OF copper	Cu_{12}[a]	Simichrome	$\rightarrow$ EP	$\rightarrow$ USR	$\rightarrow$ WB
2	LG niobium	Nb_{14}	SiC	$\rightarrow$ BCP	$\rightarrow$ DPP	$\rightarrow$ CSS $\rightarrow$ USR $\cdots$
			$\cdots$ VB	$\rightarrow$ LPR	$\rightarrow$ HPR	
2	LG niobium	Nb_{23}	SiC	$\rightarrow$ BCP	$\rightarrow$ USR	$\rightarrow$ VB $\rightarrow$ HPR $\cdots$
			$\cdots$ resurface	$\rightarrow$ BCP	$\rightarrow$ HPR	
2	G2 titanium	Ti_{24}	SiC	$\rightarrow$ HF	$\rightarrow$ USR	$\rightarrow$ VB $\rightarrow$ HPR
2	G2 titanium	Ti_{13}	SiC	$\rightarrow$ HF	$\rightarrow$ EP	$\rightarrow$ USR $\rightarrow$ VB $\cdots$
			$\cdots$ HPR			
3	LG niobium	Nb_{56}[b]	SiC	$\rightarrow$ BCP	$\rightarrow$ USR	$\rightarrow$ HPR $\rightarrow$ WB
3	LG niobium	Nb_{78}	SiC	$\rightarrow$ BCP	$\rightarrow$ USR	$\rightarrow$ HPR

[a] Legacy electrodes used for first two measurements [65, 48].
[b] Second generation electrodes, currently installed in the Ra EDM apparatus.

nium electrodes and one pair of copper electrodes without electropolishing. The legacy titanium electrodes all exhibited leakage current higher than 100 pA at 20 kV. Flooding the test chamber with argon gas and plasma discharge-conditioning the titanium electrodes was attempted without an observable benefit. Both copper electrode pairs were conditioned, with the electropolished (EP) electrodes taking significantly less time.

The legacy electrode pair Cu_{12} was mounted in a Macor holder at a 2.3 mm gap size and installed in the Ra EDM experimental apparatus [86]. The two published ^{225}Ra EDM results employed electric fields of ±6.7 kV/mm and ±6.5 kV/mm [65, 48]. The pair was retested at 20 kV / 2.3 mm = 8.7 kV/mm but exceeded the 100 pA limit. This was remedied by reducing the electric field by 25% to 6.5 kV/mm for the EDM measurement. We suspect that the primary surface of one or both of these legacy electrodes was contaminated during installation. This was a motivating factor in the development of the decontamination techniques for the new electrodes discussed in subsequent sections.

Table 3.2: Bulk material properties of electrodes. We define "strong B-impurities" as $\chi_m/(10^{-6}\ \mathrm{cm}^3\ \mathrm{mol}^{-1}) > +1000$, where χ_m is the molar susceptibility. $\chi_m(\mathrm{Nb}) = +208$.

material	ϕ (eV)	strong B impurity (%)	density $\left(\dfrac{\mathrm{kg}}{\mathrm{m}^3}\right)$	resistivity $(\mu\Omega\ \mathrm{cm})^{\mathrm{a}}$	hardness $\left(\dfrac{\mathrm{kgf}}{\mathrm{mm}^2}\right)$	outgas rate $\left(\dfrac{\mathrm{Torr\ nL}}{\mathrm{s\ cm}^2}\right)$
Nb [b]	4.3	2.7×10^{-2}	8570	15.2	134.6	30
Cu [c]	4.65	2.5×10^{-7}	8960	1.543	35.0	16.3
Ti [d]	4.33	5.5×10^{-1}	4506	39	99.0	184
SS [e]	4.34	$8.1 \times 10^{+1}$	8000	69.0	176	42.8
Mo [f]	4.6	1.4×10^{-2}	10200	4.85	156.0	36.7
References	[104, 105]	[106]	[106, 107]	[108, 109]	[110, 107]	[111, 112]

[a] Resistivity measured at 273 K.
[b] Hardness measured at 473 K. Outgas rate estimated from the correlation between Cu, SS, and Nb desorption.
[c] Hardness measured for single crystal (III) at 293 K. Outgas rate measured for unbaked OF high-conductivity after ten hours.
[d] Hardness measured for iodide-annealed, 99.99% purity at 293 K. Outgas rate measured for unbaked OF high-conductivity after ten hours.
[e] SS = stainless steel. Hardness measured for designation type 304. Outgas rate measured for unbaked, electropolished NS22S after ten hours.
[f] Hardness measured at 293 K.

3.1.2 Consideration of materials for new electrodes

We selected large-grain niobium and grade-2 titanium (middle and right electrodes in Figure 3.2) for testing after reviewing accelerator physics literature. The bulk properties of these metals and other commonly used high voltage metals are catalogued in Table 3.2. Our goal is to use the material that sustains the highest electric field strength while minimizing leakage current and magnetic impurities that could introduce EDM systematic effects. Stainless steel was excluded from our testing due to its relatively high ferromagnetic content but its properties are nevertheless included for reference.

Large-grain niobium electrodes with a cathode area of 3170 mm^2 have been tested to fields as high as 18.7 kV/mm [102]. Fine-grain appears to perform slightly worse, perhaps because the higher grain boundary density increases particulate adherence to the
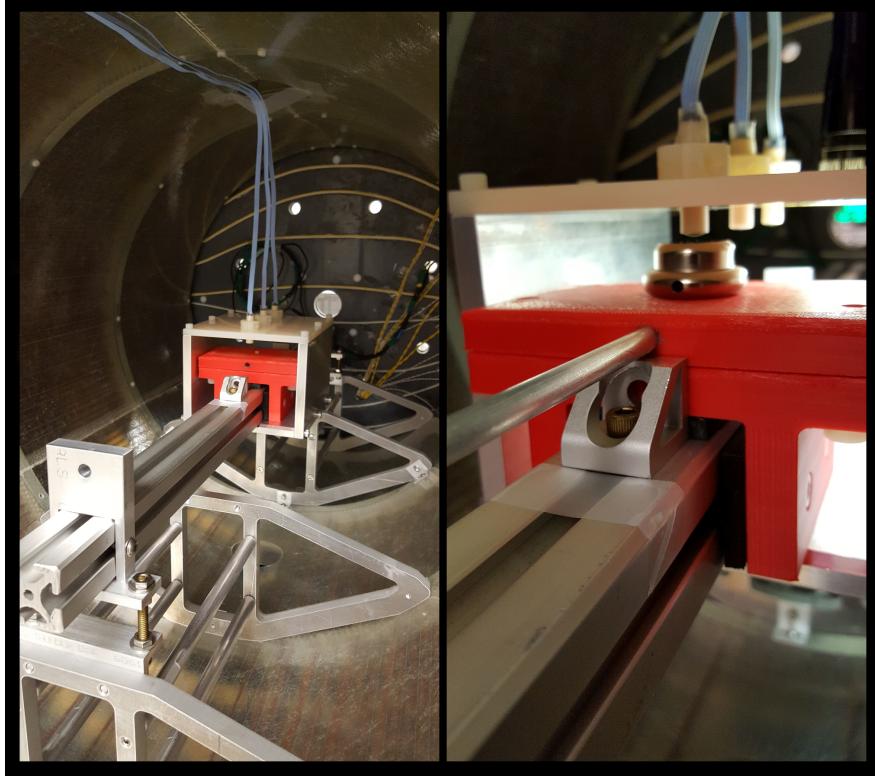
Figure 3.3: The magnetization rail system sits inside a mu-metal shield.

electrode surface [113]. The highest reported electric field for gap sizes near 1 mm that we found is 130 kV/mm using an asymmetric titanium anode and molybdenum cathode with an effective area of 7 mm^2 [114]. The effective area of the Ra EDM electrode is 200 mm^2, approximately a factor of thirty larger. There is evidence that larger stressed areas are prone to lower breakdown voltages, suggesting that a miniaturized Ra EDM electrode geometry could improve the maximum stable electric field [115].

In the presence of high electric fields, an oxide layer on an electrode surface could be a significant source of particle emission. Niobium oxidizes at a higher rate than titanium and oxygen-free copper [116, 117, 118, 119, 120]. However, significant oxidation rates for these materials have only been observed at temperatures in excess of 500 °C [116, 120, 119, 121, 122]. The Ra EDM experimental apparatus is pumped to ultrahigh vacuum ($< 10^{-11}$ Torr) at room temperature. We therefore expect that oxidation rates are negligibly low for any selection of the considered electrode materials.
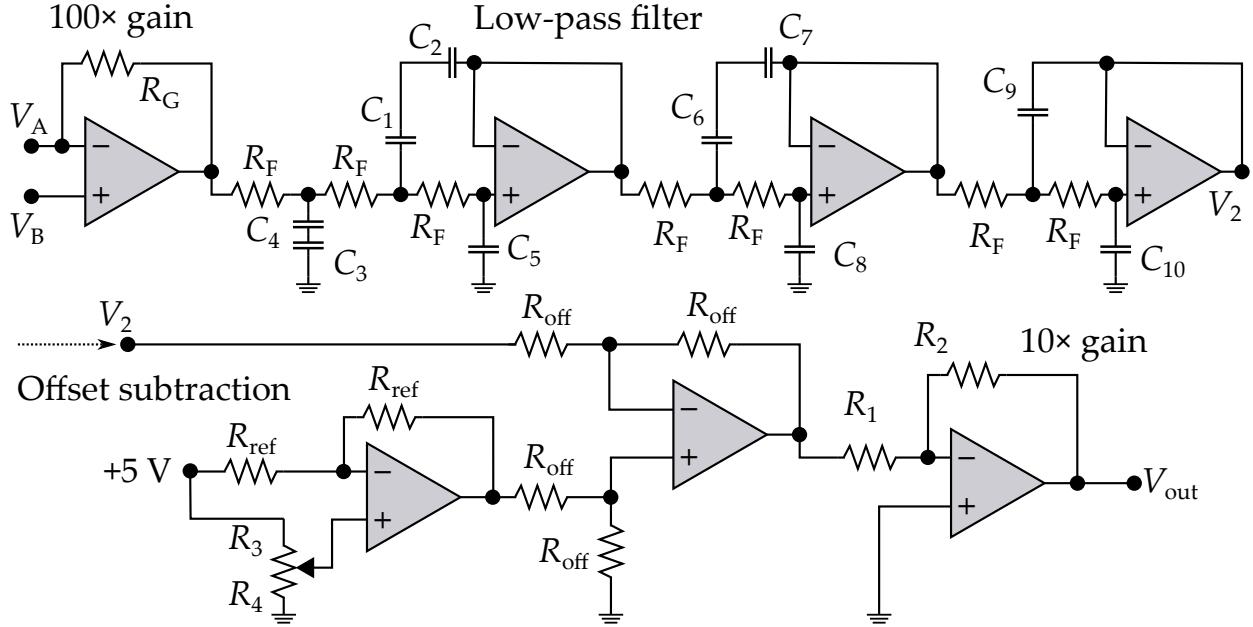
Figure 3.4: A schematic of the gradiometer circuit. Resistor and capacitor values are listed in Figure D1.

3.2 Electrode Residual Magnetization Measurements

We have considered a potential EDM systematic arising from magnetic impurities in the electrodes that change polarization with each electric field reversal. A sufficiently high concentration of such impurities could perturb the magnetic field in the radium cloud region. I describe potential effects from this systematic in Section 2.4.3.

I measured the residual magnetization of copper, niobium, and titanium electrodes in a magnetically shielded mu-metal enclosure shown in Figure 3.3. The mu-metal box is a prototype that we borrowed from our generous HeXeEDM colleagues at the Technical University of Munich (TUM). I used commercial low-noise fluxgates (Bartington Mag03IEL70) with a maximum noise floor of 6 pT/$\sqrt{\text{Hz}}$.

The residual magnetization measurement records data from each of the three fluxgates. For each measurement, the electrode is alternated between the first and third fluxgate. The fluxgate centered on the electrode is the "signal" fluxgate; the fluxgate furthest from the electrode is the "background" fluxgate. These signals are inputs to a
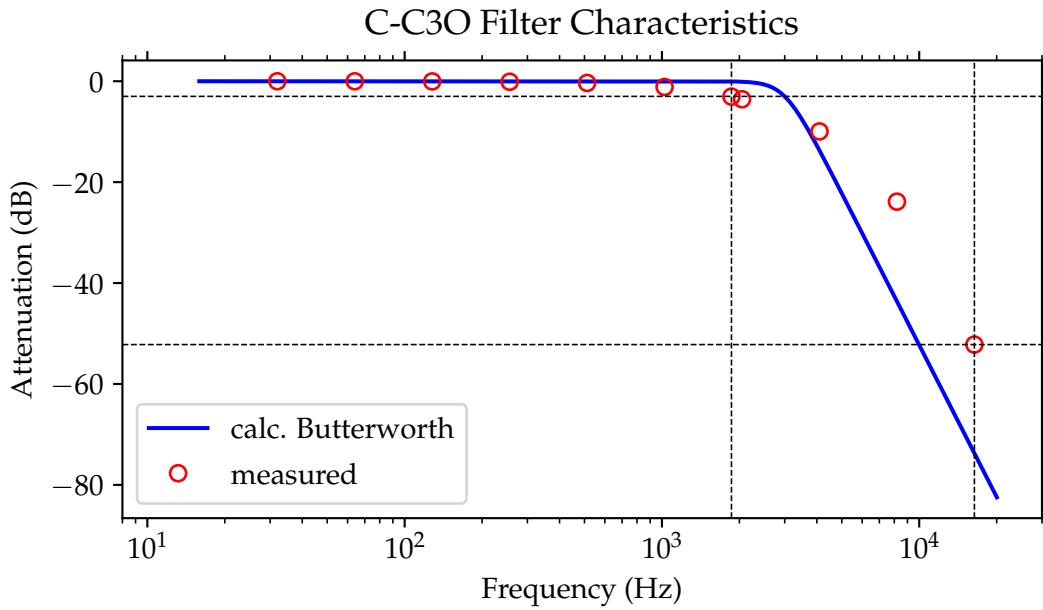
Figure 3.5: Simulated 3 kHz Butterworth lowpass curve (blue line) and measured frequency response with a waveform generator input (red circles) of the gradiometer circuit in Figure 3.4. 1.86 kHz dashed vertical line = measured cutoff frequency. 16.4 kHz dashed vertical line = fluxgate frequency, attenuated by ≈ 53 dB.

gradiometer circuit, which inputs two signals V_A and V_B to a differential op amp (shown in Figure 3.4). The signals are subtracted and amplified to isolate the residual magnetization due to the electrode. The resulting amplified, background-subtracted signal is then sent through a seventh-order low-pass filter.

The low-pass filter circuit is shown in in Figure 3.5. Because I use slightly larger capacitances than what is specified for a 3 kHz lowpass filter, my cutoff frequency is lower (1.86 kHz). I designed the filter for 60 dB attenuation at the fluxgate frequency of 16.4 kHz. In practice, I find the 16.4 kHz signal is attenuated by approximately 53 dB. The passband is very flat up to about 200 Hz, and then starts to slope downward.

I measured the residual magnetization of copper, aluminum, stainless steel, Macor, niobium, and titanium. A gradiometer measurement of a niobium electrode is shown in Figure 3.6. Our gradient signals were all on the order of approximately 400 pT due
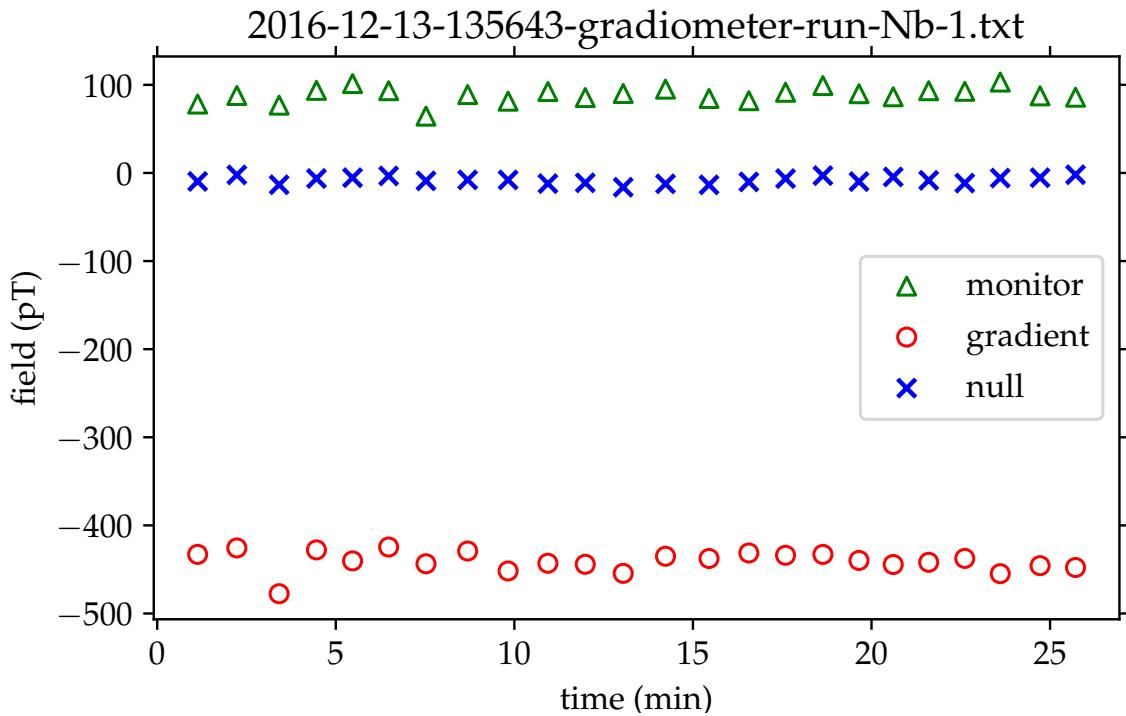
Figure 3.6: Gradiometer results for a niobium electrode. Average gradiometer signal = -440.8 ± 1.6 pT. Average monitor signal = 88.2 ± 1.3 pT. Average null signal = -8.5 ± 0.1 pT.

to the fluxgate potting limiting the minimum sensor-surface distance to ≈ 15 mm (see Figure D2). Titanium was the most magnetic, in agreement with the magnetic properties listed in Table 3.2.

We also sent a pair of titanium electrodes to colleagues at the University of Science and Technology of China (USTC). They measured the residual magnetization of a pair of titanium electrodes to ≤ 5 nT with a custom 5 mm atomic vapor cell magnetometer that allowed them to place their sensor approximately 8 mm from the surface. The residual magnetization measurements with the MSU fluxgate measurements and USTC magnetometer measurements are shown in Figure 3.7.

Because of the higher residual magnetization of the titanium electrodes, we decided to use large-grain niobium for radium spin precession frequency measurements.
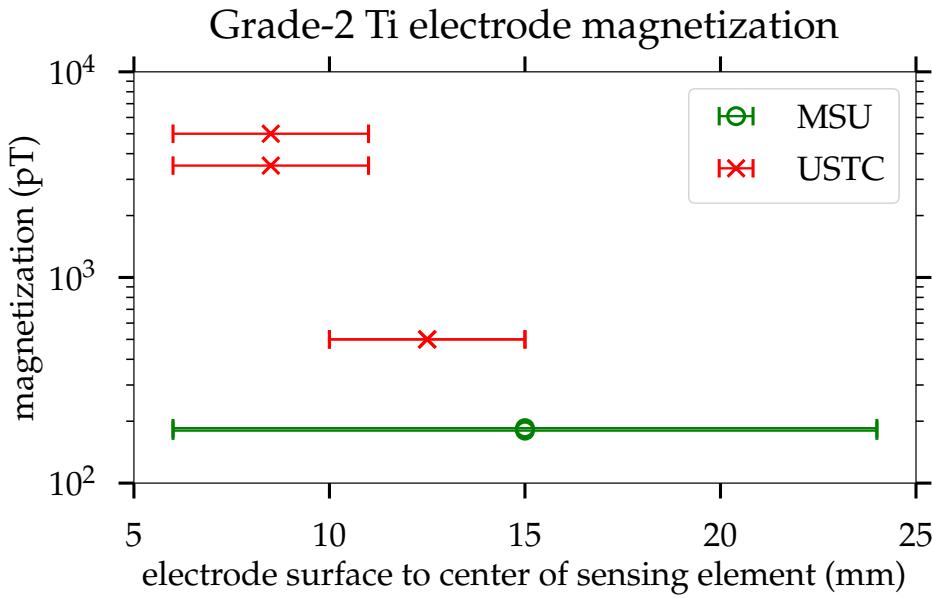
Figure 3.7: Residual magnetization measurements of grade-2 titanium electrodes using commercial fluxgates (MSU) and a custom magnetometer (USTC).

3.3 Review of High Voltage Surface Processing Applications

Electrode performance depends on the material, geometry, gap size, vacuum pressure, applied voltage magnitude, voltage polarity, voltage frequency, and the electrode surface condition. The analysis described in this thesis benchmarks the benefit of conventional high gradient surface processing techniques for our unique electrode geometry and operational requirements. In this section I will briefly describe some of the use cases of high-voltage accelerator applications that inspired us.

Radiofrequency (RF) cavities are designed to accelerate and, in some cases, bunch an incoming beam of particles. The AC accelerating potential is typically applied across a large gap (> 5 mm) [113]. They are usually made of large-grain or fine-grain niobium and are often cooled to superconducting temperatures to reduce residual losses.

Electron guns provide electron sources for beam experiments. These applications typically use a conical ("point") small-area cathode and a relatively large-area flat ("plane") anode to generate high-intensity current. Electron guns can be AC or DC and provide
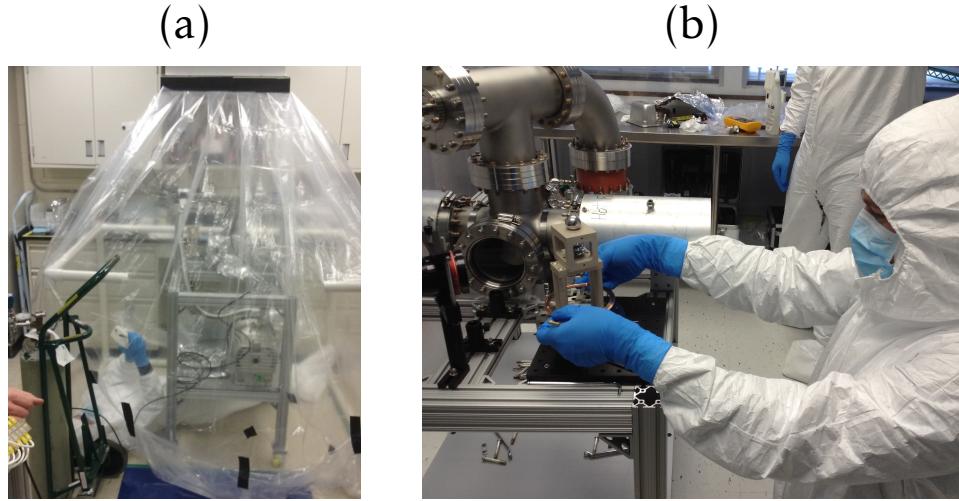
Figure 3.8: (a) I built a portable clean room with a $2' \times 2'$ HEPA filter (SAM22 MS NCR). (b) The NSCL detector clean room. It has several HEPA units and accommodates the test station and up to three personnel.

a stable electron beam for hundreds of hours. For long-pulse (DC) gun types, applied voltages reach hundreds of kilovolts and gap sizes of tens of millimeters [102].

Electrode geometry and operating voltage is optimized to steer charged particles and simplify their motion in storage ring EDM experiments. The particle spins precess in multiple planes through their electric and magnetic dipole interactions with the applied electric and magnetic fields. The particle spin precession frequency can be constrained to a single plane relative to the momentum vector by appropriately choosing the strength of the applied fields. Applied voltages can range from a few kV to ≈ 240 kV and electrode gaps range from 30–120 mm [123, 124].

3.3.1 Second generation electrode surface processing

We fabricated four pairs of large-grain niobium electrodes and two pairs of grade-2 titanium electrodes in two separate batches. Surface treatment procedures for each electrode pair are catalogued in Table 3.1 (batches 2 and 3). For this phase of the high voltage development, our goal was to increase the electrode field strength from 6.5 kV/mm to 15 kV/mm or better .
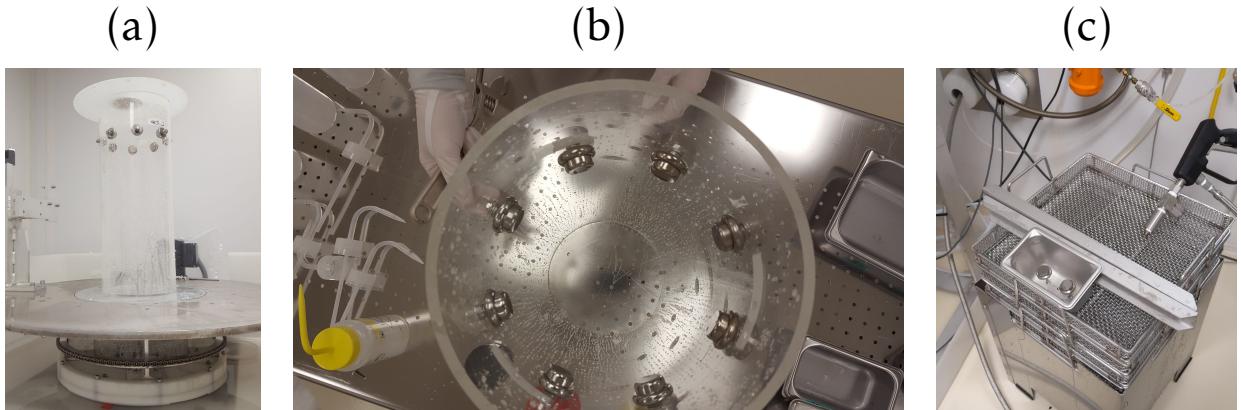
Figure 3.9: Electrode high pressure rinse equipment. (a) The electrodes are mounted on an acrylic cylindrical shell centered on a turntable. As the apparatus rotates, a concentric high pressure rinse 'wand' rinses the electrodes. (b) The electrodes are mounted so that the primary surfaces face the wand. (c) We switched to a rinse gun because the water quality was better.

With this in mind, we used processing procedures informed by discussions with Jefferson Lab accelerator physicists and a review of the literature. The general recipe is to first mechanically polish, chemical polish, then high-pressure rinse (HPR) the electrodes. Chemical polishing and HPR with ultrapure water (UPW) significantly improves electric field strength and stability [102, 114, 125, 126]. For an overview of chemical polishing, including electropolishing and buffered chemical polishing (BCP), we refer the reader to [127, 128, 129, 130, 131, 132, 133]. Comparing the machined dimensions to optical measurements of the polished electrodes (discussed in Section 3.4.2), I find that mechanical and chemical polishing reduces our electrode dimensions by approximately 100 μm.

Recently, centrifugal barrel polishing has been shown to reduce the required conditioning time compared to chemical etching [134]. This is an encouraging prospect for conditioning Ra EDM electrodes to significantly higher fields in a future phase of development.

The four titanium electrodes (Ti_1, Ti_2, Ti_3, and Ti_4) were mechanically polished with silicon carbide after fabrication. Their mean surface roughness averages were measured in the range 16–23 nm using a profilometer (MicroXAM) in a clean room. We electropol-
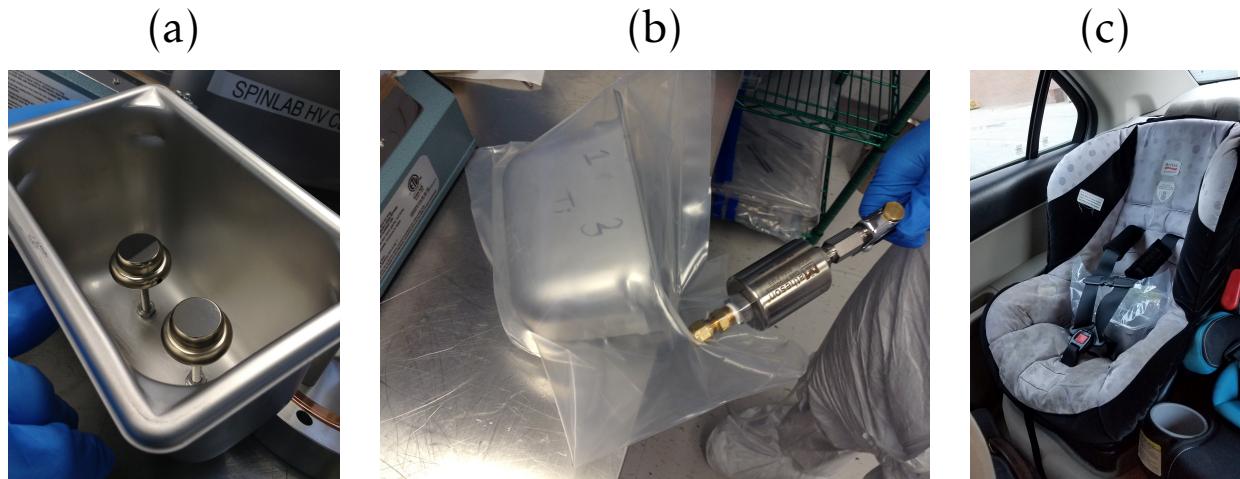
Figure 3.10: Electrode storage and transport. (a) Each electrode pair is mounted from the base in a stainless-steel bin. (b) The electrodes are labeled by etching the material and electrode number on the outside of the bin. (c) We recommend buckling up the electrodes for car trips.

ished pair Ti_{13} commercially and remeasured the electrode surfaces. We observed an increase in the surface roughness of the electropolished titanium electrodes by $\approx 50\%$ and microprotrusions in the range 1–10 μm.

3.3.2 Clean rooms and high pressure rinsing

We developed our clean room technique by building a clean room in the lab and installing a pair of electrodes. The Spinlab portable clean room is shown in Figure 3.8a. The HEPA filter is safely secured overhead. I taped 2 mil polyethylene sheeting in a pleat fashion. Then I used PVC pipes to frame a $5' \times 4'$ area under the filter, over which the sheeting was draped. I validated the clean room to Class 100 with a NIST-calibrated particle detector.

We decontaminate the electrodes in clean rooms at the Facility for Rare Isotope Beams (FRIB) after polishing. The electrodes are cleaned with detergent and rinsed with pure water in an ultrasonic bath in a staging area. They are rinsed in a second ultrasonic bath with UPW inside a Class 100 clean room. The electrodes are then high pressure-rinsed with UPW at 1200 psi for twenty minutes.

Table 3.3: Surface decontamination comparison. P = rinse pressure, T = rinse time, CR = clean room, RR = rinse resistivity.

Lab	P (psi)	T (min)	RR (MΩ cm)	CR (Class)	Ref.
CERN	1500	30	18	100	[127]
JLab	1200	20	> 18	-	[102]
KEK	1100	5	80	100	[114]
MSU	1200	20	18.1	100	This work

We used two HPR methods, shown in Figure 3.9. First, we rinsed the electrodes simultaneously with a turntable and high pressure rinse wand. When we later rinsed a repolished niobium electrode pair (Nb_{23}), the water quality of the turntable setup degraded. We instead used a high pressure rinse gun as shown in Figure 3.9c. After HPR, the electrodes dry in the clean room for several days before being sealed in poly tubing backfilled with dry, filtered nitrogen. A summary of clean room and HPR parameters from several high-gradient development groups is given in Table 3.3.

The cleaned electrodes rest in either in the high voltage test station or in a sealed container, as shown in Figure 3.10. The electrodes have approximately 1" clearance from the container walls on the side and bottom, and 2" below the upper edge. For storage and transport, they are sealed in two layers of clean room tubing and are backfilled with purified, dry nitrogen. The nitrogen is filtered at the point of use by a 0.2 μm membrane filter.

3.4 Electrode Discharge-Conditioning

3.4.1 High voltage test station

A schematic of the MSU high voltage test station is shown in Figure 3.11. Electrode pairs are mounted to a polyether ether ketone (PEEK) holder inside a six-way cross vacuum chamber. To estimate the steady-state leakage current flowing through the holder itself, we model the four "arms" as resistors in parallel with length $\ell = 2 \times 1.6 + 0.1 = 3.3$ cm
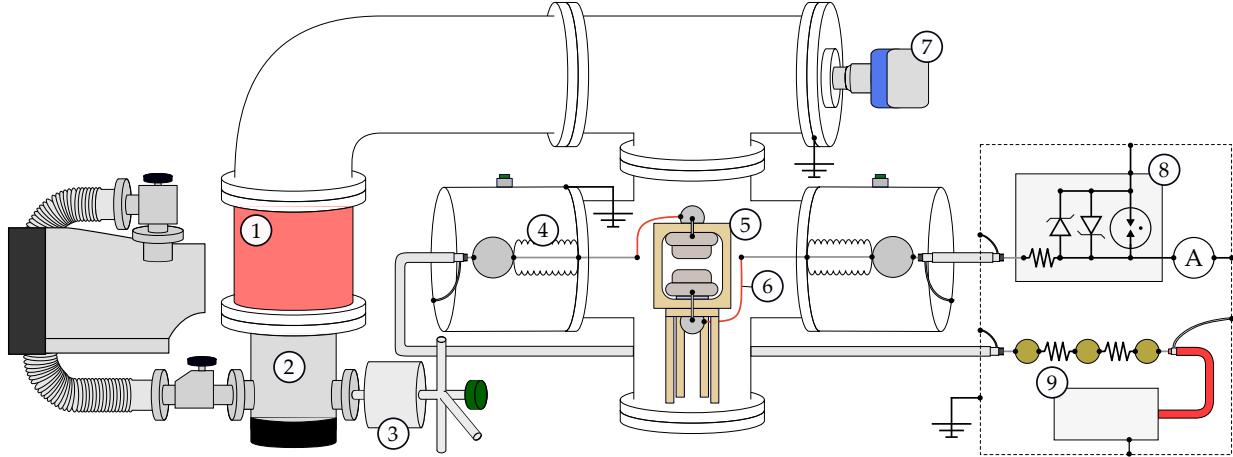
Figure 3.11: MSU HV test apparatus. ① 9699334 Agilent Turbo-V vibration damper ② Pfeiffer HiPace 80 turbomolecular pump with foreline Edwards nXDS10i A736-01-983 dry scroll rough pump and two valves ③ Matheson 6190 Series 0.01 μm membrane filter and purge port ④ Ceramtec 30 kV 16729-03-CF feedthrough ⑤ 0.312 in.^{2} electrodes in PEEK holder (resistivity 10^{16} MΩ cm) ⑥ 20 AWG Kapton-insulated, gold-plated copper wire ⑦ MKS 392502-2-YG-T all-range conductron/ion gauge ⑧ Shielded protection circuit: Littelfuse SA5.0A transient voltage suppressor, EPCOS EX-75X gas discharge tube, Ohmite 90J100E 100 Ω resistor in series with Keithley 6482 2-channel picoammeter ⑨ Ohmite MOX94021006FVE 100 MΩ resistors in series with Applied Kilovolts HP030RIP020 HV.

and cross-sectional area $A = (1.27 \text{ cm})^2$. From Ohm's law, the steady-state leakage current $\bar{I}$ [A] is:

$$\bar{I} = \frac{V}{R} = 4 \, \frac{V \, A}{\rho \, \ell} \, , \tag{3.1}$$

where V [V] is the applied voltage and $\rho = 10^{16}$ Ω cm is the PEEK holder resistivity. The factor of 4 comes from the equivalent resistance of the parallel leakage paths. With an applied voltage of 30 kV, I estimate $\bar{I}_{\max} \approx 6$ pA.

The vacuum chamber is maintained at 10^{-7} Torr with a turbomolecular pump (Pfeiffer Hipace 80). At this pressure the mean free path of residual gas molecules is over a meter, significantly larger than the dimensions of the chamber. The Ra EDM apparatus typically operates at ultrahigh vacuum (UHV) pressures ($< 10^{-11}$ Torr) in the region of the electrodes and trapped atoms [48]. The test station does not involve any trapping of atoms and so we only require a pressure low enough such that the atmospheric con-

stituents do not collide on a length scale close to our gap size of a few millimeters. The mean free path of an atom or molecule λ [m] is given by [135]:

$$\lambda = \frac{1}{\sigma n} \tag{3.2}$$

$$= \frac{k_B T}{\sigma} \frac{1}{P} , \tag{3.3}$$

where

σ $[m^2]$ is the collisional cross section,

k_B [J/K] is the Boltzmann constant,

T [K] is the temperature in the vacuum chamber,

P [Pa] is the pressure, and

n $[m^{-3}]$ = $P/(k_B T)$ is the number density for non-interacting particles, i.e. in the limit of the ideal gas equation.

For an oxygen molecule with a cross section of $\approx 5 \times 10^{-20}$ m^2 [136] and a vacuum pressure of $\approx 5 \times 10^{-5}$ Torr, the mean free path is over a meter. With a roughing pump and turbomolecular pump (TMP) we typically operate at pressures $\approx 2 \times 10^{-7}$ Torr, well below minimum requirements.

The test station is frequently brought to atmospheric pressure for upgrades and electrode installations. We perform this work in clean rooms that are validated to Class 100 or better with a NIST-calibrated particle counter (Lighthouse Handheld 3016). The chamber is backfilled with dry, high-purity nitrogen through a 0.01 micron gas membrane particle filter (Matheson 6190 Series) while venting the chamber and after clean room operations. During initial evacuation the pump rate is controlled at 1 Torr/s with foreline valves to reduce the risk of disturbing vacuum chamber surfaces.

We use polished corona ball connections inside and outside the test chamber to minimize discharge risk beyond the electrode gap region. The power supply (Applied Kilovolts HP030RIP020) and feedback resistors are mounted inside a grounded high voltage

cage. The feedthroughs are enclosed by grounded "soup can" style shields that can be flooded with dry nitrogen to reduce humidity.

We use a 2-channel picoammeter (Keithley 6482) to measure the current flowing between the electrodes. One channel is not connected and is used to track correlated drifts between the channels. A protection circuit between the electrode and picoammeter suppresses high-power transients that could damage the picoammeter. Typical discharges between the electrodes do not trigger the protection circuit. We calibrated the picoammeter with the protection circuit to within 10 pA.

3.4.2 Optical measurements of electrodes and gap sizes

The Ra EDM experiment requires a gap-measuring precision of 0.1 mm or better. I developed an imaging system to measure electrode dimensions and gap sizes without making contact with the electrode. The system uses a CMOS camera and bi-telecentric machine lens (Thorlabs MVTC23024). A schematic of the optical imaging system is shown in Figure 3.12.

To test the electrodes at different gap sizes, we adjust the gap size *in situ* by translating the bottom electrode vertically with a high-precision linear drive (MDC 660002). The assembly is shown in Figure 3.13a.

I calibrated the optical system by imaging the gap size over a range of lengths corresponding to drive positions. The gap size is measured in pixels and converted to millimeters. A plot of one gap calibration measurement is shown in Figure 3.13b. The offset parameter is related to the initial gap size and can vary between calibrations if the linear drive direction is reversed. We calibrated the optical imaging system using the linear drive to a gap-measuring precision of 1% of its pixel-conversion specification of 19.8 μm/px.

I tested electrode performance over gap sizes ranging 0.4–2.5 mm before removing the linear drive and standardizing the gap size to 1 mm for testing. This gap size was
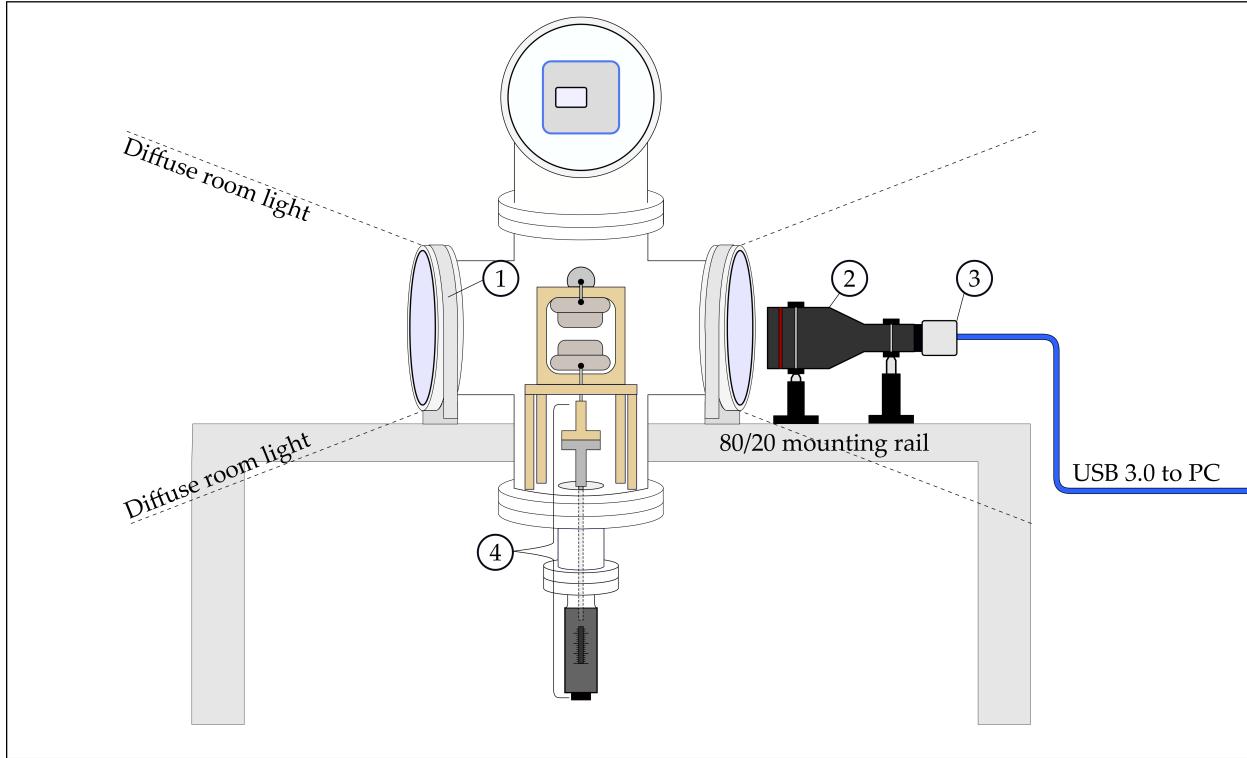
Figure 3.12: The imaging components of the HV apparatus. This is a profile view of the apparatus after rotating the schematic in Figure 3.11 by 90° and removing non-imaging components. ① worm-drive rail mount ② Thorlabs MVTC23024 magnification (M) = 0.243, 4.06" working distance (WD) telecentric lens ③ Edmund Optics EO-2323 monochrome CMOS camera, 4.8 μm square pixels ④ Adjustable Electrode Gap Assembly: MDC 660002 linear motion 0.001" graduated, 1" travel adjustable drive and custom PEEK mount interface with angular adjustment.

chosen to ensure electric field uniformity over the length scale of the atom cloud and avoid accidental heating of the electrodes by trapping lasers. The ODT beam diameter constrains the atom cloud diameter to 100 μm .

We used the optical imaging system electrode measurements to fabricate the EDM electrode holder for the niobium electrode pair Nb_{56}, shown in shown in Figure 2.4. The EDM electrode holder is designed for a 1.0 ± 0.1 mm gap size.

3.4.3 Data acquisition and filtering settings

A complete description of acquisition and filtering settings used for each tested pair of electrodes is given in Table 3.4. We record the power supply current, power supply volt-

(a)   (b)
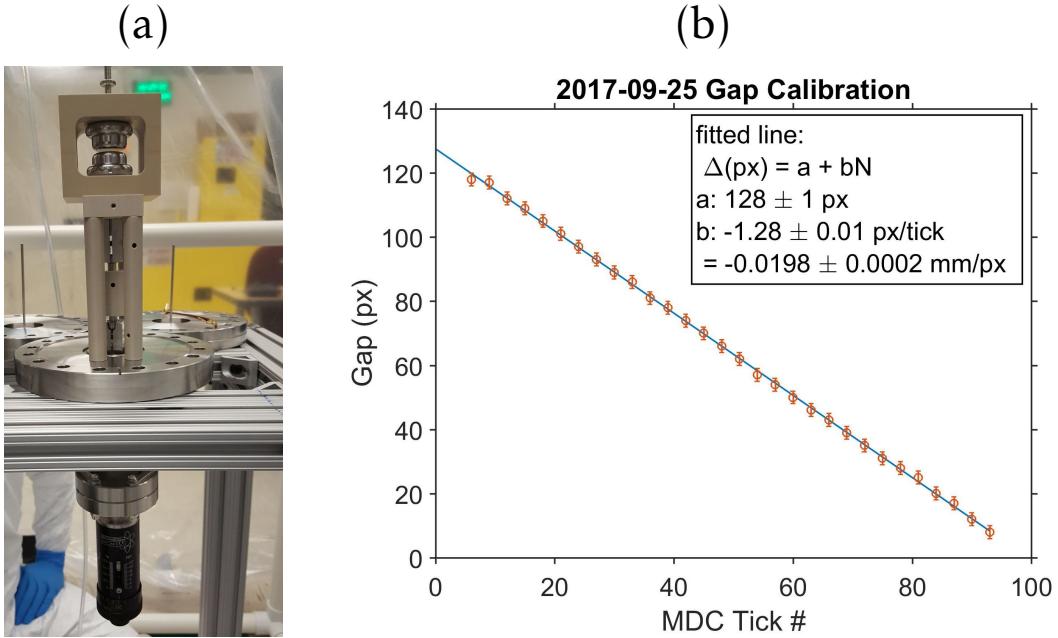
Figure 3.13: (a) The linear adjustable electrode gap assembly (b) A weighted line is fit to a scatter plot of gap size vs. drive position and a conversion from pixels to inches is determined.

age, vacuum pressure, leakage current, and rough pump foreline pressure with a 16-bit, 250 kS/s data acquisition device (NI DAQ USB-6218) connected to an office model desktop PC. Each input channel uses a ±10 V range. The analog signals are digitally filtered to remove 60 Hz outlet noise and mechanical vibrations from the vacuum pumps. We initially sampled data at 16 kHz but later increased the sample rate to 30 kHz after upgrading the RAM and hard disk of the DAQ PC. The mean and standard deviation for each recorded data point is calculated from 8192 samples.

We removed the outlet noise filters after conditioning several pairs of electrodes because they introduced artificial shapes in the signal waveform. Comparing the leakage current data of electrode pairs with different filtering settings, we found that the digital filters did not significantly affect the distribution of the dataset discussed in Section 3.4.4. As I will discuss in Section 3.4.10, we are sensitive to absolute currents as small as $\sigma \approx 25$ pA with the acquisition settings described in Table 3.4.

Table 3.4: 5σ Data acquisition and filtering settings. Used filters indicated by filled-in circles. SR = sample rate.

| pair | DAQ | | Digital filters | | | | |
	SR (kHz)	$\frac{\text{samples}}{\text{point}}$	25–35 Hz bandstop	55–65 Hz bandstop	109–113 Hz bandstop	115-125 Hz bandstop	7.5 kHz lowpass
Nb$_{56}$	16	8192	●	●	●	●	●
Nb$_{78}$	16	8192	●	●	●	●	●
Ti$_{13}$	30	8192	○	○	○	○	●
Nb$_{23}$	30	8192	○	○	○	○	●

3.4.4 Identifying electrode discharges

We average 8192 samples at sample rates of 16 kHz for electrode pairs Nb$_{56}$, Nb$_{78}$ and 30 kHz for Ti$_{13}$, Nb$_{23}$, corresponding to a recorded data point every 512 ms and 273 ms, respectively. Since each high voltage magnitude and polarity setting lasts for a time period of 60 seconds, this corresponds to about 120 samples collected per time period at 16 kHz and 220 samples collected per time period at 30 kHz.

The distribution of each 60 s time period in a conditioning shift is modeled as a Gaussian distribution. An example of a Gaussian fit to one 60 s time period distribution is shown in Figure 3.14. The fit is reasonable and discharges are clearly distinguished from the rest of the data.

I define a "discharge" as any standard deviation exceeding the Gaussian 5σ threshold above the mean value $\bar{x}$. We typically observe discharge sizes in the range 100–1000 pA, but it is not uncommon to observe larger discharge sizes around 1–10 nA.

To estimate discharge magnitudes, I report the median value of the standard deviations in each 60 s time period. We expect to see high rates of discharges during conditioning. Small discharges occurring at a stable rate are beneficial and do not damage the electrode surfaces.

Our discharge counting method does not exclude discharges that could occur at another part of the test station, for example the high voltage feedthroughs. Therefore, we
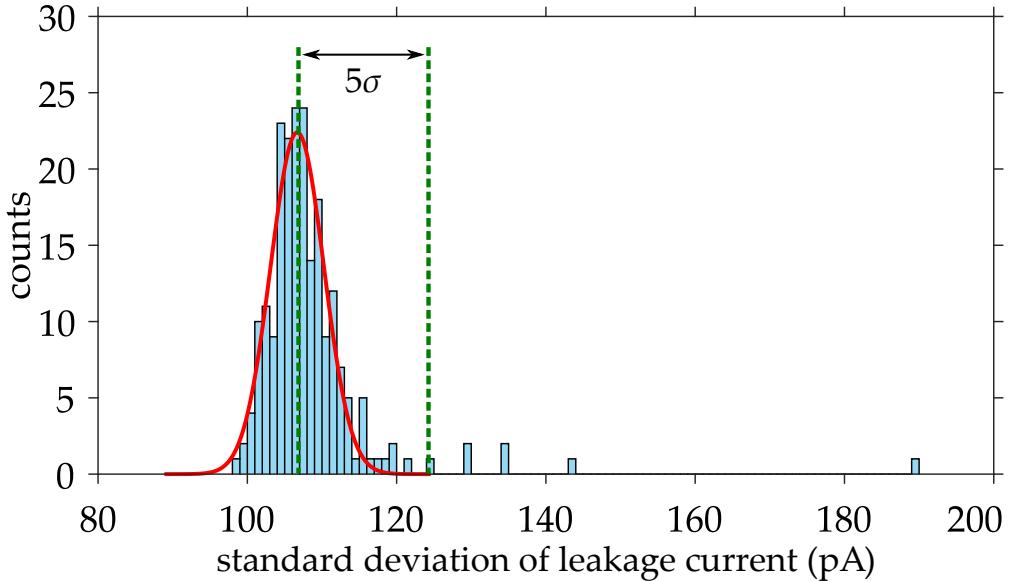
Figure 3.14: Nb$_{23}$ at +22 kV/mm over one 60 second cycle during the final hour of conditioning. From the Gaussian fit (solid red line) we determine the mean to be $\bar{x} \pm \sigma = 106.7 \pm 3.6$ pA. There are 207 total data points. We identified 7 events exceeding the $\bar{x} + 5\sigma = 125$ pA threshold as discharges.

expect our reported discharge rates are conservative overestimates of the true electrode discharge rate.

Additionally, we calculate the steady-state leakage current $\bar{I}$ by fitting a Gaussian to the sample means, rather than the standard deviations, of each 60 s time period. Electronic offsets and drifts are removed by subtracting the mean current measured by the picoammeter during the zero voltage time periods neighboring each high voltage time period. An example of $\bar{I}$ measurements measured over a four-hour conditioning shift for Nb$_{56}$ is shown in Figure 3.15.

Since the integration time for each data point at 30 kHz is 273 ms, $\bar{I}$ is insensitive to discharges, which typically last ≈ 1 ms. To illustrate, we can compare the discharges identified by the mean data and the standard deviation in the third hour of a 26.2 kV conditioning shift of Ti$_{13}$. Histograms of the discharges identified by the standard deviations are shown in Figure 3.16. I count a polarity-combined 111 discharges with the standard deviation data over one hour. Using a similar analysis with the sample means, I
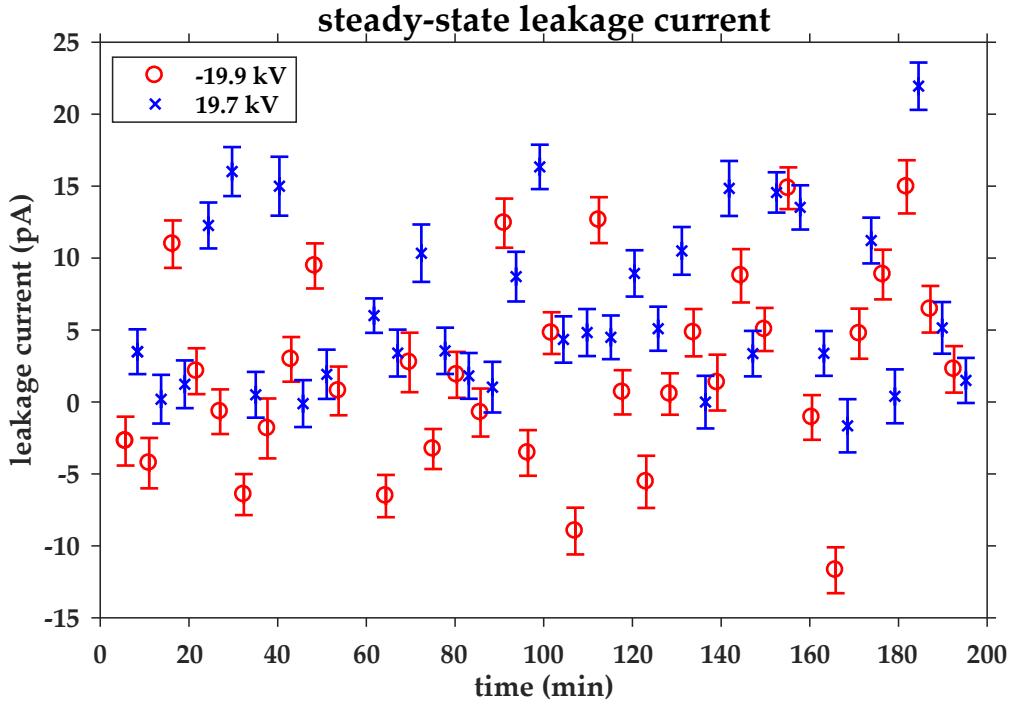
Figure 3.15: The offset-subtracted average leakage currents for each positive and negative high voltage time period during conditioning at 20 kV with Nb$_{56}$ at a gap size of 1 mm.

count only 11 events outside of the 5σ threshold during the same time period.

My analysis code models the leakage current and calculates the discussed performance metrics. The accuracy of the analysis was independently verified. Code and data availability may be found in Appendix B.

3.4.5   Discharge-conditioning procedure

Our goal is maximize the electric field strength while minimizing the discharge rate and discharge size. We condition the electrodes at DC voltage, alternating the voltage polarity every 60 s. The voltage is applied to the top electrode. The periodic voltage waveform is chosen to simulate the EDM measurement and is more challenging to stabilize than holding off a static unipolar field. Each conditioning shift at one high voltage magnitude
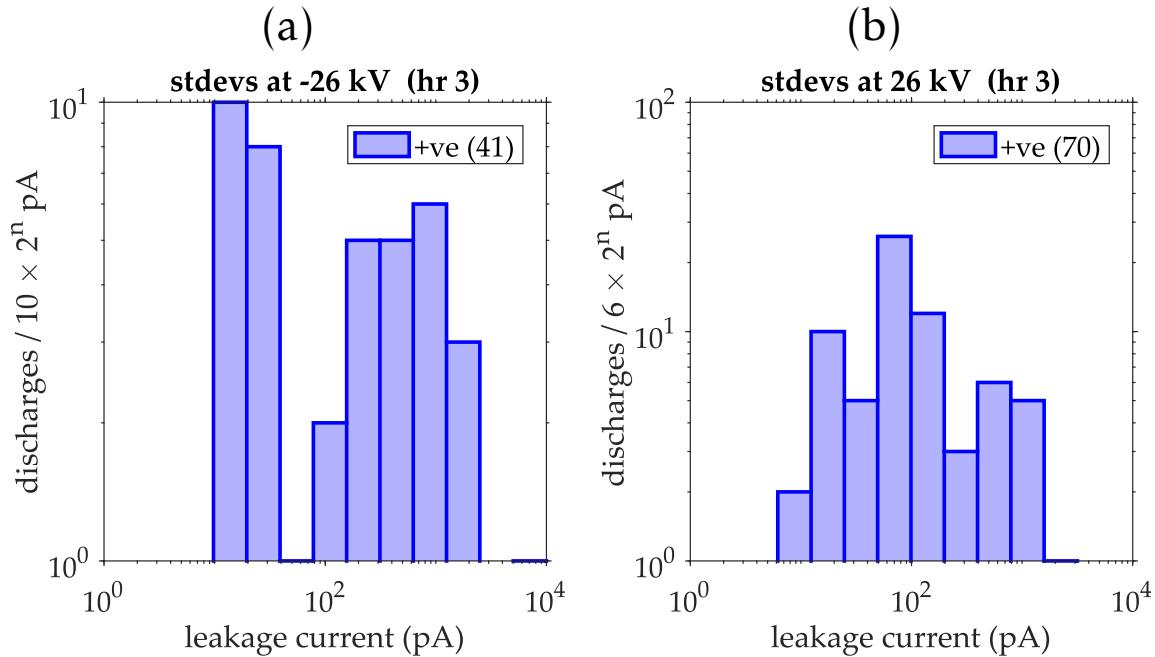
Figure 3.16: Histograms of all the discharges for both polarities during the third hour of conditioning the titanium electrodes on a log-log scale.

with this periodic waveform typically lasts 3–5 hours[1].

In the final conditioning phase we validate the electrodes at some fraction of the maximum voltage to reduce the discharge rate. The validation voltage is typically 80–95% of the maximum tested voltage, consistent with the literature [100, 113].

I show the average discharge rates and discharge sizes for both polarities for all the electrodes in Figures 3.17, 3.20, 3.21, and 3.22. I define a 'baseline' value as the average discharge rate and discharge size during the first conditioning shift. Each of these figures has a baseline value that is subtracted from the data.

In Sections 3.4.6, 3.4.7, 3.4.8, and 3.4.9, I will discuss the discharge-conditioning results of each electrode pair. In Section 3.4.10, I will compare the overall performance of the electrodes.

---

[1]We found that the highest discharge rates tended to occur during the second and third hours of a shift, so we scheduled five-hour shifts when possible.
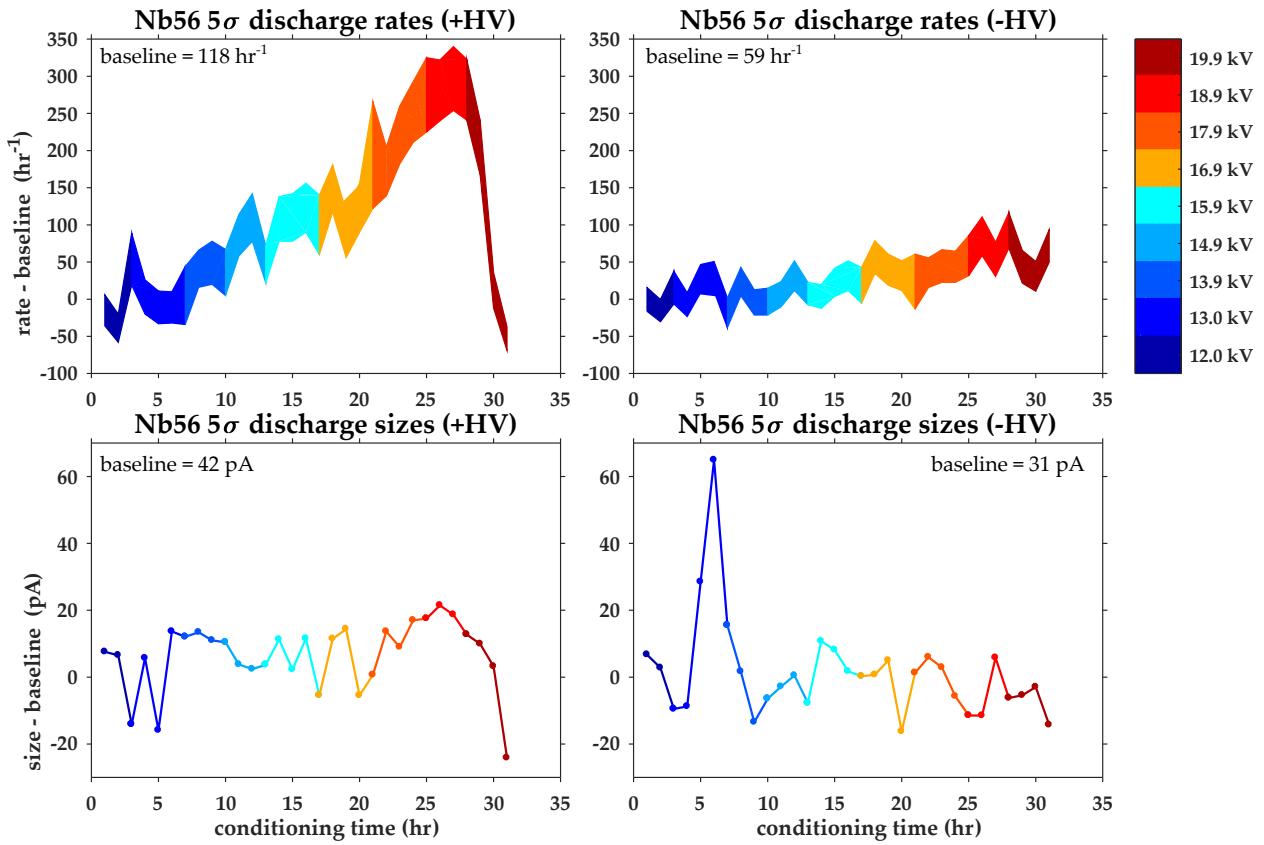
Figure 3.17: Discharge-conditioning timeline for Nb_{56} at a 1 mm gap size.

3.4.6 Conditioning results for electrode pair Nb_{56}

The average discharge rate over the course of conditioning the niobium electrode pair Nb_{56} is shown in the upper panels of Figure 3.17. At each voltage, the discharge rates, expressed in discharges per hour (dph), tend to decrease as we condition. There is a step-like increase in discharge rates when the voltage is increased. Nb_{56} was validated at 20 kV / 1 mm with an average discharge rate of 98 ± 19 dph after approximately thirty hours of conditioning.

At negative polarity, the discharge rate increases more slowly with each voltage step. However, the overall curve does not flatten at a minimum count rate as it does at positive polarity. This suggests that additional conditioning could further suppress discharges at negative polarity. It's also possible that the test station design facilitates a higher discharge rate at negative polarity. We will explore this in the near future by conducting
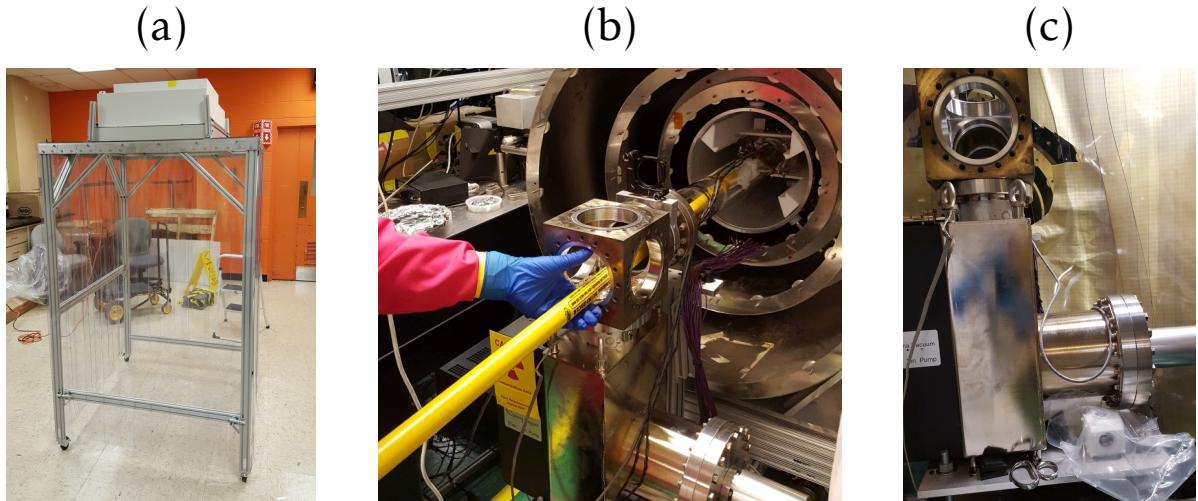
Figure 3.18: Installation of niobium electrode pair Nb_{56} in Ra EDM apparatus. (a) ANL portable clean room with aluminum beams, plastic drapes, and a $4' \times 2'$ HEPA filter. (b) The borosilicate glass tube was cleaned with a clean-room grade wipe wrapped around the end of a fiberglass pole. (c) The clean room was positioned over the electrode entry point before installing the electrodes (seen in the bottom corner).

conditioning tests while the electrodes are removed from the test station.

Nb_{56} discharge sizes are shown in the lower panels of Figure 3.17. As we will see with all the discharge plots, the discharge size behavior does not scale with the discharge rate. The largest median discharge size over the course of conditioning is 60 pA, which is relatively small compared to the typical discharge sizes of the other electrode pairs. In the last hour of conditioning the discharge sizes are 20 pA smaller than the starting discharge sizes.

As mentioned in Section 3.1.1, the legacy copper electrodes were conditioned to 10 kV/mm but could only be operated at 6.5 kV/mm after installing them in the Ra EDM apparatus. For the second generation electrodes, I made two major improvements to the technique to prevent a similar reduction in field strength. First, our electrodes are now preserved in Class 100 (ISO 5) or better clean room environments during both conditioning and transport as described in Sections 3.3.1 and 3.4.1. Second, we used the new, rigorous discharge-conditioning analysis described Section 3.4.4 for Nb_{56} and the elec-

heater tape

RGA

X

feedthru heater bottom

MOT

bellows heater bottom

high voltage
feedthroughs

X

bellows heater top

feedthru heater top

TiSub
pump

getter
pump

X: thermocouple position
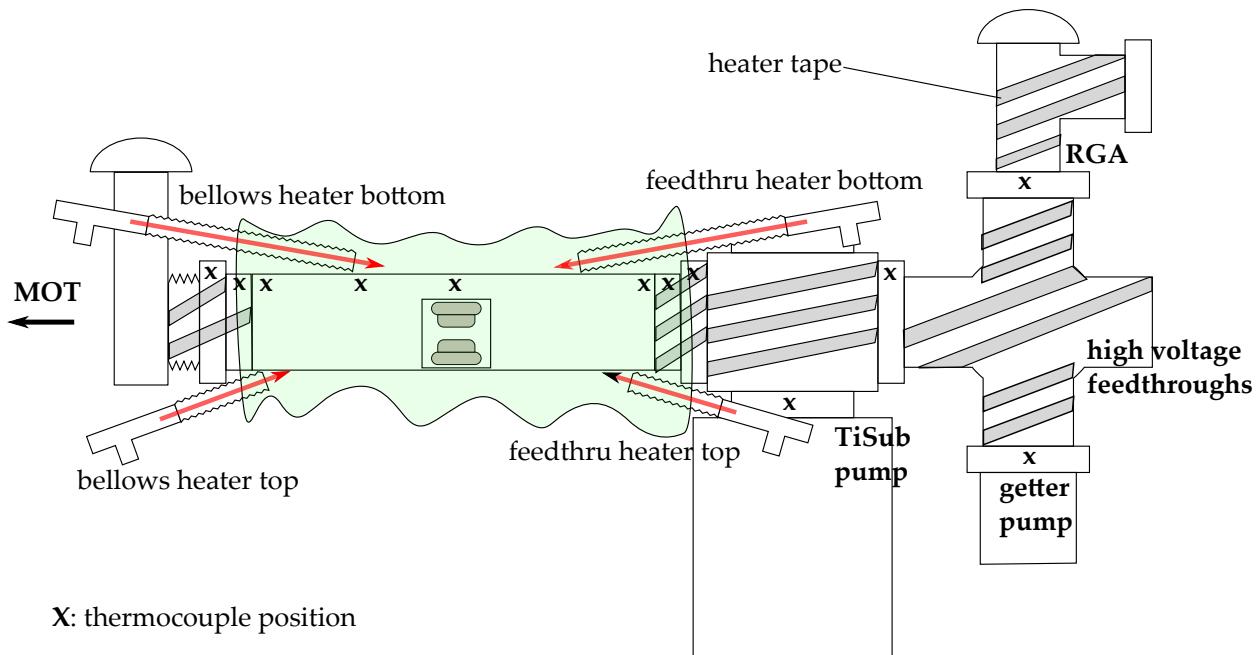
Figure 3.19: A schematic of the water bake of the Ra EDM experimental apparatus following the installation of the new electrode pair.

trodes discussed in the subsequent sections.

Nb_{56} was installed in the Ra EDM apparatus on May 15, 2018 in the conditions shown in Figure 3.18. Details will be discussed in Section 3.4.13.

Following installation, I "baked" the EDM apparatus by heating the borosilicate tube and high voltage vacuum components at 120 °C for three days and then increased the temperature to 150 °C for approximately five weeks. This temperature is high enough to remove moisture that was introduced during the electrode installation. The vacuum pressure dropped by more than three orders of magnitude over the course of the water bake.

A schematic of the water bake is shown in Figure 3.19. To equalize the temperature throughout the system, I used heater tape, foil, and several heat guns. I monitored the temperature with thermocouples.

After the water bake, I revalidated electrodes Nb_{56} at 20 kV/mm. This electrode pair will be used for upcoming second generation EDM measurements and is expected a factor
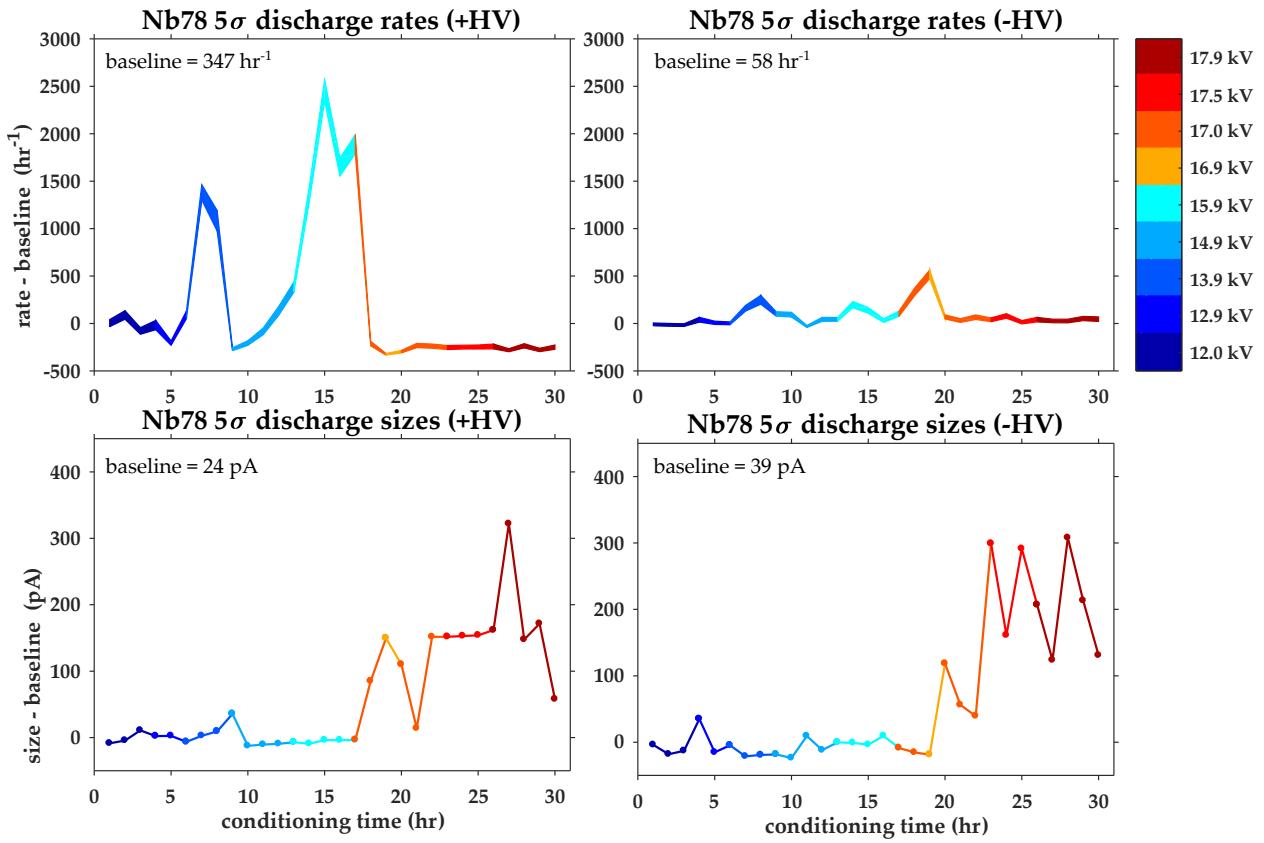
Figure 3.20: Discharge-conditioning timeline for Nb_{78} with a 1 mm gap size.

of 3.1 improvement to our EDM measurement sensitivity.

3.4.7   Conditioning results for electrode pair Nb_{78}

Discharge rates and sizes for the second pair of niobium electrodes Nb_{78} are given in Figure 3.20. We started conditioning Nb_{78} at 12 kV/ 1 mm, the same electric field as Nb_{56}. The initial discharge rates are occasionally in excess of 1000 dph, or about once every three seconds for several hours with discharge sizes of 50 pA. The high discharge rate coupled with low discharge size is an indication that we are operating at an ideal voltage for discharge-conditioning. During the last 10 hours of conditioning the discharge rates decrease to less than the initial rates. The final conditioning shift was performed at 17.8 kV/mm.

These electrodes were packaged according to our procedure described in Section 3.3.2
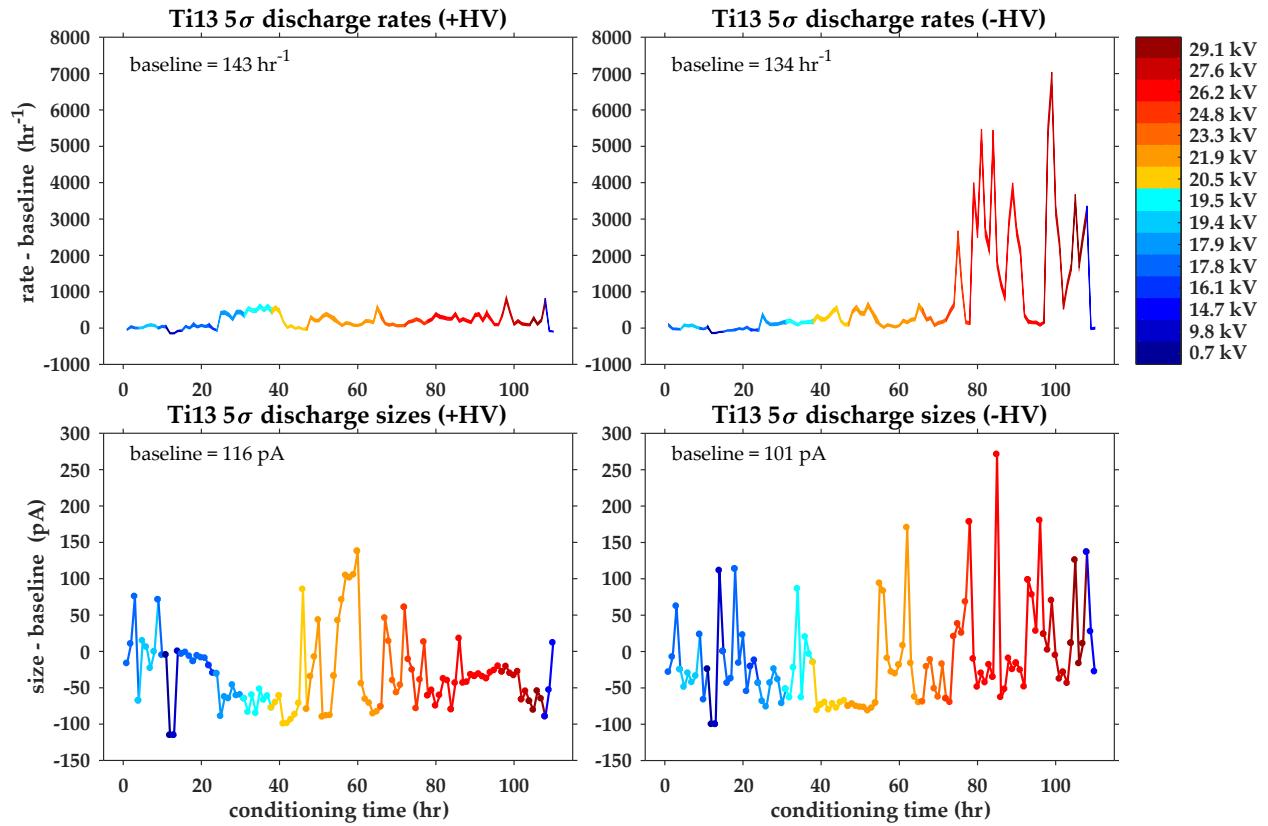
Figure 3.21: Discharge-conditioning timeline for Ti_{13} at a 0.9 mm gap size.

and shipped to USTC, where they are being used in a new ytterbium EDM measurement.

3.4.8 Conditioning results for electrode pair Ti_{13}

We changed our data acquisition and digital filter settings for Ti_{13} and the pair that we will discuss in Section 3.4.9 (see Table 3.4). To reach electric fields higher than 20 kV/mm, we conditioned the titanium electrodes for 110 hours, four times longer than the previous pairs.

Discharge rates and sizes for the titanium electrodes are shown in Figure 3.21. We started conditioning the electrodes at 14.9 kV/ 0.9 mm = 16.5 kV/mm. The initial discharge sizes are approximately 100 pA, significantly higher than Nb_{56} and Nb_{78}. The discharge rates did not consistently decrease over the course of several shifts at 19.4 kV. At hour 12, we reduced the voltage to 0.7 kV for one shift to verify that the discharge

rates decrease before resuming testing at higher voltages.

The discharge rate increases from 290 dph to 5550 dph when stepping the voltage from −26.2 kV to −27.6 kV. This step-like 'switching on' of leakage emission sites is consistent with our expectations, given the physical picture of conditioning we describe in Section 2.6. In principle, the emission sites, which may be thought of as microprotrusions, are ablated after spending sufficient time discharge-conditioning the electrodes. The factors influencing the required amount of time include the smoothness of the high-gradient surfaces, the gap size, and the applied voltage. We were unable to significantly reduce the discharge rates at 27.6 kV / 0.9 mm = 30.7 kV/mm despite more than twenty hours of conditioning at that field strength.

During the final shift, we reduced the voltage to 14.7 kV / 0.9 mm = 16.3 kV/mm and again observed the discharge rates returning to the baseline. Ti_{13} can likely be conditioned to perform stably at $\approx$ 24 kV, or 85% of the maximum applied voltage with additional conditioning. However, the concentration of magnetic impurities in our titanium electrodes (shown in Table 3.2) is likely too high to be used for an EDM measurement.

3.4.9   Conditioning results for electrode pair Nb_{23}

I initially tested Nb_{23} at a 0.4 mm gap with fields as high as +52.5 kV/mm and −51.5 kV/mm using the traditional hold-off or "current-conditioning" method [100]. Then I discharge-conditioned the electrodes with the periodic waveform described in Section 3.4.4 to 27.5 kV/mm. However, a large discharge of $\approx$ 100 nA during a 30 kV/mm conditioning shift triggered a current avalanche that rapidly increased the leakage current and damaged the electrodes.

I was unable to recover meaningful performance after several conditioning attempts. The electrodes were removed from the test station and repolished the surface according to Table 3.1. Then I reinstalled Nb_{23} and repeated the conditioning at a 1 mm gap.

Repolished Nb_{23} discharge rates and sizes are shown in Figure 3.22. The rates stay
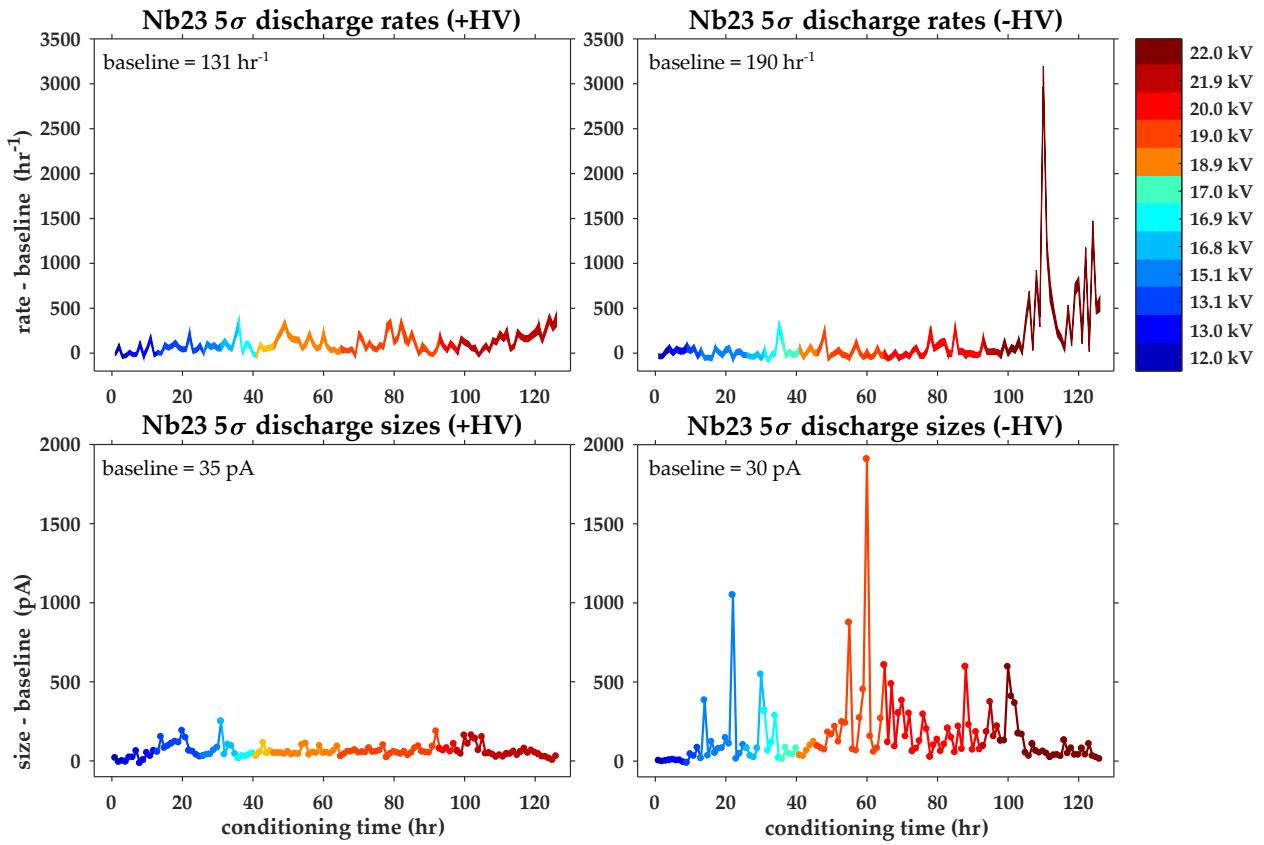
Figure 3.22: Discharge-conditioning timeline for Nb$_{23}$ at a 1 mm gap size.

near the baseline, about 200 dph for both polarities up to 20 kV. When we increased the voltage from 20 kV to 22 kV, the discharge rates at negative polarity become as high as 3000 dph (about once every second). The discharge sizes were low, less than 500 pA, so we continued conditioning at this voltage. Despite conditioning the electrodes at 22 kV/mm for more than twenty hours, the discharge rate remained high. I expect that reducing the voltage by $\approx$ 1 kV will restore the baseline discharge rate.

For this pair of electrodes, repolishing and reconditioning allowed us to recover 80% of the original electric field performance.

3.4.10 Comparison of overall electrode performance

Table 3.5 compares the electric fields tested and discharge rates observed for all of the conditioned electrode pairs averaged over both polarities. E_i is the electric field strength

Table 3.5: Electrode conditioning summary. E_i = initial field strength. $E_{\max}$ = max field strength. E_f = final validated field strength. R_i (R_f) = initial (final) discharge rate. $\bar{I}$ = steady-state current at E_f.

pair	E_i (kV/mm)	$E_{\max}$ (kV/mm)	E_f (kV/mm)	$\dfrac{E_f}{E_i}$	$\dfrac{R_f}{R_i}$	$\bar{I}$ (pA)
Nb_{56}	11.9	19.8	19.8	1.7	1.6	< 10
Nb_{78}	12.0	17.9	17.9	1.5	0.9	< 10
Ti_{13}	19.8	32.3	29.1	1.5	2.2	< 30
Nb_{23}	12.0	22.0	21.9	1.8	1.3	< 25

at the start of the conditioning, while $E_{\max}$ is the electric field strength at the end of the conditioning. E_f is the final validated field strength, and may be reduced to $\approx 85\%$ of $E_{\max}$ for more stable performance.

The initial electric field is 12 kV/mm for the niobium electrodes and 16.5 kV/mm for the titanium electrode pair. I chose these field strengths because the discharge rate and discharge size was sufficiently low. The maximum and final electric fields depended entirely on the performance of the electrodes.

All the electrodes were discharge-conditioned to higher than our original goal of 15 kV/mm. The steady-state currents $\bar{I}$ at E_f are under the EDM experimental threshold of 100 pA.

One metric for characterizing discharge-conditioning is to compare the electric field strength ratio E_f/E_i versus the discharge rate ratio R_f/R_i. My expectation for successful conditioning is that the electric field scaling should be comparable, and ideally larger than the discharge rate ratio. We were able to scale the electric field more quickly than the discharge rates for all the niobium electrodes. For Nb_{78}, the final polarity-averaged discharge rates were lower than the initial discharge rates. As discussed in Section 3.4.8, the Ti_{13} discharge rate outpaced the electric field strength increase at 30.7 kV/mm.

Of particular note is the polarity dependence of the electrode discharge rates. In all cases except for Nb_{23}, the negative polarity discharge rates are significantly higher than
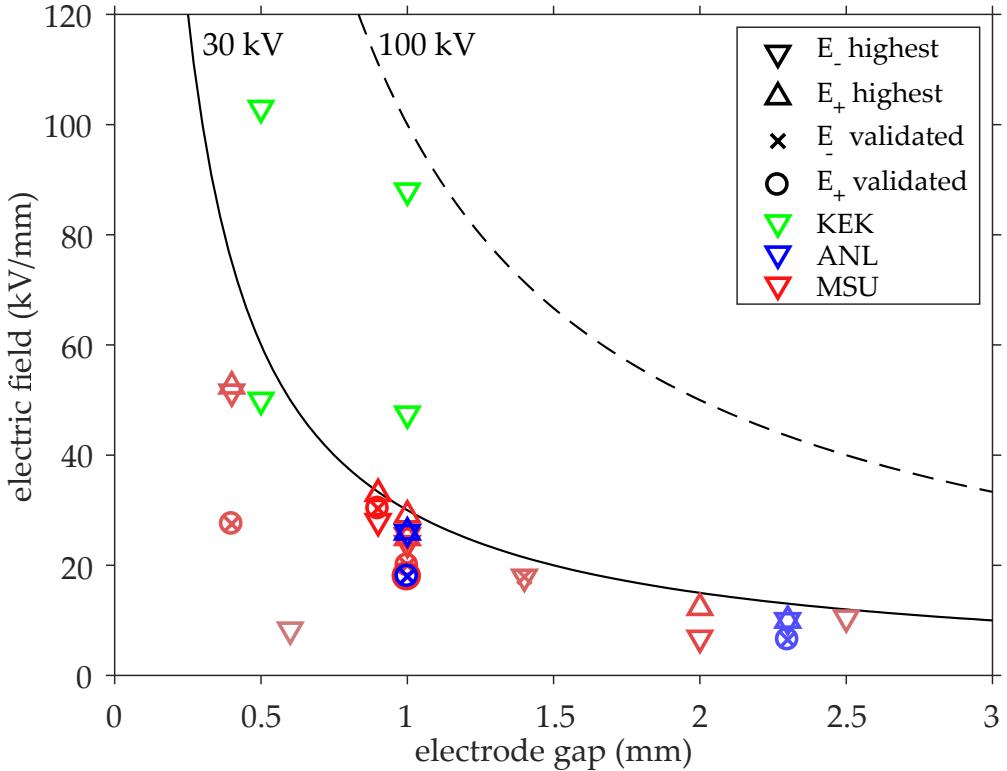
Figure 3.23: A plot of electric fields reached by electrode pairs. Blue data are electrodes used in the Ra EDM apparatus. Green data are electron gun electrodes tested with a −100 kV power supply [114]. Red data are electrodes tested at MSU. Brighter, more intense colors are more recent results.

the discharge rates at positive polarity. Polarity-correlated discharge rates could be a consequence of the asymmetry of our setup, as illustrated by Figure 3.11. Our goal for the next phase in high voltage development is to design a more symmetric setup that will alternate the role of grounded and charged electrode. In addition to increasing the electric field strength capability, we expect the new setup to aid the investigation of polarity-correlated discharge rates.

3.4.11 Comparison of electrode performance with other systems

A comparison of the maximum stable electric field performance of electrode pairs prepared at ANL [65, 48], the High Energy Accelerator Research Organization (KEK) [114], and MSU is shown in Figure 3.23. We tested a maximum electric field of +52.5 kV/mm
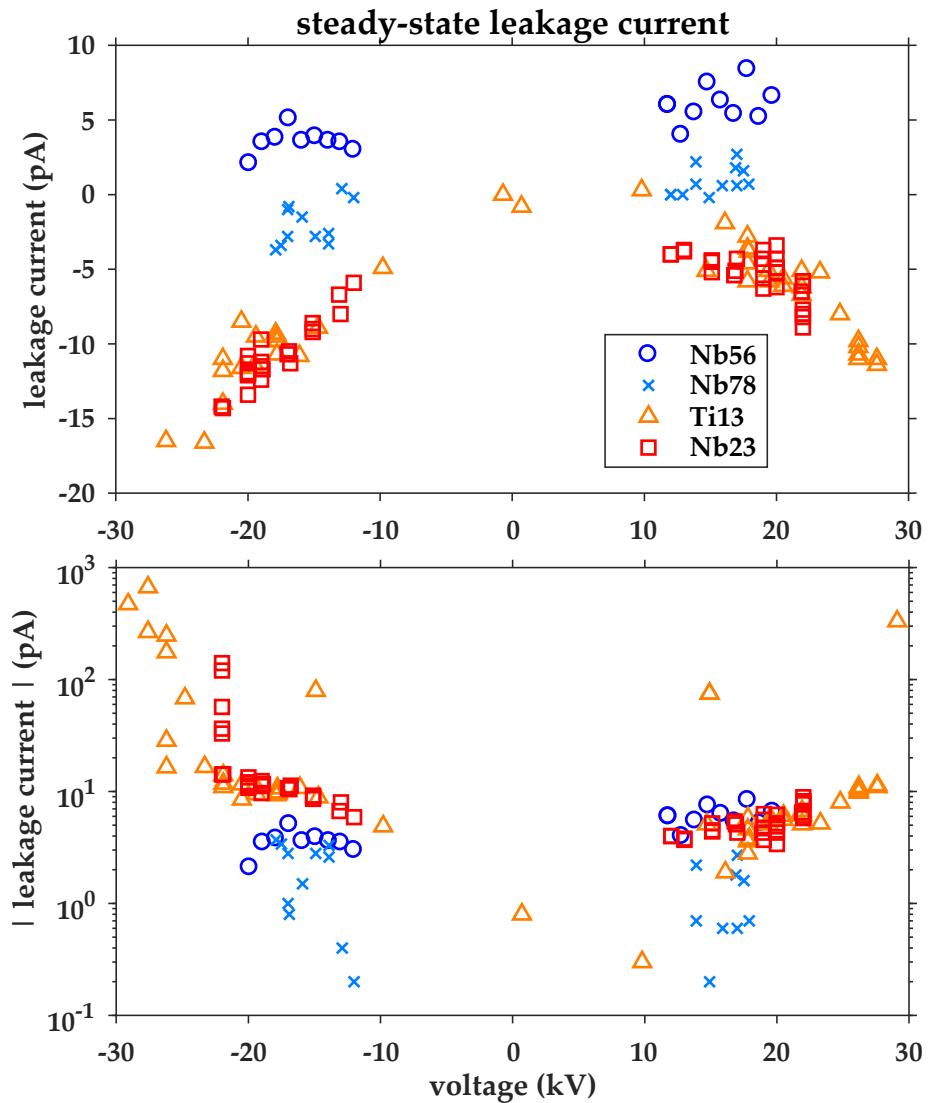
Figure 3.24: Weighted averages of the steady-state leakage current on linear and log scales. Errors are on the order of 0.1 pA.

and -51.5 kV/mm with one of our niobium pairs of electrodes (Nb$_{23}$) at a gap size of 0.4 mm. The electrode conditioning results described by Furuta et. al are a useful, if imperfect comparison. Their electrode size is and electrode gap size is similar, but they use an asymmetric electrode geometry and a unipolar power supply. The KEK group pairs a stainless steel spherical anode with "button-shaped" cathodes made from refined, high-purity 316L stainless steel ("Clean-Z"), titanium, and molybdenum.

The data in Figure 3.23 suggests that fields in the realm of 100 kV/mm are attainable

in principle. Electrode geometry, high-gradient surface area, high voltage polarity, and the nature of the voltage waveform are some of the parameters that may limit the ultimate performance of our electrodes.

At present, the main limiting factor of the Ra EDM electric field strength is the 30 kV maximum output of the high voltage power supply.

3.4.12 Steady-state leakage current analysis

We plot the weighted average steady-state leakage current for each applied voltage for all the electrodes in Figure 3.24. Each data point represents the average of one polarity at one voltage setting over an entire shift. For example, Figure 3.15 shows the "raw data" that's averaged into ± 20 kV data points for Nb_{56} and plotted in Figure 3.24.

In Section 3.4.4, I stated that the steady-state leakage current is calculated by subtracting the signal measured during the zero-voltage time periods that occur between each high voltage time period. This zero-voltage background subtraction removes the instrument offsets and linear drift, but does not account for high-voltage correlated systematics.

The power supply voltage monitor and current monitor signals scale with voltage magnitude. Because we sample data on one DAQ card, a small amount of signal from adjacent and non-adjacent input channels can affect each other. Each leakage current value $\bar{I}$ from Figure 3.24 can be written as the true leakage current $\bar{I}^{(0)}$ plus correlated systematics:

$$\bar{I}^{(0)} + \delta I_{\text{VMON}}(V) + \delta I_{\text{IMON}}(V), \tag{3.4}$$

where $\delta I_{\text{VMON}}(V)$ and $\delta I_{\text{VMON}}(V)$ are voltage magnitude-correlated systematics.

I estimate the voltage magnitude-correlated systematics assuming an applied high voltage of 30 kV. At this voltage, the signal size of the voltage monitor $V_{\text{VMON}} \approx 10$ V and $V_{\text{IMON}} \approx 0.4$ V. The current monitor channel is adjacent to the leakage current signal and the voltage monitor signal is non-adjacent. From the DAQ datasheet (NI DAQ USB-

6218), I assume the adjacent channel crosstalk is -75 dB and the non-adjacent crosstalk is -95 dB. This gives a total crosstalk signal of

$$V_{\text{CT}} \approx (+0.4 \text{ V}) \times 10^{-(75/20)} + (10 \text{ V}) \times 10^{-(95/20)} \approx +0.3 \text{ mV}$$

The picoammeter range is 200 nA and the analog voltage output is inverting on a 10 V scale, so the crosstalk voltage shifts the leakage current signal at both high voltage polarities by

$$+0.3 \text{ mV} \times (-200 \text{ nA})/10 \text{ V} = -6 \text{ pA}$$

The magnitude of voltage-correlated systematics is on the order of the sampling resolution of the 16-bit DAQ card. There is also a polarity-dependent crosstalk systematic, but this effect is negligible at the ≈ 1 pA level.

Taking high-voltage correlated systematics into account, the steady-state leakage currents in Figure 3.24 are subject to systematic uncertainty at the ≈ 10 pA level.

The steady-state leakage current versus voltage trend is modestly linear with an ohmic resistance of 40 kV/10 pA $\approx 10^{16}$ Ω. We observe large leakage currents > 100 pA, correlated with high discharge rates, for Ti_{13} and Nb_{23} beyond 22 kV. In the most extreme case, we measured $\bar{I} \approx -670$ pA during conditioning Ti_{13} at -27.6 kV.

The steady-state leakage current must be less than 100 pA to avoid systematics that could mimic an EDM signal at our current statistical sensitivity. This criterion is similar to metrics used in other electrode development groups [102, 114]. Our steady-state leakage current sensitivity is limited to ≈ 25 pA. At the Nb_{56} final validated field strength of 20 kV/mm, the measured steady-state leakage current is below this upper limit.

3.4.13 Transportation and installation of electrodes in Ra EDM apparatus

Moving the Nb_{56} electrodes from the MSU high voltage test station to the ANL EDM apparatus posed the highest risk of surface contamination. Before transport, I packaged them in a Class 100 clean room at the National Superconducting Cyclotron Laboratory

(NSCL). The electrodes were mounted in a cleaned stainless steel container by their base to minimize their risk of contact with any surface, as seen in Figure 3.1. I double-bagged and sealed the container and electrodes in clean room tubing and backfilled with particle-filtered dry nitrogen.

I transported the electrodes from MSU to ANL in December 2017.

Starting in February 2018, I constructed a custom portable clean room at ANL. I used a NIST-calibrated particle counter to verify that the clean room was within Class 100 limits. The portable clean room is shown in Figure 3.18a. On May 13, 2018, I unpacked Nb_{56} in the portable clean room and assembled in a new Macor holder designed for an electrode gap of 1 mm. I packaged the electrodes and Macor holder in backfilled poly tubing, as before.

On May 15, 2018, the Ra EDM science chamber front end was disassembled (shown in Figure 3.18b) and the legacy copper electrodes were removed.

The portable clean room was positioned over the science chamber opening. The clean room and science chamber were cleaned and validated at Class 100 standard. A view from inside the clean room is shown in Figure 3.18c. Finally, the electrodes were removed from their packaging and installed in the science chamber on May 15, 2018.

The EDM apparatus was vacuum pumped and water baked as described in Section 3.4.6. On July 22, 2018, I revalidated the Nb_{56} electrode performance to 20 kV/mm.

I worked at Argonne National Laboratory (ANL) from February 2018 through August 2018. During that time I worked on the upgrade for the longitudinal atom slower ("Blue slower") project. I'm the third author on the publication describing our fluorescence measurements branching fraction measurements [90].

First, I'll describe the Blue Slower project in the context of the Ra EDM experiment. Then I'll describe the experimental setup for the measurements, including the lasers needed. Then we'll discuss the fluoroscopy measurements of the atomic transitions of interest. Finally, I'll talk about the analysis that we use to find the intensity of the Blue slower transitions.

4.1   Radium laser cooling with the Zeeman slower

To measure an EDM, we need to trap atoms between two high voltage electrodes to perform spin precession frequency measurements (see Figure 2.1). From Equation 2.3, the statistical sensitivity of the EDM measurements scales as $\sqrt{N}$, where N is the number of atoms precessing between the electrodes. Our goal is to interrogate as many atoms as possible, i.e. maximize N.

Radium atoms exit an effusive oven with some angular distribution $j(\theta)$, where θ is the angle from the longitudinal axis, and velocity distribution $g(v)$, where v [m/s] is the speed. After radium atoms exit the oven, they are collimated with a retro-reflected transverse laser to reduce the angular spread.

Next, the atom beam propagates through a Zeeman slowing section. The details of the Zeeman slower are given in Section 2.2.1. A tapered solenoid coil around the beamline Zeeman-shifts the transition frequency to compensate for the Doppler effect. The result is a fraction of atoms that are sufficiently slowed for trapping.

Red slower

15 ns $^3F_2^o$

$^1P_1^o$ 5.5 ns

R1

$^1D_2$ 385 μs

$^3P_1^o$ 420 ns

$^3D_3$

$^3D_2$

510 μs $^3D_1$

red (weak)
714 nm

$^1S_0$

Blue slower

15 ns $^3F_2^o$

$^1P_1^o$ 5.5 ns

R3

blue (strong)
483 nm

$^1D_2$ 385 μs

R2

$^3P_1^o$ 420 ns

$^3D_3$

$^3D_2$

R1

510 μs $^3D_1$

red (weak)
714 nm

$^1S_0$
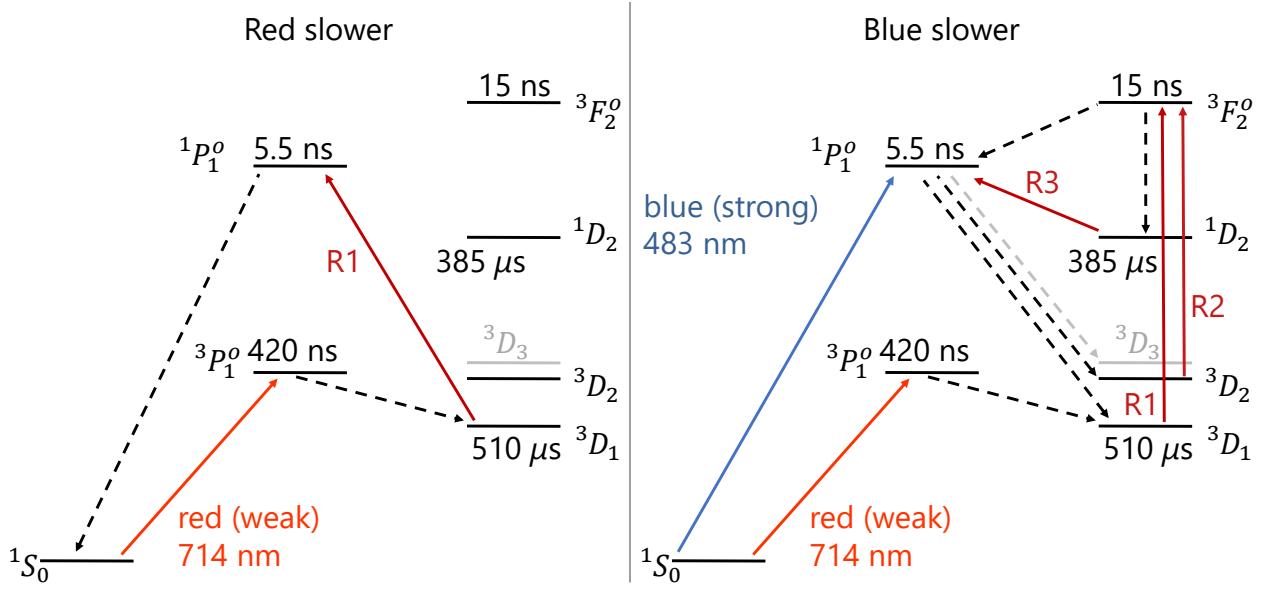
Figure 4.1: Left: the current "red" Zeeman slowing scheme. $R1 = 1429$ nm.
Right: the envisioned "blue" Zeeman slower upgrade. $R1 = 698$ nm, $R2 = 712$ nm, $R3 = 2752$ nm.

We currently use the $^1S_0 \rightarrow {}^3P_1^o$, or "red" cycling transition to decelerate the radium atoms. In this scheme, shown in side (a) Figure 4.1, radium atoms are excited to $^3P_1^o$ with a Ti:Saph laser at 714 nm. They decay to $^3D_1$ with a half-life of 422(20) ns [137, 138]. To circumvent the relatively long lifetime of this metastable state, an additional laser is used to "repump" atoms to $^1P_1^o$, where they decay to the ground state after approximately 5 ns. This scheme is simple, requiring only a single repump laser. Using the red cycling transition, we can slow atoms with an initial velocity of ≤ 60 m/s, or about 0.2% of all the atoms exiting the oven. The momentum of any atoms exiting the oven at a speed greater than 60 m/s is too large to sufficiently slow for trapping.

For the next phase of the radium Zeeman slower, we'll use an additional, stronger cycling transition to slow down a larger fraction of the atoms exiting the oven. The $^1S_0 \rightarrow {}^1P_1^o$, or "blue" cycling transition, delivers a stronger momentum kick to the atom and can be cycled about 80 times quicker than the red cycling transition. The blue slower upgrade will be assembled upstream of the red slower and calibrated to slow atoms to
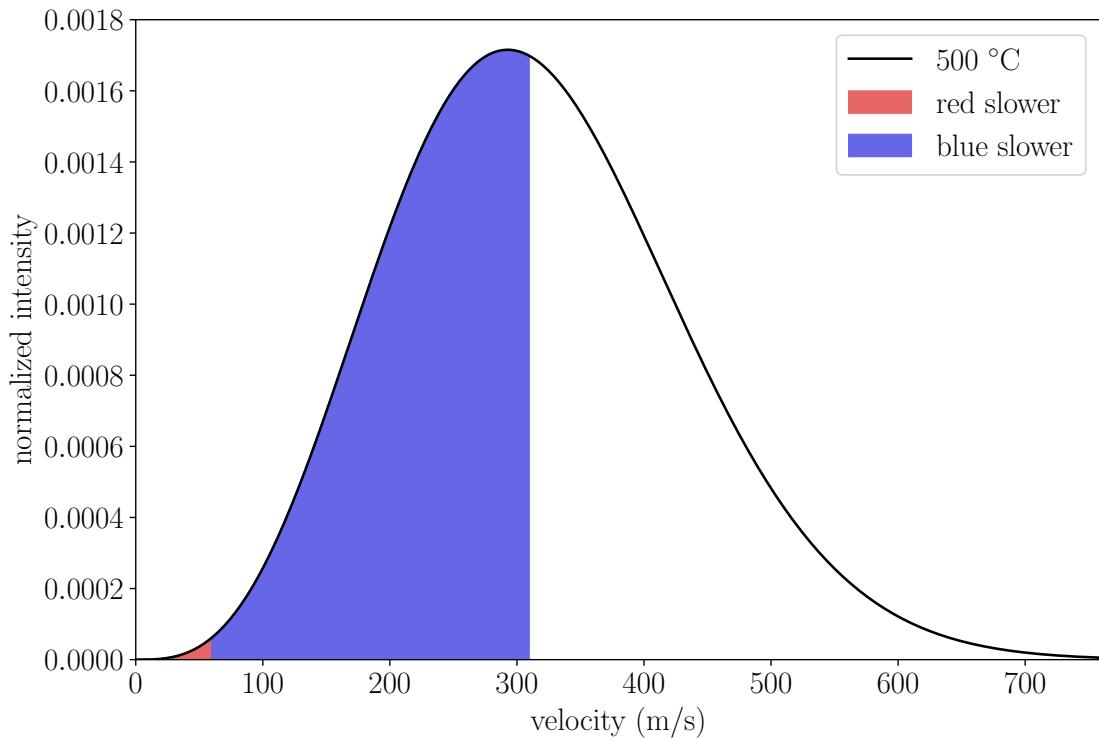
Figure 4.2: The Maxwell-Boltzmann speed distribution of radium atoms exiting the oven. The estimated fraction of atoms that can be sufficiently slowed for trapping are shaded according to the slowing scheme.

60 m/s, so the red slower can be used with or without the blue cycling transition.

The Maxwell-Boltzmann speed distribution of radium atoms exiting a 500 °C oven is shown in Figure 4.2. The shaded area of the curve represents the relative amount of atoms that can be trapped for the red slower (shaded red) and the blue slower (shaded blue). The blue slower upgrade is expected to trap more than 50% of atoms exiting the oven and will yield approximately 100 times more trappable atoms than the red slower alone.

The blue slower cycling scheme is more complex and requires consideration of additional decay channels than the red cycling scheme. Once $^1P_1^o$ is populated, there are four non-cycling deexcitation paths that the atoms can take. Electric dipole, or E1 transitions of the lowest atomic excited states of radium are shown in Figure 4.3. New repump lasers

are required for decay states with significant branching fractions. They need sufficiently high intensity to saturate each of these transitions. The fractional rate of atoms deexciting from initial state $| i \rangle$ to one possible decay state $| k \rangle$ is known as the branching ratio $BR(| i \rangle \rightarrow | k \rangle)$ [unitless]: [a]

$$BR(| i \rangle \rightarrow | k \rangle) = \frac{g_k f_{ik}}{\lambda_{ik}^2} \Big/ \sum_\ell \frac{g_\ell f_{i\ell}}{\lambda_{\ell k}^2}, \tag{4.1}$$

where

g_k' [unitless] is the degeneracy of $| k \rangle$,

f_{ik} [unitless] is the oscillator strength of the transition $| i \rangle \rightarrow | k \rangle$, or the ratio of power absorbed by the atom to that absorbed by a classical oscillator, and

λ_{ik} [m] is the transition wavelength from $| i \rangle \rightarrow | k \rangle$.

The decay strengths are sometimes expressed in terms of the transition matrix element $|D_{ik}|$ rather than f_{ik} in theory calculations. The two are related by $f_{ik} \propto \frac{|D_{ik}|^2}{g_i \lambda}$.

> **$E1$-allowed atomic transitions:**
>
> $\Delta J = 0, \pm 1$ except for gs $\rightarrow$ gs transitions
>
> $\Delta M = 0, \pm 1$ except for gs $\rightarrow$ gs transitions when $\Delta J = 0$
>
> one electron jump with $\Delta \ell = \pm 1$
>
> **LS coupling:**
>
> $\Delta S = 0$
>
> $\Delta L = 0, \pm 1$ except for gs $\rightarrow$ gs transitions

The envisioned repumping scheme is shown in Figure 4.1. One of the possible non-cycling states, $^3D_3$, is predicted to have a surprisingly weak branching ratio. Another state, $^1D_2$, is normally a forbidden transition (E1, $\Delta S = 0$), but is predicted to have a

---

[a]We are technically calculating branching fractions, but this is the nomenclature used in our paper. The true branching ratio is the ratio of one branching fraction to another branching fraction.
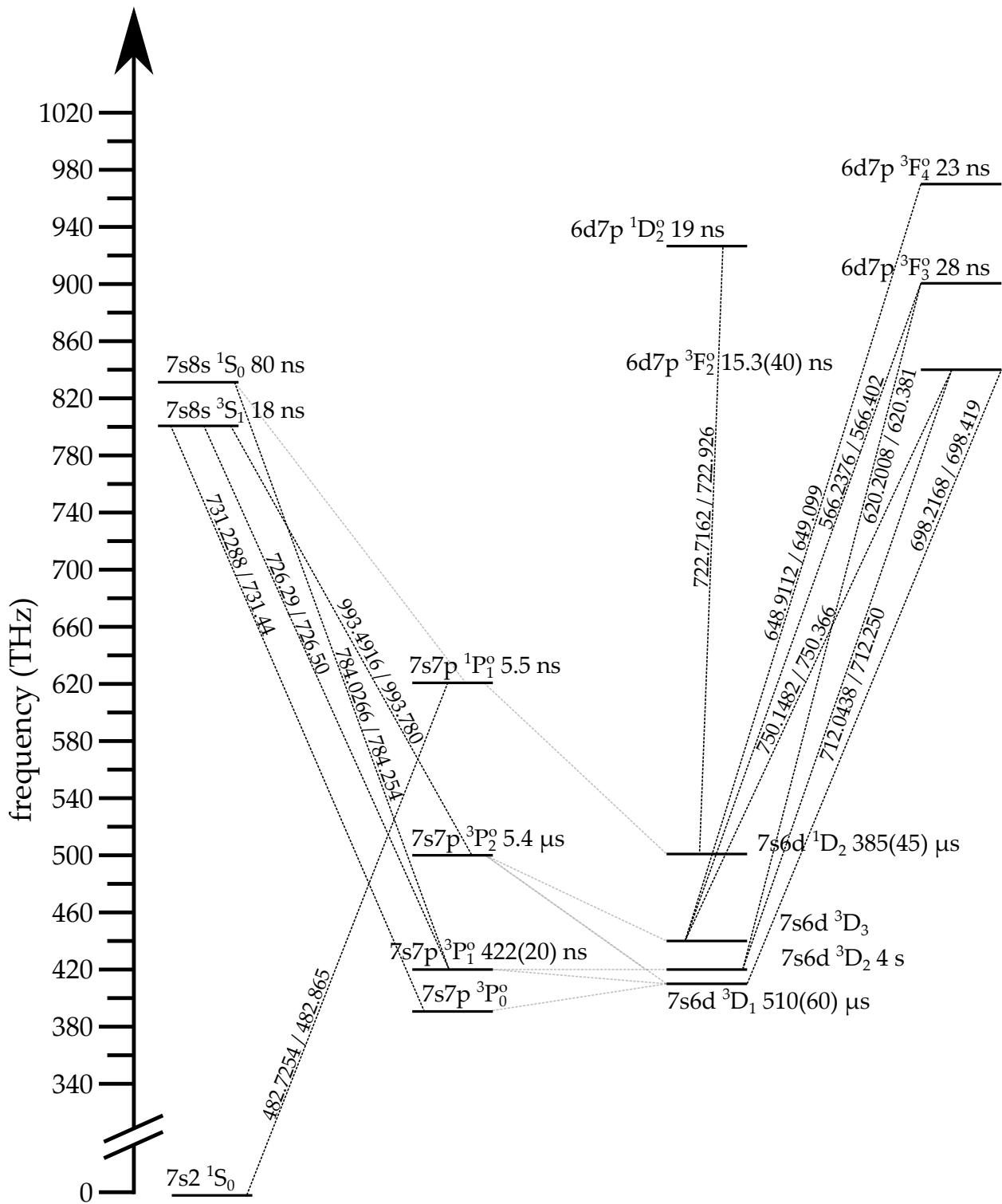
Figure 4.3: An energy level diagram of the fifteen lowest energy levels and E1-allowed transitions of ^{226}Ra. Measured lifetimes: $7s7p\ ^3P_1^o$ [137], $6d7p\ ^3F_2^o$ [90], $7s6d\ ^3D_1$ [139], $7s6d\ ^1D_2$ [140]. Calculated lifetimes: $7s6d\ ^3D_2$ [141], all other transitions [89]. Wavelengths are labeled along transition lines in [nm] in vacuum/air.
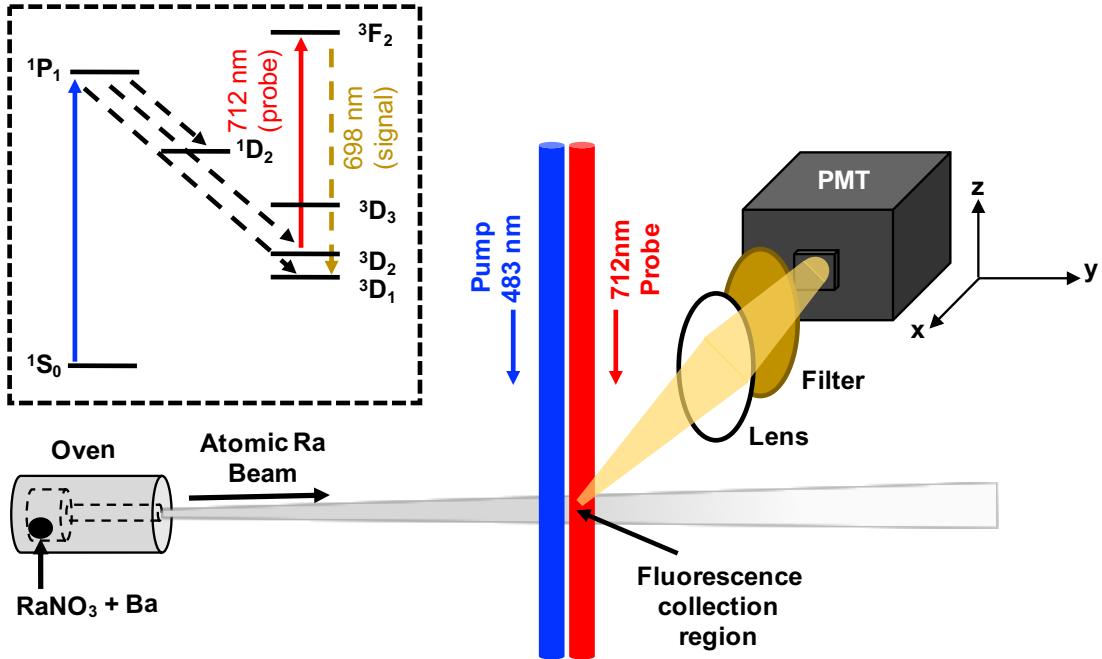
Figure 4.4: A schematic of the branching ratio fluoroscopy setup. Inset: energy diagram for measuring the $^3D_1$ branching ratio.

favorably strong branching ratio [89]. This is due to the total angular momentum $J = L+S$ coupling of the parent state $^3F_2^o$. The high intensity of $^1D_2$ will allow us to "flip" the spin of the $^3F_2^o$ state and repump along the transition $^1D_2 \rightarrow {}^1P_1^o$.

My goal was to measure the $^1P_1^o$ decay channels using laser-induced fluoroscopy to experimentally verify the predicted branching ratios for the Blue slower upgrade. This was necessary because implementing the blue slowing scheme requires lasers that can provide sufficient power at each transition. The requisite power depends on the branching fraction intensity of $^1D_2$ and the ^3D_J states. In the case of $^3D_3$, the branching ratio is predicted to be low enough that we can neglect repumping that state without significant atom loss.

To measure the fluorescence from a signal state, we populate all the D states with a 483 nm pump laser resonant with the $^1S_0 \rightarrow {}^1P_1$ transition. Then we depopulate one of the strong decay states, either $^3D_1$ or $^3D_2$, with a second probe laser. Finally, we detect the fluorescence to the decay channel of interest with a PMT and an appropriately chosen

Table 4.1: Transitions and wavelengths for branching ratio measurement.

transition	wavelength (nm)	laser
$^1S_0 \rightarrow\, ^1P^o_1$	482.7254	blue imaging laser
$^1D_2 \rightarrow\, ^3F^o_2$	912.6919	NIR diode laser
$^3D_1 \rightarrow\, ^3F^o_2$	698.2168	tunable Ti:Saph laser
$^3D_2 \rightarrow\, ^3F^o_2$	712.0438	tunable Ti:Saph laser

bandpass filter. A schematic is shown in Figure 4.4. A list of the transitions and the lasers used to excite the state to $^3F^o_2$ is given in Table 4.1. By measuring the fluorescence of the transitions using all the possible configurations, we can construct a system of equations that allows us to solve for individual branching ratios.

4.2   Lasers for the branching ratio measurement

The pumping transition and three of the four transitions of interest were accessible with two existing Ra EDM lasers. I used the imaging & polarizing laser (Moglabs external cavity diode) for the $^1P^o_1$ transition at 483 nm. I used the Zeeman slower laser (Spectra-Physics Matisse ring-cavity Titanium:Sapphire) for the $^3D_1$ (698 nm) $^3D_2$ (712 nm) and $^3D_3$ (750 nm) transitions.

I assembled a diode laser from to probe $^1D_2$. It's a TO-can 300 mW-rated laser diode (Thorlabs M9-915-0300) actively cooled with a temperature mount, as shown in Figure 4.5a. The light passes through an optical free-space isolator and an anamorphic prism pair.

The laser wavelength is tuned with a thermoelectric temperature controller (ILX LDT-5412) and powered with a precision current source (ILX LDX-3525). I assembled a circuit that interfaces the thermoelectric temperature controller (TEC) and current source to the laser and connects the instruments to the laboratory safety interlock (Figure 4.5b).

A pickoff feeds laser light into a spectrometer (Ocean Optics FLAME-VIS-NIR-ES). I used the spectrometer to calibrate the laser wavelength as a function of TEC set point. I
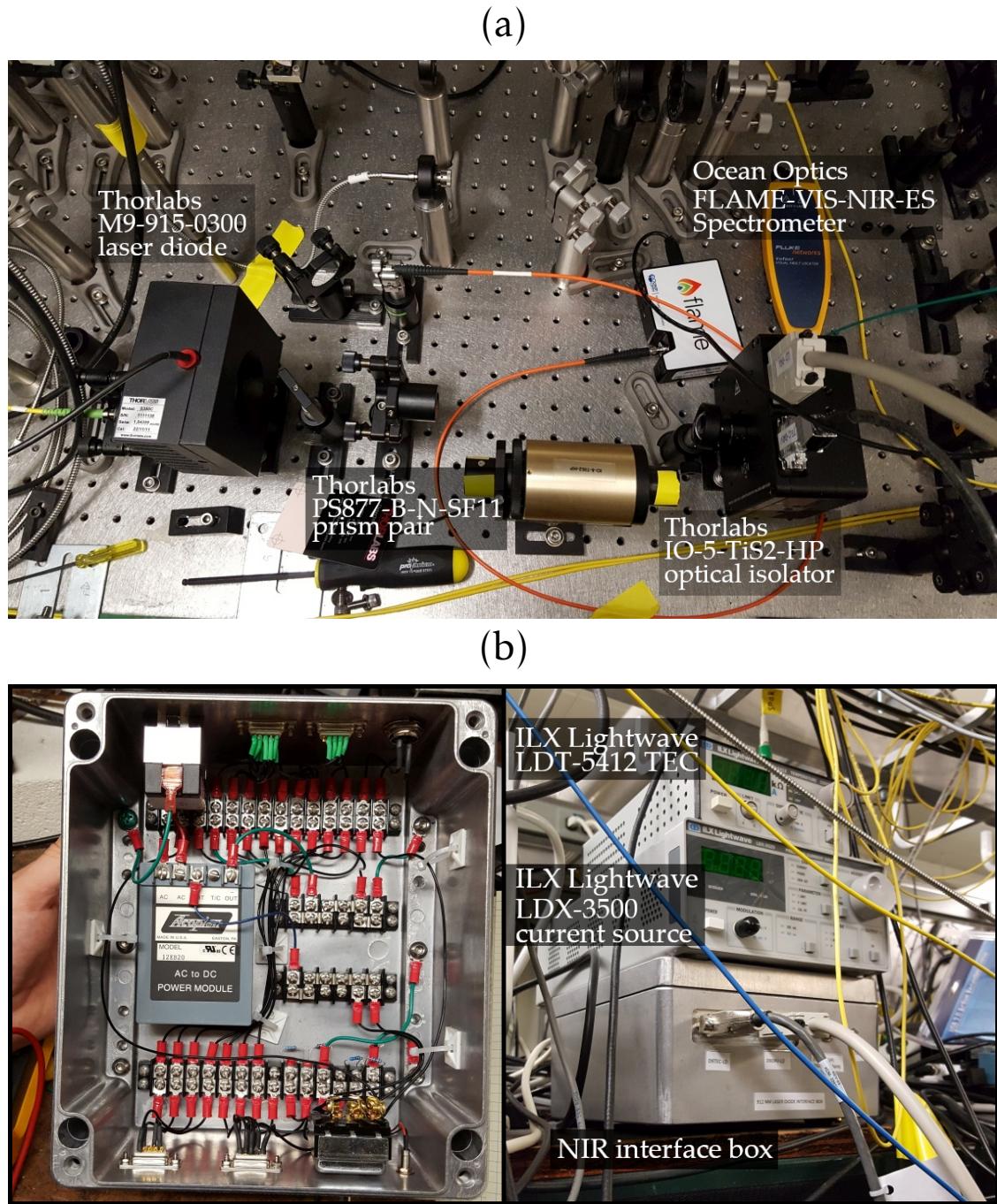
Figure 4.5: (a) NIR laser diode in a temperature-controlled mount. During fluoroscopy measurements, the power meter is removed and laser light is coupled to the fiber behind it. (b) Left: Custom NIR interface box circuit. Right: The current source, thermoelectric temperature controller, and custom interface box used for the NIR laser diode.
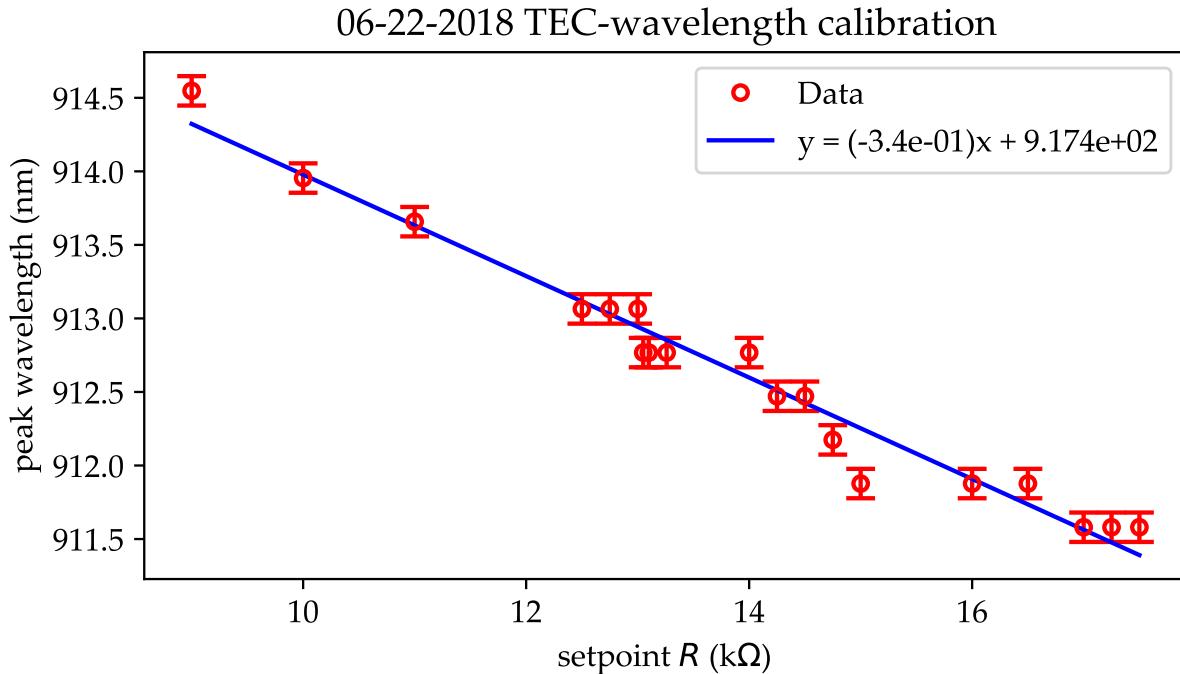
Figure 4.6: A fit of the near-infrared (NIR) diode laser wavelength to the temperature controller resistance setting.

plotted the wavelength vs. set point and fit the data in Figure 4.6. The data is reasonably modeled with a linear fit.

4.3   Radium fluoroscopy experimental setup

The lasers interact with the radium atoms just outside the oven in a six-way vacuum cross. First, the atoms first traverse the 483 nm pumping beam to populate all the singlet and triplet D states. After the pumping beam, one of the states $^{2S+1}D_J \rightarrow {}^3F_2^o$ is driven with a "probe" laser, which is the NIR or Ti:Saph depending on the transition.

To collimate the beams and orient them parallel to each other, they are all fiber-coupled to a small stage shown in Figure 4.7. I set the beam diameters with lenses positioned at the fiber exits. A series of dichroic mirrors combine the beams so that they are parallel and closely grouped. A periscope mirror directs the beam above the viewport, while a final mirror steers them vertically down through the fluorescence region ap-
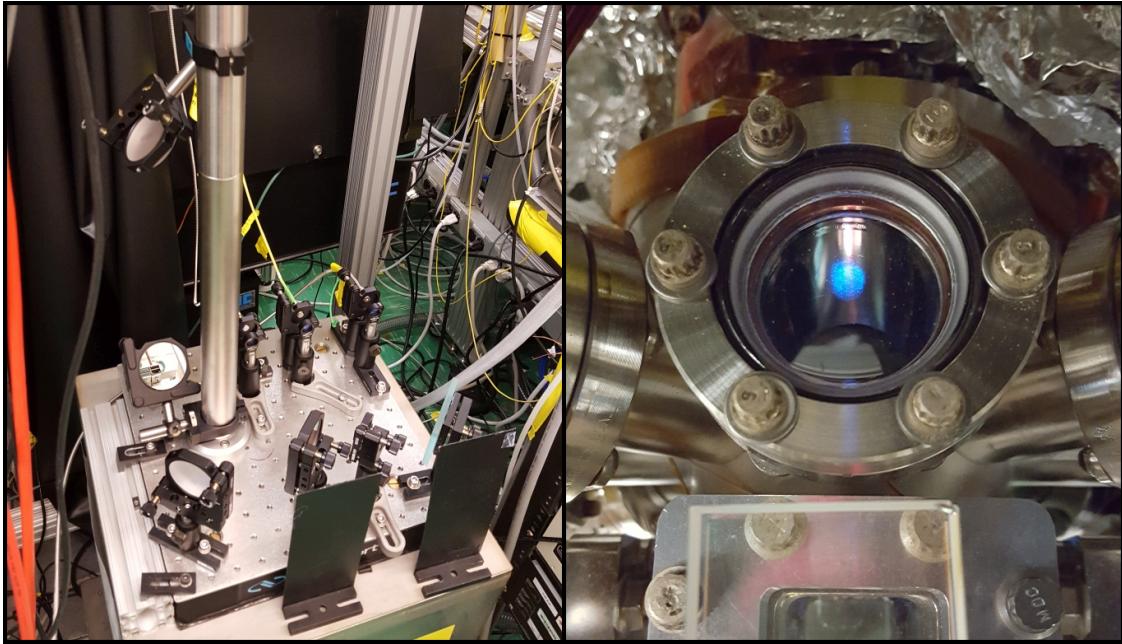
Figure 4.7: Left: the three fibers are combined with dichroics and sent to the fluorescence mirror with a telescope mirror setup. Right: a top-down view of the blue laser light passing through the viewport into the fluorescence region.

proximately 2 m away (Figure 4.7). An 8 mm × 6 mm photomultiplier tube (Hamamatsu R2949) is positioned perpendicular to the atomic beam and laser axes. A collection lens focuses the fluorescence onto the PMT sensor. We place a bandpass filter appropriate for the transition wavelength of interest between the collection lens and PMT.

4.4   Radium fluoroscopy data acquisition

The PMT counts are recorded by a USB data acquisition card (DAQ) (National Instruments USB-6341) with an onboard timer every second. To scan the wavelength over a transition, we use a signal generator to send a waveform to an acousto-optical modulator (AOM). The waveform generator frequency is also sent to the DAQ.

I created a LabView program that logs the PMT counts and AOM frequency as a function of time. A screenshot is shown in Figure 4.8. On the main graph, the raw PMT count is plotted with a user-defined N-sample average. The bottom graph plots the acousto-optical modulator frequency setting. The user can run a laser sweep with a frequency
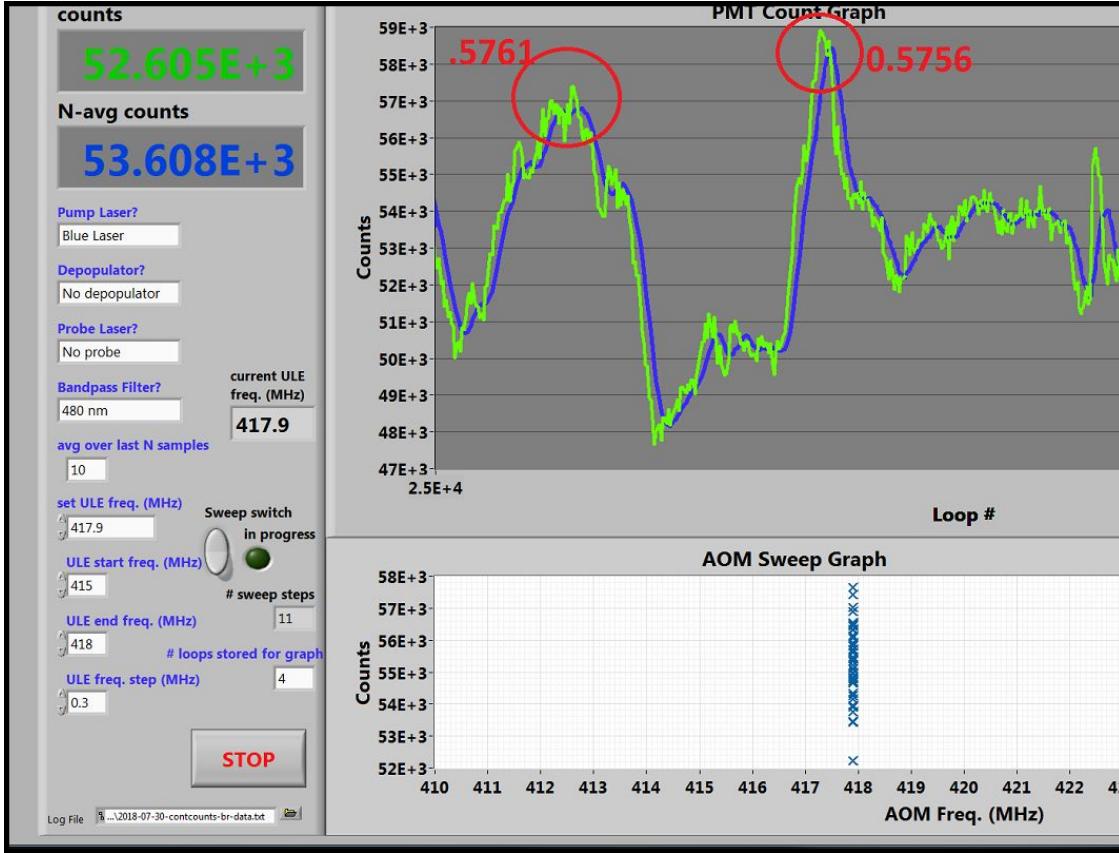
Figure 4.8: A screenshot of the VI I wrote for recording PMT counts for the branching ratio measurements.

step size of their choosing. The filters installed on the PMT and the lasers being used are specified in the box on the left and the settings are mapped to integers which are saved to a text file along with the PMT counts and AOM settings.

4.5 Measurement

To measure the fluorescence of one of the $^3F^o_2$ decay channels, I first identified the $^1P^o_1$ resonant wavelength. I installed the 698 nm bandpass filter on the PMT sensor and looked for peak counts which would indicate that $^3D_1$ is populated. The literature excitation wavenumber is 20715.71 cm^{-1} [142]. We usually measure the transition at around 20715.6042 cm^{-1}, about $\Delta\lambda = \Delta k / k^2 \approx 0.0025$ nm difference. This is within the range that our wavemeter tends to drift.
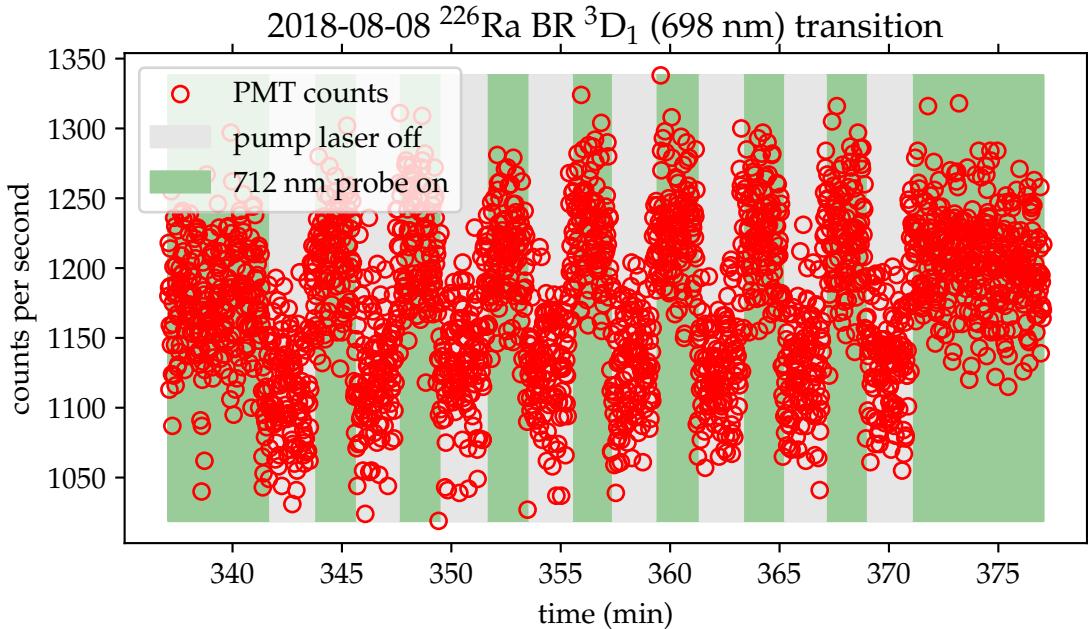
Figure 4.9: Fluorescence signal of the $^3F_2^o \rightarrow\ ^3D_1$ transition while depopulating the $^3D_2$ state with a 712 nm probe laser.

In addition, we shift the blue imaging laser wavelength with two AOMs, a double-pass set to -447 MHz and a single-pass set to $+80$ MHz. This means that we look for resonance at around:

$$20715.6042 \text{ cm}^{-1} - \frac{(2 \times 447 - 80) \text{ MHz}}{3 \times 10^{10} \text{ cm/s}} = 20715.5771 \text{ cm}^{-1}$$

To scan the pump laser frequency, I manually changed the current source driving the blue imaging laser and read the wavemeter. I found peak fluorescence at $20715.5756 \text{ cm}^{-1}$, shown in Figure 4.8.

A schematic of the fluorescence measurement technique is shown in Figure 4.4. After identifying the pump transition frequency, I installed the PMT bandpass filter that gates on the "signal" transition $^3F^o{}_2 \rightarrow\ ^{2S+1}D_J$. Then I used a probe laser to depopulate a different D state with total angular momentum J'. I repeated the search for a fluorescence signal correlated with the signal transition.

I took a series of "triplet" measurements by integrating the fluorescence signal in al-

ternating cycles of blocking and unblocking the pump beam. This allows us to separate the signal transition from background light. In Figure 4.9, I identify a signal peak using this scanning method.

4.6 Results

For each transition, I integrated for 100 seconds for each cycle of blocked and un-blocked pump beam. This gave us enough statistics to sufficiently reduce the uncertainty of the sample mean. The PMT reports counts, so we model population with a Poissonian distribution. The standard deviation scales with the root of the number of samples taken, or $\sigma = \sqrt{N}$. Integrating for 100 seconds is a short enough timescale to manually stabilize laser frequency and wash out short-term frequency drifts.

Each 100 s integration period is reduced to a single weighted average and shown in Figures 4.10, 4.11, 4.12, 4.13, 4.14, 4.15. To get a count due only to the signal, I subtract a weighted average of the background measurements before and after each (signal + background) measurement:

$$S_i = A_i - B_{i-1} \frac{t_i - t_{i-1}}{t_{i+1} - t_{i-1}} - B_{i+1} \frac{t_{i+1} - t_i}{t_{i+1} - t_{i-1}} , \tag{4.2}$$

where

S_i [unitless] is the ith signal-only term,

A_i [unitless] is the ith measurement and is a (signal + background) measurement,

B_i [unitless] is the ith measurement and is a background-only measurement, and

t_i [s] is the median time of the ith measurement.

The background-subtracted average PMT counts for six configurations and an index of their associated plots are summarized in Table 4.2. We were able to measure two of the four transitions during my ANL fellowship.

Our PMT is significantly less sensitive to the ${}^3\text{F}_2^o \rightarrow {}^1\text{D}_2$ 912 nm transition. Initial efforts did not yield a convincing fluorescence measurement of ${}^1\text{D}_2$. I attempted using

Table 4.2: Measured PMT signals of decays from $^3F_2^o$.

probe	signal	note	signal count	Fig.	pump (mW)	probe (mW)	T (°C)
$^3D_2$	$^3D_1$		80.8(24)	4.10	2.5	4.8	441
$^1D_2$	$^3D_1$		2.3(18)	4.11	2.5	4.8	441
$^3D_2$	$^3D_1$		57.5(36)	4.12	2.6	6.0	491
$^3D_2$	$^3D_3$	beams blocked	−1.9(45)	4.13	2.5	4.8	441
$^3D_2$	$^3D_3$	pump resonant	42.0(58)	4.14	2.6	6.0	491
$^3D_2$	$^3D_3$	pump detuned	45.6(70)	4.15	2.6	6.0	491

the NIR laser to depopulate $^1D_2$ for a measurement of the $^3D_3$ signal in Figure 4.11. The signal was consistent with zero, suggesting that there was insufficient probe power. The excitation power for $^1D_2$ was later increased by reducing the linewidth the NIR laser.

I started the search for the $^3F_2^o \rightarrow {}^3D_2$ transition, but background PMT counts were greater than 4×10^5 counts s^{-1}. The atomic oven could have contributed to the high background. The expected signal strength was < 100 counts s^{-1}, so I prioritized measurements of the other transitions.

In one measurement, I carried out the measurement procedure with both beams blocked using a second beam block downstream of the pump laser beam block (Figure 4.13). The 750 nm PMT bandpass filter was installed for $^3D_3$ measurements. As expected, the signal-only measurements are indistinguishable from the (signal+background) measurements. The total weighted average for the signal measurement is consistent with zero counts (1σ). The no-beam measurement measures the ambient lighting inside the chamber, e.g. from the atomic oven, and also provides a baseline measurement of the counts for the installed bandpass filter. Finally, over the course of the measurement the PMT counts drifted down by ≈ 100 counts. From this we can expect an approximately linear drift of 1–2 counts hr^{-1}.

To measure the $^3D_3$ transition, I installed the 750 nm PMT bandpass filter and made two measurements. In the first measurement, I tuned the pump (483 nm) and probe
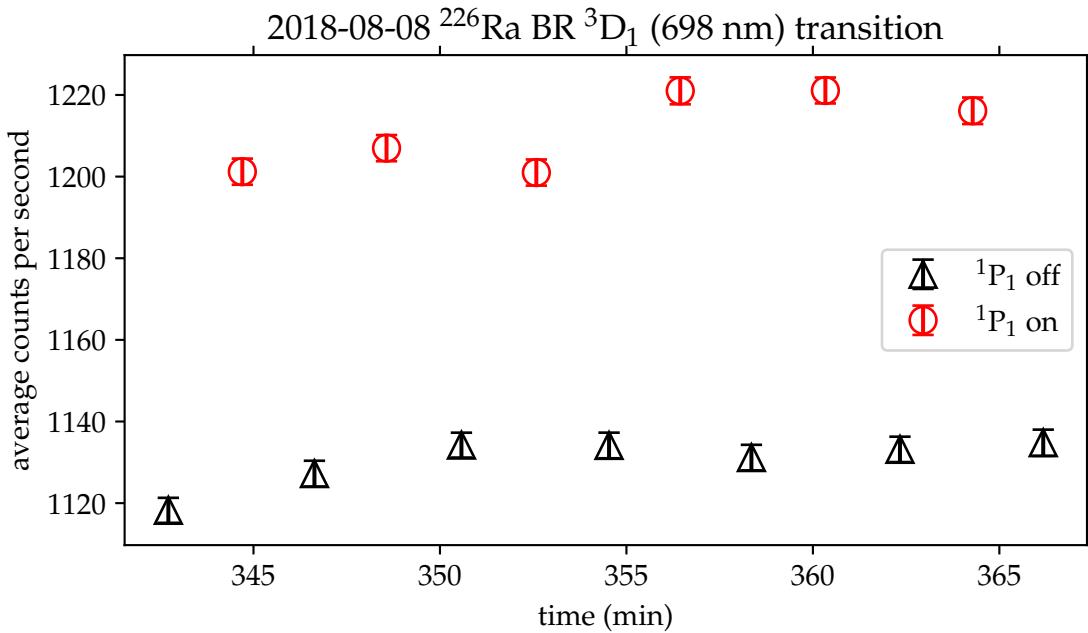
Figure 4.10: 8/8/2018 Averaged fluorescence signal of the $^3F_2^o \to\, ^3D_1$ transition while depopulating the $^3D_2$ state with a 712 nm probe laser.

(712 nm) beams to their resonant wavelengths (Figure 4.14). In the second measurement, I detuned the pump beam so that the D states would not be populated (Figure 4.15). The difference between the two measurements, which gives us the fluorescence signal of the $^3D_3$ transition, is $42.0 \pm 5.8 - (45.6 \pm 7.0) = -3.6 \pm 12.8$ counts s^{-1}. Our measured result is consistent with zero. As expected, this transition is too weak to be measured by our method.

To measure the $^3D_1$ transition, I installed the 698 nm PMT bandpass filter. I took measurements for two different configurations. In the first configuration, I depopulated the $^3D_2$ state with the 712 nm. I measured the fluorescence twice for this configuration over two days (Figures 4.10, 4.12). In both cases, I measure nonzero count rates, but there is a ≈ 30 counts hr^{-1} discrepancy between the two days. For the first (8/8) measurement, we used a pump beam power of 2.5 mW and a probe beam power of 4.8 mW. For the second (8/9) measurement, we used a pump beam power of 2.6 mW and a probe beam power of 6.0 mW. Despite the higher power, the (signal + background) measurements are
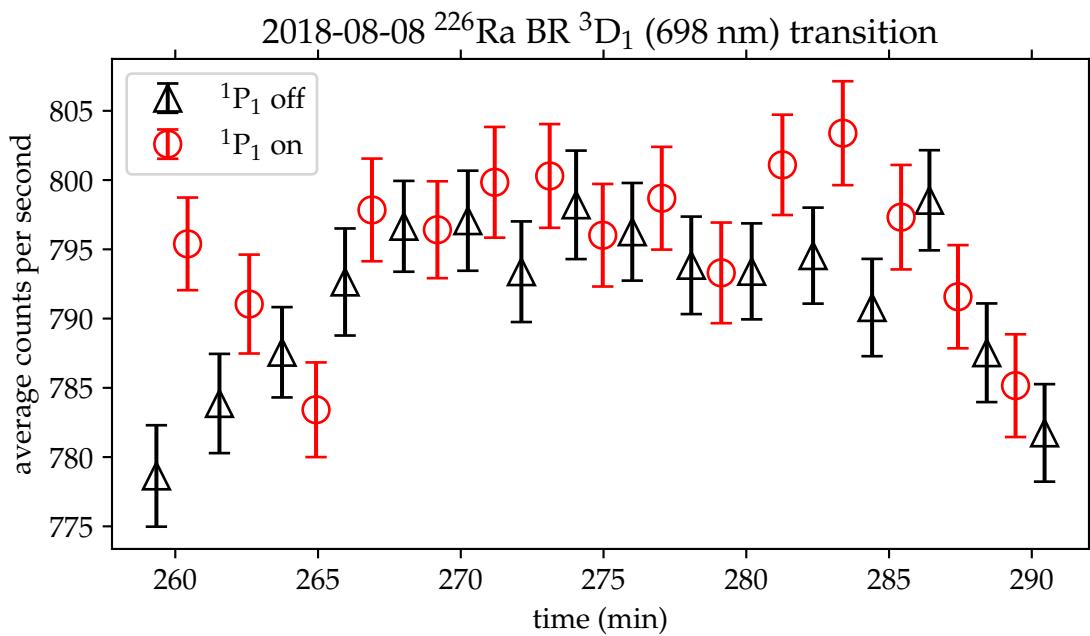
Figure 4.11: 8/8/2018 Averaged fluorescence signal of the $^3F_2^o \rightarrow\, ^3D_1$ transition while depopulating the $^1D_2$ state with a 912 nm probe laser.
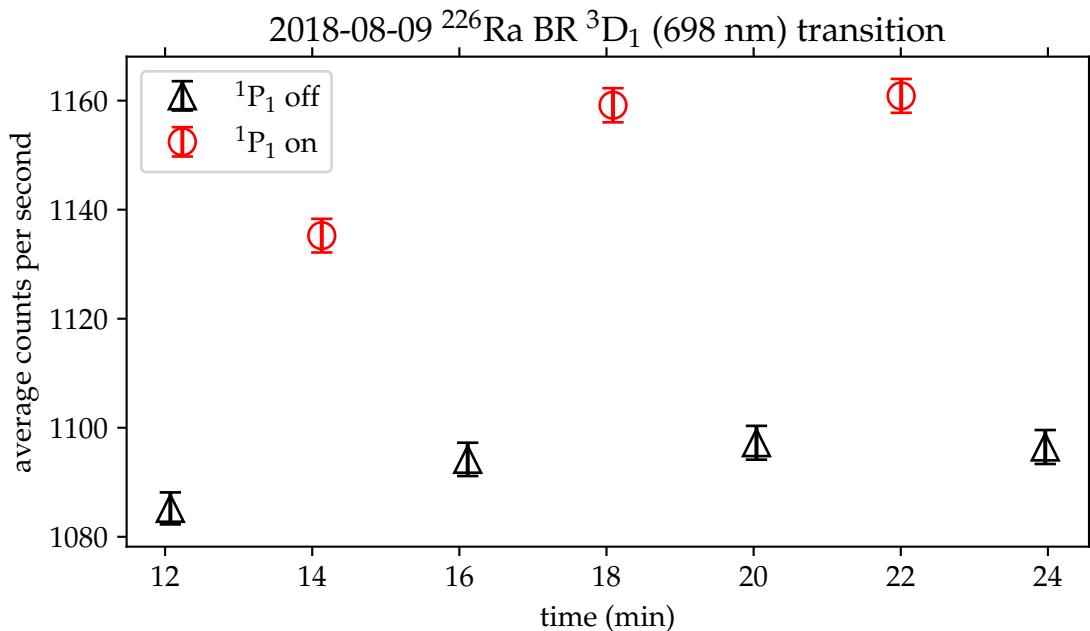
Figure 4.12: 8/9/2018 Second measurement of $^3F_2^o \rightarrow\, ^3D_1$ transition while depopulating the $^3D_2$ state with a 712 nm probe laser.
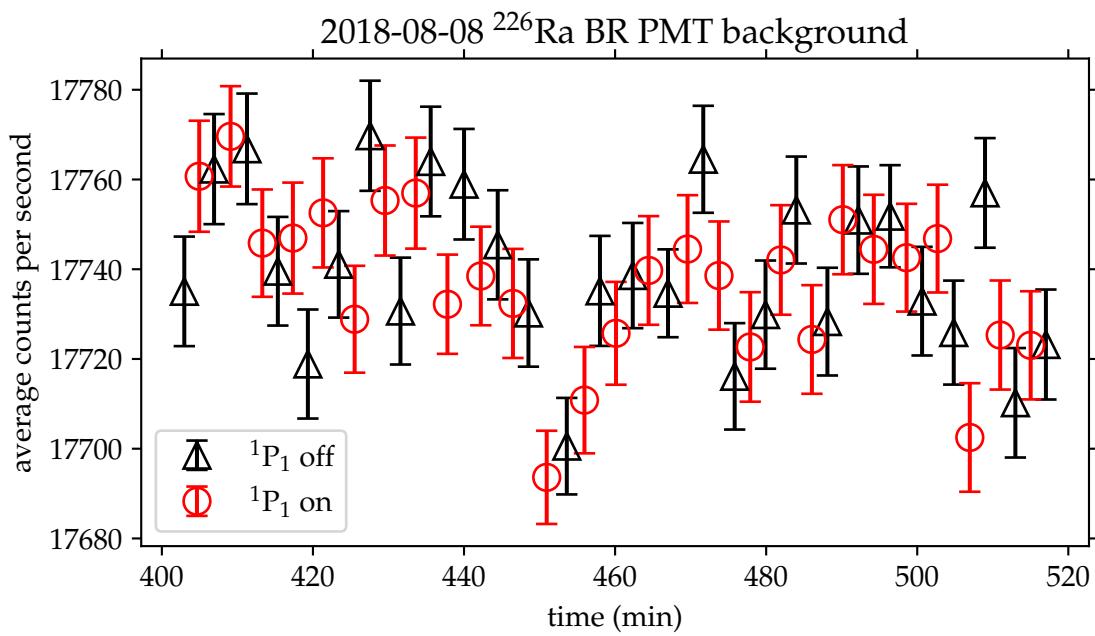
Figure 4.13: 8/8/2018 Average fluorescence signal with pump beam and probe beams blocked.
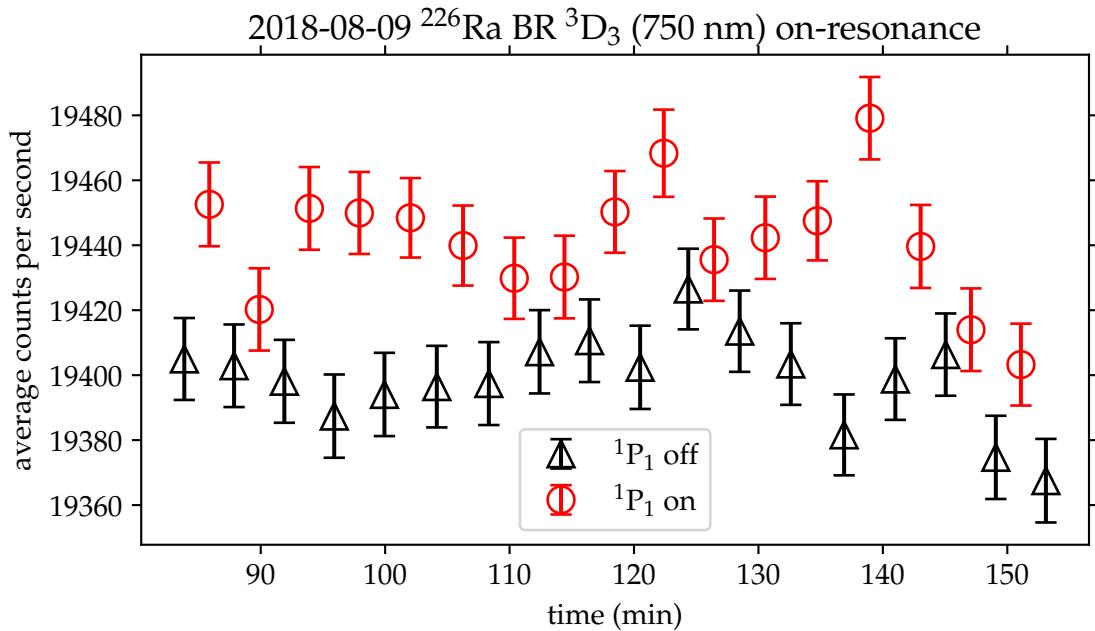
Figure 4.14: 8/9/2018 Average fluorescence signal of the $^3F_2^o \rightarrow ^3D_3$ transition with the pump beam tuned on resonance.
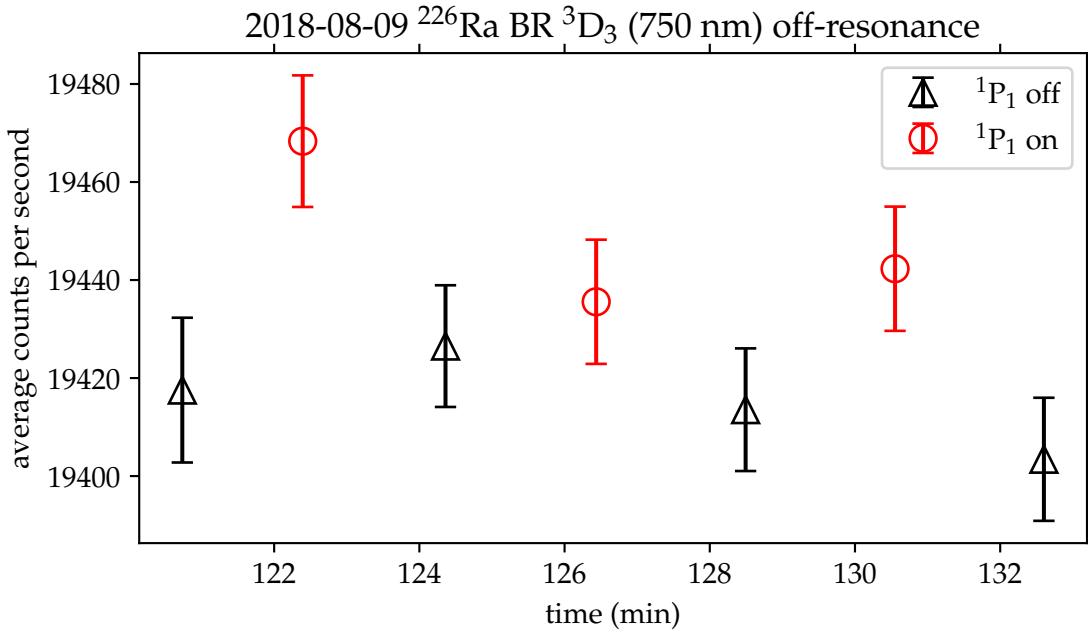
Figure 4.15: 8/9/2018 Average fluorescence signal of the $^3F^o_2 \rightarrow{}^3 D_3$ transition with the pump beam tuned off resonance.

smaller by ≈ 50 counts s^{-1}. This is likely due to depletion of the atom source.

4.7 Analysis

After constructing the fluoroscopy setup and calibrating the lasers, refined laser sweeps were performed to capture atomic lineshapes of each of the transitions. In this section, I will show how we extracted branching fractions from the lineshape data.

We measure a fluorescence signal by sweeping the laser frequency across the resonance frequency. Then we fit the measured data to a function $\mathcal{L}$ characterizing the lineshape, given by the following:

$$\mathcal{L} = D \sum_{n=1}^{n_{\text{max}}} p^{n-1}(1-p)[1 - \text{CDF}(\Lambda, n)] + C_0 \,, \tag{4.3}$$

$$n = 0, \ 1, \ 2, \ \ldots \tag{4.4}$$

where

n [dimensionless] is the number of photons scattered before an atom deexcites,

112

p [dimensionless] is the branching ratio to the probe state,

D [arbitrary] is the amplitude of the lineshape, and

C_0 [arbitrary] is an offset.

The probability that n photons are scattered before decaying to the signal state is given by a Poissonian cumulative distribution function $\text{CDF}(\Lambda, n)$:

$$\text{CDF}(\Lambda, n) = \frac{\Gamma[n+1, \Lambda]}{n!}, \tag{4.5}$$

$$\Gamma(\ell, \Lambda) = \int_\Lambda^\infty t^{\ell-1} \exp(-t) dt, \tag{4.6}$$

$$\ell = n + 1 > 0,$$

where $\Gamma(\ell, \Lambda)$ is the incomplete upper gamma function. The lineshape is characterized the Poissonian weight Λ:

$$\Lambda = \sum_y \tau \, \bar{n}(y) \, f \, \sigma_0 \, \mathbb{V}(\omega = \omega_0; \gamma, \sigma_D), \tag{4.7}$$

$$\bar{n}(y) = \frac{P}{\hbar \omega \Delta y^2} \frac{\sum_x I(x, y)}{\sum_{x,y} I(x, y)}, \tag{4.8}$$

$$\mathbb{V}(\omega = \omega_0; \gamma, \sigma_D) = \frac{1}{\sigma_D} \int_0^\infty \exp\left[-\left(\frac{v' - v_a}{\sigma_D}\right)^2\right] \frac{\gamma/(4\pi^2)}{(v - v')^2 + (\gamma/4\pi)^2} dv', \tag{4.9}$$

$$\gamma = 2 \sum_i A_{ki} = \frac{8\pi \, \sigma_0}{g_k} \sum_i \frac{g_i}{\lambda_{ik}^2} f_{ik}, \tag{4.10}$$

$$\sigma_0 = e^2/(4\epsilon_0 \, m_e \, c) = 2.65400886 \times 10^{-6} \text{ m}^2/\text{s}, \tag{4.11}$$

where

A_{ki} [Hz] is the Einstein spontaneous decay rate ("A-coefficient") for $|\, k \,\rangle \to |\, i \,\rangle$,

γ [Hz] is the Lorentzian width,

ω_0 [rad/s] is the resonant frequency of the atomic transition,

m_e [kg] is the electron mass,

e [C] is the elementary charge,

c [m/s] is the speed of light in vacuum,

ϵ_0 [F/m] is the vacuum electric permittivity,

P [W] is the power of the excitation laser,

Δy [m] is the beam image pixel width,

$I(x,y)$ $\left[\text{W m}^{-2}\right]$ is the intensity of the laser at a pixel with coordinates (x,y),

$g_i = 2J_i + 1$ is the degeneracy of $|\,i\,\rangle$ with total angular momentum J_i,

τ [s] is the laser-atom interaction time as the atom traverses one pixel length, and

$\bar{n}(y)$ $\left[\text{W m}^{-2}\right]$ is the photon intensity on an atom at coordinate y.

The branching ratio of the atomic transition $i \to k$ is given by the following:

$$p_{ik} = \frac{A_{ki}}{\gamma/2}, \tag{4.12}$$

where p_{ik} is the probability that an atom in state i decays to state k.

The parameters of the fit are f_{ik}, D_i, $\omega_{0,i}$, γ, and C_i. k is the $^3\text{F}_2^o$ state. $i = \{1,2,3\}$ corresponds to states $^1\text{D}_2$, $^3\text{D}_2$, and $^3\text{D}_1$, respectively. There are $3 + 3 + 3 + 1 + 3 = 13$ total parameters to fit. We measured the Doppler-broadened linewidth on the $^1\text{S}_0 \to {}^3\text{P}_1$ (714 nm) to be $\gamma/2 = 2.32$ MHz.

The branching ratio (or branching fraction) R_{ki} is the intensity of $|\,i\,\rangle \leftrightarrow |\,k\,\rangle$ relative to all other allowed transitions from $|\,k\,\rangle$:

$$R_{ki} = \frac{A_{ki}}{\sum_i A_{ki}} \tag{4.13}$$

The branching ratio can be related to dipole-allowed transition amplitude matrix elements through the Einstein A-coefficient:

$$A_{ki} = \frac{1}{g_k} \frac{16\pi^2 \, \nu^3}{3\epsilon_0 h c^3} |D_{ik}|^2, \tag{4.14}$$

where ν [Hz] is the frequency of the transition and $|D_{ik}|$ [C m] is the dipole-allowed transition amplitude matrix element on the transition $|i\rangle \to |k\rangle$.

The oscillator strength f_{ik} the ratio of the power absorbed by an atom on $|i\rangle \to |k\rangle$ to the power absorbed by a classical oscillator with eigenfrequency $\omega_{ik} = (E_k - E_i)/\hbar$. The oscillator strength is related to the Einstein A-coefficient by the following:

$$A_{ki} = \frac{2\pi e^2}{m_e \, c \, \epsilon_0 \, \lambda^2} \frac{g_i}{g_k} f_{ik}, \tag{4.15}$$
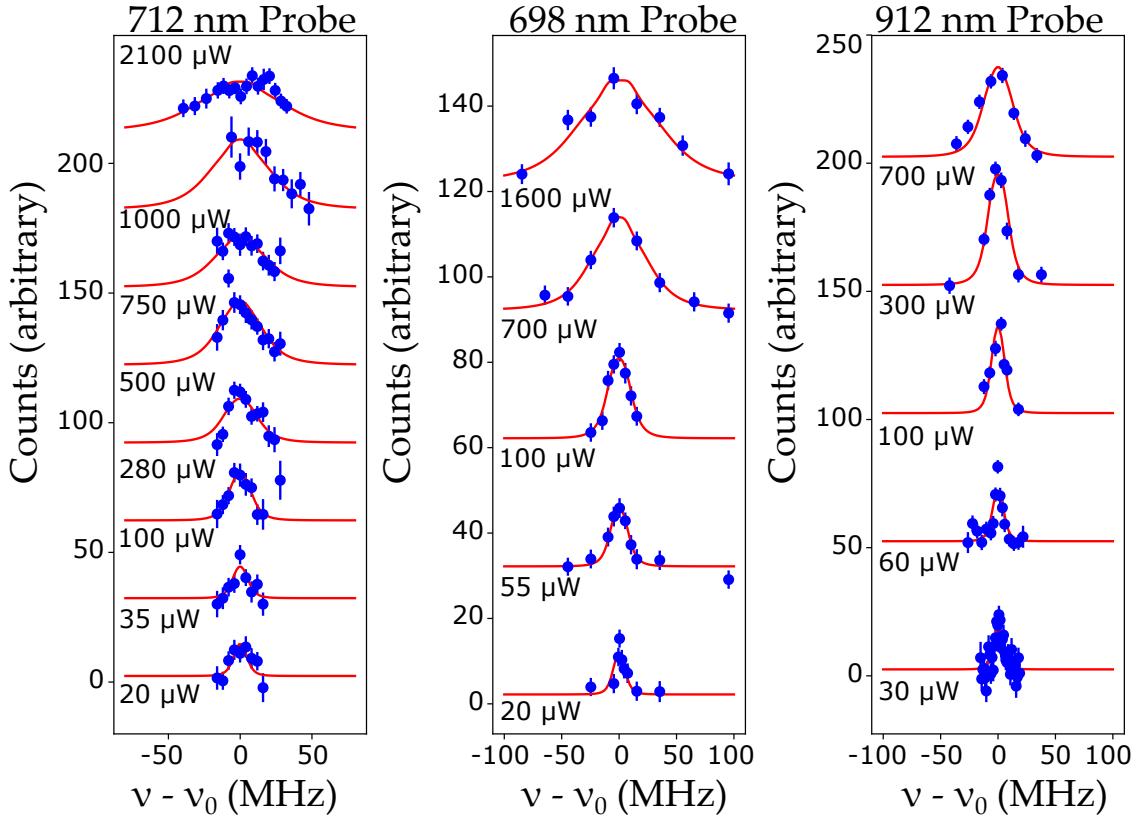
Figure 4.16: Lineshape fits for the $^3F_2^o$ decay channels at different probe laser powers.

where m_e [kg] is the mass of the electron.

We measured the fluorescence signal from $^3D_1$, $^3D_2$, and $^1D_2$ over a range of probe laser powers as shown in Figure 4.16. The $^3D_3$ fluorescence is too weak to accurately fit a lineshape. For this transition we took a ratio of the fluorescence for $^3D_3$ to $^3D_1$ and determined a branching ratio upper limit of 0.4% [90].

The theoretical branching ratios calculated from the dipole transition amplitude and our measured branching ratios derived from the line profile in Equation 4.3 are given in Table 4.3. We measured the $^3D_1$ and $^3D_2$ branching ratios to be a factor of two smaller and a factor of two larger than the predicted values, respectively. The $^1D_2$ branching ratio measurement is a factor of three smaller than the predicted value, but at 5% the branching fraction intensity is large enough for the blue slower scheme depicted in Figure 4.1.

The measurements are qualitatively consistent with the theoretical values, and we

Table 4.3: Calculated branching fractions (BF) and oscillator strengths from $^3F_2^o$.

transition	wavelength (nm)	f_{ik} (measured)	BF (theory) %	BF (measured) %
$^3F_2^o \rightarrow {}^3D_1$	698.21510	0.25 ± 0.08	54.0	31 ± 11
$^3F_2^o \rightarrow {}^3D_2$	712.04341	0.32 ± 0.12	31.8	64 ± 24
$^3F_2^o \rightarrow {}^3D_3$	750	–	0.0359	< 0.4
$^3F_2^o \rightarrow {}^1D_2$	912.68277	0.041 ± 9	14.2	5.0 ± 1.1
		References		
	[90]	[90]	[89]	[90]

conclude that $^3D_3$ is weak enough to neglect repumping and $^1D_2$ is strong enough to use as a spin-flipping repumping channel.

CHAPTER 5

CALIBRATING THE ATOMIC BEAM FLUX FROM AN EFFUSIVE OVEN

The Ra EDM experiment uses an effusive oven to generate a directed beam of radium atoms. A fraction of the atoms are laser-cooled and trapped for spin precession frequency measurements. In the first phase of the Single Atom Microscope (SAM) experiment, an atomic beam of neutral atoms is implanted in a solid noble gas film. Both projects require precise knowledge of the atomic beam intensity and distribution to accurately count the rate of atoms exiting the oven.

In the MSU atomic beam fluorescence (ABF) measurement, we illuminate the directed atomic beam with a laser beam tuned to the atomic transition frequency. The laser is scanned over an appropriate frequency range spanning the atomic transition(s) of interest. The resulting laser induced fluorescence (LIF) of the atomic beam is captured by a photodetector positioned perpendicular to the plane formed by the atomic beam axis and laser beam axis. From this data we can plot the atomic absorption line profile and determine the oven atom rate.

I will motivate the ABF experiment in Section 5.1. Then, I will describe the hyperfine structure and hyperfine transition studies for relevant isotopes in Section 5.2 This will be followed by a discussion of atomic absorption line profiles for the case of a directed atomic beam intersecting a weak-pumping fluorescent laser in Section 5.3. I will describe previous ABF measurements in Section 5.4. In Section 5.4, I will compare the measurements to simulated spectra. I will conclude the chapter with suggestions for improved ABF measurements in Section 5.5.
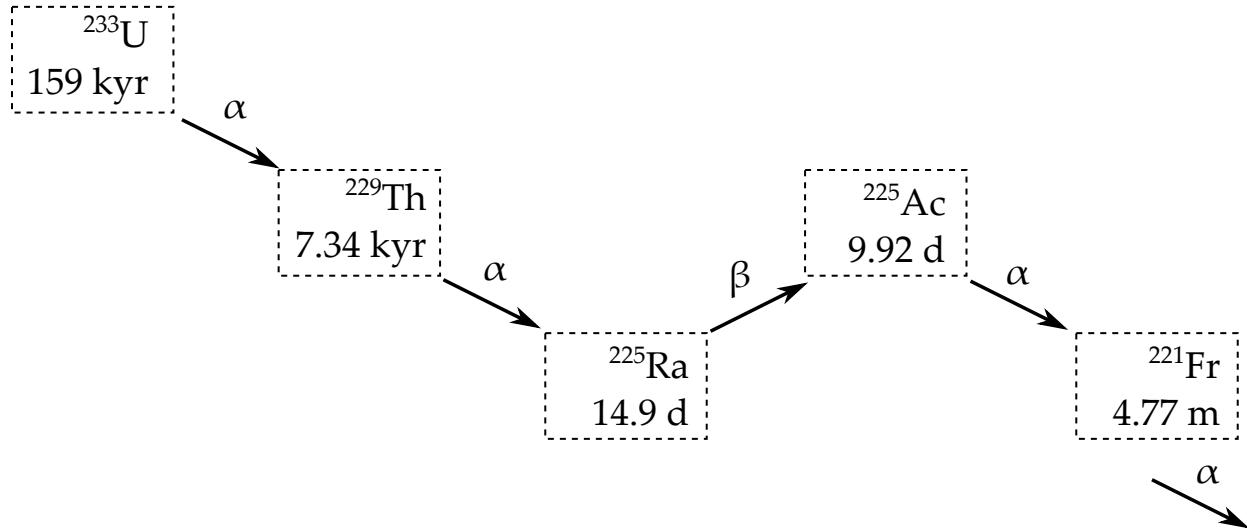
Figure 5.1: Decay scheme of ^{225}Ra. Alpha and beta-decay are denoted by α and β, respectively. Half-lives are from the National Nuclear Data Center. kyr = 1000 years. d = days. m = minutes.

5.1 Motivation

5.1.1 Radium source for electric dipole moment experiment

The Facility for Rare Isotope Beams (FRIB) is linear accelerator at MSU that is planned to be fully operational in 2022. Exotic nuclei will be generated by impinging a uranium beam on a water-cooled graphite target. This will create primary, desired isotopes, along with many secondary isotopes. The primary isotopes will be directed to experimental halls, while secondary isotopes will be extracted from the target water reservoir (for details, see Paige Abel's thesis [92]). The process of extracting the isotope of interest from the FRIB target coolant and preparing an oven-loadable atom sample is the "isotope harvesting" process.

The Ra EDM experiment (ANL, MSU) used ^{225}Ra ($I = 1/2$) prepared at Oak Ridge National Lab (ORNL) in the first two EDM measurements [65, 48]. A decay scheme of radium is shown in Figure 5.1. Radium is produced at ORNL from a ^{229}Th stockpile and sent to ANL as radium nitrate salt. Then we dissolve the salt in nitric acid and add

metallic barium to the solution before wrapping the radium-barium solution in foil and placing it in the oven crucible [48].

Radium-225 has become increasingly sought after for medical research in recent years. The daughter isotope, ^{225}Ac, has been identified as an effective isotope for targeted alpha therapy [143]. The new demand for ^{225}Ra oversubscribes the current available supply and makes an EDM campaign with ^{225}Ra from ORNL unlikely for the foreseeable future.

We're addressing this challenge in two ways. As a stop-gap measure, we will acquire commercially-available ^{223}Ra (nuclear spin $I = 3/2$, half-life 11.43 days) and recalibrate the EDM laser cooling and trapping setup at ANL for ^{223}Ra EDM measurements.

Simultaneously, we are developing a ^{225}Ra harvesting program at FRIB. The harvesting efficiency of a ^{225}Ra source for a new Ra EDM experiment will be evaluated with ABF measurements. I discuss my work in effusive oven atom flux calibrations for isotope harvesting and noble gas implantation in this chapter.

In the most recent 2015 Ra EDM experiment, we used an oven load of 10 mCi (discussed in detail in Section 2.2.3):

$$10 \text{ mCi} = 10 \times 10^{-3} \text{ Ci} \times 3.7 \times 10^{10} \text{ Bq/Ci}$$

$$= 3.7 \times 10^8 \text{ Bq},$$

where Bq are decays per second. ^{225}Ra has a half-life $t_{1/2} = 14.9$ days $= 1.29 \times 10^6$ s, or equivalently a mean lifetime of $\tau = t_{1/2}/\log(2) = 1.86 \times 10^6$ s. The decay constant is $\gamma = 1/\tau = 5.38 \times 10^{-7}$ s^{-1}. That corresponds to an initial oven load of $N_0 = 10 \text{ mCi}/\gamma \approx 7 \times 10^{14}$ atoms.

FRIB is expected to produce secondary radium isotopes, including ^{225}Ra. We will be able to extract radium from the target coolant and chemically purify an oven-loadable sample analogously to the ORNL method. The new source will deliver ^{225}Ra more frequently and in larger quantities than the two previous Ra EDM measurements.

Our goal is to develop an ABF measurement with the aid of computational tools to measure the oven atom rate to within 20%. We can compare this rate to the initial source

size to quantify our isotope harvesting ability. The critical atom and geometry-dependent property is the number of photons emitted by the atom during the fluorescence interaction, or "photon-atom yield" η [dimensionless]:

$$\eta = \frac{dN_\gamma/dt}{dN_a/dt}, \tag{5.1}$$

where dN_a/dt $\left[s^{-1}\right]$ is the atom oven exit rate and dN_γ/dt $\left[s^{-1}\right]$ is the rate of photons emitted from the atoms.

The photon-atom yield is dependent on the properties of the isotope, electronic transition, pumping (excitation) laser, atomic angular distribution, and photodetector.

In 2017, I worked on the ABF-commissioning study of stable ytterbium isotopes. We were successful in measuring an ytterbium spectrum and establishing the proper operation of vacuum chambers, laser equipment, and data acquisition. We used a laser power of approximately 800 mW for the $^1P_1^o$ (398.8 nm) transition. In 2019, the ABF sensitivity was improved with a measurement of the rubidium $^2P_{1/2}^o$ transition (795 nm) for the SAM project (for details, see Ben Loseth's thesis [144]). Using a lower laser power range of 10 μW to 10 mW, the SAM team improved the sensitivity of the method and identified all the hyperfine transitions in the spectrum.

The Yb apparatus was disassembled to build the rubidium SAM ABF setup. After the rubidium ABF measurement, I assembled a new ABF setup. The new setup, which I will refer to as the "Atomic Flux" apparatus, will be used for isotope harvesting ABF measurements. I designed an in-vacuum light-collecting setup that will be installed in the Atomic Flux apparatus to improve the light collection efficiency by an estimated two orders of magnitude (details in Section 5.5.2).

Our timeline for the isotope harvesting efficiency measurement begins with a new ABF measurement of stable ytterbium in the Atomic Flux apparatus. This will calibrate the new setup and will be aided by computational modeling (discussed in Section 5.3) to make an accurate atom rate count. Then we will repeat the ABF measurement with commercially-available calcium chips. This will allow us to calibrate the setup for cal-

Table 5.1: A selection of atomic transitions of the Yb ground state, $^1S_0$. Values from NIST. I = intensity. λ, ν = resonant wavelength, frequency. τ = lifetime. A = Einstein A-coefficient.

excited state	I (arb.)	λ (nm)	ν (THz)	τ (ns)	A (MHz)
$6s6p\,^1P_1^o$	1000	398.799	751.53	5.21	192
$6s6p\,^3P_1^o$	130	555.6466	539.387	869.6	1.15
$\left(^2F_{7/2}^o\right)5d_{5/2}6s^2\,(7/2,\,5/2)^o$	130	346.437	865.11	15.7	68.3

cium and improve the sensitivity of the measurement. Next, we will dissolve commercial calcium in water, simulating the initial conditions of an FRIB harvest. The dissolved calcium will be harvested and prepared as a nitrate with barium in foil, identical to the ORNL/ANL source preparation procedure. We'll measure the fluorescence of the dissolved calcium and determine the harvesting efficiency by comparing the initial source size and measured atom rate.

5.1.2 Rubidium flux measurements

The Single Atom Detection (SAM) project aims to measure rare nuclear reactions, on the order of one event per day, relevant to nuclear astrophysics by capturing reaction products in a transparent, frozen noble gas film and counting the products with LIF. A prototype microscope was built to demonstrate the method by implanting rubidium atoms in a krypton film and counting the rubidium atoms before and after implantation. First, an effusive oven source was used as a rubidium source. Then the prototype was placed on the ReA3 beamline and two accelerator experiments were carried out: krypton ions implanted in a krypton film, followed by rubidium ions implanted in a new krypton film [144].

In the offline rubidium ABF measurement, a rubidium source was placed in an oven similar to the Yb and Ra ovens, but with a much narrower nozzle (discussed in Section 5.3.7). The oven was heated to oven temperatures ranging from 25–220 °C to generate a directed atomic beam. The beam passed a fluorescence chamber, like the Yb setup.

After the fluorescence chamber, the atoms were implanted in a noble gas frozen film target.

Like the isotope harvesting project, the effusive oven rubidium measurement requires a careful measurement of the atomic angular distribution. I present analysis of the rubidium ABF measurements in the context of modeling the lineshape of the fluorescence spectrum to derive an absolute calculation of the atomic flux for isotope harvesting studies.

5.2 Hyperfine spectrum

5.2.1 Atomic state notation

The electronic configuration of the ground state of neutral ytterbium "Yb(I)" is explicitly labeled in the following manner:

$$1s^2 2s^2 2p^6 3s^2 3p^6 3d^{10} 4s^2 4p^6 4d^{10} 5s^2 5p^6 4f^{14} 6s^2 \; {}^1S_0$$

The filled electron shells can be abbreviated in the LS-coupling scheme with principal quantum number n, the angular momentum, and spin with the following notation:

$$n \; {}^{2S+1}L_J \, ,$$

$$L = (S, \; P, \; D, \; F \dots) \mapsto L = (0, \; 1, \; 2, \; 3 \dots) \, ,$$

where S is the spin, L defines the total electronic orbital angular momentum L, and $J = L + S$ is the total electronic spin of the atom. In this notation the ground state becomes $6 \; {}^1S_0$, often shortened to ${}^1S_0$. For the fluorescence measurement, we're probing the strong transition ${}^1S_0 \rightarrow {}^1P_1^o$. A list of selected ground state transitions is given in Table 5.1.

Nucleons configure within the nucleus analogously to electron orbitals. When there are one or more unpaired nucleons, there is a net, nonzero nuclear spin I. The total angular momentum F of the atom is then described by the sum of electronic and nuclear

Table 5.2: Ytterbium total strength factors for $^1S_0$ $(F) \rightarrow$ $^1P_1^o$ (F').

isotope	$\mathbb{S}_{1/2}$	$\mathbb{S}_{3/2}$	$\mathbb{S}_{5/2}$	$\mathbb{S}_{7/2}$
^{171}Yb	2/6	4/6	·	·
^{173}Yb	·	4/18	6/18	8/18

angular momentum:

$$F = I + J, \ I + J - 1, \ \dots, |I - J|$$

To completely capture an atomic transition, we need to label the total angular momentum as well. In the case of ^{171}Yb $(I = 1/2)$, one of the possible transitions can be written in the following manner:

$$^1S_0 \ (F = 1/2) \rightarrow {}^1P_1^o \ (F' = 3/2),$$

where F and F' is the initial and final total angular momentum. The ground state of this transition has $J = L = S = 0$, so F can only be $1/2$. In general, both the initial and final total angular momentum can both take on multiple values.

5.2.2 Atomic transition intensity

Hyperfine splitting is present in atoms with nonzero nuclear spin and shifts the transition frequency of the hyperfine transition $|\, i \, F \, \rangle \rightarrow \big|\, f \, F' \, \big\rangle$ relative to the transition $|\, i \, \rangle \rightarrow |\, f \, \rangle$. To simulate the hyperfine spectrum of Yb, we need to distribute the populations of the nonzero nuclear spin isotopes among its degenerate states. We will assume that the magnetic sublevels m_F are equally populated and that the pumping laser is unpolarized. The unpolarized assumption implies that the transitions $m_F - m_{F'} = +1, 0, -1$ are equally likely.

We'll look at the case of ^{171}Yb $(I = 1/2)$, where there is no hyperfine structure in the ground state. The transition of interest, $^1S_0$ $(F) \rightarrow {}^1P_1^o$ (F'), has a final electronic angular momentum $J' = 1$. The total angular momentum of the excited state can take on possible values of $F' = 3/2, \ 1/2$.

Table 5.3: Rubidium relative strength factors for $^2S_{1/2} \rightarrow\ ^2P_{1/2}$. Wigner 6-$j$ values calculated with an online version of the Root-Rational-Fraction package [145].

isotope	S_{33}	S_{32}	S_{23}	S_{22}	S_{21}	S_{12}	S_{11}
^{85}Rb	4/9	5/9	7/9	2/9	·	·	·
^{87}Rb	·	·	·	1/2	1/2	5/6	1/6

The allowed magnetic sublevels are $m_{F'} = F', F'-1, ..., -F'$, which gives a degeneracy of $g_{F'} = 2F'+1$. For unpolarized laser light, we can characterize the intensity of the hyperfine transition by the degeneracy. I define the intensity, or "total strength factor" $\mathbb{S}_{F'}$ as the following:

$$\mathbb{S}_{F'} = \frac{g_{F'}}{\sum_i g_{F'_i}} \tag{5.2}$$

Total strength factors for the Yb isotopes with nonzero nuclear spin are given in Table 5.2.

Next we consider the general case of hyperfine structure in both the ground state and excited state. The strength of a transition $|F\ m_F\rangle \rightarrow |F'\ m_{F'}\rangle$ driven by a resonant photon (e.g., from a laser) is proportional to the dipole matrix element:

$$\langle F m_F | e\vec{\mathbf{r}} | F' m_{F'} \rangle , \tag{5.3}$$

where e is the electron charge and $\vec{\mathbf{r}}$ is a spherical tensor of rank 1. I follow Steck's method [146] to calculate the relative strength of each branch in a transition with hyperfine splitting. The relative hyperfine transition strength factor $S_{FF'}$ [unitless] is given by:

$$S_{FF'} = (2F'+1) \cdot (2J+1) \cdot \begin{Bmatrix} J & J' & 1 \\ F' & F & I \end{Bmatrix}^2 , \tag{5.4}$$

$$\sum_{F'} S_{FF'} = 1 , \tag{5.5}$$

where we have used the Wigner 6-j symbol, which is derived from the Clebsch-Gordon coefficient $\langle F\ m_F | F'\ m_{F'} \rangle$. For ^{85}Rb $F = 3 \rightarrow F' = 2$, I calculate the following strength

Table 5.4: Rubidium total strength factors for $^2S_{1/2} \to {}^2 P_{1/2}$.

isotope	$\mathbb{S}_{33}$	$\mathbb{S}_{32}$	$\mathbb{S}_{23}$	$\mathbb{S}_{22}$	$\mathbb{S}_{21}$	$\mathbb{S}_{12}$	$\mathbb{S}_{11}$
^{85}Rb	28/108	35/108	35/108	10/108	$\cdot$	$\cdot$	$\cdot$
^{87}Rb	$\cdot$	$\cdot$	$\cdot$	15/48	15/48	15/48	3/48

factor:

$$S_{32} = (5) \cdot (2) \cdot \left(\frac{1}{3} \sqrt{\frac{1}{2}} \right)^2 = \frac{5}{9}$$

Table 5.3 lists the relative hyperfine transition strength factors for the rubidium isotopes.

The relative strength factors provide fractional strengths for the different branches F', given an initial F. However, we need an additional factor to distinguish the relative intensities for different initial F. For example, in ^{85}Rb, we need to know the relative intensity between the transitions for $F = 3$ versus $F = 2$.

For a transition driven by unpolarized laser light, the total strength factor for each transition is by found multiplying each $S_{FF'}$ by the degeneracy g_F and normalizing to a weighted sum:

$$\mathbb{S}_{FF'} = \frac{g_F \cdot S_{FF'}}{\sum_{FF'} g_F \cdot S_{FF'}} \tag{5.6}$$

where $\mathbb{S}_{FF'}$ is the total strength factor with initial and final angular momentum F and F'. For example, $\mathbb{S}_{32} = 35/108$ for ^{85}Rb. The total strength factors for the transition $^2S_{1/2} \to {}^2P^o_{1/2}$ are given in Table 5.4.

5.2.3 Frequency of transitions

The resonance frequency of an atom depends on the isotope number and hyperfine structure. In the case of ytterbium, there are seven stable naturally-occurring isotopes. Two of these isotopes have hyperfine structure with $2 + 3 = 5$ hyperfine transitions. In total, there are ten resonance peaks. Abundance, mass, and nuclear spin values are listed in Table A3.

Table 5.5: Literature values of the hyperfine constants of Yb, Rb, and Ca isotopes with nonzero nuclear spin.

isotope	level	A_{HF} (MHz)	B_{HF} (MHz)	Ref.
^{171}Yb	$^1\text{P}_1$	$-214.173(53)$	0.0	[147]
^{173}Yb	$^1\text{P}_1$	$-57.682(29)$	$+609.065(98)$	[147]
^{87}Rb	$^2\text{S}_{1/2}$	$+3417.341\,305\,452\,145(45)$	0.0	[148]
^{87}Rb	$^2\text{P}_{1/2}$	$+407.25(63)$	0.0	[148]
^{85}Rb	$^2\text{S}_{1/2}$	$+1011.910\,813\,0(20)$	0.0	[148]
^{85}Rb	$^2\text{P}_{1/2}$	$+120.527(56)$	0.0	[148]
^{43}Ca	$^1\text{P}^o_1$	$-15.46(15)$	$-9.7(7)$	[149]
^{47}Ca	$^1\text{P}^o_1$	$-16.20(23)$	$+4.1(6)$	[149]

To first order, there are two contributions to shift of an atom's energy level due to a nonzero nuclear spin: a magnetic dipole moment and electric quadrupole moment term. The magnetic dipole hyperfine shift term ΔE_{m1} [MHz] is defined as the following [150]:

$$\Delta E_{\text{m1}} = \frac{1}{2} A_{\text{HF}}\, K\,, \tag{5.7}$$

$$K = F(F+1) - J(J+1) - I(I+1)\,, \tag{5.8}$$

where A_{HF} [MHz] is the magnetic dipole hyperfine constant.
The electric quadrupole interaction term is defined as follows:

$$\Delta E_{\text{e2}} = \frac{1}{4} B_{\text{HF}}\, \frac{\frac{3}{2}K(K+1) - 2I(I+1)J(J+1)}{I(2I-1)J(2J-1)}\,, \tag{5.9}$$

where ΔE_{e2} [MHz] is the electric quadrupole hyperfine shift term and B_{HF} [MHz] is the electric quadrupole hyperfine constant. A_{HF} and B_{HF} are experimentally measured parameters for each isotope with nonzero I. Together, we have the total first-order hyperfine structure shift, ΔE_{HF} [MHz]:

$$\Delta E_{\text{HF}} = \Delta E_{\text{m1}} + \Delta E_{\text{e2}} \tag{5.10}$$

Equation 5.10 gives the hyperfine shift with respect to the state $^{2S+1}\text{L}_J(I,F)$. Literature values of hyperfine constants for Yb, Rb, and Ca isotopes are listed in Table 5.5. I calculated ΔE_{HF} for each state with hyperfine structure in Yb, Rb, and Ca in Table 5.6.

Table 5.6: Calculated hyperfine shifts ΔE_{HF} of ytterbium, rubidium, and calcium. Total angular momentum $F = I + J$

isotope	state	I	F	ΔE_{HF} (MHz)
^{171}Yb	$6s6p\,^1\mathrm{P}^o_1$	1/2	1/2	+214.2
^{171}Yb	$6s6p\,^1\mathrm{P}^o_1$	1/2	3/2	−107.1
^{173}Yb	$6s6p\,^1\mathrm{P}^o_1$	5/2	3/2	+224.5
^{173}Yb	$6s6p\,^1\mathrm{P}^o_1$	5/2	5/2	−544.9
^{173}Yb	$6s6p\,^1\mathrm{P}^o_1$	5/2	7/2	+296.5
^{85}Rb	$5s\,^2\mathrm{S}_{1/2}$	5/2	2	−1770.8
^{85}Rb	$5s\,^2\mathrm{S}_{1/2}$	5/2	3	+1264.9
^{85}Rb	$5s\,^2\mathrm{P}_{1/2}$	5/2	2	−210.88
^{85}Rb	$5s\,^2\mathrm{P}_{1/2}$	5/2	3	+150.62
^{87}Rb	$5s\,^2\mathrm{S}_{1/2}$	3/2	1	−4271.7
^{87}Rb	$5s\,^2\mathrm{S}_{1/2}$	3/2	2	+2563.0
^{87}Rb	$5s\,^2\mathrm{P}_{1/2}$	3/2	1	−508.75
^{87}Rb	$5s\,^2\mathrm{P}_{1/2}$	3/2	2	+305.25
^{43}Ca	$4s4p\,^1\mathrm{P}^o_1$	7/2	9/2	−57
^{43}Ca	$4s4p\,^1\mathrm{P}^o_1$	7/2	7/2	+22
^{43}Ca	$4s4p\,^1\mathrm{P}^o_1$	7/2	5/2	+64
^{47}Ca	$4s4p\,^1\mathrm{P}^o_1$	7/2	9/2	−56
^{47}Ca	$4s4p\,^1\mathrm{P}^o_1$	7/2	7/2	+13
^{47}Ca	$4s4p\,^1\mathrm{P}^o_1$	7/2	5/2	+75

There is also an "isotope shift" in the transition frequency due to the different atomic masses. The calculation of the isotope shift is complex (see, for example, Woodgate [150]). The isotope shift of ytterbium is approximately linear for the even isotopes. I estimated the hyperfine isotope shifts by interpolating the even-nucleon shifts as inputs for the computational modeling discussed in Section 5.3.

5.3   Modeling the spectral line profile of a directed atomic beam

The atomic angular distribution must be well-characterized to accurately count atoms in a directed beam from an effusive oven. I developed a Python program that simulates a laser sweep and generates a fluorescence spectrum for a given set of isotopes. The
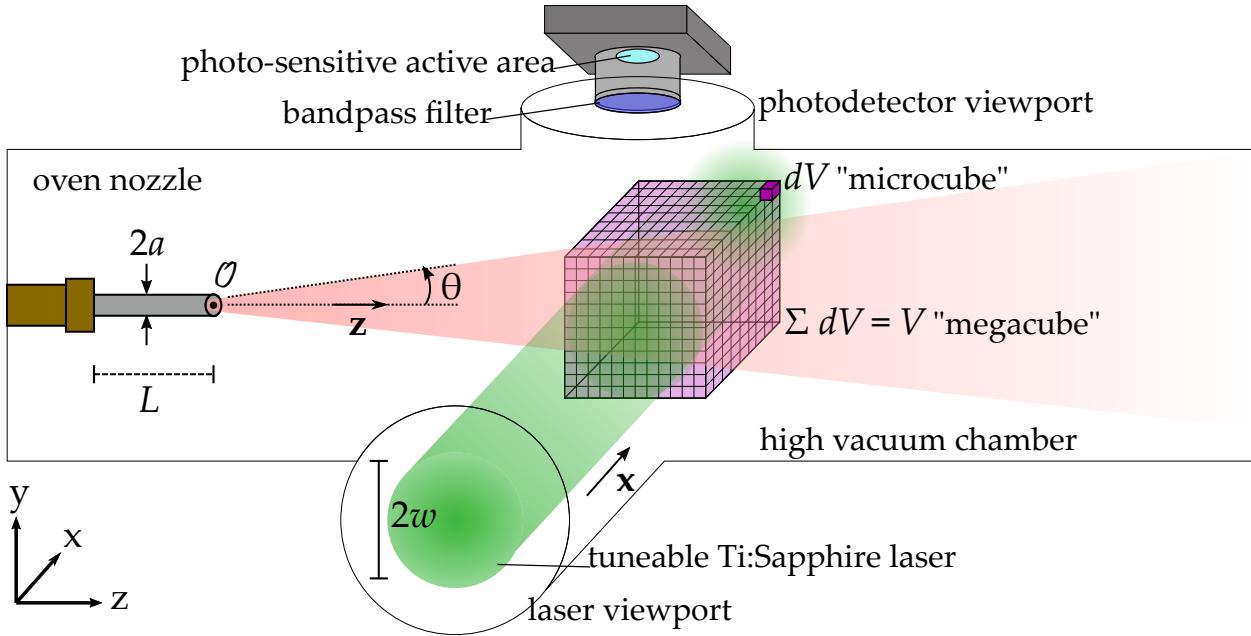
Figure 5.2: A schematic (not to scale) of the atomic beam fluorescence setup. This is generalized to be applicable to all three setups discussed in this chapter.

program models the vacuum geometry, laser profile, photodetector, and atomic oven geometry. The simulation also accepts an angular distribution input, which we will vary to match the simulation to LIF measurements.

5.3.1 The ABF apparatus and calculating the photodetector signal

A schematic of the beamline is shown in Figure 5.2. An atom source, such as a metal ingot, is loaded into an effusive oven. The oven is heated and emits atoms from the oven nozzle with a geometry-dependent angular distribution $j(\theta)$, where θ is the angle with respect to the nozzle axis $\hat{z}$.

The atoms enter a fluorescence chamber where a resonant laser propagates perpendicular to the nozzle axis along $\hat{x}$. The chamber is a six-way cross. Perpendicular to the zx plane, a photodetector is mounted at the window of the cross arm. For the measurements discussed in this chapter, we use an avalanche photodiode (Thorlabs 410APD2) with a 0.5 mm diameter circular active area. The laser is scanned over an appropriate frequency range and a fraction of the light emitted by atoms absorbing the laser light is captured

M Squared SolsTiS continuous wave Ti:Saph with ECD-X doubling cavity

Lithium triborate crystal
doubling cavity 350-500 nm
2 W

IR pickoff

Fiber couple output

Pump:
532 nm 18 W
diode laser
(SPROUT-G)

Doubling cavity output

700--1000 nm 7 W
5 kHz FWHM Ti:Saph
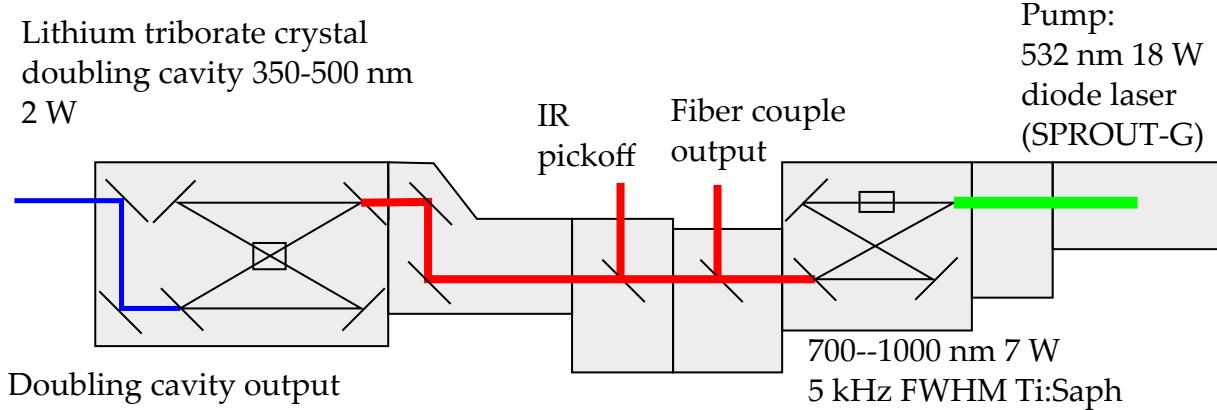
Figure 5.3: Schematic of laser system.

by the avalanche photodetector (APD). A schematic of the ABF laser setup is shown in Figure 5.3.

The voltage output of the APD $V(\nu)$ [V] is given by the following:

$$V(\nu) = P_d(\nu) \times \mathcal{R}_M(\lambda) \times G, \tag{5.11}$$

where

$P_d(\nu)$ [W] is the incident fluorescent light power at frequency ν,

$\mathcal{R}_M(\lambda)$ [A/W] is the detector responsivity at wavelength λ,

M (the "M-factor") is the gain, and

G [V/A] is the transimpedance gain.

We will use a NIST-traceable power meter to calibrate the APD (Thorlabs 410-APD2) wavelength response and gain for the flux measurements. For simulations, I estimate the response using the manufacturer specifications (see Appendix C).

5.3.2 Calculating the fluorescence power on the photodetector

The APD voltage signal is proportional to the fluorescent power incident on the photodetector. Given an active sensor area A_d $\left[\text{m}^2\right]$, the incident power $P_d^q(\nu_\gamma)$ [W] is given by

the following:

$$P_d^q(\nu_\gamma) = \int \int \frac{h\nu_\gamma}{v_a} \, \Phi_a(\vec{\mathbf{r}}) \, F^q(\nu_\gamma, \vec{\mathbf{r}}) \, dV_a \frac{dA_d}{4\pi \left| \vec{\mathbf{d}} - \vec{\mathbf{r}} \right|^2} \, , \tag{5.12}$$

where

$q = 1, 0, -1$ for σ^+, π, and σ^- polarized light, respectively,

$F \left[\text{s}^{-1} \right]$ is the single atom fluorescence rate,

$\vec{\mathbf{d}} \, [\text{m}]$ is the position of the center of the photodetector surface,

$v_a \, [\text{m/s}]$ is the component of the atom velocity along the z axis, and

$\Phi_a(\vec{\mathbf{r}}) \left[\text{m}^{-2} \, \text{s}^{-1} \right]$ is the atom flux at position $\vec{\mathbf{r}}$.

As we will see in the next section, the atom photon emission rate is related to the fluorescent power through the atomic flux of the oven.

5.3.2.1 Calculating the atomic flux, vapor pressure, and the atom rate

We consider a position $\vec{\mathbf{r}}$, where the origin is defined as the oven nozzle exit in Figure 5.2. At this location, the atomic flux $\Phi_a(\vec{\mathbf{r}}) \left[\text{m}^{-2} \, \text{s}^{-1} \right]$ is given by the following:

$$\Phi_a(\vec{\mathbf{r}}) = \frac{dN_a}{dt} \frac{j(\theta)}{r^2} \, , \tag{5.13}$$

$$\frac{dN_a}{dt} = \frac{n_o v_a A_o}{4\pi} \, , \tag{5.14}$$

$$n_o = \frac{P}{k_\text{B} T} \, , \tag{5.15}$$

where

$j(\theta) \, [\text{unitless}]$ is the atomic angular distribution at polar angle θ,

$n_o \left[\text{m}^{-3} \right]$ is the atom number density,

$A_o \left[\text{m}^2 \right]$ is the cross-sectional area of the oven nozzle,

$P \, [\text{Pa}]$ is the saturated vapor pressure of the atoms, and

$T \, [\text{K}]$ is the oven temperature.
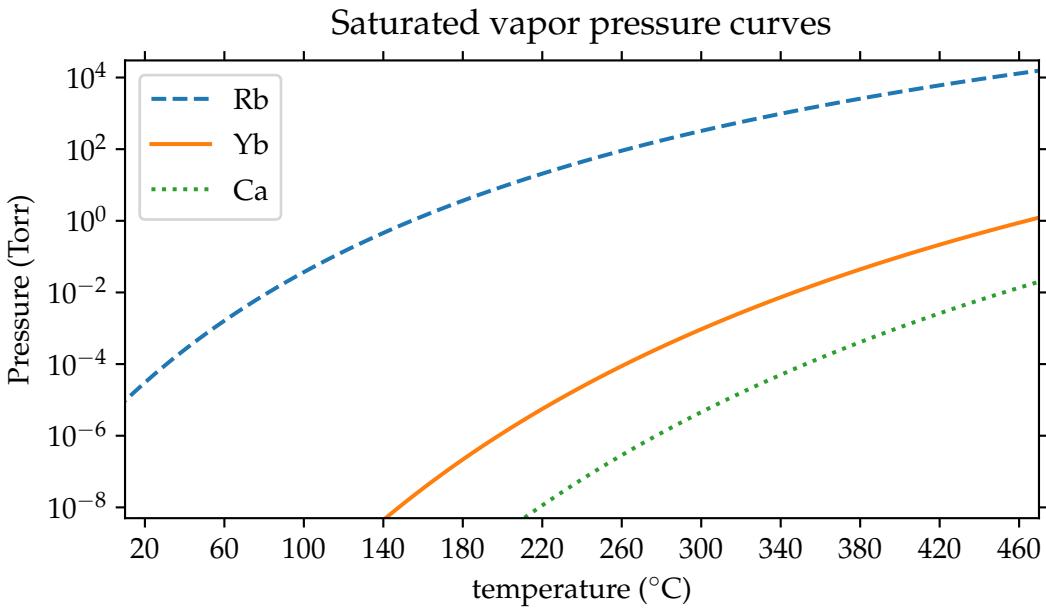
Figure 5.4: Saturated vapor pressure curve for ytterbium, calcium, and rubidium.

The vapor pressure is the pressure at which the gaseous atoms are in thermodynamic equilibrium with its solid phase. The vapor pressure is saturated when the vaporization and condensation rates are equivalent. We use the following empirical equation to determine the saturated vapor pressure P of the oven:

$$\log_{10} \frac{P}{P_0} = \Delta + A + \frac{B}{T} + C \log_{10} T + \frac{D}{T^3}, \tag{5.16}$$

$$\Delta = \begin{cases} 2.881, & P_0 = 1 \text{ Torr}, \\ 5.006, & P_0 = 1 \text{ Pa} \end{cases}$$

The constants A, B, C, and D are properties of the oven atom species. For an oven temperature of 300 °C, $P = 9.4 \times 10^{-4}$ Pa $= 7.1 \times 10^{-6}$ Torr:

$$n_o = 1.2 \times 10^{17} \text{ atoms m}^{-3}, \qquad \frac{dN_a}{dt} = 1.7 \times 10^{13} \text{ atoms s}^{-1}$$

I plotted vapor pressure curves for Yb, Rb, and Ca in Figure 5.4. Vapor pressure coefficients are listed in Table A4.

I simulated the photodetector signal for a range of temperatures with an ytterbium oven source and oven nozzle ratio $\gamma = 0.25$ in Figure 5.5. At ≈ 250 °C the calculated

131

signal is 10 μV, which is the limit of the measurement sensitivity of the ABF measurement without light-collecting optics. This corresponds to an atom oven rate of approximately 10^{12} atoms per second.

For an oven temperature of 300 °C, nozzle ratio $\gamma = 0.25$, with an oven nozzle radius of 1.5875 mm, and atoms traveling at $v_a = 232.3$ m/s along $\hat{z}$ 13.2 cm downstream from the nozzle, I calculate an atomic flux of:

$$\Phi \approx 10^{15} \text{ atoms m}^{-2} \text{ s}^{-1}$$

We can now estimate the total power on the photodetector using the calculated atom rate and Equation 5.12. In the case of the Yb $^1S_0 \to {}^1P_1^o$ transition, a perfectly on-resonance laser yields an order-of-magnitude estimate:

$$
\begin{aligned}
P_d \approx & \frac{\left(6.63 \times 10^{-34} \text{ J Hz}^{-1}\right)\left(751.5 \times 10^{12} \text{ Hz}\right)}{4\pi \left(230 \text{ m/s}\right)} \left(1.0 \times 10^{15} \text{ m}^{-2}\text{s}^{-1}\right)\left(4.1 \times 10^6 \text{ s}^{-1}\right) \\
& \times \left(\pi(3.5 \times 10^{-3} \text{ m})^2(30 \times 10^{-3} \text{ m})\right)\left(3.3 \times 10^{-5} \text{ sr}\right) \\
& \approx 2.7 \times 10^{-11} \text{ W}
\end{aligned}
$$

This is reasonably close to the fully integrated solution of 3.47×10^{-11} W . From Equation 5.11, the converted photodetector voltage is 0.196 mV.

5.3.3 The single atom fluorescence rate

The following discussion presumes a two-level system of atomic states a (the ground state) and b (the excited state) in a radiation field such as the electric field produced by a laser. The single atom fluorescence rate $F(v_\gamma, \vec{\mathbf{r}})\left[\text{s}^{-1}\right]$ in the laser interaction region from Equation 5.12 is the rate at which an atom in state b emits a photon and decays to a :

$$F(v_\gamma, \vec{\mathbf{r}}) = b(v_\gamma, \vec{\mathbf{r}})\, A = \frac{b(v_\gamma, \vec{\mathbf{r}})}{\tau_0}, \tag{5.17}$$

where

v_γ [Hz] is the frequency of the laser,
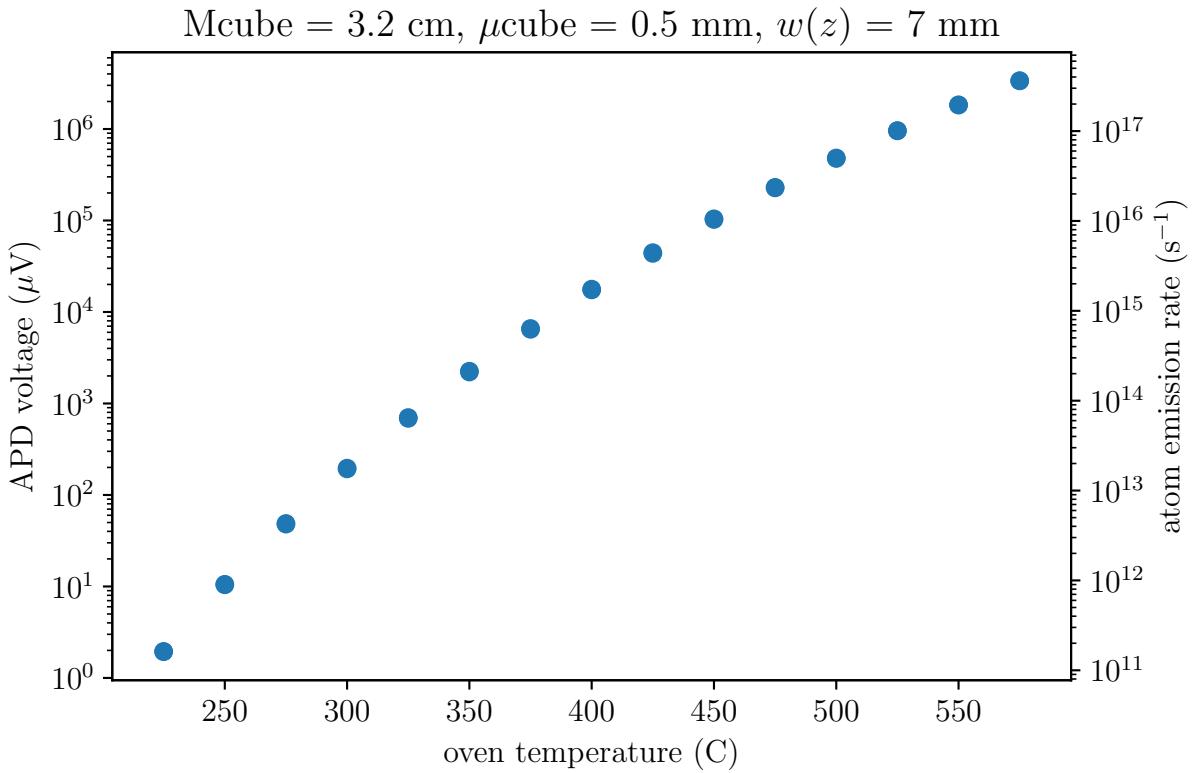
Figure 5.5: Calculated fluorescence signal as the oven temperature is varied using a laser power of 10 mW.

$\vec{\mathbf{r}}$ [m] is the position of the atom,

A [Hz] is the spontaneous emission rate Einstein A-coefficient, and

τ_0 [s] is the lifetime of the atomic state when a photon of wavelength λ_0 is absorbed by the atom.

The fraction of atoms in the excited state $b(\nu_\gamma, \vec{\mathbf{r}}, t)$ [unitless] is derived from the population rate equations with equal stimulated excitation and emission rates $R\left[s^{-1}\right]$ and the spontaneous decay rate from b to a, given by the Einstein A-coefficient $A = 1/\tau_0 \left[s^{-1}\right]$:

$$\frac{da}{dt} = -Ra + Rb + \frac{b}{\tau_0}, \tag{5.18}$$

$$\frac{da}{dt} = +Ra - Rb - \frac{b}{\tau_0}, \tag{5.19}$$

$$a + b = 1 \tag{5.20}$$

133
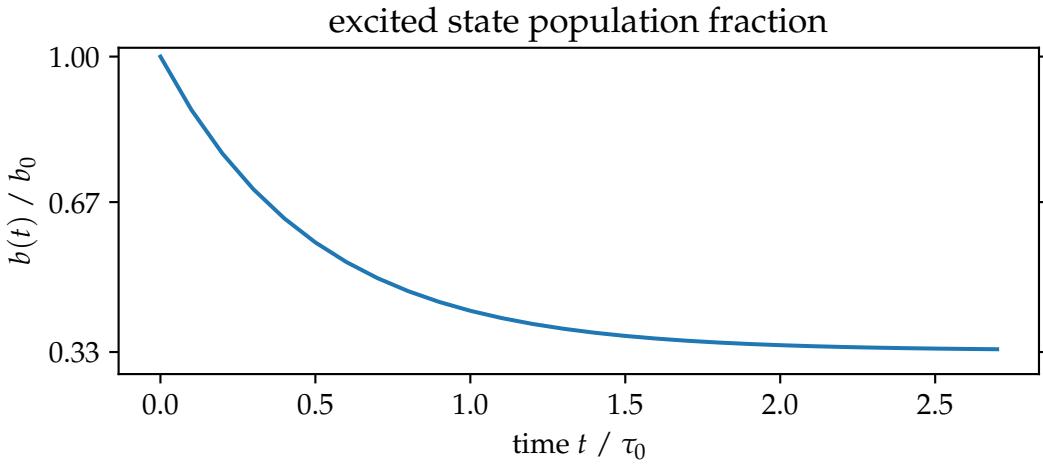
Figure 5.6: Excited state population of a two-level system for $R = 2 \times 10^8$ s^{-1} and $\tau_0 = 5$ ns.

Solving these equations yields the fraction of atoms in b at time t:

$$b(t) = b_0 \exp\left(-\frac{t}{\tau^*}\right) + \left(\frac{R\tau_0}{1 + 2R\tau_0}\right) \times \left[1 - \exp\left(-\frac{t}{\tau^*}\right)\right],$$ (5.21)

$$\tau^* = \frac{\tau_0}{1 + R\tau_0},$$ (5.22)

where b_0 [unitless] is the population fraction of b at $t = 0$.

As an example of the time to reach population equilibrium, I'll use rounded $^1P_1^o$ numbers: $R = 2 \times 10^8$ s^{-1}, $\tau_0 = 5$ ns. In the limit $t \to \infty$, we get the steady-state expression for the fraction of atoms in b:

$$b(\nu_\gamma, \vec{r}) = \lim_{t \to \infty} b(\nu_\gamma, \vec{r}, t) = \frac{R(\nu_\gamma, \vec{r})\tau_0}{1 + 2R(\nu_\gamma, \vec{r})\tau_0}$$

In our example, $b(\nu_\gamma, \vec{r}) = 1/3$. Figure 5.6 plots the excited state fraction vs. times for factors of the mean lifetime τ_0. After less than three lifetimes, the fraction has converged to 1/3 to within 1%. During this time an atom passing through a laser-generated electric field would travel a distance:

$$\approx 300 \text{ m/s} \times 15 \text{ ns} = 4.5 \ \mu\text{m}$$

We typically use laser diameters of 5–10 mm, making the steady-state approximation quite reasonable for our setup. Upcoming ABF measurements will be performed in the

Table 5.7: Values used for Yb $^1S_0 \rightarrow$ $^1P_1^o$ atom excitation rate $R(\nu_\gamma, \vec{r})$.

parameter	definition	value
T	oven temperature	$300\,^\circ\text{C}$
ν_a	resonant transition frequency of the atom	7.51526×10^{14} Hz
FWHM	full width-half max of the laser	5.0×10^6 Hz
P_γ	laser power	1.0×10^{-2} W
$w(z)$	beam radius	1.0×10^{-2} m
ρ	radial distance from laser axis	0.0 m
f_a	atomic transition oscillator strength	1.37
$\mathcal{R}_M$	detector responsivity at 398.8 nm	11.3 A/W
G	transimpedance gain	5×10^5 V/A
r	interaction-sensor distance	7.74×10^{-2} m
$\nu_{p,z}$	most probable speed atom speed along $\hat{z}$	232.3 m/s
A_{det}	sensor area	1.96×10^{-8} m^2
F	atom fluorescence rate	4.1×10^6 s^{-1}
ν_0	emitted photon frequency	7.51526×10^{14} Hz
$\mathcal{V}$	interaction volume	8×10^{-9} m^3

'weak pumping limit,' or $R(\nu_\gamma, \vec{r})\tau_0 << 1$. In this limit, $b(\nu_\gamma, \vec{r}) \approx R \cdot \tau_0$ and the single atom fluorescence rate is equivalent to the excitation rate:

$$F(\nu_\gamma, \vec{r}) = \frac{1}{\tau_0} R \cdot \tau_0 = R(\nu_\gamma, \vec{r}) \quad \text{(weak pumping limit)} \qquad (5.23)$$

I've plotted the single atom excitation rate in Figure 5.7 using ytterbium transition values listed in Table 5.7.

5.3.4 The Doppler-free excitation rate

The Doppler-free atom absorption cross section $\sigma(\nu, \nu_a) \left[\text{m}^2 \right]$ is defined as follows:

$$\sigma(\nu, \nu_a) = \frac{h\nu}{c} B_a \times \mathbb{L}(\nu, \nu_a, A), \qquad (5.24)$$

$$B_a = \frac{\pi r_e c^2}{h\nu} f_a, \qquad (5.25)$$

$$\mathbb{L}(\nu, \nu_a, A) = \frac{A/(4\pi^2)}{(\nu - \nu_a)^2 + (A/4\pi)^2} = \frac{\delta\nu_n/(2\pi)}{(\nu - \nu_a)^2 + (\delta\nu_n/2)^2}, \qquad (5.26)$$

where

$B_a \left[\text{s}^{-1} \right]$ is the Einstein absorption B-coefficient,
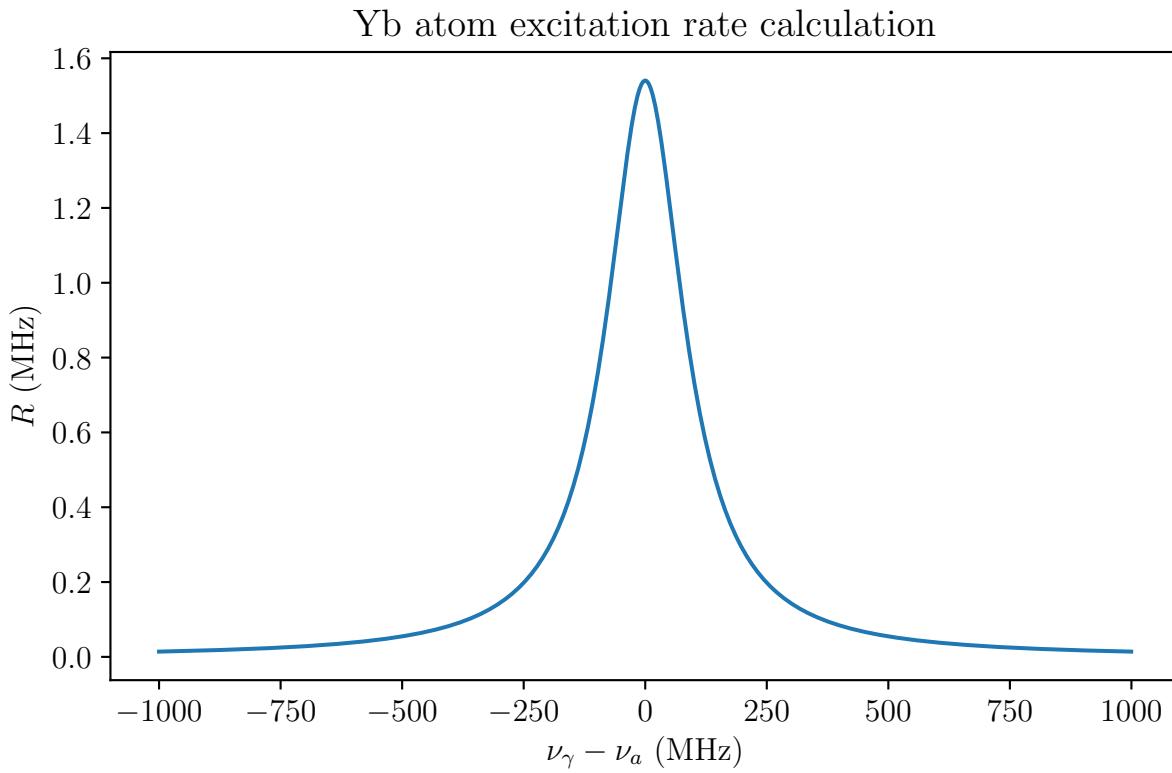
Figure 5.7: The weak pumping limit Yb single atom laser excitation rate using the parameters in Table 5.7.

$\mathbb{L}(\nu, \nu_a, A) \left[\text{Hz}^{-1}\right]$ is the probability of atomic transition per unit frequency,

f_a [unitless] is the atomic transition oscillator strength, and

$\delta\nu_n = A/2\pi$ [Hz] is the natural linewidth.

The natural linewidth, also known as the halfwidth, is the width of the line profile of an atomic transition at which the amplitude is one half the central frequency peak maximum. The Lorentzian natural linewidth is sometimes referred to as a full-width half-maximum, but we will reserve that term for referring to the laser profile.

For the Yb $^1P_1$ transition, $A = 1.92 \times 10^8$ s^{-1} and $\delta\nu_n = 30.6$ MHz.

The rate at which a Doppler-free single atom absorbs a resonant photon for a given atomic

transition in a radiation field is defined as the atom excitation rate $R(\nu_\gamma, \nu_a, \vec{r})$:

$$R(\nu_\gamma, \nu_a, \vec{r}) = \int_0^\infty \phi(\nu, \nu_\gamma, \mathsf{FWHM}, \vec{r}) \, \sigma(\nu, \nu_a) \, d\nu \,, \tag{5.27}$$

$$\phi(\nu, \nu_\gamma, \mathsf{FWHM}, \vec{r}) = \frac{P_\gamma}{h\nu} \, \mathbb{S}(\vec{r}) \times \mathbb{G}(\nu, \nu_\gamma, \mathsf{FWHM}) \,, \tag{5.28}$$

$$\mathbb{S}(\vec{r}) = \frac{I(\vec{r})}{P_\gamma} = \frac{2}{\pi w^2(z)} \exp\left[-\frac{2\rho^2}{w^2(z)}\right] \,, \tag{5.29}$$

$$\mathbb{G}(\nu, \nu_\gamma, \mathsf{FWHM}) = \frac{2\sqrt{\log 2/\pi}}{\mathsf{FWHM}} \exp\left[-4\log(2)\frac{(\nu - \nu_\gamma)^2}{\mathsf{FWHM}^2}\right] \,, \tag{5.30}$$

where

ν_a [Hz] is the resonant transition frequency of the atom,

FWHM [Hz] is the full width-half max of the laser,

$\phi(\nu, \nu_\gamma, \mathsf{FWHM}, \vec{r}) \left[\mathrm{m}^{-2}\right]$ is the local photon flux,

$\mathbb{S}(\vec{r}) \left[\mathrm{m}^{-2}\right]$ is the fraction of all photons per unit area,

P_γ [W] is the laser power,

$I(\vec{r}) \left[\mathrm{W\,m}^2\right]$ is the laser intensity,

$w(z)$ [m] is the beam radius,

ρ [m] is the radial distance from the laser beam longitudinal axis, and

$\mathbb{G}(\nu, \nu_\gamma, \mathsf{FWHM}) \left[\mathrm{Hz}^{-1}\right]$ is the fraction of all photons per unit frequency.

Now we're in a position to plug everything into Equation 5.27 and separate $R(\nu_\gamma, \nu_a, \vec{r})$ into a prefactor and an integral over frequency:

$$R(\nu_\gamma, \nu_\alpha, \vec{r}) = \frac{P_\gamma}{h\nu_\gamma} \frac{2\pi r_e c f_a}{\pi w^2(z)} \exp\left[-\frac{\rho^2}{w(z)}\right] \times \frac{2}{\pi A} \, \mathcal{L}(\nu, \nu_\gamma, A, \mathsf{FWHM}) \,, \tag{5.31}$$

$$\mathcal{L}(\nu, \nu_\gamma, A, \mathsf{FWHM}) = \frac{\pi A}{2} \int_0^\infty \frac{\sqrt{4\log(2)/\pi}}{\mathsf{FWHM}} \exp\left[-4\log(2)\frac{(\nu - \nu_\gamma)^2}{\mathsf{FWHM}^2}\right] \mathbb{L}(\nu, \nu_a, A) \, d\nu \,, \tag{5.32}$$

where we have redefined the integral factor $\mathcal{L}(\nu, \nu_\gamma, A, \mathsf{FWHM})$ [dimensionless] as the "line-shape overlap" function.

$\mathcal{L}$ can be solved numerically, but I found that the narrow width of the peak was not properly integrated by some the standard Python and MatLab solvers, such as

the Fortran-based `QUADPACK` . I instead used the simpler composite trapezoidal in-tegration routine `numpy.trapz()` . I approximated the integration limits of v to $\left[v_\gamma - 3(\text{FWHM}), v_\gamma + 3(\text{FWHM})\right]$, beyond which the exponential term rapidly drives R to 0. A plot of the single atom excitation rate for the Yb $^1S_0 \rightarrow {}^1P_1^o$ transition is shown in Figure 5.7.

5.3.5 Doppler broadening for a directed atomic beam

The SAM and Flux ABF setups use an effusive oven to generate an atom vapor beam. As seen in the experimental layout in Figure 5.2, we've chosen the origin to be the exit point of the nozzle, so that $\vec{r}$ and $\vec{v}$ have identical trajectories. The laser is oriented perpendicu-lar to the atom beam axis, along $\hat{x}$. Atom trajectories at some angle θ from the atom beam axis $\hat{z}$ will also have a velocity component aligned with the laser.

I define the angle between the laser axis and the atom velocity at position $\vec{r}$ as α [rad]:

$$\cos(\alpha) = \frac{\vec{r} \cdot \hat{x}}{\left\| \vec{r} \right\|} \tag{5.33}$$

When $\alpha = \pi/2$, the Doppler shift between the atom and laser is $\cos(\pi/2) = 0$.

We assume the atoms in our directed beam are non-interacting particles at thermody-namic equilibrium. For this scenario we model the speed distribution of the atom beam as a Maxwell-Boltzmann distribution $g(v)$ $[\text{m/s}]^{-1}$ at oven temperature T [K], given by the following:

$$g(v) = \sqrt{\frac{2}{\pi}} \left(\frac{m}{k_B T} \right)^{3/2} v^2 \exp\left[-\left(\frac{v}{v_p} \right)^2 \right], \tag{5.34}$$

$$v_p = \sqrt{\frac{2k_B T}{m}}, \qquad \int_0^\infty g(v)\, dv = 1, \tag{5.35}$$

where

v [m/s] is the atom speed,

v_p [m/s] is the most probable atom speed,

k_B [J/K] is the Boltzmann constant, and

m [kg] is the mass of the atom.

For ^{174}Yb exiting a 300 °C oven, the most probable speed is $v_p = 234$ m/s. The most probable speed of For ^{85}Rb exiting a 100 °C oven is $v_p = 270$ m/s.

The Doppler broadening effect depends on both α and the velocity of the atom. To first order, the Doppler term is given by the following:

$$1 - \frac{v}{c}\cos(\alpha)$$

The first-order Doppler term is incorporated by modifying the atom absorption cross section (Equation 5.24) $\sigma(\nu, \nu_a) \rightarrow \sigma_D(\nu, \nu_a)$:

$$\sigma_D(\nu, \nu_a, \vec{r}) = \frac{h\nu}{c} B_a \times \mathbb{L}_D(\nu, \nu_a, A), \tag{5.36}$$

$$\mathbb{L}_D(\nu, \nu_a, A, \vec{r}) = \frac{A/(4\pi^2)}{[\nu - \nu_a(1 - \cos(\alpha)v/c)]^2 + (A/4\pi)^2} \tag{5.37}$$

The modified excitation rate includes the additional speed integral from σ_D:

$$R(\nu_\gamma, \nu_a, \vec{r}) = \int_0^\infty \int_0^\infty \phi(\nu, \nu_\gamma, \mathsf{FWHM}, \vec{r})\, \sigma_D(\nu, \nu_a, \vec{r})\, g(v)\, d\nu dv \tag{5.38}$$

Equation 5.38 has the practical effect of broadening the spectral profile width.

The linear Doppler full width at half maximum FWHM_D [Hz] is given by:

$$\mathsf{FWHM}_D = \frac{\sqrt{8k_B T \log 2\,/m}}{c} v_a \sin(\theta), \tag{5.39}$$

$$= 2.92 \times \sqrt{T/m}\, v_a \sin(\theta) \times 10^{-20}, \tag{5.40}$$

where c [m/s] is the speed of light in vacuum and θ [rad] is the polar angle of the atom relative to the beam axis.

The natural linewidth $\delta\nu_n$ of the Yb $^1P_1^o$ transition is approximately 30.6 MHz. I calculate a Doppler broadened linewidth of $\delta\nu_D = 121$ MHz using an oven temperature of 300 °C = 573.15 K and a maximum angle of $\theta = 0.12435$ rad.

Our fluorescence measurement uses a directed atomic beam with a large angular distribution and requires the general form of the excitation rate in Equation 5.38. A common alternative fluoroscopy setup uses collimation downstream of the oven to suppress angular dependence on atom intensity. In this case the atoms move uniformly along $\hat{z}$, so θ is small and $\alpha \approx \pi/2$. The broadening term in the denominator of the modified Lorentzian reduces to $\nu_a(1 - \cos(\alpha)v/c) \rightarrow \nu_a$, significantly simplifying the calculation of the atom excitation rate.

5.3.6 The atomic angular distribution and photodetector solid angle

Now that we can calculate the atomic flux, excitation rate, and photodetector power, it's natural to reexamine the photon-atom yield first shown in Equation 5.1.

The photon emission rate dN_γ/dt can be written as follows:

$$\frac{dN_\gamma}{dt} = \frac{4\pi d^2 P_d(\nu_\gamma)}{A_d h \nu_\gamma},$$

(5.41)

where

$\vec{d}$ [m] is the position of the center of the photodetector surface,

ν_a [m/s] is the component of the atom velocity along $\hat{z}$, and

A_d [m^2] is the photodetector active area.

Using Equation 5.41, we can rewrite the photon-atom yield η in terms of $P_d(\nu_\gamma)$:

$$\eta = \int \int \frac{1}{\nu_a} \frac{d_y^2}{A_d} \times j(\theta) \times F(\nu_\gamma, \vec{r}) \times \frac{dV_a}{r^2} \frac{dA_d}{\left|\vec{d} - \vec{r}\right|^2},$$

(5.42)

where d_y [m] is the distance along $\hat{y}$ from the center of the fluorescence volume to the photodetector surface.

In the next section, I will describe the model for the angular distribution $j(\theta)$. Then I'll detail the solid angle calculation in Section 5.3.8.
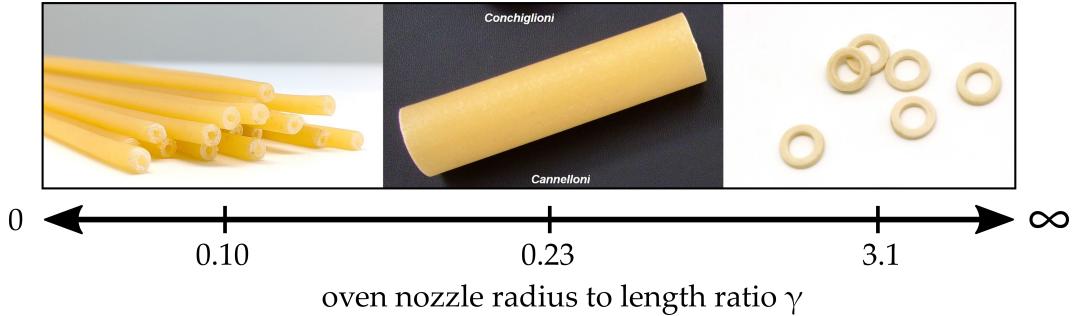
Figure 5.8: From left to right, in order of increasing noodle diameter-to-length: *bucatini*, *cannelloni*, *anellini* noodles. Images obtained under the CC0 1.0 Universal (CC0 1.0) Public Domain Dedication License.[a]

5.3.7 Atomic angular distribution

The oven nozzle geometry is shown schematically in Figure 5.2. The distribution of the atoms flowing through the nozzle depends on the nozzle aspect ratio. Long nozzles collimate the beam, while shorter nozzles permit a higher atom flux. We can characterize the nozzle by the ratio of the radius to length, or the oven nozzle ratio γ:

$$\gamma = \frac{2a}{L}, \tag{5.43}$$

where a [m] is the nozzle radius and L [m] is the nozzle length.

It's natural (and delicious) to think of the oven nozzles as different kinds of noodles. A diverse selection of noodles is shown in Figure 5.8. As $\gamma \to \infty$, one can imagine a shorter and wider noodle, for example *anellini*. For $\gamma \to 0$, the nozzle is very long compared to its diameter, similar to *bucatini*. The Yb nozzle ratio is closest to the *cannelloni* geometry, with $\gamma = 0.1250''/0.5000'' = 0.2500$. The calcium oven nozzle ratio will be identical to the ytterbium nozzle ratio.

Collisions between the atoms exiting the channel affect the resulting angular distribution. We use the tube length Knudsen number K_{nL} to characterize the density of atoms in the oven channel [151]:

$$K_{nL} = \frac{\lambda}{L}, \tag{5.44}$$

---

[a]https://creativecommons.org/publicdomain/zero/1.0/deed.en

141

(a)
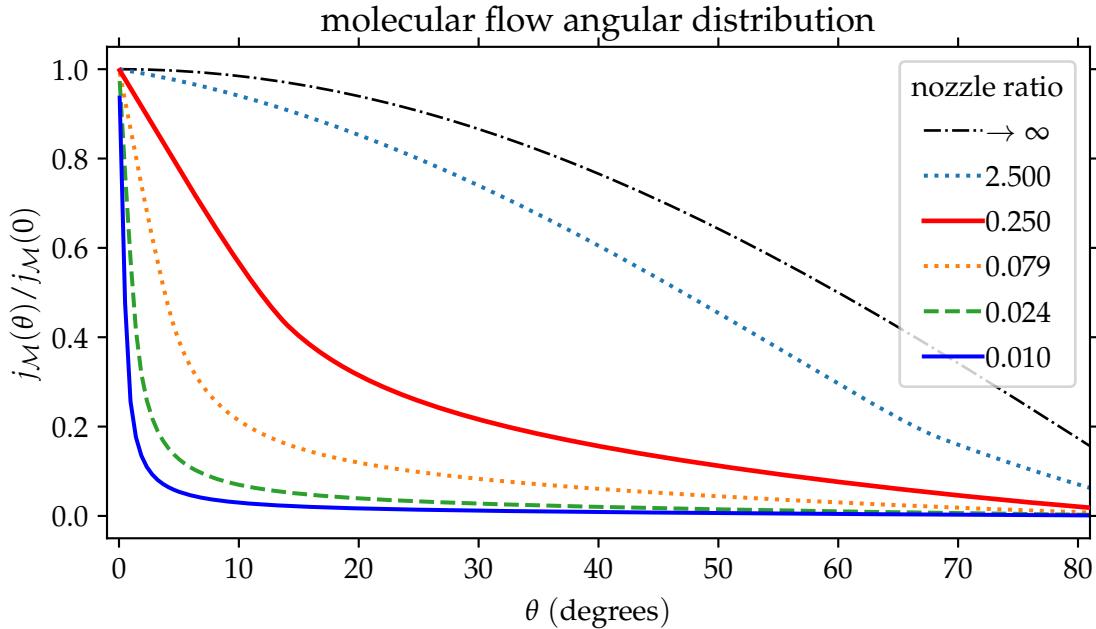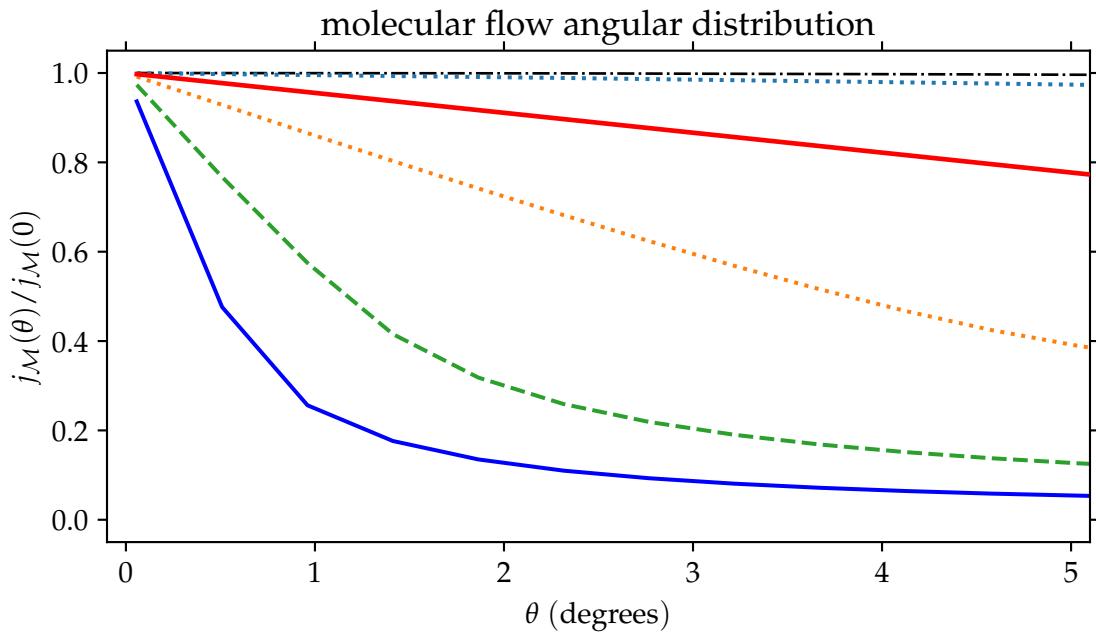
Figure 5.9: The atomic angular distribution of for a range of nozzle ratios. (a) 80 degree range, all lines converge to an intensity of zero at 90 degrees (b) Zoomed in to within 5 degrees. The legend appears in the order of descending intensity. Middle solid line = ytterbium and calcium ratio $\gamma = 0.25$. Dashed line = radium $\gamma = 0.024$. Bottom solid line = rubidium $\gamma = 0.01$.

where λ [m] is the mean free path of the atoms in the channel. Atom-oven states with Knudsen numbers in the range $K_{nL} > 10$ are classified as the "molecular flow" regime, where the only significant atom interactions are collisions along the nozzle channel wall. Atoms in intermediate regime, $K_{nL} \leq 10$ must take atomic collision effects into account. For the ytterbium nozzle ($\gamma = 0.25$), $K_n > 10^4$ for oven temperatures less than 330 °C. For the rubidium nozzle ($\gamma = 0.01$), $K_n > 10$ for oven temperatures less than 100 °C.

In the molecular flow limit, the angular distribution of atoms exiting the oven $j_{\mathcal{M}}(\theta)$ [unitless] at some angle θ [rad] with respect to the beam axis $\hat{\mathbf{z}}$ is given by [151]:

$$j_{\mathcal{M}}(\theta) = \begin{cases} \zeta_0 \cos\theta + \dfrac{2}{\pi}\cos\theta\left[(1-\zeta_0)R(p) + \dfrac{2}{3}(\zeta_1 - \zeta_0)\dfrac{1-(1-p^2)^{3/2}}{p}\right], & p \leq 1 \\ \zeta_0 \cos\theta + \dfrac{4\gamma}{3\pi}(\zeta_1 - \zeta_0)\dfrac{\cos^2\theta}{\sin\theta}, & p \geq 1 \end{cases} \tag{5.45}$$

$$\zeta_0 = \frac{1}{2} - \frac{1}{3\gamma^2}\left[\frac{1-2\gamma^3 + (2\gamma^2 - 1)\sqrt{1+\gamma^2}}{\sqrt{1+\gamma^2} - \gamma^2 \sinh^{-1}(1/\gamma)}\right], \tag{5.46}$$

$$\zeta_1 = 1 - \zeta_0, \tag{5.47}$$

$$R(p) = \cos^{-1}(p) - p\sqrt{1-p^2}, \tag{5.48}$$

$$p = \frac{1}{\gamma}\tan\theta, \tag{5.49}$$

where

ζ_0 [dimensionless] is the channel exit collision parameter,

ζ_1 [dimensionless] is the channel entrance collision parameter,

$R(p)$ [dimensionless] is the noodle parameter, and

p [dimensionless] is the noodle angle.

A plot of the normalized angular distribution is over a wide range of angles and magnified to within several degrees in Figure 5.9a and Figure 5.9b. The rubidium nozzle ($\gamma = 0.01$) is designed to collimate the distribution to within several degrees. By contrast, the intensity of atoms exiting the ytterbium and calcium nozzle ($\gamma = 0.25$) is significant even at 50 degrees. In the case of a nozzle width much longer than the nozzle length
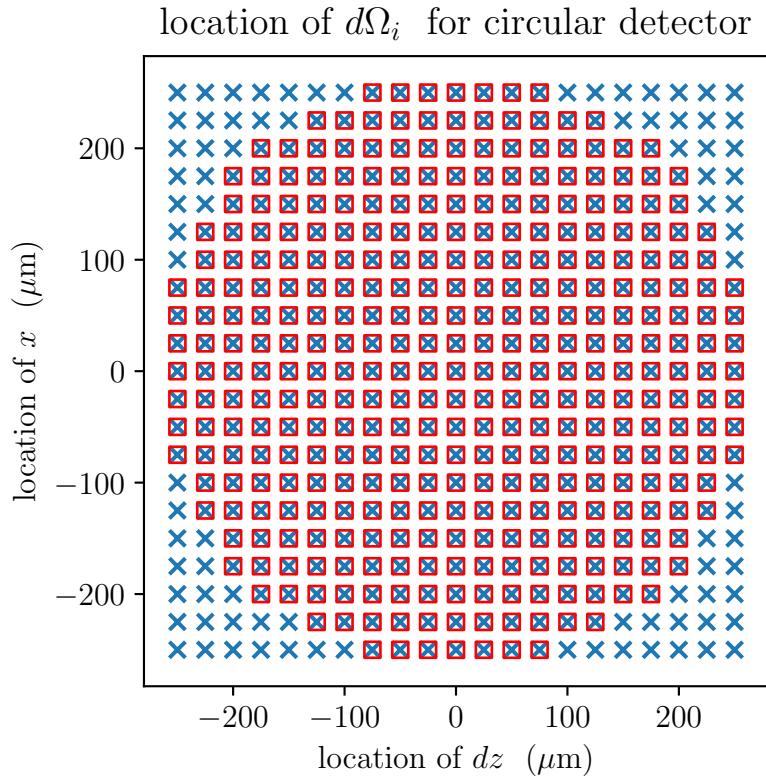
Figure 5.10: A grid of the points used to numerically integrate the solid angle of a circular detector. We start with a 2×2 square mesh and cut out a circle (shown with red squares) to obtain the result.

(think *anellini*), $j_\mathcal{M}$ approaches a cosine distribution:

$$\lim_{\gamma \to \infty} j_\mathcal{M}(\theta) = \cos\theta$$

5.3.8 Solid angle calculation

Atomic beam fluorescence is measured with an avalanche photodiode with a 0.5 mm diameter active surface (Thorlabs 410-APD2). I investigated solid angle coverage calculations using both approximation and a numerical method for different detector sizes and distances from the fluorescence region.

The $dA_d / |\vec{\mathbf{d}} - \vec{\mathbf{r}}|^2$ term in Equation 5.12 can be rewritten as the solid angle coverage

of the photodetector:

$$d\Omega_{\text{det}} = \frac{dA_d}{\left|\vec{\mathbf{d}} - \vec{\mathbf{r}}\right|^2} \tag{5.50}$$

The "$1/r^2$" approximation $\Omega \approx A_{\text{det}}/d_y^2 = 3.3 \times 10^{-5}$ sr is reasonably accurate for this geometry, but this breaks down for larger detectors or shorter fluorescence-detector distances.

A map of the vertices of each detector surface area element is shown in Figure 5.10. To make use of parallel processing, I initialize the detector infinitesimal elements as a square grid.Then I apply a boundary condition to use elements within the radius of the detector to calculate the solid angle. I calculate $\Omega_\circ = 3.27 \times 10^{-5}$ sr with the Atomic Flux detector using 441 elements with side length $R_{\text{det}}/10 = 0.25$ mm/10 = 25 μm.

When the detector is large ($R_{\text{det}} \approx 12.7$ mm) or close ($d_y \approx 40$ mm) to the fluorescence region, the solid angle calculation is highly dependent on the detector shape. This is also true for the light collection implementation that I discuss in Section 5.5.2. The solid angle of a square detector, such as that used in the SAM solid noble gas measurement [144], deviates from the solid angle of an equivalent-surface area circular detector by tens of percent as the solid angle is compared at different positions in the fluorescence region.

5.3.9 Tying everything together into an atomic beam fluorescence simulation

The previous sections of this chapter describe the necessary calculations that are inputs for a ABF simulation code I developed in the Python programming language. In Section 5.3.7, I showed analytic expressions for the atomic angular distribution $j(\theta)$. In practice, the functions as written do not capture all the features of a measured spectrum. The ABF simulation provides a comparison to a measured spectrum and allows us to numerically derive $j(\theta)$ and the effective oven nozzle geometry.

The simulation integrates over the interaction volume where the atomic beam passes through the laser radiation field. I approximate the true volume as a simple right rectan-

atom-photon yield response, $w(z) = 7$ mm, megacube $= 3.2$ cc
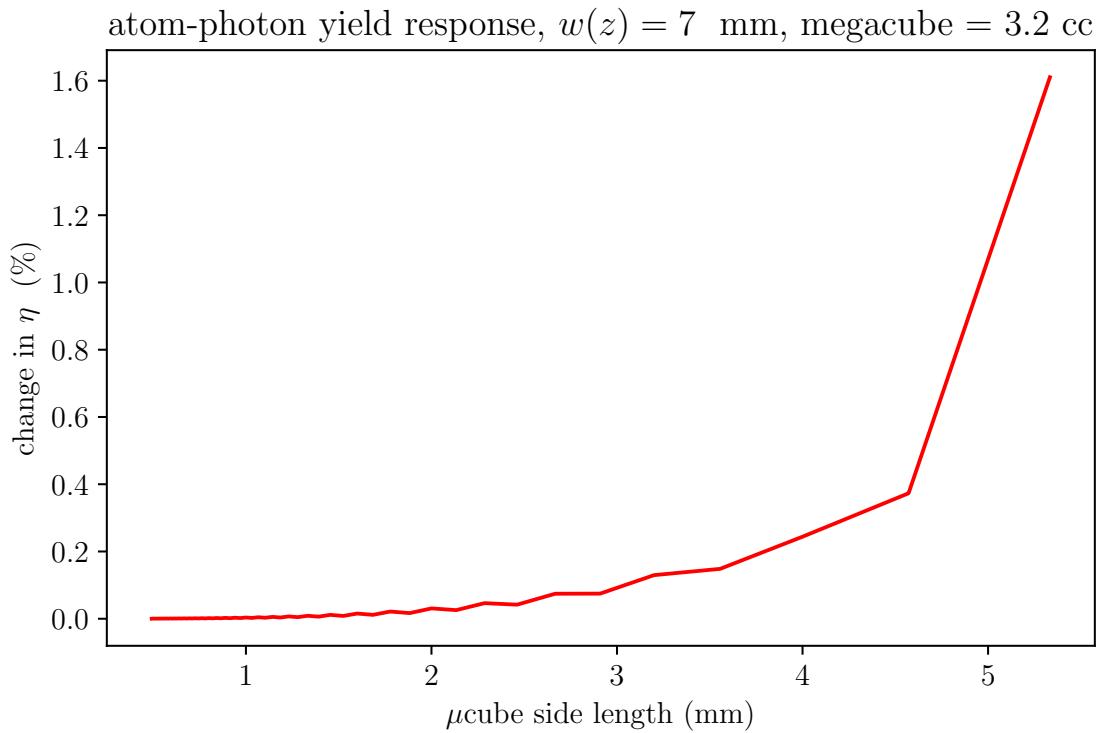
Figure 5.11: The photon-atom yield percent change as the number of subdivisions of the fluorescence volume is varied. The megacube side length is 32 mm, the laser width is 7 mm.

gular prism, which I define as the "megacube" $\mathcal{V}$ $\left[\text{m}^3\right]$:

$$\int d\mathcal{V} = \int \int \int dx\, dy\, dz = \mathcal{V} \quad \text{"megacube"}$$

Each infinitesimal volume element $dxdydz$ is called a "microcube." These terms are depicted in Figure 5.2.

I studied the effect of varying the megacube and microcube size. In Figure 5.11, I fixed the mega cube to $32 \times 32 \times 32$ mm cube for the Flux ABF oven nozzle ($\gamma = 0.25$) and varied the micro cube size. I found that the change in the calculated photon-atom yield changed by less than .1% when using a microcube size of 1 mm or less.

For the rubidium oven ($\gamma = 0.01$), the angular intensity changes significantly over even one degree, as shown in Figure 5.9b. This requires an appropriately small microcube and is computationally expensive.
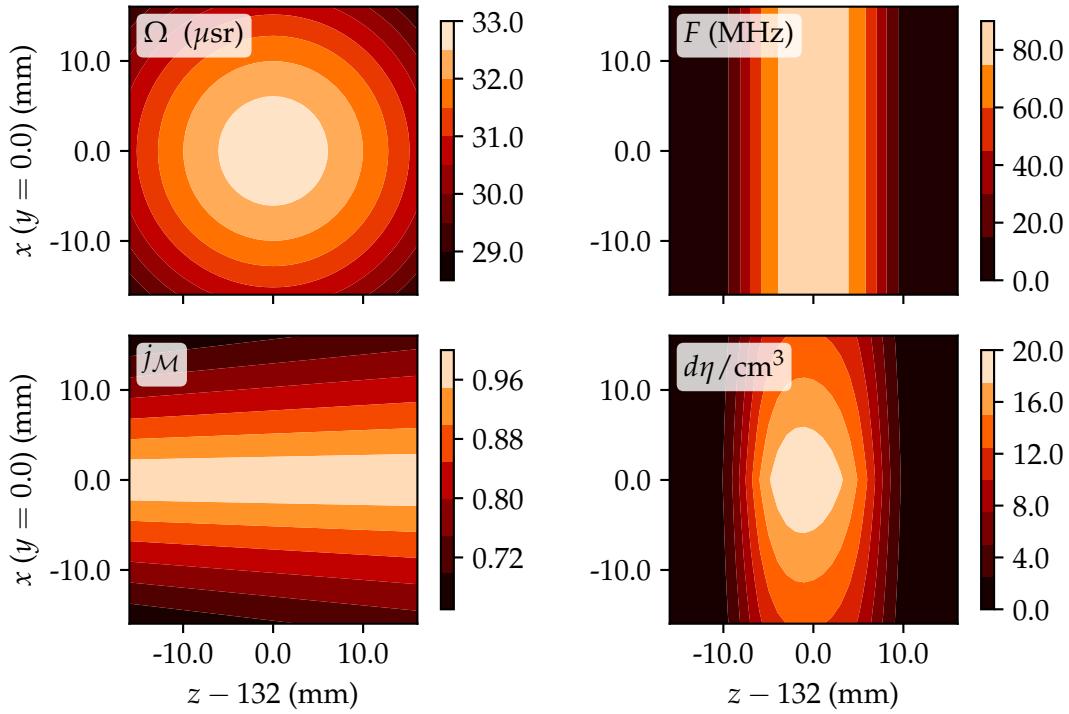
Figure 5.12: The integral of η in the plane $y = 0$. In this plane, the photodetector at $y = 76.2$ mm viewing angle is constrained by the inner diameter of the vacuum cross (30.226 mm). The scanning area available to the photodetector is 15.52 mm square.

The atomic beam fluorescence simulations discussed in the following sections are computed with 68921 microcubes of side length of 0.3902 mm in a megacube with a 16 mm side length.

Figure 5.12 shows *zx* plane contour plots of the integrand of the solid angle, fluorescence rate, angular distribution, and photon-atom yield for an ytterbium ABF simulation. These terms represent significant pieces of the ABF simulation and are combined in the manner prescribed by Equation 5.42. Each *zx* "slice" of Ω, $F(\nu_\gamma, \vec{r})$, and $j(\theta)$ is integrated over a vertical range corresponding to the megacube side length to determine η.

5.4 Comparing simulations to data

5.4.1 Yb fluorescence and power broadening

The commissioning ytterbium ABF measurement was performed in 2017. Laser power data was recorded by a Thorlabs powermeter that measured laser intensity sampled from a 8:92 pellicle beamsplitter. We used a laser scan step size of 9 MHz at the Ti:Sapphire output which is frequency-doubled to 17.9 MHz at the external doubling cavity.

I used a sum of seven Voigt profiles (convolution of a Gaussian and Lorentzian distribution) plus a constant offset $C + \sum_{i=1}^{7} \mathbb{V}_i$ to fit the spectrum in Figure 5.13a. The dashed lines are individual fitted peaks, and the solid line is the overall fit.

The triple peak consisting of ^{172}Yb and ^{171}Yb ($F = 3/2, 7/2$) is difficult to decouple given the relative coarseness of the scan size. The Voigt fitting function prefers to under-weight the amplitude ^{173}Yb($I = 3/2$) and over-weight the two more populated states.

To find a convergent fit, I condensed the triple peak into one Voigt profile. The fractional residual of the spectrum fit is shown in Figure 5.13b. The fit models the data to within 10% except for the boundaries of the laser scan and in the region between ^{174}Yb and the triple peak.

A table of the calculated, measured, and literature transition frequencies are given in Table 5.8.

The Gaussian widths σ are allowed to vary independently and range from 40–80 MHz. The saturation intensity $I_s(\nu, \nu_a)$ $\left[\text{W m}^{-2} \right]$ of a single atom is given by the following:

$$I_s(\nu, \nu_a) = \frac{h\nu A}{2\sigma(\nu, \nu_a)}, \tag{5.51}$$

where $\sigma(\nu, \nu_a)$ is the cross section of the atom given by Equation 5.24. In the case of the Yb $^1P_1^o$ transition, $\nu_a = 7.515 \times 10^{14}$ Hz and I calculate the following resonant cross section

(a)
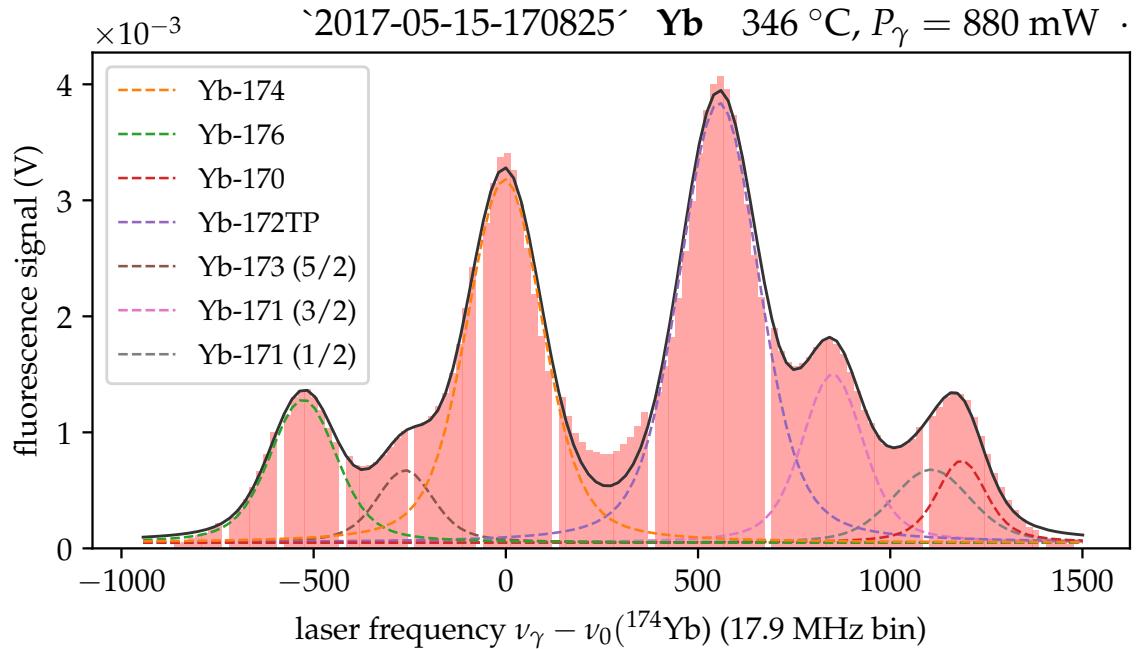
(b)
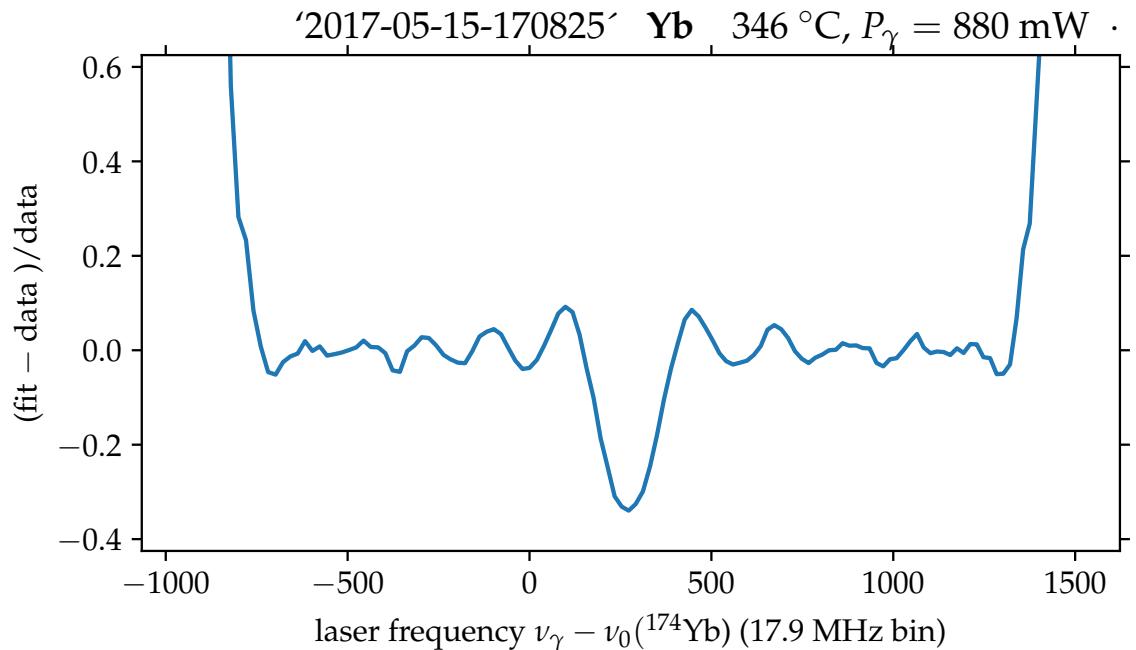
Figure 5.13: Yb 5/15/2017 ABF measurement. Yb-172TP = triple peak consisting of ^{172}Yb, ^{173}Yb($F = 7/2$), and ^{173}Yb($F = 3/2$). (a) Seven-peak Voigt fit + constant offset to data (b) Fractional residual of fit (y axis truncated for clarity).

Table 5.8: Calculated, measured, and literature values of the $^1S_0 \to {}^1P_1^o$ transition frequencies with respect to ^{174}Yb($I = 0$, $F = 1$).

isotope	Calc. Δv (MHz)	Meas. Δv (MHz)	Ref. [147] (MHz)
^{168}Yb ($I = 0$, $F = 1$)	+1887.4		
^{170}Yb ($I = 0$, $F = 1$)	+1192.4	+1183(18)	+1192.393(66)
^{171}Yb ($I = 1/2$, $F = 1/2$)	+1077.0	+1106(67)	+1153.696(61)
^{171}Yb ($I = 1/2$, $F = 3/2$)	+755.76	+849.6(59)	+832.436(50)
^{172}Yb ($I = 0$, $F = 1$)	+533.3	+554.9(16)	+533.309(53)
^{173}Yb ($I = 5/2$, $F = 3/2$)	+491.11		
^{173}Yb ($I = 5/2$, $F = 5/2$)	−278.28	−261(10)	−253.418(50)
^{173}Yb ($I = 5/2$, $F = 7/2$)	+563.12		
^{176}Yb ($I = 0$, $F = 1$)	−509.3	−526.7(44)	−509.310(50)

and saturation intensity:

$$\sigma_0 = \sigma(v_a, v_a) = 7.58 \times 10^{-14}\ \text{m}^2\,,$$

$$I_0 = I_s(v_a, v_a) = 63\ \text{mW cm}^{-2}$$

Saturation intensities for the Yb, Rb, and Ca transitions of interest are listed in Table 5.9.

I estimate a broadened linewidth of 260 MHz for Figure 5.13a. With a laser intensity of approximately $I_\gamma = 863\ \text{mW} / \pi\ (0.35\ \text{cm})^2 = 2240\ \text{mW/cm}^2$, the saturation factor is:

$$I_\gamma/I_0 = 36$$

The power-broadened transition linewidth A_s [Hz] can now be calculated:

$$\frac{A_s}{2\pi} = \frac{A}{2\pi}\left(1 + \frac{I}{I_0}\right)^{1/2} \approx 6.1\ \frac{A}{2\pi} \tag{5.52}$$

From this I estimate a linewidth of $A_s/2\pi \approx 190$ MHz. The fitted linewidths range from 150–245 MHz in Figure 5.13a. The closest-matching transition is ^{176}Yb with a linewidth of 206 ± 16 MHz.

In Figure 5.14 I show a simulated ytterbium spectrum with a laser intensity of:

$$10\ \text{mW}/\left(\pi\ 0.35\ \text{cm}^2\right) = 26\ \text{mW/cm}^2$$

Table 5.9: Saturation intensities and oscillator strengths for selected ytterbium, rubidium, and calcium transitions. ν = frequency, A = Einstein A-coefficient (NIST values). f_a = oscillator strength. f_a(Rb) from [146]. f_a(Ca) from [152]. I_0 = saturation intensity.

transition	ν (THz)	A (MHz)	f_a	$I_0 \left[\text{mW/cm}^2 \right]$
Yb $6s^2\,{}^1S_0 \to 6s6p\,{}^1P_1^o$	751.53	192	1.37	63
Rb $5s\,{}^2S_{1/2} \to 5p\,{}^2P_{1/2}^o$	377.107 43	36.0	0.34231(33)	1.5
Ca $4s^2\,{}^1S_0 \to 4s4p\,{}^1P_1^o$	709.078 235	220	1.75	61
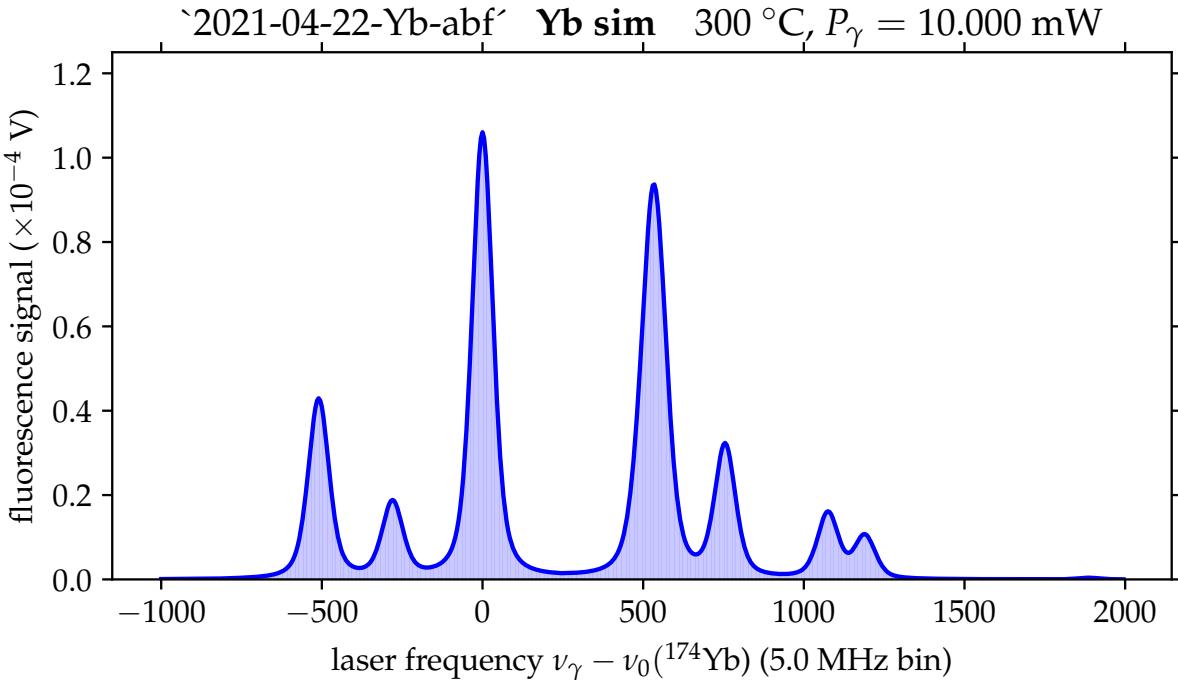
Figure 5.14: Simulated Yb fluorescence spectrum in the weak pumping limit.

This is well below the saturation intensity and in the weak pumping limit (Equation 5.23. The Doppler broadening is significantly reduced and the ^{170}Yb and ^{171}Yb ($F = 1/2$) peaks are easily resolved. The peak voltage is on the order of hundreds of μV, which we're easily sensitive to.

In the next Yb ABF measurement, we will reduce the laser intensity to the simulated intensity and use a smaller laser scan step size of 5 MHz to control Doppler broadening and improve our sensitivity to individual transitions in the cluster peak.

Table 5.10: A selection of atomic transitions of the Rb ground state, $5s\,^2S_{1/2}$. Intensity values and wavelengths from NIST, lifetime values from [153]. I = intensity. λ, ν = resonant wavelength, frequency. τ = lifetime. A = Einstein A-coefficient.

excited state	I (arb.)	λ (nm)	ν (THz)	τ (ns)	A (MHz)
$5p\,^2P^o_{3/2}$	1000	780.027	384.230 35	26.25(8)	38.1
$5p\,^2P^o_{1/2}$	500	794.760	377.107 43	27.75(8)	36.0

All the numbers used for calculating the flux, excitation rate, and photon-atom yield are given in Table 5.7. Now I will show explicit calculations for a selection of the values.

Origin-to-photodetector distance r:

The distance from the center of the atomic beam to the front surface of the APD detector r [m] is the sum of the distances of (1) the center of the 2.75" 6-way cross to the top of the flange (Kurt J. Lesker C6-0275) (2) the width of the cage plate (Thorlabs LCP01) (3) the distance from the APD (Thorlabs APD410A2) flange to the active surface of the detector:

$$r = 62.484 \text{ mm } + 12.7 \text{ mm } + 2.2 \pm 0.3 \text{ mm } = 77.4 \pm 0.3 \text{ mm}$$

Most probable atom speed along nozzle axis $v_{p,z}$:

To find the most probable speed $v_{p,z}$ [m/s], I used an oven temperature of $T = 573.15$ K and the mass of ^{174}Yb found in Table A3. This gives $v_p = 234.08$ m/s. For a flux calculation, we are interested in the component of the velocity that is parallel to the axis of the oven nozzle. Therefore we need to know the maximum divergence angle of the atomic beam exiting the nozzle. The ytterbium oven nozzle has a length of 1/2" and a diameter of 1/8". If we bisect the cone forming the boundary of beam, the divergence angle is:

$$\theta = \arctan \frac{0.5 \times 0.1250''}{0.5000''} = 0.12435 \text{ rad}$$

The longitudinal component of the most probable velocity is given by:

$$v_{p,z} = \cos(\theta) v_p = 232.3 \text{ m/s}$$

Table 5.11: Calculated rubidium transition frequencies (hyperfine + isotope shifts) with respect to the transition of ^{85}Rb, $\nu_0\left(^{85}\text{Rb}\right) = \nu\left(^2\text{S}_{1/2} \rightarrow {}^2\text{P}^o_{1/2}\right) = 377.107$ THz.

isotope	$5s\,^2\text{S}_{1/2} \rightarrow 5s\,^2\text{P}^o_{1/2}$			$\nu - \nu_0\left(^{85}\text{Rb}\right)$ [MHz]
	F	$\rightarrow$	F'	
^{85}Rb	2	$\rightarrow$	2	+1560.0
^{85}Rb	2	$\rightarrow$	3	+1921.5
^{85}Rb	3	$\rightarrow$	2	−1475.8
^{85}Rb	3	$\rightarrow$	3	−1114.3
^{87}Rb	1	$\rightarrow$	1	+3840.5
^{87}Rb	1	$\rightarrow$	2	+4654.5
^{87}Rb	2	$\rightarrow$	1	−2994.2
^{87}Rb	2	$\rightarrow$	2	−2180.2

Laser-atom interaction volume $\mathcal{V}$:

I'm assuming that the interaction volume $\mathcal{V}\left[\text{m}^3\right]$ is a 2 mm cube:

$$\mathcal{V} = \ell^3 = 8 \times 10^{-9}\ \text{m}^3$$

The 2017 Yb measurement used a high laser power that does not satisfy the weak pumping limit (Equation 5.23). The ABF simulation code is intended for weak pumping limit analysis.

5.4.2 Rubidium fluorescence

A table of relevant properties of the $5^2\text{S}_{1/2} \rightarrow {}^2\text{P}^o_{1/2}$ transition are shown in Table 5.10.

Seventeen ABF measurements were performed with a 0.54 cm laser diameter at powers ranging from 10 μW to 9.8 mW and oven temperatures ranging from 25–220 °C [144]. A Ti:Sapphire identical to that of the Atomic Flux laser (Figure 5.3) is used to generate the 795 nm laser beam. The beam is picked off at the Ti:Saph output and before any frequency mixing or doubling. The laser light is linearly polarized but is fiber-coupled to

the fluorescence chamber. The fiber does not conserve polarization and we assume that the light is unpolarized, or equal parts σ^+, π, and σ^- components.

I performed fits of each rubidium isotope peak in the spectra with Voigt line profile fits. I also included a constant offset to fit the background. Each Voigt peak $\mathbb{V}_i$ has four adjustable parameters: the Gaussian standard deviation σ_i, the peak center ν_i, the Lorentzian FWHM γ_i, and the amplitude C_i. For each dataset, I allowed the Lorentzian FWHM of the ^{85}Rb$(F = 3 \to F' = 2)$ vary within bounds, then fixed that value for the remaining peaks. This leaves a total of 1 peak $\times$ 4 + 7 peaks $\times$ 3 + 1 background = 26 free parameters for each dataset.

I calculated the total transition frequency given for each rubidium isotope in Table 5.11. The laser frequency axis origin is fixed by setting the ^{85}Rb$(F = 3 \to F' = 2)$ peak center -1475.8 MHz from the origin.

A representative rubidium ABF spectrum fit and associated residual is shown in Figure 5.15a and Figure 5.15b. Peak widths range from 350–500 MHz, significantly larger than expected. The residual shows general agreement to within 20%, with discrepancies as large as 300% in the peak-free regions. At lower laser powers (tens of μW), the discrepancy in peak height is more pronounced as the peaks are sharper. As we increase the laser power towards 9.8 mW, the broader peaks are more closely matched by a Voigt curve.

I simulated a rubidium spectrum with a laser power 50 μW corresponding to a laser intensity of 0.22 mW / cm^2 in Figure 5.16a. At this laser intensity, I calculate an on-resonance atom excitation rate of $R(\nu_0) \approx 1.3 \times 10^6$ s^{-1}. The lifetime from Table 5.10 is 27.8 ns, so this simulation satisfies the weak pumping requirement $R\tau << 1$.

I chose an oven temperature of 100 °C to constrain the angular distribution to the molecular flow regime. The peak widths are 20 MHz, a factor of twenty smaller Doppler broadening than the measured data. Note that above 100 °C, the Knudsen number for the rubidium oven is $K_n < 10$ and the Maxwellian and molecular flow treatment that we
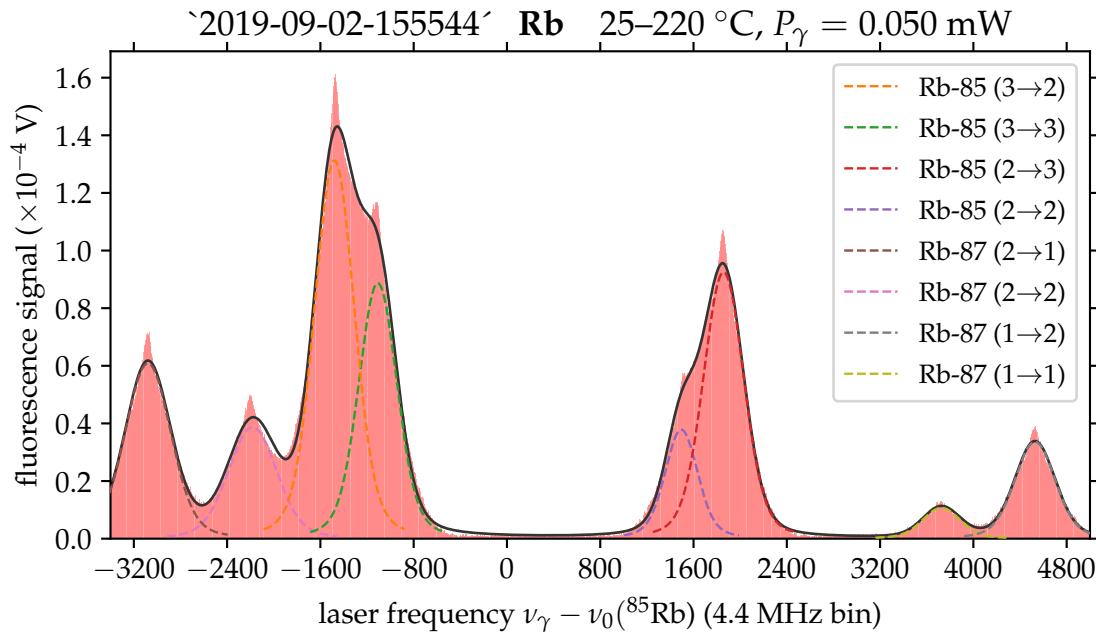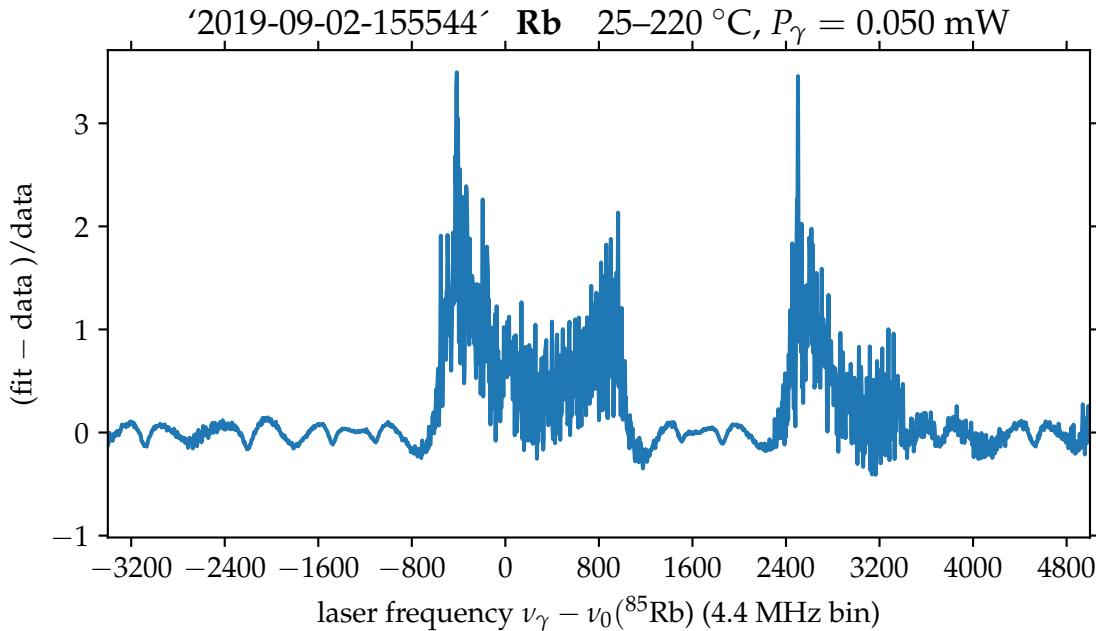
Figure 5.15: A measured rubidium ABF spectrum with a laser power of 50 μW. (a) Voigt lineshape fit to fluorescence signal vs. laser frequency (b) Fractional residual of the fit.
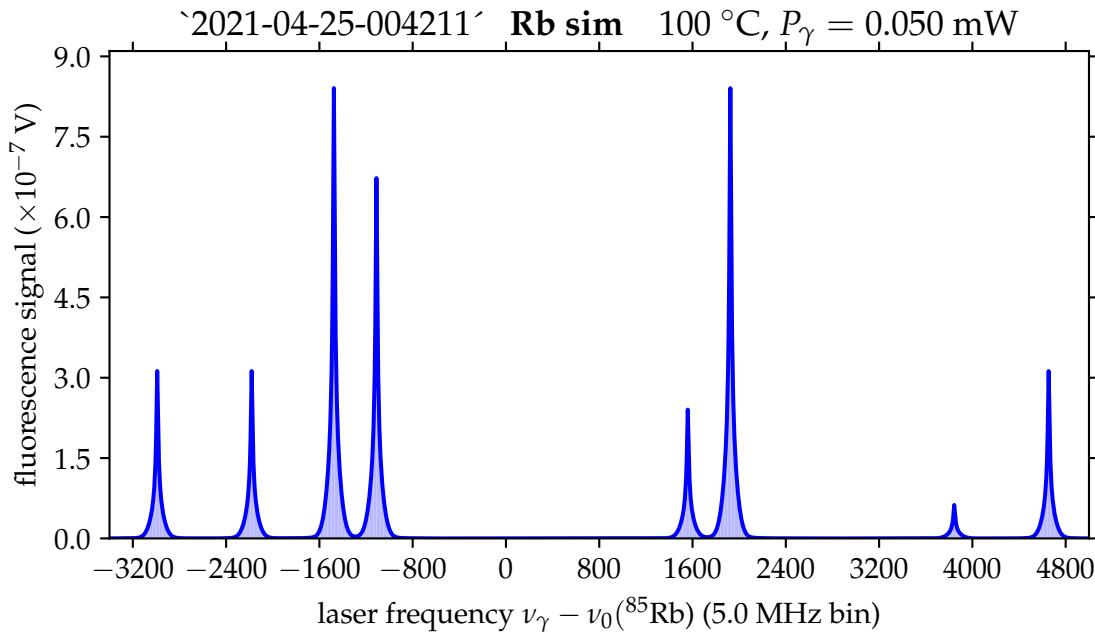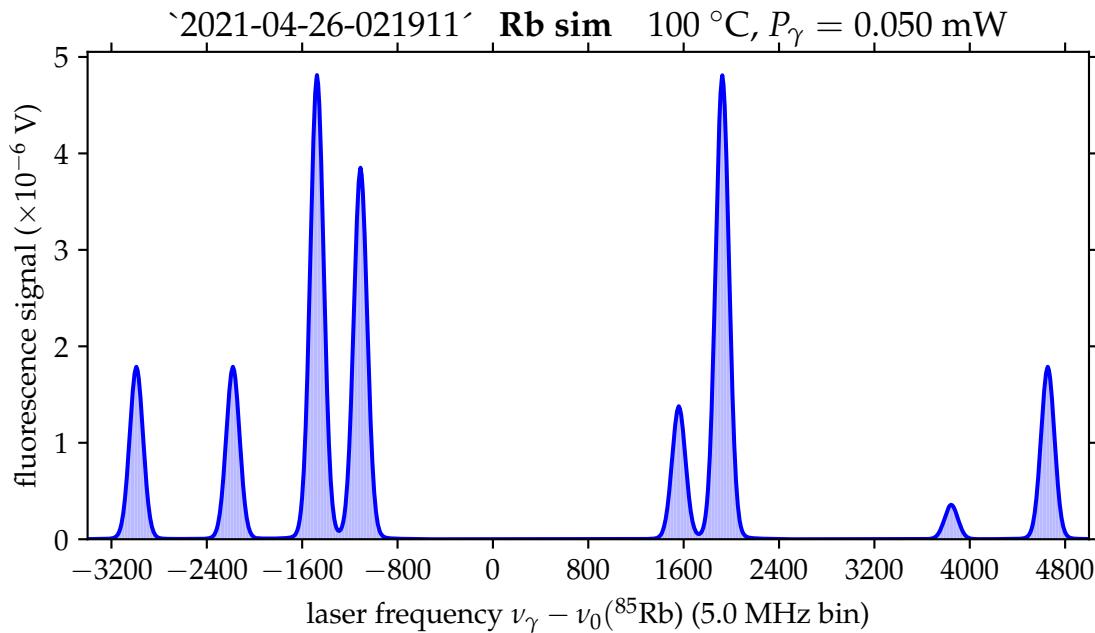
Figure 5.16: Simulated Rb fluorescence spectrum in the weak pumping limit. Laser power = 50 μW, laser radius = 2.7 mm. (a) Collimated beam with nozzle ratio $\gamma = 0.01$ (b) uncollimated beam with nozzle ratio $\gamma \to \infty$.

use becomes an increasingly crude approximation.

Figure 5.16a assumes the machined dimensions of the rubidium nozzle ratio of $\gamma = 0.01$. The range of oven temperatures in the measured data is reported in the range of 25–220 °C. Because the measured line profiles are wider than expected, it raises the nefarious possibility that a data run at ≈ 220 °C liquified some of the metallic rubidium. In this scenario, some of the rubidium could have "leaked" out of the oven crucible and some fraction of the way down the nozzle [144]. Indeed, I noted a colorless film on the surface of the oven crucible when troubleshooting the SAM ABF setup.

We can interpret the potential leakage distance of the rubidium as a free parameter of the nozzle ratio. For example, if the liquid traveled halfway down the nozzle, this would double the effective nozzle ratio. If the liquid traveled 100% down the nozzle, this would effectively be a completely uncollimated oven source ($\gamma \rightarrow \infty$).

To investigate the fluorescence for an uncollimated atomic beam, I repeated the simulation with the same oven and laser settings while setting the nozzle ratio to $\gamma \rightarrow \infty$. The full width of the transitions in Figure 5.16b is 130 MHz, about a third of the measured peak widths. This is closer to what is measured, though the peaks are still a factor of ≈ 3 narrower than the measured data.

Moving beyond the ABF simulation, I further investigate the effect of rubidium leakage with an oven temperature of 220 °C. I assume a modified rubidium nozzle ratio that allows nonzero $j(\theta)$ at $\theta \approx 20$ degrees, for example $\gamma' \approx 0.25$. With these parameters, I estimate a maximum broadening of 225 MHz using Equation 5.40. This is still significantly smaller than the measured spectrum peak widths, suggesting that additional factors are contributing to the broadening.

Nozzle-laser alignment, oven temperature, laser intensity, background light, and laser polarization differences between experiment and simulation are all possible contributing factors to the discrepancy in linewidth. The nozzle and laser axis are nominally perpendicular to each other. A misalignment would introduce larger angles between the atom

(a)
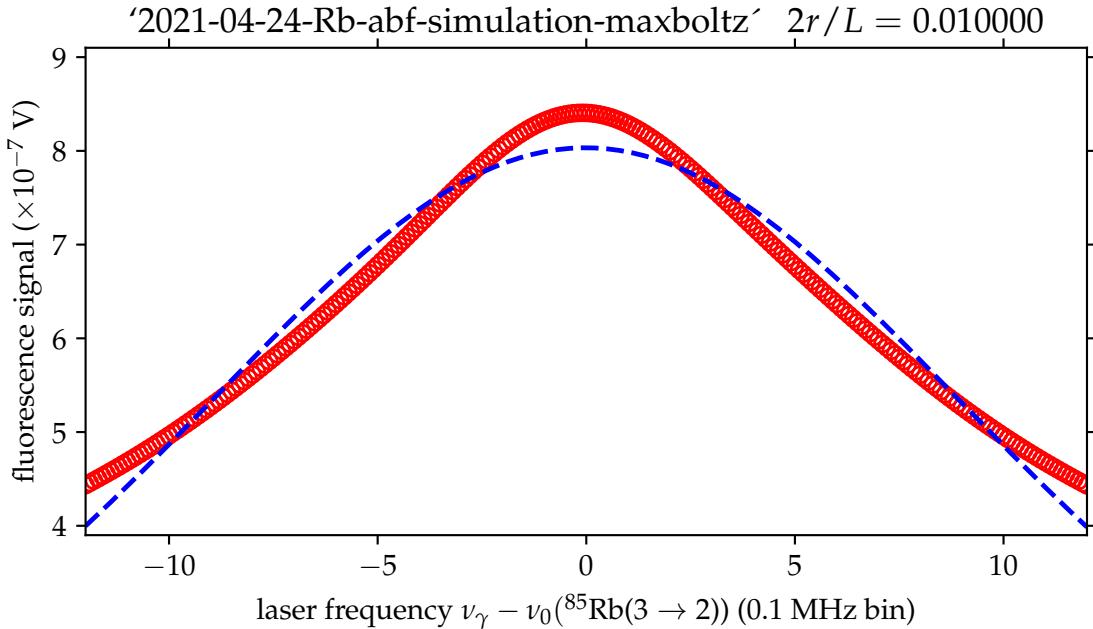
(b)
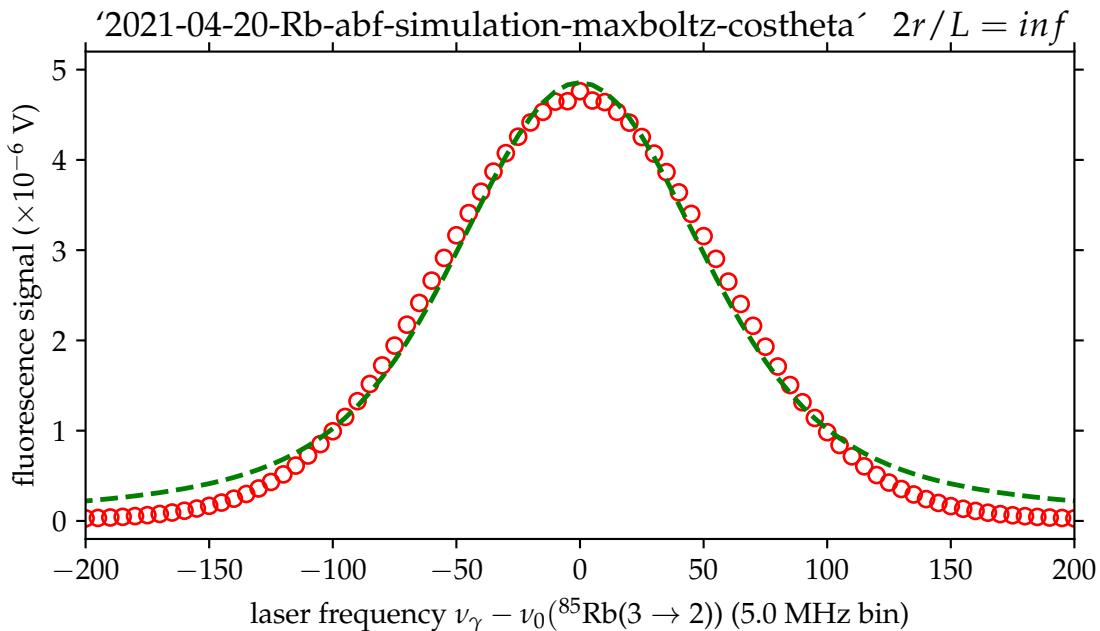
Figure 5.17: Voigt fits to simulated fluorescence (red circles) with collimated and uncollimated angular distributions. (a) Collimated distribution, corresponding to one of the peaks in Figure 5.16a (b) Uncollimated distribution, corresponding to one of the peaks in Figure 5.16b.
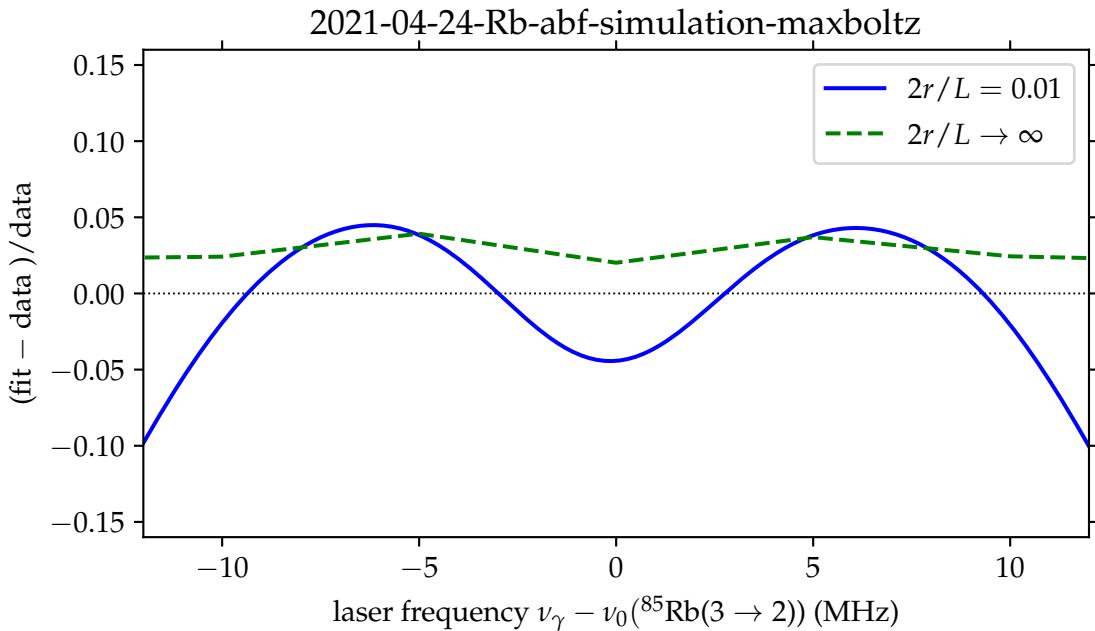
Figure 5.18: Residuals of fits to simulated Rb transitions in Figures 5.17b, 5.17a.

and laser photon trajectories (α) and increase Doppler broadening.

Assuming the excess broadening is purely due to a misalignment between the nozzle axis and laser axis, I calculate a misalignment of $\delta\theta \approx 20$ degrees would account for the observed peak widths.

We've seen that the measured rubidium transitions aren't completely captured by the Voigt lineshape. The true lineshape of a directed atomic beam is the generalized Doppler-broadened expression discussed in Section 5.3.5.

With the general expression for Doppler broadening, I simulated a single rubidium peak with a nozzle ratio $\gamma = 0.01$ (Figure 5.17a) and $\gamma \to \infty$ (Figure 5.17b). Then I fit Voigt profiles to the peaks. The oven and laser settings are identical to Figure 5.16a. The collimated transition is sharply peaked and required a finer laser scan step to capture the shape. From the fit, I find that the collimated linewidth is narrow with FWHM $= 23.88 + / - 0.10$ MHz and the uncollimated transition is broad with FWHM $= 120.69 \pm 0.79$ MHz.
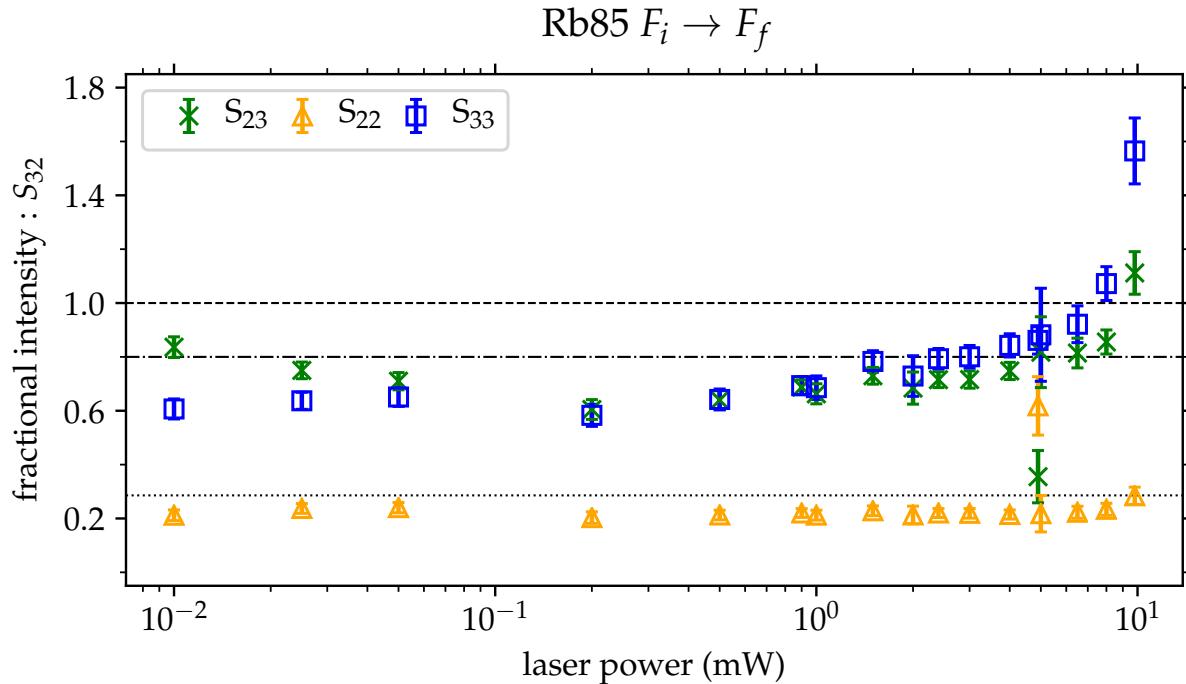
Figure 5.19: Measured total strength factor ratios $\mathbb{S}_{FF'} / \mathbb{S}_{32}$ of ^{85}Rb. The horizontal lines are expected total strength factor ratios for an unpolarized laser beam using the values from Table 5.4. Dashed line $\mathbb{S}_{23} / \mathbb{S}_{32} = 1$; dot-dashed line $\mathbb{S}_{33} / \mathbb{S}_{32} = 0.8$; dotted line $\mathbb{S}_{22} / \mathbb{S}_{32} = 0.2857$

The Voigt fit struggles to simultaneously reproduce the transition peak and tails of a fluorescence spectrum of a directed atomic beam. For the cases of a highly collimated and uncollimated oven nozzle, the transition peak and tails are underestimated in the former and overestimated in the latter. The peak fit mismatch is clearly seen in the fractional residuals for both angular distributions in Figure 5.18. The uncollimated fit is accurate to within approximately 4% within 10 MHz of the peak, owing to the transition broadness. Off scale, the fit is 10%-accurate within 75 MHz of the resonance but then diverges by more than +1000% as one moves further out. The collimated fit is accurate to within approximately 5% within 6 MHz of the resonance and then sharply converges to $\approx -100\%$ farther from resonance.

I integrated the fitted peak areas of the seventeen measured spectra to find the total strength factors and plotted $\mathbb{S}_{FF'} / \mathbb{S}_{32'}$ (Figure 5.19) and $\mathbb{S}_{FF'} / \mathbb{S}_{22'}$ (Figure 5.20) as a
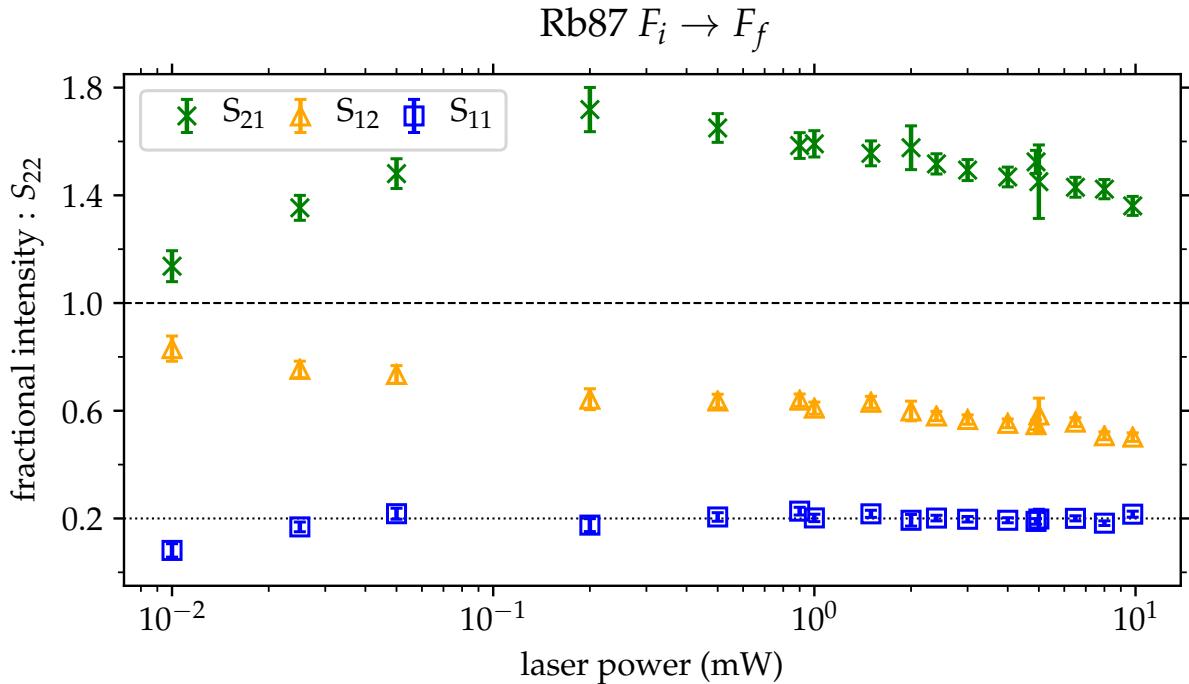
Figure 5.20: Measured total strength factor ratios $\mathbb{S}_{FF'} / \mathbb{S}_{22}$ of ^{87}Rb. The horizontal lines are expected total strength factor ratios for an unpolarized laser beam using the values from Table 5.4. Dashed line $\mathbb{S}_{21} / \mathbb{S}_{22} = 1$, equivalently $\mathbb{S}_{12} / \mathbb{S}_{22} = 1$; dotted line $\mathbb{S}_{11} / \mathbb{S}_{22} = 0.2$

function of laser power. The standard deviations are calculated from the uncertainty in the spectrum fits. These measured ratios are compared with the predicted strength factors for perfectly unpolarized light from Table 5.4.

In ^{85}Rb plot, the strength factors $\mathbb{S}_{23}$, $\mathbb{S}_{22}$, and $\mathbb{S}_{33}$ are divided by $\mathbb{S}_{32}$. Dashed horizontal lines are the predicted ratios $\mathbb{S}_{FF'}/\mathbb{S}_{32}$ which are calculated for the condition that the laser light is perfectly unpolarized. The plotted ratios are all smaller than expected up to laser powers of 1 mW, indicating that $\mathbb{S}_{32}$ is large. The intensities of the $F = 2 \rightarrow F' = 3$ and $F = 3 \rightarrow F' = 3$ transitions increase as the laser power is increased from 1–10 mW, inverting the relationship between the transitions at around 5 mW.

For the ^{87}Rb plot, I divide the strength factors $\mathbb{S}_{21}$, $\mathbb{S}_{12}$, and $\mathbb{S}_{11}$ by $\mathbb{S}_{22}$. The ratios $\mathbb{S}_{21}/\mathbb{S}_{22}$ and $\mathbb{S}_{12}/\mathbb{S}_{22}$ are predicted to be unity. Instead, the two ratios are anticorrelated, with $(2 \rightarrow 1)$ at higher intensity than expected and $(1 \rightarrow 2)$ is 20–40% lower than
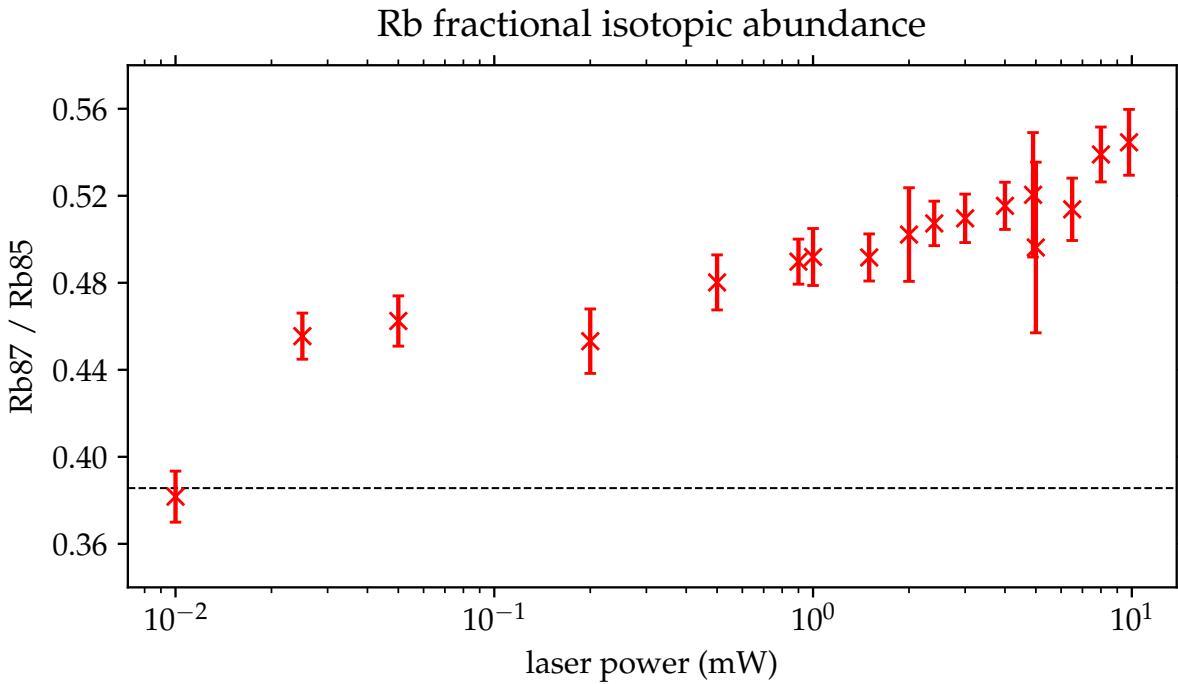
Figure 5.21: Measured abundance ratio of ^{87}Rb to ^{85}Rb. Dashed line = 0.3856 is the calculated ratio using the NIST database values listed in Table A5.

expected. Starting at a laser power of approximately 300 mW, $\mathbb{S}_{21}$ approaches unity logarithmically and $\mathbb{S}_{12}$ deviates by a similar amount. At the maximum power of 10 mW, $\mathbb{S}_{21} \approx 1.4$ and $\mathbb{S}_{21} \approx 0.5$

In both Figure 5.19 and Figure 5.20, the weakest strength factors are the least sensitive to laser power.

Similarly, I calculated the isotopic abundances and plotted the isotope ratio as a function of laser power in Figure 5.21. At the lowest laser power of 10 μW, the measured abundance ratio is consistent with the NIST value of ^{87}Rb / ^{85}Rb = 0.3856. The ratio increases to 0.46 when the laser power is increased to 30 μW. As the laser power is increased, the ratio increases approximately logarithmically to 0.53 at 10 mW.

These results suggest that there are laser power-correlated effects that influence both the strength factors and the isotopic ratios. From Table 5.9, the saturation intensity of rubidium is around 2 mW/cm^2. Assuming the laser radius is 0.27 cm [144], I expect the

Table 5.12: A selection of atomic transitions of the Ca ground state, $4s^2\ ^1S_0$. Intensity values and wavelengths from NIST. $^3P_1^o$ lifetime from Drozdowski et. al [154]. I = intensity. λ, ν = resonant wavelength, frequency. τ = lifetime. A = Einstein A-coefficient.

excited state	I (arb.)	λ (nm)	ν (THz)	τ (ns)	A (MHz)
$4s5p\,^1P_1{}^o$	140	272.1645	1101.1861	3.7×10^3	0.27
$4s4p\,^1P_1{}^o$	1000	422.6727	709.078235	4.5	220
$4s4p\,^3P_1{}^o$	500	657.2777	455.986217	$5.7(3)\times10^5$	0.0018

ratios to be insensitive to laser powers up to $\approx 200\ \mu$W. However, we see the surprising result that the ratios are affected by the laser power well below this threshold.

5.4.3 Simulations of a calcium spectrum

I simulated a calcium fluorescence spectrum of the $4s4p\,^1P_1^o$ transition (τ = 4.5 ns) in Figure 5.22. Atomic properties of this transition and several others are listed in Table 5.12.

I use the same oven nozzle dimensions (γ = 0.25) and laser settings (P_γ = 10 mW, r = 3.5 mm, I = 26 mW/cm^2) as the ytterbium simulation in Figure 5.14. The Ca simulation also satisfies the weak pumping limit requirement $R(\nu_\gamma, \vec{r})\tau_0 << 1$.

Calculated and literature transition frequencies are listed in Table 5.13. The transition intensity of the most abundant isotope, ^{40}Ca, will be more than an order of magnitude larger than the next most abundant isotope. The bottom panel is a log-scale plot that shows the smaller peaks.

The simulated calcium signal of the dominant peak is approximately 50 nV, several orders of magnitude lower than the ytterbium fluorescence. This is because of the relatively low vapor pressure of calcium. The oven temperature can be increased to compensate for the low vapor pressure, but this will also increase the Doppler broadening. Because of the smaller atomic mass, the calcium peaks will be significantly wider than the ytterbium peaks for equivalent oven temperatures.

We will use the Atomic Flux apparatus, pictured in Figure 5.23a, to measure the

(a)

`2021-04-22-Ca-abf´ **Ca sim** 250 °C, $P_\gamma = 10.000$ mW

(b)

`2021-04-22-Ca-abf´ **Ca sim** 250 °C, $P_\gamma = 10.000$ mW
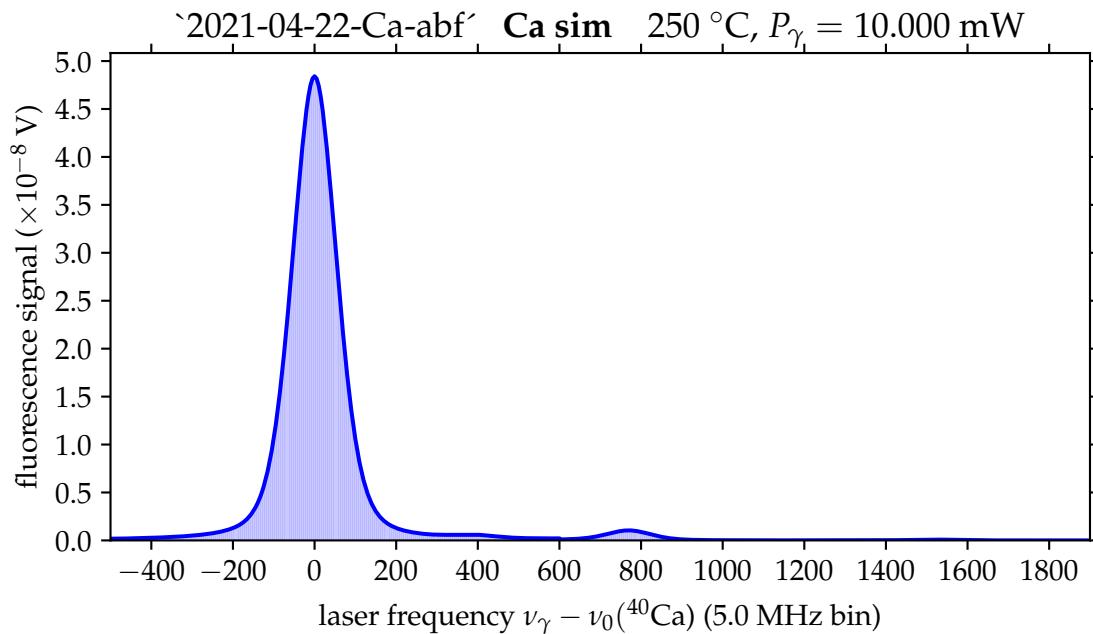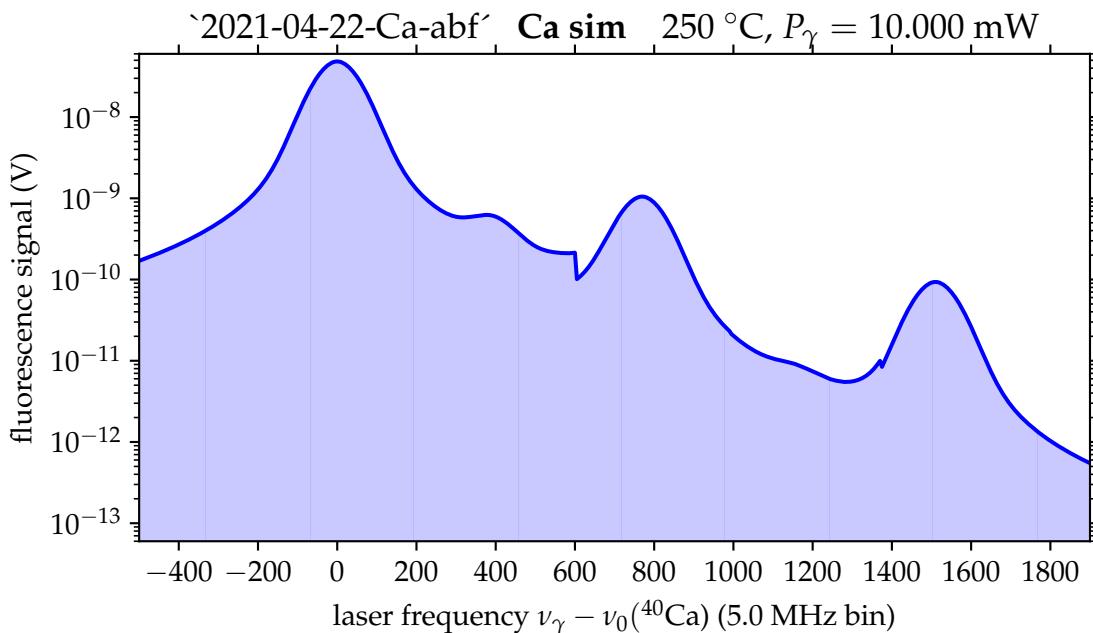
Figure 5.22: Simulated calcium fluorescence spectrum in the weak pumping limit. Log scale calcium fluorescence spectrum simulation to show the weaker transitions. The small signal discontinuities at 600 MHz and 1400 MHz are numerical artifacts.

Table 5.13: Calculated and literature transition frequencies (hyperfine + isotope shifts) with respect to the transition of ^{40}Ca, $\nu_0\left(^{40}\text{Ca}\right) = \nu\left(^1S_0 \rightarrow {}^1P_1^o\right) = 709.078$ THz. Reference value for $\nu\left(^{46}\text{Ca}\right)$ from [155], all others from [156].

A	$4s\,^1S_0 \rightarrow 4p\,^1P_1$			$\nu - \nu_0\,(^{40}\text{Ca})$ [MHz]	
	F	$\rightarrow$	F'	Calculated	Reference
42	0	$\rightarrow$	1	+393.5	+393.1(4)
43	9/2	$\rightarrow$	9/2	+555.3	
43	7/2	$\rightarrow$	7/2	+634.2	+611.8[a] +610.7(6)[a]
43	5/2	$\rightarrow$	5/2	+676.2	
44	0	$\rightarrow$	1	+773.8	+773.8(2)
46	0	$\rightarrow$	1	+1159.8	+1159.8(7)
48	0	$\rightarrow$	1	+1513.0	+1513.1(4)

[a] "center of gravity" values, which is the average of the hyperfine peak frequencies weighted by their relative isotopic abundances.

atomic beam fluorescence of calcium. I expect to improve the ABF measurement sensitivity by a factor of 100 or more with the addition of a light collection setup (discussed in Section 5.5.2). The light collection gain will amplify the calcium APD signal to approximately 10 μV, a readily measurable fluorescence signal. Detecting the next most abundant isotope ^{44}Ca peak, on the order of 1 nV without light collection, would be a powerful demonstration of the ABF measurement sensitivity.

The oven temperature and laser power can also be cautiously increased to boost the fluorescence signal. At an oven temperature of 250 °C, the calcium linewidth is already significantly Doppler-broadened with FWHM = 200 MHz. However, ^{40}Ca is approximately 400 MHz from the neighboring ^{42}Ca peak, so one can trade off the additional broadening if a higher fluorescence signal is needed. The simulated laser intensity is 10 mW / $\pi(0.35$ cm$)^2$ = 26 mW / cm^2. This could be increased by up to a factor of 2 and still remain below the saturation intensity.

5.5 Suggested improvements to measurement technique

5.5.1 Tracking laser polarization and magnetic field

Competing properties of the ABF measurement could be driving the hyperfine transition strength factor dependence on pumping laser power, for example the ^{85}Rb $\mathbb{S}_{32}$ transition in Section 5.4.2.

The weak pumping threshold from Equation 5.23 is approximately 200 μW, assuming a pumping laser radius of 0.27 cm. The four lowest-power ratios in of each of the Figures 5.19, 5.20, and 5.21 range from 10–200 μW . With a perfectly unpolarized laser beam and negligible magnetic fields, I expect the rubidium transition ratios to be insensitive to laser powers below the 200 μW threshold. Instead, we see laser power-correlated trends in the data starting at the 10–50 μW range.

The 795 nm Ti:Sapphire laser output is linearly polarized. The output is fiber-coupled to the ABF chamber with an optical fiber that is not polarization-maintaining, so we assume the pumping laser light is perfectly unpolarized. It may be that some residual polarization is present after fiber coupling. A significant degree of linear or circular polarization would modify the magnetic sublevel transition amplitudes. My strength factor calculations are only valid for an unpolarized laser beam.

It's also possible that the ambient magnetic field, which we take to be on the scale of Earth's field (≈ 60 μT), is significantly affecting the transitions. However, the literature suggests that transition probability dependence on external magnetic fields are not significant below ≈ 1 mT [157].

Several improvements can be made to future ABF measurements. To control magnetic field-correlated effects, we can screen external magnetic fields and measure the magnetic field uniformity in the fluorescence region, e.g. with fluxgates. We can measure the pumping laser polarization to verify our assumptions about the strength factor calculations and filter out any residual linear or circular polarization, if necessary.
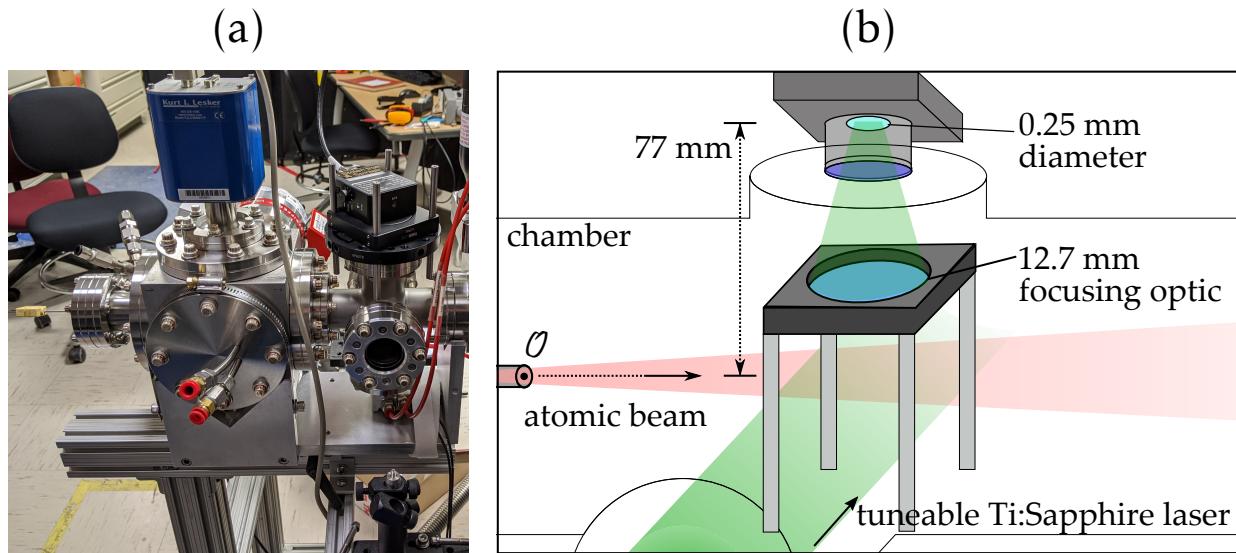
Figure 5.23: (a) the Atomic Flux apparatus. (b) Schematic of in-vacuum light collection setup (not to scale).

In the case of the rubidium experiment, the majority of the measured ratios do not satisfy the weak pumping condition $R\tau << 1$. Our next ABF experiment should concentrate data collection at low laser intensities in the weak pumping regime. For the case of a 0.27 cm laser diameter, most of the fluorescence measurements could be made below 200 μW. We observed laser power-correlated effects as low 50 μW corresponding to 0.22 mW/cm^2. It would be very interesting to see more measured ratios at below this intensity.

5.5.2 Increasing the signal size with light collection

A limiting factor on the photon-atom yield η is the solid angle coverage of the photodetector. I calculate a solid angle of ≈ 33 μrad (Figure 5.12) in the center of the fluorescence region of the Atomic Flux apparatus with our 0.5 mm diameter active surface APD positioned 77 mm (Table 5.7) away.

To improve the solid angle, I considered two scenarios. In the first scenario, the APD can be moved closer to the fluorescence using a smaller vacuum chamber. If we replace
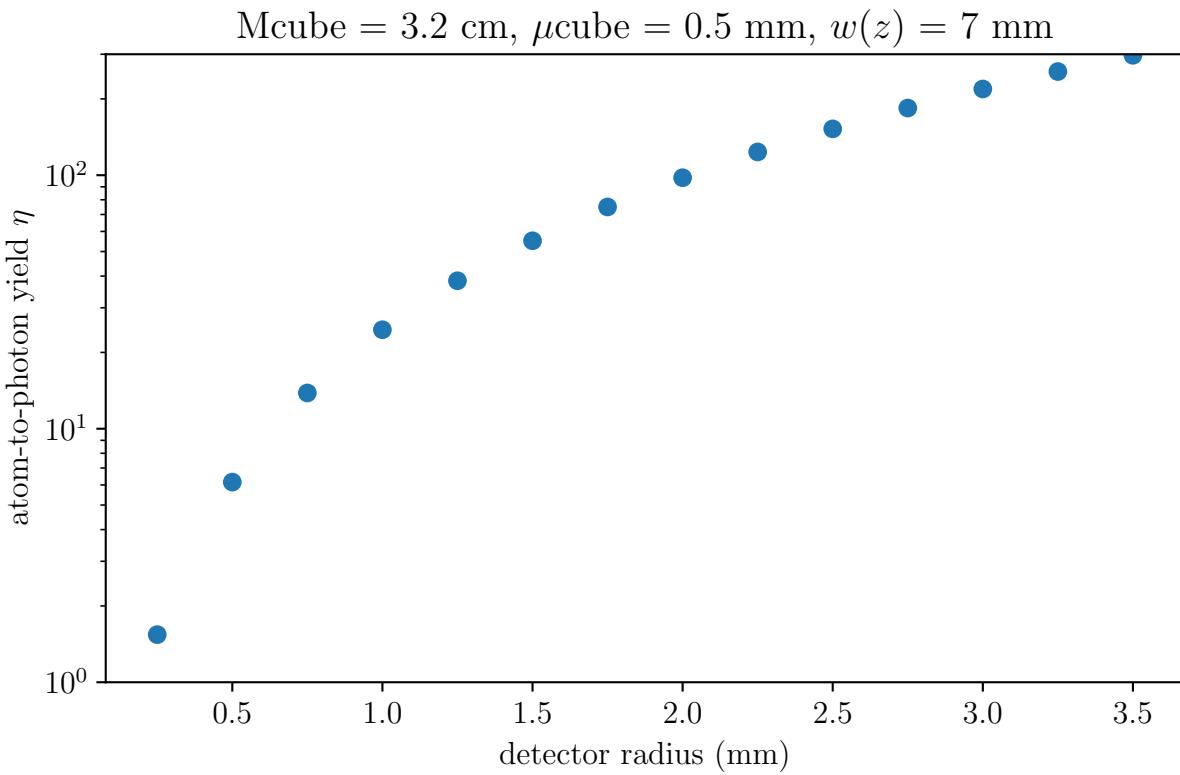
Figure 5.24: The atom-to-photon yield if we use a light-focusing lens, or, equivalently, increase the detector area. The laser width is 7 mm in this calculation. Assuming only rays perpendicular to the detector surface are focused onto the detector, we get maximum light collections for a detector radius of half the laser width, or 3.5 mm.

our 2.75" window vacuum cross with a commercial 1.33" setup, the distance from the fluorescence center to the APD would be reduced by approximately half, or $d_y \approx 30$ mm. I estimate a factor of approximately 5 increase in the solid angle by reducing the APD distance in this manner.

The more promising scenario is to place a light collection lens in the vacuum chamber between the fluorescence region and the APD. I designed an in-vacuum light collection setup, shown in Figure 5.23b. The lens is a 1/2" biconvex lens with a 20 mm focal distance that is mounted to a 16 mm cage plate. The cage plate is mounted to the bottom vacuum flange using threaded rods. The distance of the light collection lens to the center of the fluorescence volume is adjustable so the position can be optimized for maximum signal
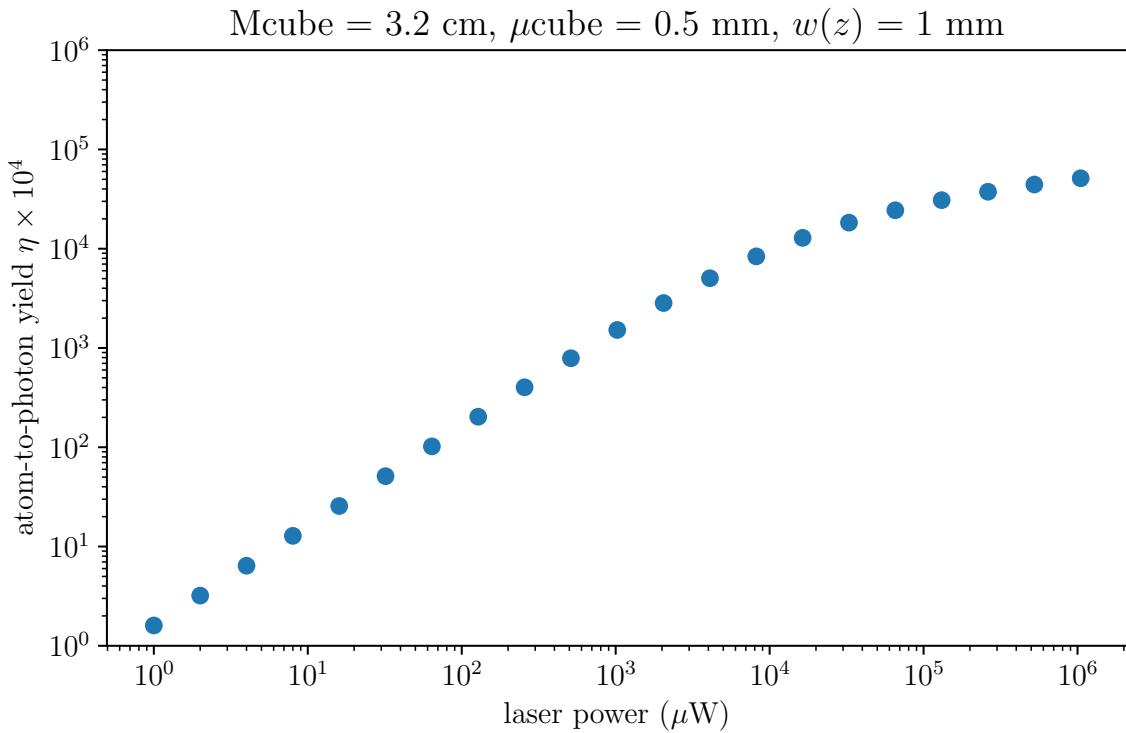
Figure 5.25: The atom-to-photon yield as we vary the laser beam power. μcube side length is 0.5 mm, megacube side length is 3.2 cm. $\eta_{\mathrm{max}} = 1.523$ for $w = 7$ mm.

on the photodetector active surface.

The photon-eta yield increases with increasing solid angle coverage of the photodetector (Equations 5.42 and 5.50). To estimate the gain in the solid angle, I make the assumption that all fluorescence photons reaching the light collection lens surface is focused directly onto the photodetector. At the center of the fluorescence volume I calculate an enhanced solid angle of 78 mrad, a factor of 2400 higher than a setup without light collection.

Since η is a volume integral, the solid angle enhancement will vary by fluorescence location. To simulate the enhancement in η I approximate the light collection gain by increasing the photodetector area. A plot of the atom-to-photon yield as we increase the detector area is shown in Figure 5.24. From the plot I estimate that the light-collecting lens will increase fluorescence sensitivity by at least a factor of 100.
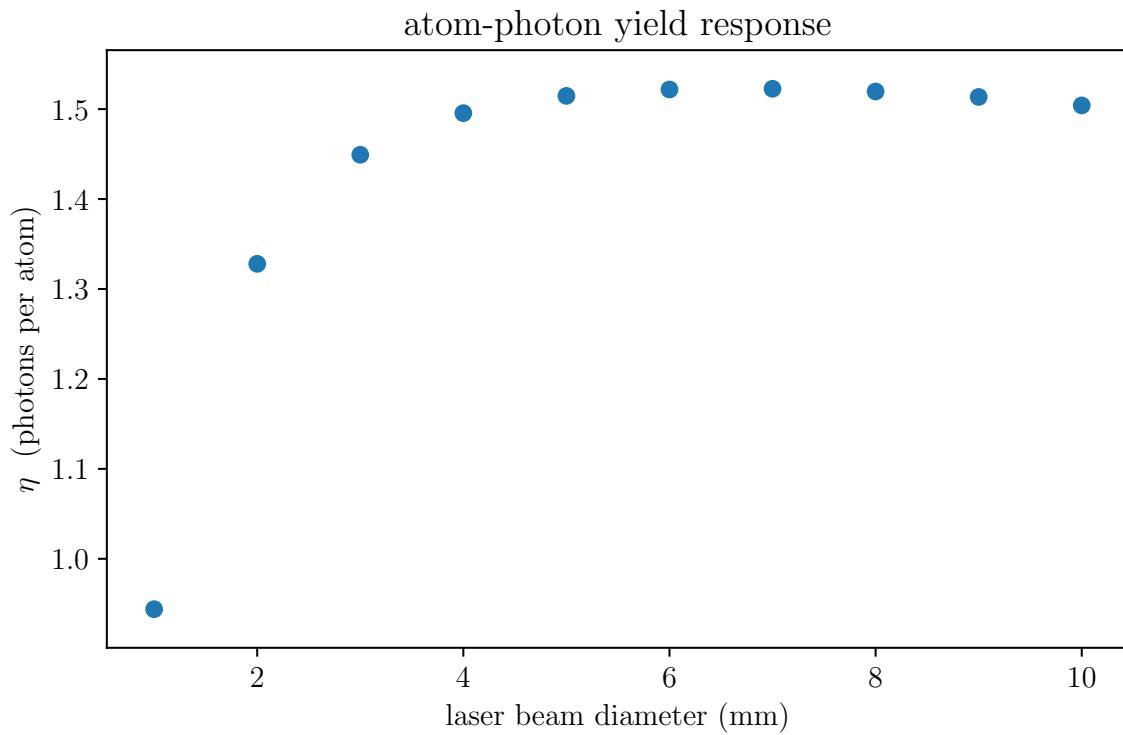
Figure 5.26: The atom photon yield as we vary the size of the laser beam width. μcube side length is 0.5 mm, megacube side length is 3.2 cm. $\eta_{\mathrm{max}} = 1.523$ for $w = 7$ mm.

5.5.3 Increasing the signal size with a calibrated pumping laser and atomic oven

I studied η dependence on a range of laser power and beam widths for a simulated ytterbium ABF measurement with oven nozzle ratio $\gamma = 0.25$. In Figure 5.25 I plotted η for laser powers ranging from 1 μW–1 W, keeping the laser width fixed at 1 mm. I also plotted the photon-atom yield for laser widths ranging from 1 mm–10 mm, keeping the power fixed in Figure 5.26. I expect that the trends in these figures are also relevant for the calcium ABF measurement, which will use the same oven nozzle ratio and a $^1\mathrm{P}^o_1$ atomic transition.

These plots show that the laser width can be calibrated to maximize η for a given laser intensity. The simulated data depends on the atomic distribution $j(\theta)$. We've seen from the rubidium analysis in Section 5.4.2 that our understanding of the atomic distribution

is limited, so the simulated optimized laser width should only be used as a starting point.

A careful calibration of the ABF measurement parameters is especially important for calcium, which is expected to have a very small fluorescence signal. The photon-atom yield depends on the overlap between the atomic angular distribution and the pumping laser. The atomic angular distribution is controlled by the oven nozzle ratio. The laser beam power and diameter should be chosen to maximize η while satisfying the weak pumping requirement.

CHAPTER 6

PRECISION GAMMA-RAY INTENSITY MEASUREMENTS

As a fellow of the Nuclear Science and Security Consortium (NSSC), I had the opportunity to research nuclear security applications in nuclear physics. I went to Lawrence Livermore National Laboratory (LLNL) to develop a new precision gamma-ray spectroscopy experiment from January 1 2019 to March 29 2019.

6.1 Introduction

6.1.1 Gamma-ray spectroscopy and stockpile stewardship

The United States and other nuclear powers minimize nuclear weapon threats by negotiating treaties that limit nuclear weapon stockpile inventory and ban intrusive weapons testing, including above-ground and underground detonation. These treaties have mechanisms that provide members with rights to limited inspections each other's stockpiles and validate the number of stockpiled warheads.

Fissile material occasionally falls under the investigative purview of nuclear security, for example in the case of stockpile verification, recent weapons testing, or weapons trafficking. The size and nature of a sample can be determined by measuring the intensity of the radiation of the daughter isotopes in the sample. A high precision radiation measurement can provide insight on the composition and timescale of the original material the sample is derived from.

Gamma-ray spectroscopy is used to characterize nuclear decay spectra to derive nuclear properties from isotopes of interest. One facet of gamma-ray spectroscopy is studying the possible decay paths an excited nucleus can take in order to decay to a more stable nucleus. This is particularly useful application for nuclear forensics and nuclear security, as the number of fissions that occurred in a nuclear sample can be quantified by mea-

suring the intensity of the photons, or gamma-rays, emitted by the nuclei of the fission daughter isotopes.

6.1.2 Long-lived fission isotopes

Nuclear induced fission can be initiated by impinging a neutron on a ^{235}U nucleus. To a lesser effect, fission can also be initiated by other uranium isotopes and some thorium and plutonium isotopes. We'll limit the scope of this discussion to a ^{235}U nucleus.

After the incoming neutron is captured by the ^{235}U, an excited state of ^{236}U is formed. The ^{236}U nucleus will primarily fission into two unstable isotopes of mass number $A_1 \approx 90$ and $A_2 \approx 145$, roughly a 2:3 ratio. $236 - A_1 - A_2$ free neutrons will be ejected as well. The process is statistical so the number of nucleons in each isotope daughter fluctuates.

Figure 6.1 is a simplified example of a simplified $A = 147$ decay chain of a nuclear fission isotope. ^{147}Ce is the first ^{236}U descendent in this decay chain. ^{147}Ce has a half-life of 56 seconds and a relative proportion of decays from its parent nucleus, or independent yield (IY), of 1.9%. The daughter is neutron-rich and will decay to a more stable nucleus by converting one of its neutrons to a proton via the weak force:

$$^{A}_{Z}X \rightarrow \, ^{A}_{Z+1}X' + e^- + \overline{\nu_e} \, , \tag{6.1}$$

where

$^{A}_{Z}X$ is the original nucleus with A nucleons and Z protons,

$^{A}_{Z+1}X'$ is the product nucleus with A nucleons and $Z+1$ protons,

e^- is an electron, and

$\overline{\nu_e}$ is an electron antineutrino.

5/2-

$^{147}_{58}$Ce$_{89}$

β-

Q = 3430 keV

I_β

$T_{1/2}$ = 56.4 s

5.6   5/2-   467.5 keV

5.6   5/2-   362 keV

37   5/2+   0 keV

$^{147}_{59}$Pr$_{88}$

β-

Q = 2697 keV

I_β

$T_{1/2}$ = 13.4 min

10.2   3/2+   1310.8 keV

23.4   3/2+   792.5 keV

0   5/2-   127.9 keV

2.5   5/2-   0 keV

$^{147}_{60}$Nd$_{87}$

β-

Q = 896.0 keV

I_β

$T_{1/2}$ = 10.98 d

5/2+, 7/2+
685.9 keV

2.43

5/2+, 7/2+
531 keV

15.4

5/2+
91.1 keV

80.2

7/2+
0 keV

≤ 0.15

$^{147}_{61}$Pm$_{86}$

β-

Q = 224.6 keV

$T_{1/2}$ = 2.62 yr
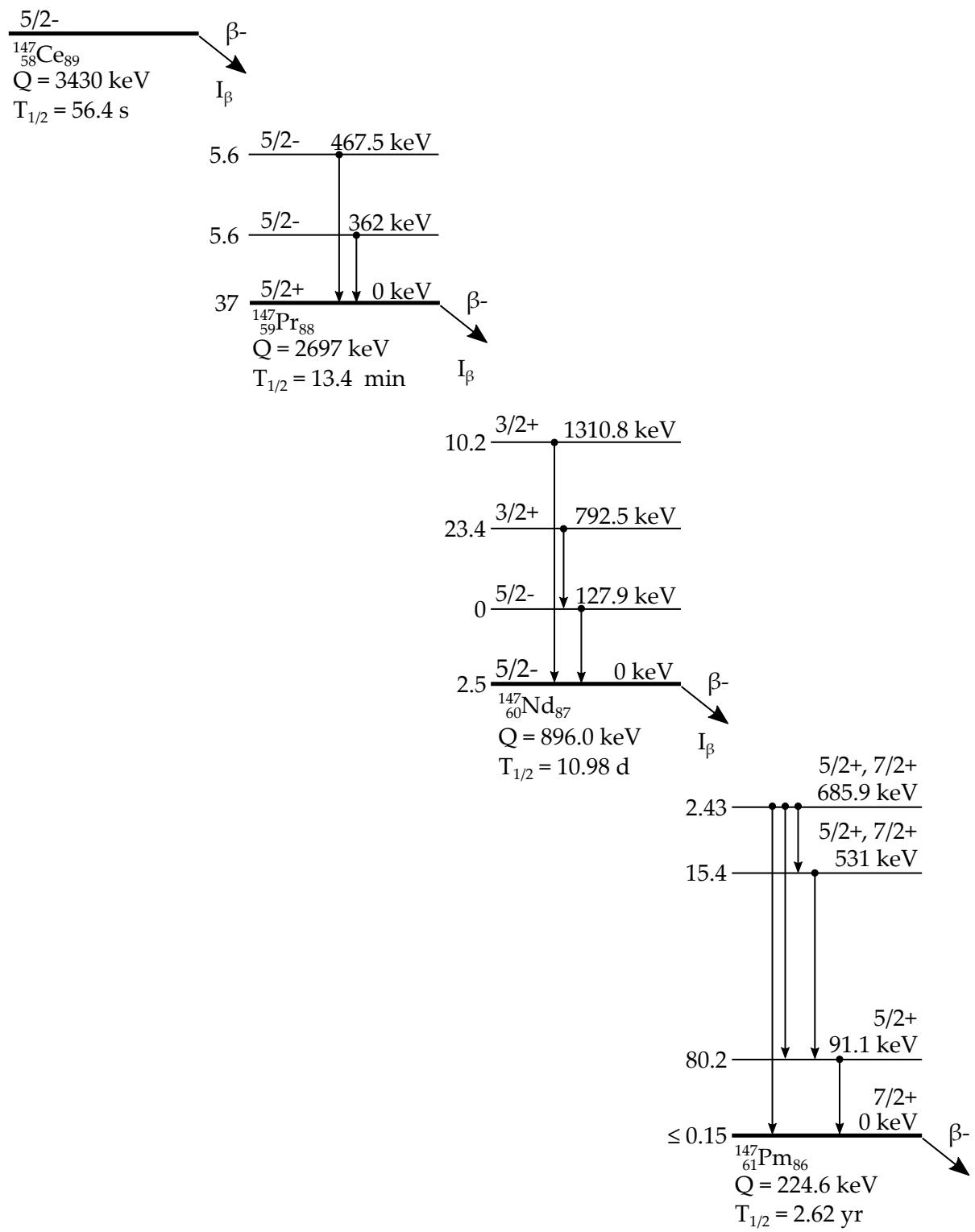
Figure 6.1:   A simplified example of one of the possible ^{236}U decay chains. Data from [158].

174

Table 6.1: Gamma-ray decays from a selection of long-lived fission isotopes. δ(BR) = branching ratio uncertainty.

isotope	γ-ray (keV)	Q-value (keV)	δ(BR) (%)	half-life (days)	Ref.
^{95}Zr	724.192 ± 0.004	1123.6 ± 1.8	0.50	64.03	[159]
^{95}Zr	756.725 ± 0.012	1123.6 ± 1.8	0.40	64.03	[159]
^{156}Eu	811.77 ± 0.05	2449 ± 5	8.2	15.19	[160]
^{147}Nd	531.016 ± 0.022	896.0 ± 0.9	2.2	10.98	[161]
^{147}Nd	91.105 ± 0.002	896.0 ± 0.9	2.5	10.98	[161]
^{144}Ce	133.515 ± 0.002	318.7 ± 0.8	1.7	284.91	[162]
^{161}Tb	74.56669 ± 0.00006	593.0 ± 1.3	4.9	6.89	[163]
^{127}Sb	685.5 ± 0.5	1581 ± 5	5.6	3.85	[164]
^{111}Ag	342.13 ± 0.02	1036.8 ± 1.4	4.9	7.45	[165]

^{147}Ce beta-decays to a new isotope with a longer half-life. After several beta-decays down the chain in Figure 6.1, the half-life approaches an order of hours or days. This is long enough that a sample of such material could be transported from a scene to a laboratory for spectroscopy analysis. These isotopes are known as long-lived fission isotopes.

In order to usefully quantify the number of nuclear fissions that occurred in a sample of decayed material, an uncertainty of 2% or better in the branching ratio of the isotope of interest is desired. Table 6.1 shows a representative list of long-lived fission isotopes. The primary beta-decay branching ratios of ^{95}Zr are known to sub-percent precision. The branching ratio uncertainties of the other isotopes are relatively large, ranging from 1.7% to 8.2%. The reasons for the relatively imprecise measurements of these isotopes' decay properties vary. It may be due to using impure samples, having insufficient counting statistics, or internal conversion competing with β^- decay. Sometimes the sources are difficult to fabricate, for example if the accelerator used to produce the source cannot deliver a sufficiently pure and/or intense beam. The substrate the isotope is collected on may attenuate the signal if the gamma-ray of interest is low-energy.

A precision β^- branching ratio measurement for long-lived fission isotopes is being developed at Lawrence Livermore National Laboratory. The new method uses thin samples produced at the Californium Rare Isotope Breeder Upgrade (CARIBU) and a nearly
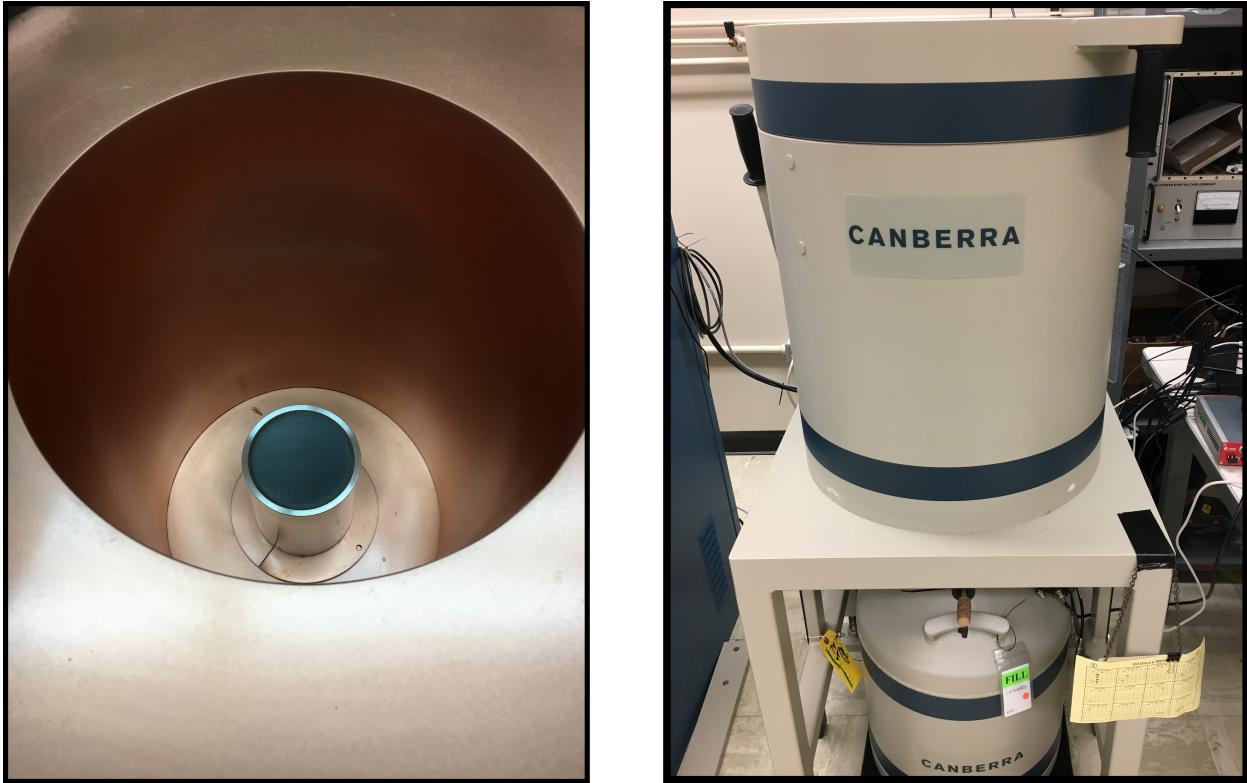
Figure 6.2: LLNL gamma-ray detector setup.

100%-efficient 4π beta counter. A proof-of-principle measurement was performed using a high purity germanium (HPGe) detector meticulously calibrated at Texas A&M University [166, 167].

In 2017 they measured the two primary branching ratios of ^{95}Zr [168]. The two primary β^- decays, $\gamma_1(\text{keV}) = 724.2$ and $\gamma_2(\text{keV}) = 756.7$, were measured with 0.6% precision, in agreement with the literature values shown in Table 6.1 [169].

The Zr measurement validated the new sample preparation, calibrated gamma-ray detection, and β^--coincidence measurement. The goal of the LLNL gamma-ray spectroscopy group is to improve the branching ratio measurements of additional long-lived fission isotopes such as those listed in Table 6.1 to better than 1 % precision.

For the next phase of the long-lived fission isotope gamma-ray spectroscopy experiment, the isotope sample will be measured in a new detection system at LLNL, shown in Figure 6.2. The newly-assembled detector is a broad energy germanium (BEGe) de-
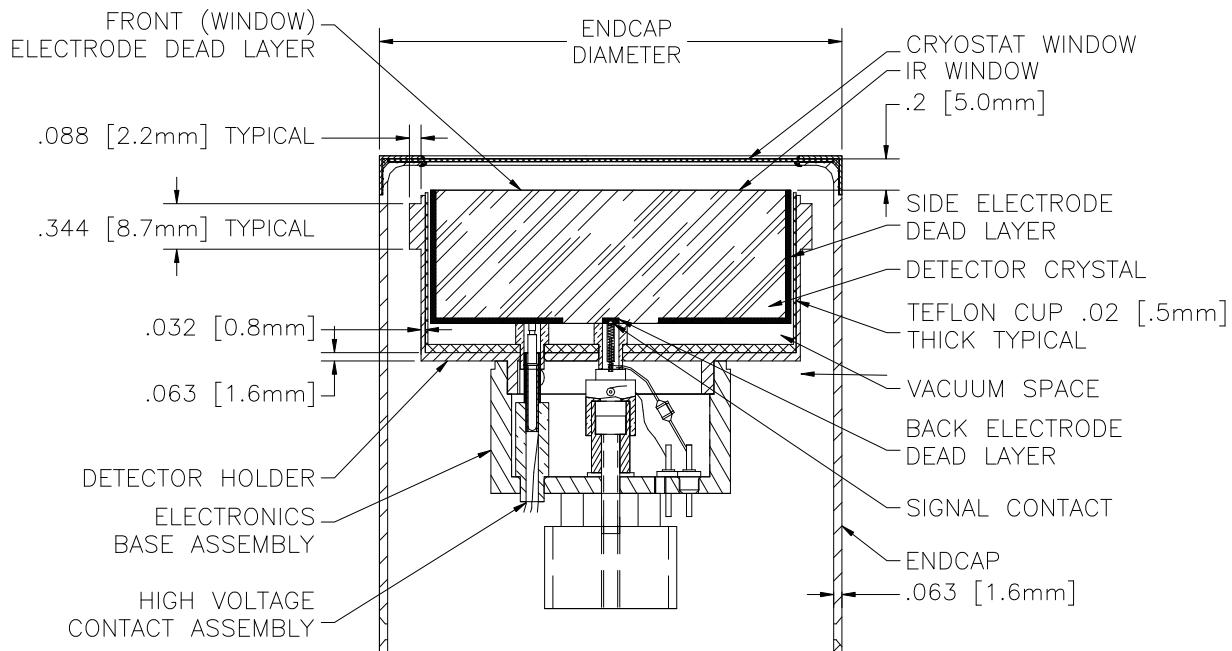
Figure 6.3: A schematic of the LLNL BEGe detector. Model by Canberra, Mirion Technologies. Used with permission.

tector (schematic shown in Figure 6.3), so-named for its sensitivity to gamma-rays in the range ≈ 0.01–3 MeV. This model has a particularly thin front layer of inactive, or "dead" germanium of about 0.3 μm, more than an order of magnitude thinner than a standard HPGe design. Unlike standard "coaxial" detectors, the BEGe does not have a significant bullet-hole design on the bottom surface of the detector, which preserves the volume of active germanium and simplifies modeling.

The LLNL BEGe detector is mounted on an ultra low-background preamplifier (Canberra iPA) inside a lead shield with an additional inner layer of high purity copper (Canberra 777 series), shown in Figure 6.2. The shield blocks both external effects like cosmic radiation and emission from the lead lining itself. Data acquisition is handled by a CAEN DT5780 dual digital multichannel analyzer.

6.1.3   HPGe calibration

In order to measure the intensity of a gamma-ray, the efficiency of the detector must be known at that gamma-ray energy. Efficiencies at several energies are typically provided by the manufacturer, and in many cases interpolation is sufficient to calculate reasonable gamma-ray intensities of well-understood isotopes. However, high precision measurements of hard-to-measure fission isotopes require correspondingly well-calibrated detectors. A detector can be calibrated by using a gamma-ray source of a known intensity and deriving the efficiency. We're interested in the efficiency of the full gamma-ray deposition, or the full-energy peak efficiency [170]. This ignores gamma-rays that partially deposit, or scatter, in the detector. Standardized samples of reference sources, such as ^{152}Eu, ^{241}Am, and ^{60}Co, are readily available off the shelf.

The full-energy peak efficiency of a detector at gamma-ray energy E_γ, or $\epsilon(E_\gamma)$, is given by the following:

$$\epsilon_\gamma = \frac{R}{S \times P_\gamma}, \tag{6.2}$$

$$R = NT^{-1}, \tag{6.3}$$

$$S = A_0 \exp(-\lambda t), \tag{6.4}$$

where

$R\ \left[\mathrm{s}^{-1}\right]$ is the full-energy peak count rate,

T [s] is the detector live time,

N [dimensionless] is the detector count,

S [Bq] is the source strength,

A_0 [Bq] is the source initial activity,

$\lambda\ \left[\mathrm{s}^{-1}\right]$ is the source decay constant, and

P_γ is the probability that the source emits a photon at E_γ, i.e. its branching ratio.

For this experiment it's useful to use the half-life rather than the decay constant. The
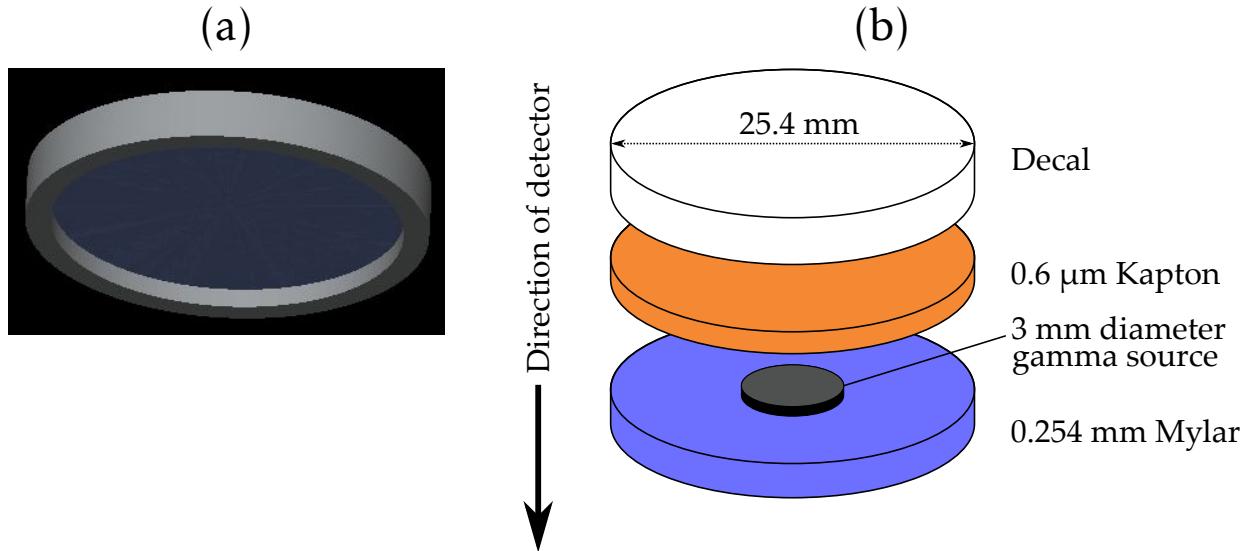
Figure 6.4: (a) Geant4 model of the gamma-ray source. (b) Expanded schematic of the gamma ray source geometry (not to scale).

two share an inverse relationship:

$$t_{1/2} = \frac{\ln 2}{\lambda}, \tag{6.5}$$

where $t_{1/2}$ [s] is the half-life. We measured the absolute gamma-ray detection efficiency of the detector using a set of ten standardized sources with gamma-ray emission spanning 14 keV–1.4 MeV. The sources are calibrated isotopes with well-understood gamma-ray branching ratios are high-intensity and well-measured at useful energies. The geometry is a Type M "scatterless" geometry (shown in Figure 6.4).

Each sample has a thin 3 mm diameter deposition of an isotope whose primary gamma-ray branching ratio is measured to sub-percent level, except for ^{241}Am, whose primary gamma-ray branching ratio ($\gamma = 59.54$ keV) is measured to within 1.1%. The initial activities of the samples are measured to within 3% by the manufacturer (Eckert & Ziegler).

To measure the efficiency spectrum of the detector, the samples were mounted on a plastic holder as shown in Figure 6.5. The holder is similar to a stackable CD holder. The plastic holder has a tray design for loading samples at different heights. There is no base so it can be centered over the detector.
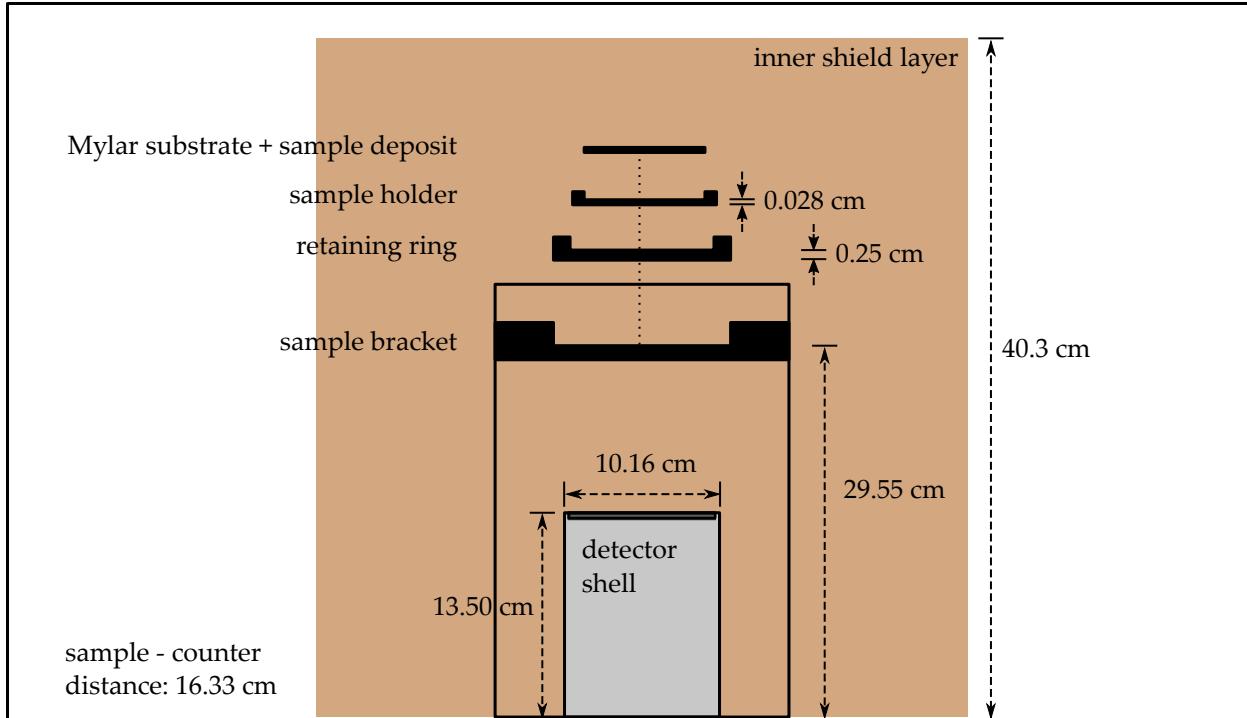
Figure 6.5: Schematic of detector-sample configuration.

We took a suite of gamma-ray source measurements for two different sample-source distances. Measuring efficiencies at two different distances offers a robust way to benchmark a numerical model of the detector system, since an on-axis displacement would result in an efficiency change due solely to geometry. For each measurement, we placed the sample at one of two distances and collected statistics until enough counts were in the peaks corresponding to the primary β^- decay branching ratio energies of the sample. An example of a measured spectrum of a ^{60}Co sources is shown in Figure 6.6.

The gamma-ray collection efficiency of the detector scales as d^{-2}, where d is the distance from the source to the front surface of the detector. The sample should be close enough to collect enough statistics in a reasonable amount of time ($\approx$ hours to days) but far enough away to avoid pileup effects on the detector. Our goal is to achieve a measurement uncertainty of better than 0.1%, corresponding to a minimum detector peak count N:

$$\frac{\sigma_{\text{Poisson}}}{N} = \frac{\sqrt{N}}{N} \leq 10^{-3} \rightarrow N \geq 10^6 \tag{6.6}$$
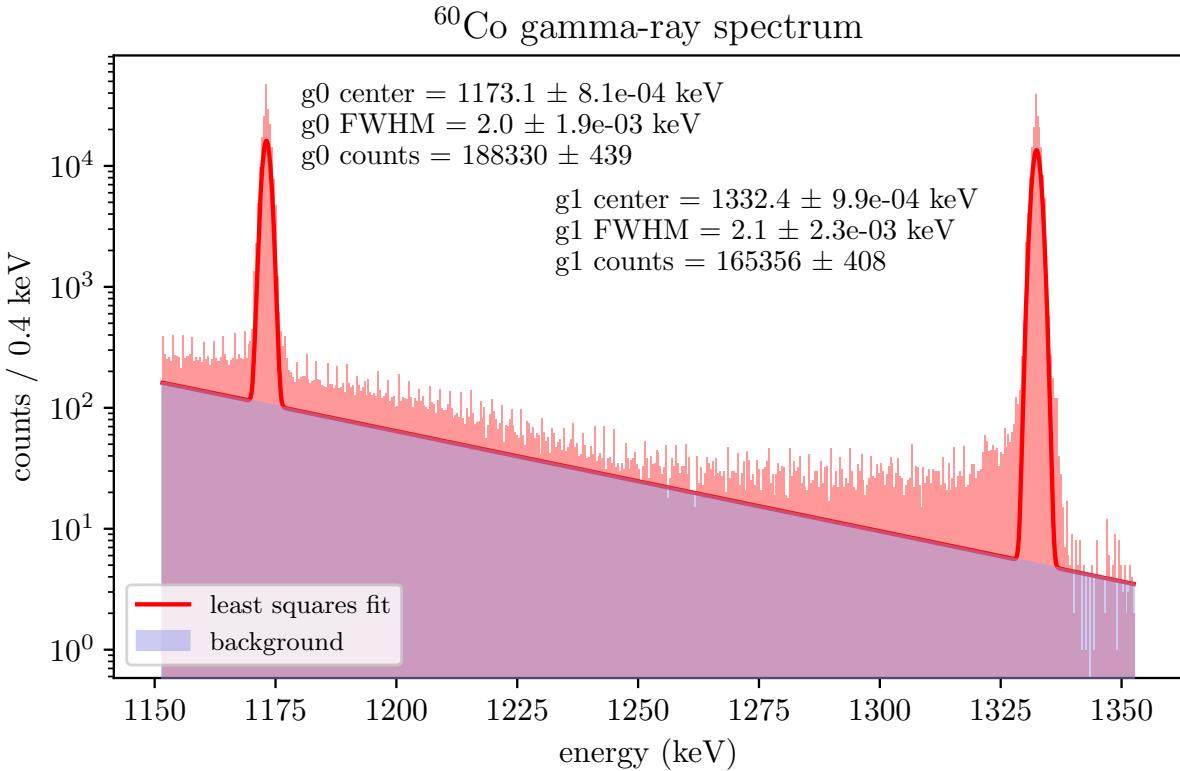
Figure 6.6: Fits for the 1173 keV and 1332 keV ^{60}Co gamma-ray spectrum.

For the LLNL HPGe detector, this corresponds to a detector-sample distance of 10–15 mm.

The measured efficiencies and their uncertainties of the HPGe detector are shown in Figure 6.7a and Figure 6.7b. The shape is characteristic of many efficiency spectra of semiconductor detectors. There is a logarithmic increasing efficiency from low energy (< 100keV), a peak at the "knee" at around 90 keV, and a logarithmic decreasing efficiency from the knee onwards. The effective bandwidth of the detector is about 2 MeV.

6.1.4 Monte Carlo simulation

I started with a boilerplate model of a HPGe detector within a background shield in Geant4. The original model generates a number of gamma-rays at an energy specified by the user with random initial vectors from a point source. An example of a detector measurement of a gamma source is shown in Figure 6.8. To clearly view the gamma-ray
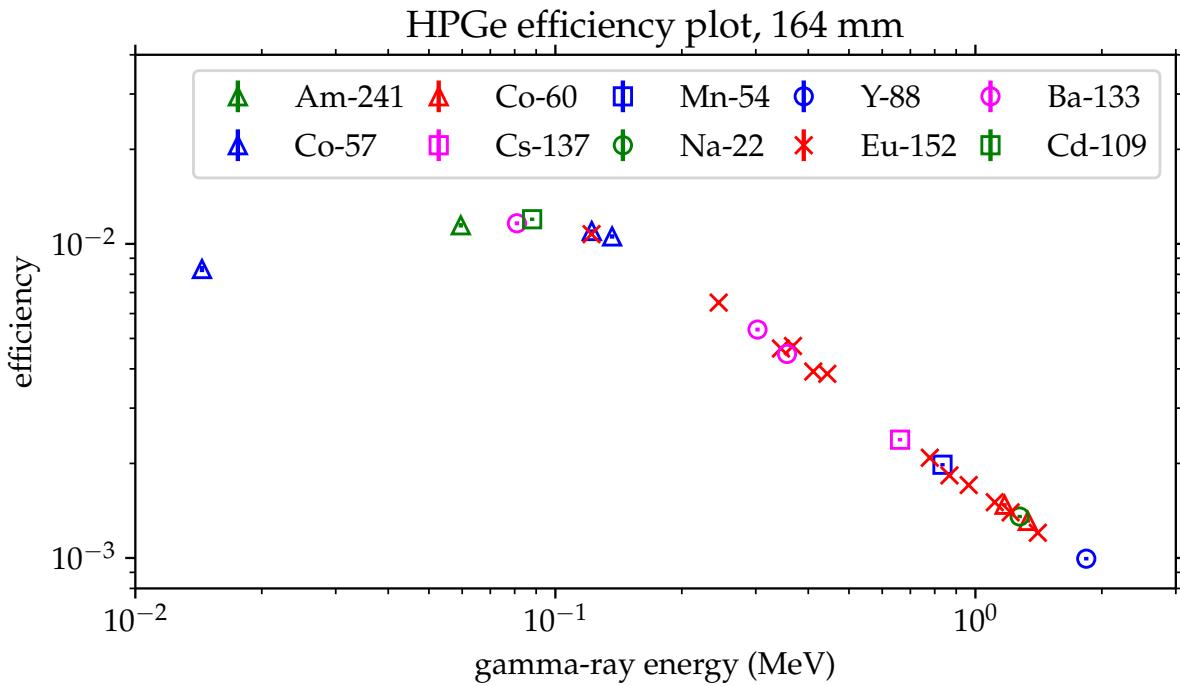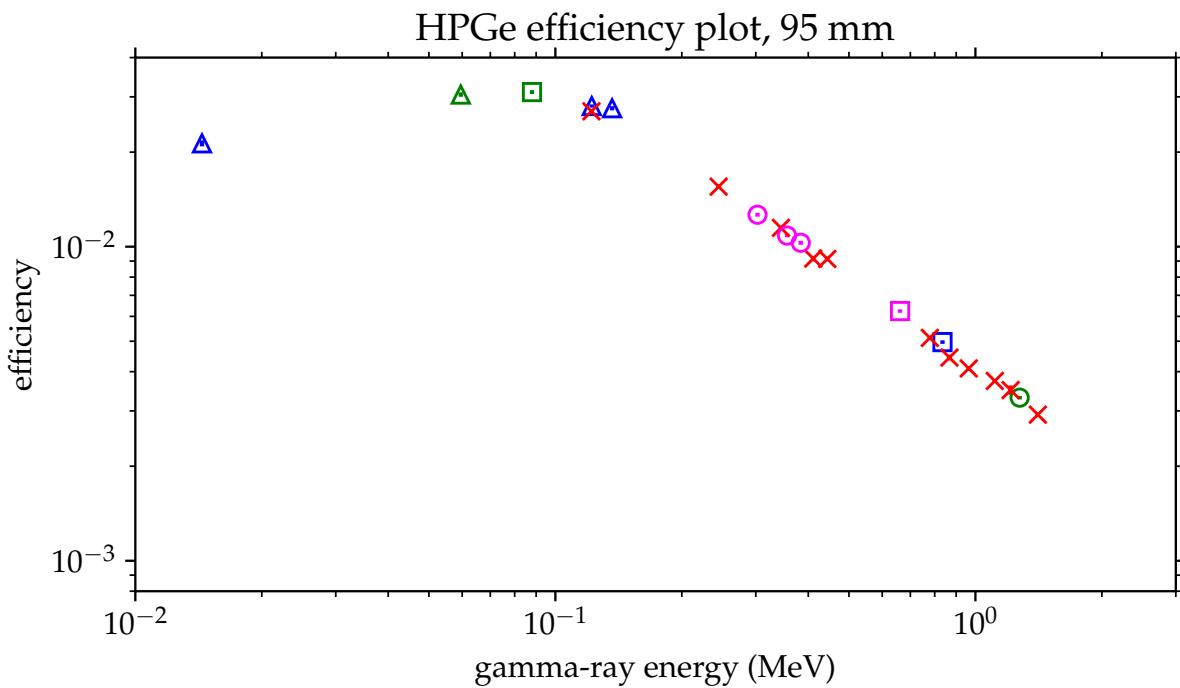
Figure 6.7: (a) Efficiency plot of HPGe with calibrated gamma sources and a sample-detector distance of 164 mm. (b) Efficiency plot of HPGe with a sample-detector distance of 95 mm
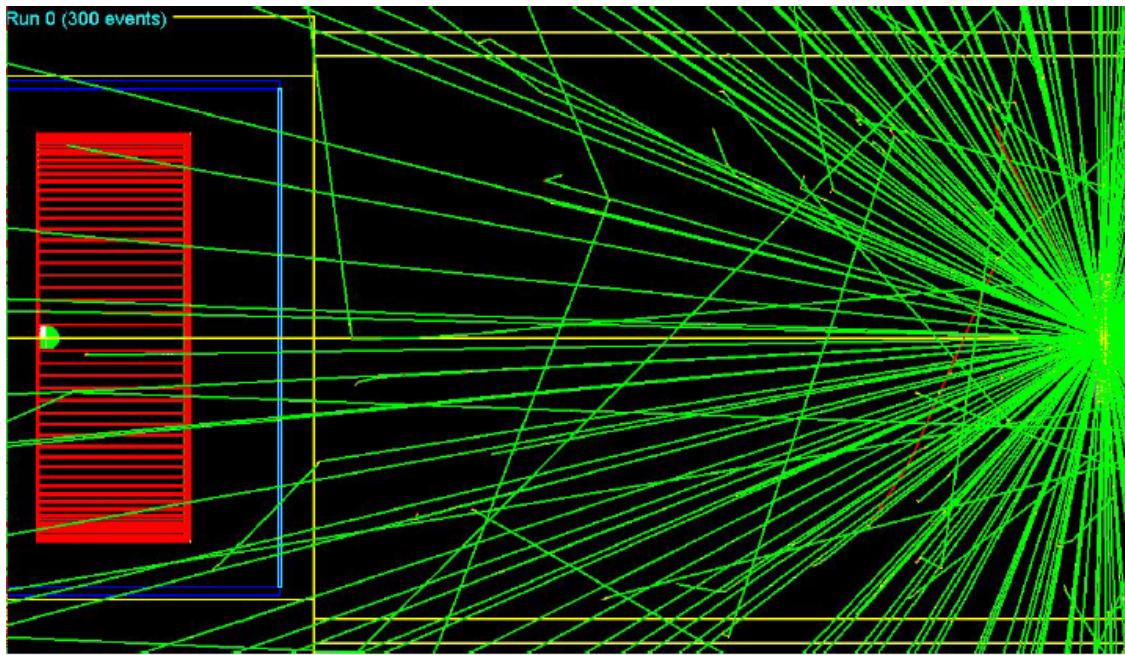
Figure 6.8: A simulation of 1 MeV gamma-rays emitting from a source (right side of graphic) above the LLNL HPGe detector (left side of graphic).

trajectories, I only simulated three hundred gamma-rays. For a simulation that I use for analysis, one million or more gamma-rays are simulated. The number of gamma-rays that are deposited in the active germanium volume of the detector are recorded. A histogram is generated with a call to the scientific coding toolkit ROOT. The histogram bin height is scaled to the number of hits in the detector.

The boilerplate detector model includes the active germanium, the front deadlayer, the shell, the detector window, and the shield. It models a more conventional detector with a bullet-hole design and a standard ($\approx 600 \ \mu$m) front deadlayer thickness. The source is a point source with no source holder geometry.

To improve the accuracy of the simulation, I updated the detector-source model to more closely match the new LLNL system. To start, I modified the detector model to match the parameters provided by the manufacturer for our new detector as shown in Figure 6.3. Over the course of the practicum, I updated the model to include additional components modify existing designs. I note a selections of improvements I made to the
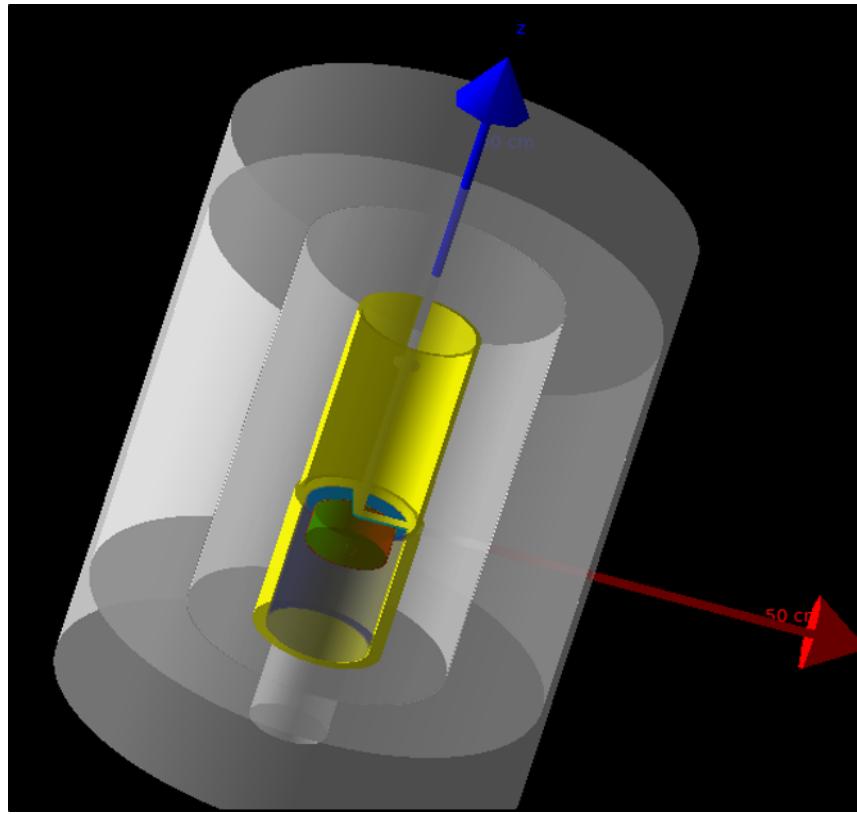
Figure 6.9: Snapshot of Geant4 model of the HPGe detector and background shield.

Monte Carlo model in the following list:

- reduce the bullet-hole depth

- add side deadlayers and back deadlayers which can be varied independently of the front deadlayer

- add an infrared film between the detector window and germanium crystal

- add a plastic concentric sample holder

- create a Type-M source geometry with the layers shown in Figure 6.4

- modify the gamma-ray source to be a uniform planar circular distribution consistent with the geometry shown in Figure 6.4

184
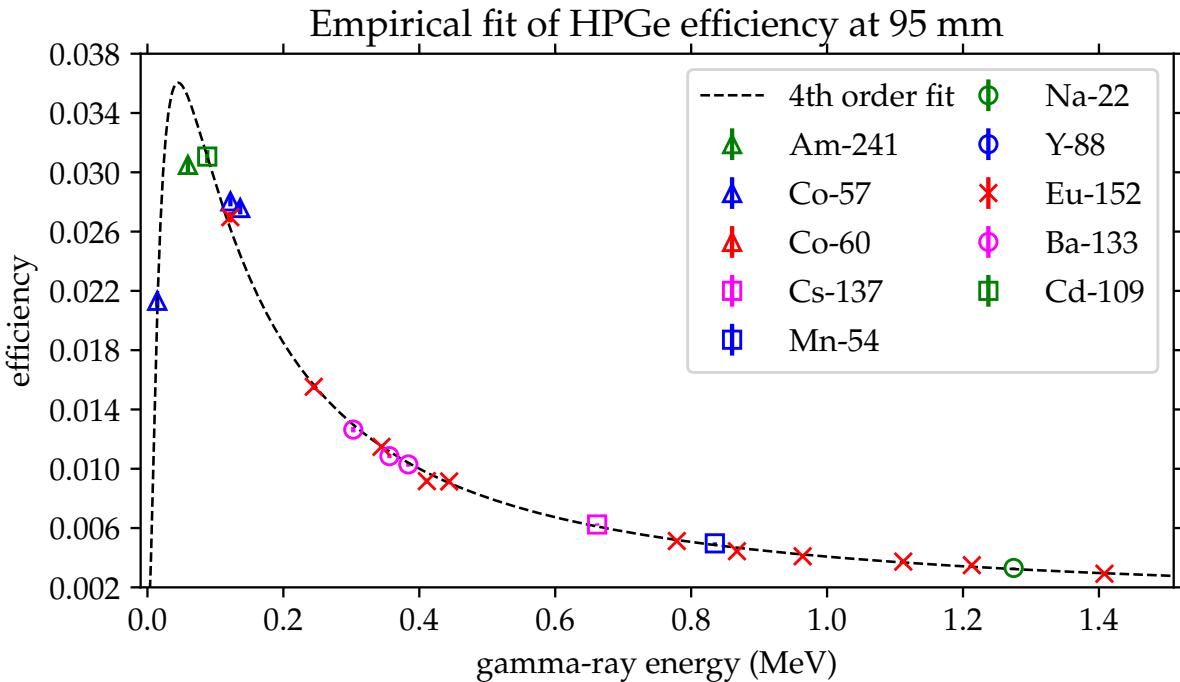
Figure 6.10: Fourth-order empirical fit to the measured efficiencies of a suite of calibrated gamma sources at a distance of 95 mm.

In Figure 6.9 I show a snapshot of the updated BEGe Geant4 Monte Carlo model. The detector is surrounded by three layers of shielding (in gray) and a concentric sample holder (in yellow). The germanium crystal is shaded in green and is surrounded by a vacuum-sealed shell. The front of the shell, which faces the gamma source, is a carbon composite cryostat window.

6.2 Results and analysis

I wrote a Bash script that wraps the single-energy efficiency calculation code and repeats the simulation for a range of energies. The efficiency calculated for each iteration is stored in a separate array. I wrote a ROOT script that fills a histogram with the stored efficiencies after the energy range is swept. The bin heights are scaled by their efficiencies. The simulated efficiencies for a given energy is the number of gamma-rays deposited in the detector divided by the number of generated gamma-rays.
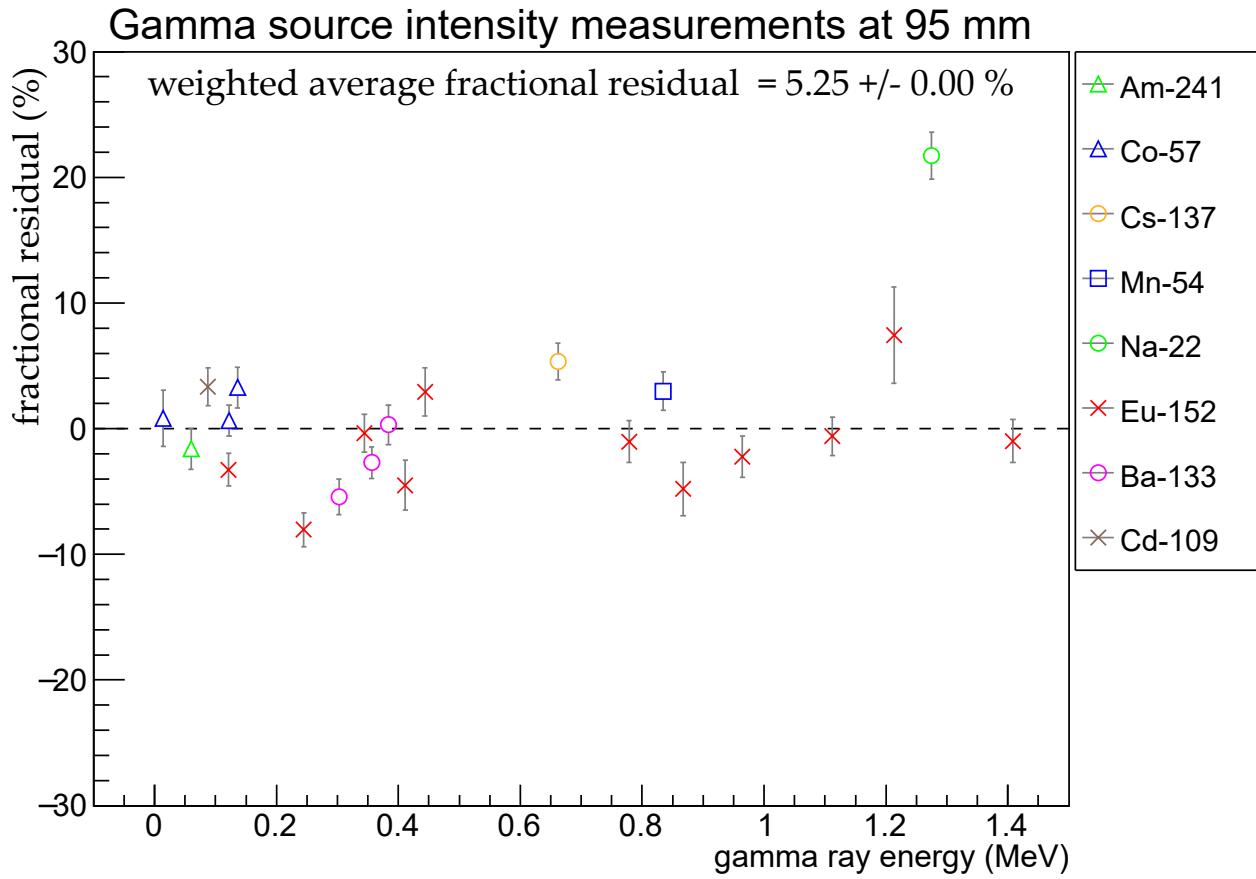
Figure 6.11: Fractional residual efficiency scatterplot with sample-detector distance of 95 mm.

One way to model HPGe detector efficiency is to fit an empirical function to the measured efficiencies. The form of the empirical fit is given by the following:

$$\log \epsilon(E) = a_0 + \sum_{n=1} a_n (\log(E))^n$$

A fourth-order fit usually fits the data well. For non-precision measurements, this is enough to characterize the HPGe efficiency curve.

The empirical fit is also useful for comparing simulated efficiencies to measured efficiencies. I wrote a ROOT script that fits a fourth-order curve to a 2D array of simulated efficiency vs. energy. The function is minimized with the FMINUIT routine. In Figure 6.10 the empirical curve is drawn and the measured data is plotted over it.

Our calibration method follows the procedure of Helmer et. al for calibrating an HPGe detector to the sub-percent level over an energy range of 3.5 MeV [166, 167].
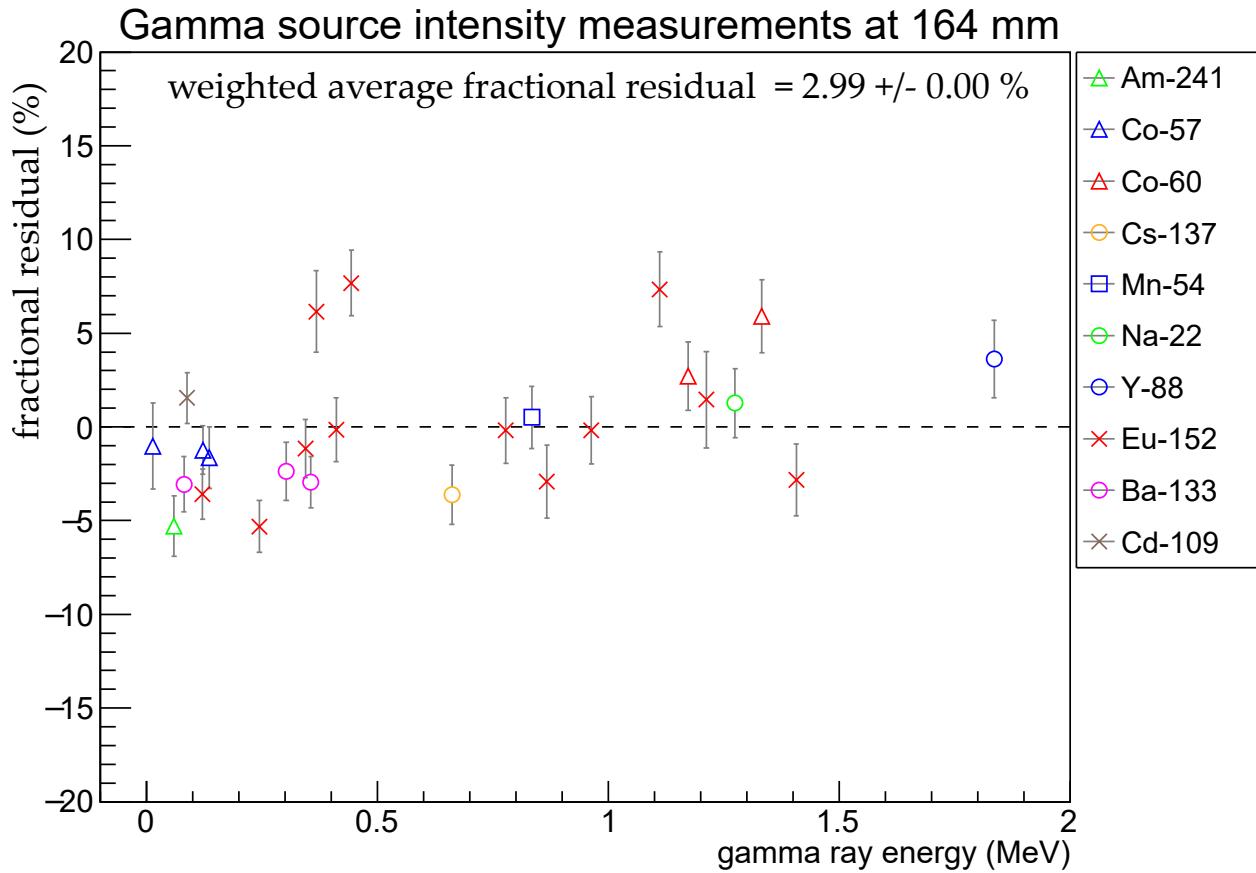
Figure 6.12: Fractional residual efficiency scatterplot with sample-detector distance of 164 mm.

The HPGe detector Monte Carlo calibration is characterized by comparing the fractional residual between the measured efficiency and the simulated efficiency of the detector at a given energy. The fractional residual of the detector efficiency at a gamma-ray of energy E_γ, or $R(E_\gamma)$, is given by the following:

$$R(E_\gamma) = \frac{\epsilon^m(E_\gamma) - \epsilon^s(E_\gamma)}{\epsilon^s(E_\gamma)} \, , \tag{6.7}$$

where $\epsilon^m(E_\gamma)$ is the measured efficiency and $\epsilon^s(E_\gamma)$ is the simulated efficiency of the detector at gamma-ray energy E_γ.

Figure 6.11 and Figure 6.12 are plots of measured vs. simulated efficiencies over an energy range of 2 MeV for a sample-source distance of 95 mm and 164 mm, respectively. Weighted-average fractional residuals are quoted for each plot. We obtain a 5.25% av-

Figure 6.13: custom-designed gamma-source holder for the LLNL HPGe detector.

erage residual for the 95 mm plot and a 2.99% residual for the 164 mm plot. This took approximately ten weeks of modeling work.

In general, the residuals appear randomly distributed about zero. However, when looking at each source individually, in many cases the residuals appear consistently underestimated or overestimated by the simulation. For example, in Figure 6.11, the ^{57}Co data points appear underestimated, but the ^{152}Eu sample appears overestimated.

We suspect that the systematic shifts in the efficiency are due to small displacements that are introduced by removing and installing the gamma sources. I will discuss our design of a new, highly repeatable sample holder in the next section.

6.3 Conclusions and Outlook

The new high purity germanium detector system at LLNL will measure gamma-ray intensities of long-lived fission isotopes to sub-percent precision. I started my practicum shortly after the new HPGe was assembled. We measured the gamma-ray intensities of a suite of standardized gamma sources to obtain the efficiency curve of the detector. Then I developed a Monte Carlo simulation code to reproduce the measured intensities. The

code is written in Geant4 and models the HPGe detection system, simulates gamma-ray efficiency of the HPGe as a function of energy, and compares the simulation deviation from measured gamma-ray intensities. I measured gamma-ray intensity of a suite of calibrated gamma-ray sources at different distances and compared the results to the simulation.

I calibrated the HPGe detector Monte Carlo model to within 3% of the measured gamma-ray efficiencies over a 2 MeV range. We believe that the leading source of uncertainty in the calibration is in the variance in gamma-ray source position when changing samples.

I designed a sample holder that mounts directly to the HPGe shell to suppress shifts in the source position between measurements. The finished gamma-ray sample holder is shown in Figure 6.13. A sheath interfaces with the endcap edge of the HPGe. The sample holder distance is fixed with stacking spacers calibrated to within a 0.2 mm tolerance that will let us vary the sample-detector distance from 2–30 cm in increments as small 1 cm. We have two sample holding adapters that will allow us to mount either a source disk for calibration measurements (left of Figure 6.13) or the 4π beta counter for long-lived fission isotope intensity measurements.

We expect that a new measurement of known gamma sources will calibrate the detector to within 1% using the position-repeatable sample holder. After the detector is sufficiently calibrated, precision measurements of long-lived fission isotopes will be possible. The goal is to measure the gamma-ray intensities of ^{147}Nd and other long-lived fission isotopes to determine the principal beta-decay branching ratios to within 1%.

CHAPTER 7

CONCLUSIONS AND OUTLOOK

The Ra EDM experiment measures the atomic electric dipole moment of ^{225}Ra. Atoms are vaporized in an oven and are collimated and cooled with resonant lasers. They are trapped in a magneto-optical trap, then transported between two high-voltage electrodes using optical tweezers. During the measurement, the atoms precess between a pair of identical plane-parallel electrodes that generate a uniform and stable DC electric field that reverses direction every measurement cycle. We used a pair of oxygen-free copper electrodes that operated at ±6.7 kV/mm at a 2.3 mm gap size and measured an EDM upper limit of 1.4×10^{-23} e cm in the first generation of measurements. For the second generation measurements, we will use a new pair of large-grain niobium electrodes whose systematic effects have been evaluated to the 10^{-26} e cm level.

I constructed a high voltage test station to condition high voltage electrodes at gap sizes of 0.4–2.5 mm with a 30 kV bipolar power supply at MSU. The test station was commissioned with a pair of copper electrodes, and the following high voltage tests were performed with niobium and titanium electrodes. I varied the electrode gap size with a high-precision linear drive and verified that the electrodes could perform reliably at 1 mm. Then, a fixed gap holder was fabricated and replaced the adjustable gap assembly. Subsequent conditioning was performed with electrode pairs at a gap of 1.0 ± 0.1 mm.

To reach fields higher than 10 kV/mm, I developed hardware and procedures to clean and preserve the surface purity of the electrodes. I built a portable clean room validated to Class 100 (ISO 5) with a NIST-calibrated particle counter and developed a clean room electrode swap procedure. Then I worked with engineers at FRIB to develop a procedure of high-pressure rinsing the electrodes with ultrapure water. I designed a packaging method for storage and transport of decontaminated electrodes. Subsequent test station work and electrode swaps were performed in the NSCL detector clean room.

Two pairs of grade-2 titanium and four pairs of large-grain niobium electrodes were fabricated and polished according to surface preparation techniques that were modified from accelerator physics literature. We discharge-conditioned three pairs of niobium electrodes and one pair of titanium electrodes, alternating the polarity of the applied DC field every 60 s to mimic the EDM measurement. Electric fields were tested as high as +52.5 kV/mm and −51.5 kV/mm. All the electrodes exhibited less than 100 pA steady-state leakage current when operated under 22 kV. We validated a pair of large-grain niobium electrodes (Nb_{56}) at 20 kV/mm with an average discharge rate of 98 ± 19 discharges per hour and a steady-state leakage less than 25 pA (1σ).

The large-grain niobium electrodes (Nb_{56}) were transported to ANL, where I constructed a portable clean room and positioned it at the EDM apparatus. Nb_{56} was installed in the Ra EDM apparatus all while preserving the electrodes in Class 100 environments. I revalidated the performance of Nb_{56} to 20 kV/mm after the apparatus vacuum pressure was restored.

Several targeted upgrades will be implemented in the second generation EDM measurements to collectively improve sensitivity by up to three orders of magnitude. The new niobium electrodes increase the electric field strength and will initially contribute an enhancement factor of 3.1 in EDM statistical sensitivity.

We plan to further increase the electric field to a factor of 7.7 during a future phase of high voltage development. This will be achieved by designing a more symmetric high voltage test chamber using a unipolar power supply that alternates the field direction by switching connections between the electrodes. Our goal is to discharge-condition electrodes to operate reliably at ±50 kV/mm over a 1 mm gap.

The new Blue Slower will use the $^1S_0 \rightarrow {}^1P_1^o$ optical cycling transition to allow us trap two orders of magnitude more atoms for spin precession frequency measurements. I built a fluoroscopy setup to characterize the additional decay channels that we will need to repump to use the blue cycling transition. The setup combines several fiber-

coupled lasers to populate and probe the deexcitation paths from the $^3F_2^o$ atomic state to several D states and measures the fluorescence intensity of each of the channels. From the fluorescence intensity we then determine the branching ratio for each decay channel. In this manner we verified the qualitative behavior of the D state branching ratios in the context of the blue Zeeman slowing scheme.

The Zeeman slower upgrade is expected to improve EDM sensitivity by an order of magnitude. In addition, a spin-selective STIRAP atom detection efficiency upgrade is being developed. STIRAP is also expected to improve sensitivity by more than one order of magnitude. Taken together with improvements to the electric field, we expect to reach an EDM sensitivity at the 10^{-26} e cm level or better.

In the near future, we will be able to harvest ^{225}Ra from the FRIB beamline. FRIB is expected to produce larger quantities of ^{225}Ra more frequently for the Ra EDM experiment than past sources. Our goal is to develop the FRIB harvesting procedure with a series of progressively sophisticated measurements with stable isotopes that have similar spectroscopic properties to radium.

The measurement is a laser induced fluorescence measurement of a directed beam of atoms from an effusive oven. We will initially use commercial, stable ytterbium as a radium surrogate to commission the flux measurement. As the measurement is refined, we will prepare a sample of stable calcium extracted from water, simulating a radium harvesting process. The calcium sample will be measured with the atomic beam fluorescence technique and allow us to benchmark the harvesting efficiency.

I assembled an atomic beam fluorescence setup that generates a directed beam of atoms from an effusive oven, illuminates the atoms with a laser beam, and captures the fluorescence with a photodetector. I wrote a program that simulates the photodetector signal as a function of the laser frequency, laser power, and oven temperature for a given atomic angular distribution and atom species. The simulation will allow us to optimize and interpret future atomic beam fluorescence measurements of ytterbium, calcium, and

other isotopes relevant for precision nuclear physics experiments.

Personal scientific contributions

The following list summarizes the tasks I performed for my thesis work.

1 Electrode material magnetization measurement

- Designed and assembled an electrode magnetization measurement setup using an external field-shielding mu-metal box and a custom mechanical translation stage.

- Configured fluxgate magnetometers above the translating stage and performed a suite of gradiometer measurements with copper, stainless steel, Macor, titanium, aluminum, and niobium electrodes and electrode-sized cylinder surrogates.

- Built a conditioning circuit with a differential op amp input and low-pass filter to amplify the magnetization signal.

2 High voltage electrode preparation, testing, and operation

- Designed and assembled a high voltage test station to discharge-condition six pairs of high voltage electrodes.

- Built data acquisition interface circuitry and housing units for a unipolar -30 kV unipolar and a ±30 kV bipolar power supply for the high voltage test station.

- Lead more than 80 conditioning shifts ranging from 3–6 hours each.

- Wrote analysis software for characterizing electrode conditioning performance.

- Designed and assembled high voltage components, including HV feedthrough shielding and in-vacuum electrode gap alignment components.

- Calibrated gap alignment with custom optical system.

- Designed, built, and assembled clean rooms for high voltage test station work at MSU and ANL.

- Performed high voltage test station maintenance and electrode installation and packaging in clean rooms at MSU, FRIB, and ANL.

- Transported a pair of conditioned niobium electrodes from MSU to ANL, assembled electrodes in holder, and assisted in installation of the electrodes in the ANL setup.

- Revalidated the electrode performance at ANL.

- First author of the publication being prepared for this work (submitted October 2020).

3   Laser cooling Zeeman slower upgrade

- Built fluoroscopy setup that fiber-couples three lasers and combines the beams with dichroic mirrors for radium laser induced fluorescence study at ANL.

- Built near-infrared diode laser and focusing components for radium fluorescence.

- Built near-infrared laser interface box which connects the thermoelectric temperature controller and current source to the diode laser and interlocks the setup to the laboratory safety system.

- Wrote data acquisition laser scanning LabView software for the radium branching ratio measurement.

- Manually searched for and found resonance frequencies for pump transition and excited state.

4   Long-lived fission isotope gamma-ray branching ratios

- Created Geant4 model of new high purity germanium gamma-ray detector at LLNL for the long-lived fission isotope gamma-ray spectroscopy experiment.

- Assisted with measurement of standardized gamma-emitting sources.

- Compared Geant4 Monte Carlo simulation of gamma source detector efficiency and measured efficiency and matched simulation to within 3% of experiment.

- Designed position-repeatable precision gamma source and 4π beta counter detector mounts to precisely fix source-detector distances.

5 Atomic beam fluorescence

- Assembled atomic beam fluorescence apparatus at for laser induced fluorescence studies of FRIB-harvested isotopes at MSU.

- Assembled vacuum hardware and atomic oven.

- Tuned titanium sapphire laser with frequency-doubling cavity to ytterbium excitation wavelength.

- Wrote analysis software that simulates an atomic beam fluorescence spectrum for user-defined atomic species and transition, oven geometry, atomic angular distribution, photodetector, and laser.

- Simulated ytterbium, rubidium, and calcium fluorescence spectra.

- Developed calculation of total atom rate count for a given photodetector fluorescence signal.

- Designed in-vacuum light-collection setup to amplify photodetector fluorescence signal.

Support

APPENDICES

APPENDIX A: Constants, units, atomic and nuclear properties

Table A1: Fundamental physical constants (from the NIST database)

constant	definition	value		
h	Planck constant	6.62607015	$\times 10^{-34}$	J Hz^{-1}
		4.135667696	$\times 10^{-15}$	$e\text{V Hz}^{-1}$
k_{B}	Boltzmann constant	1.380649	$\times 10^{-23}$	J K^{-1}
u	unified atomic mass unit	1.66053906660(50)	$\times 10^{-27}$	kg
c	speed of light in vacuum	2.99792458	$\times 10^{8}$	m s^{-1}
r_e	classical electron radius	2.8179403262	$\times 10^{-15}$	m
ϵ_o	vacuum electric permittivity	8.8541878128(13)	$\times 10^{-12}$	F m^{-1}
e	elementary charge	1.602176634	$\times 10^{-19}$	C
μ_{N}	nuclear magneton	5.0507837461(15)	$\times 10^{-27}$	J/T
μ_{B}	Bohr magneton	9.2740100783(28)	$\times 10^{-24}$	J/T
		5.7883818060(17)	$\times 10^{-5}$	eV/T
μ_{B}/h		1.39962449361(42)	$\times 10^{10}$	Hz/T
μ_0	vacuum magnetic permeability	1.25663706212(19)	$\times 10^{-6}$	N A^{-2}
m_e	electron mass	9.1093837015(28)	$\times 10^{-31}$	kg
a_0	Bohr radius	$= \dfrac{\hbar^2}{(e^2/4\pi\epsilon_0)\, m_e}$		
		$= 5.29177210903(80)$	$\times 10^{-11}$	m
$G_{\text{F}}/(\hbar)^3$	Fermi coupling constant	1.1663787(6)	$\times 10^{-5}$	GeV^{-2}

Table A2: Unit definitions.

unit	definition
Pascal (Pa)	$1\ \text{Pa} = 1\ \text{N m}^{-2}$
atmosphere (atm)	$1\ \text{atm} = 101325\ \text{Pa}$
Torr	$1\ \text{Torr} = 101325/760 = 133.3\ \text{Pa}$
bar	$1\ \text{bar} = 10^5\ \text{Pa}$
Tesla (T)	$1\ \text{T} = 10^4\ \text{gauss}$
elementary charge (e)	$1\ e = 1.602176634 \times 10^{-19}\ \text{C}$

Table A3: Angular momentum, masses, and abundances of Yb. Values from NIST.

mass number A	Nuclear spin I	mass ($\times 10^{-25}$ kg)	abundance (%)
168	0	2.7886078	0.123(3)
170	0	2.8218331	2.982(39)
171	1/2	2.8384645	14.09(14)
172	0	2.8550709	21.68(13)
173	5/2	2.8717066	16.103(63)
174	0	2.8883228	32.026(80)
176	0	2.9215952	12.996(83)

Table A4: Vapor pressure coefficients for ytterbium, rubidium, and calcium.

atom	A [1]	B [K]	C [1]	D $\left[K^3\right]$	Ref.
Yb	9.111	−8111.0	−1.0849	0.0	[171]
Rb	4.857	−4215	0.0	0.0	[108]
Ca	10.127	−9517	−1.4030	0.0	[108]

Table A5: Rubidium properties. Mass number A, nuclear spin I, isotope shift IS. Values from NIST.

^{A}Rb	I	mass ($\times 10^{-25}$ kg)	abundance (%)	IS $-\nu_0(^{85}$Rb) [MHz]
87	3/2	1.4431610	27.83	77.583(12)
85	5/2	1.4099935	72.17	0.0

Table A6: Calcium properties. Mass number A, nuclear spin I, isotope shift (IS) for the transition $^1S_0 \rightarrow \ ^1P_1^o$. ^{47}Ca atomic mass from Kramida [172]. ^{47}Ca isotope shift by Andl $et.\ al$ [149]. All other isotope shifts from Nörtershäuser $et.\ al$ [155]. All other mases from NIST.

A	I	mass ($\times 10^{-25}$ kg)	abundance (%)	IS $-\nu_0(^{40}$Ca) [MHz]
40	0	0.66359444	96.941	0.0
42	0	0.69673924	0.647	393.5
43	7/2	0.71334709	0.135	611.8
44	0	0.72989791	2.086	773.8
46	0	0.76307896	0.004	1159.8
47	7/2	7.7969848	synthetic	1348.7
48	0	0.79627088	0.187	1513.0

APPENDIX B: Code and data availability

The code used to analyze the high voltage data and generate the current discharge plots is available for use at https://zenodo.org/badge/latestdoi/294766922. The data used for the high voltage analysis may be made available for reasonable requests sent to `singhj@frib.msu.edu`.

APPENDIX C: Avalanche Photodiode Settings

The voltage output of the avalanche photodiode $V(\nu)$ [V] is given by:

$$V(\nu) = P_d(\nu) \times \mathcal{R}_M(\lambda) \times G,$$

where

$P_d(\nu)$ [W] is the incident fluorescent light power at frequency ν,

$\mathcal{R}_M = 11.3\ (24.0)$ A/W for $\lambda = 398.8\ (555.6)$ nm for M $= 50$ is the detector responsivity at wavelength,

M $\in [5, 50]$ is the gain or "M-factor", and

$G = 500$ kV/A is the transimpedance gain.

$V_{\mathrm{out}} \leq 4.1\ (2.0)$ V at high-Z (50 Ω) termination. The detector area is $A_{\mathrm{det}} = \pi(0.25\ \mathrm{mm})^2 = 0.196\ \mathrm{mm}^2$. The distance between the surface of the active detective area and the flange $= 2.2 \pm 0.3$ mm. The optical damage threshold $= 1$ mW.

APPENDIX D: Fluxgate magnetometry
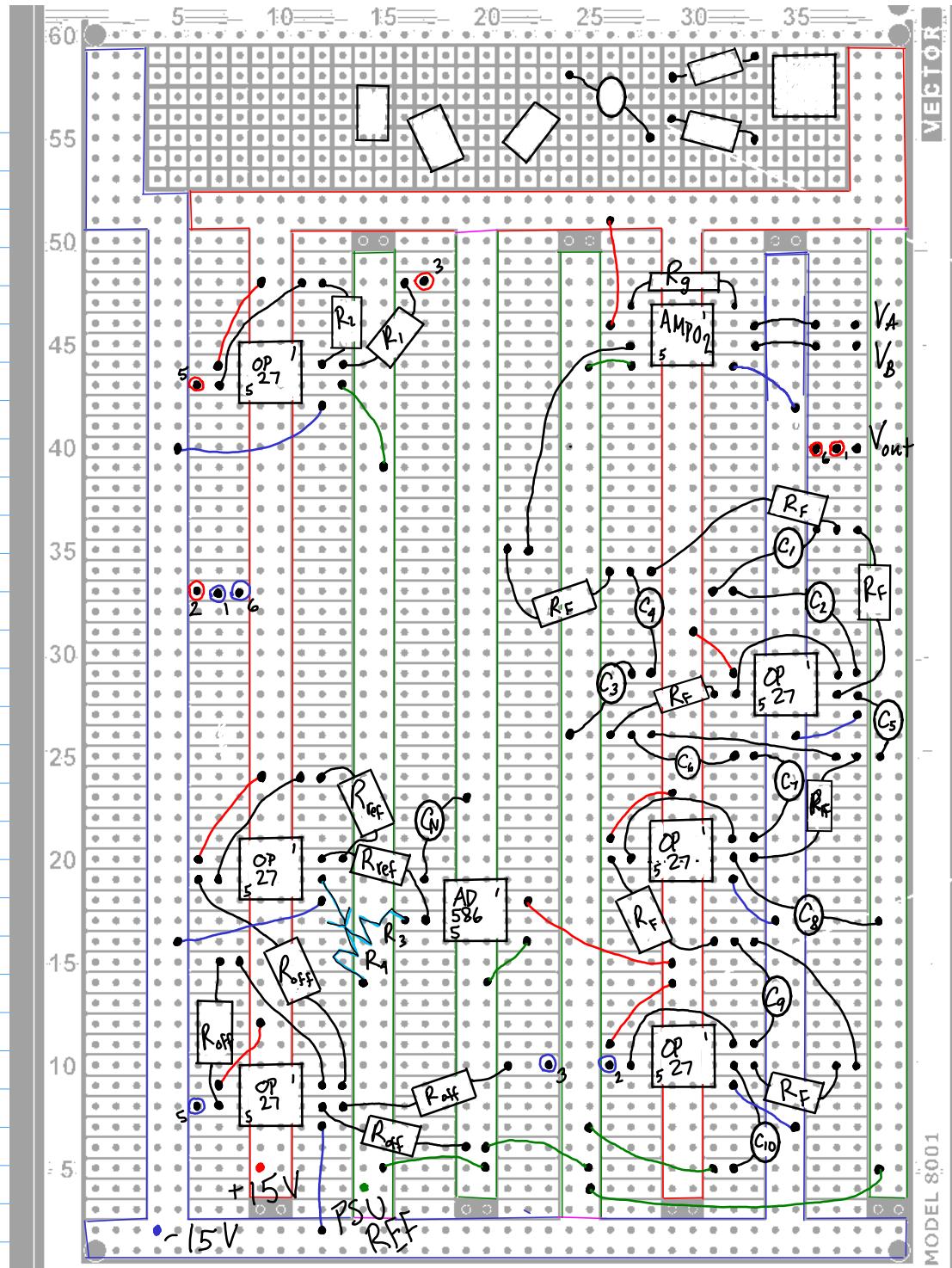
Figure D1: $C_1 = 5.6$ nF, $C_2 = 47$ nF, $C_3 = 4.7$ nF, $C_4 = 47$ nF, $C_5 = 1.5$ nF, $C_6 = 5.6$ nF, $C_7 = 100$ nF, $C_8 = 2.2$ nF, $C_9 = 15$ nF, $C_{10} = 0.82$ nF, $C_N = 1$ μF, $R_1 = 10$ kΩ, $R_2 = 100$ kΩ, $R_3 + R_4 = 10$ kΩ, $R_{\text{ref}} = 10$ kΩ, $R_F = 10$ kΩ, $R_{\text{off}} = 10$ kΩ
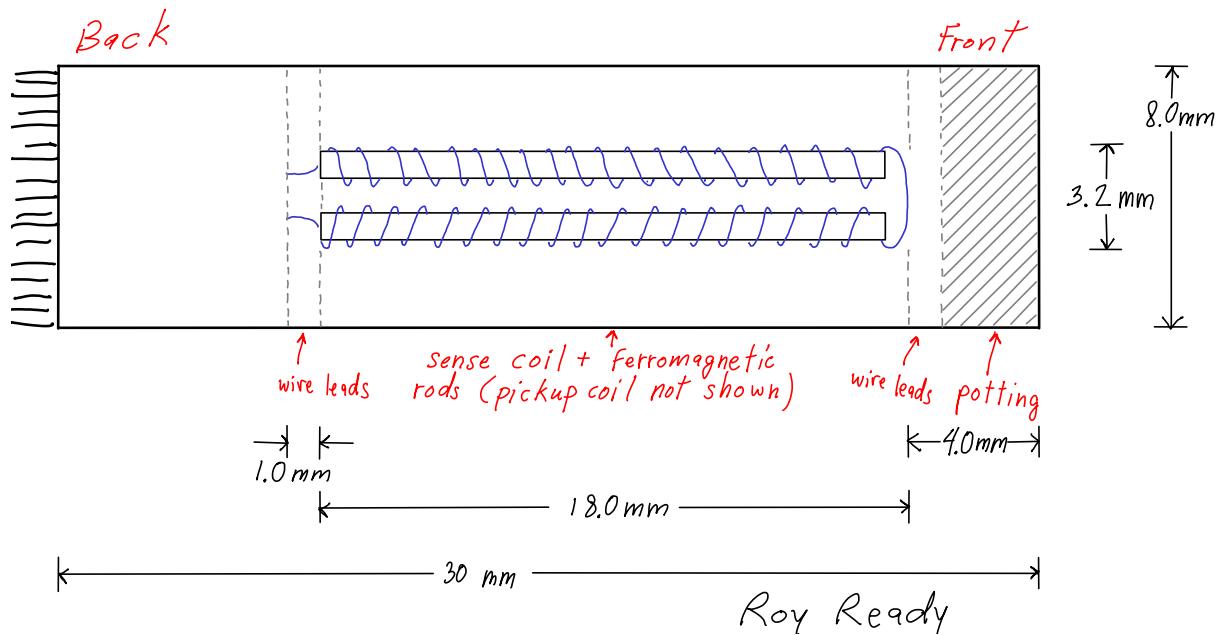
Figure D2: Bartington Mag03IEL70 fluxgate schematic for magnetization measurements.
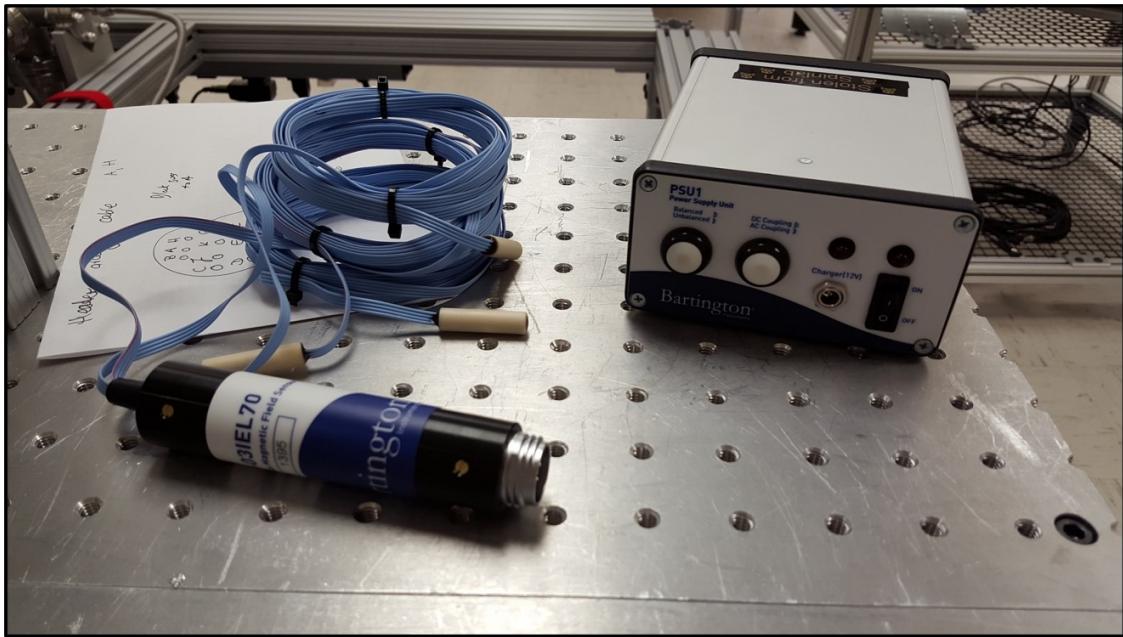
Figure D3: Fluxgate: Bartington Mag03IEL70. 16 kHz excitation frequency, noise floor is 6 $pT_{rms}/\sqrt{Hz}$. Power supply: Bartington PSU1. 5 $pT_{rms}/\sqrt{Hz}$ noise floor. Data acquisition: NI PCie-6320. 16-bit. 2 mV noise floor on 10 V scale.

BIBLIOGRAPHY

BIBLIOGRAPHY

[1]   B. Odom, D. Hanneke, B. D'Urso, and G. Gabrielse. New measurement of the electron magnetic moment using a one-electron quantum cyclotron. *Phys. Rev. Lett.*, 97:030801, Jul 2006.

[2]   G. Gabrielse, D. Hanneke, T. Kinoshita, M. Nio, and B. Odom. Erratum: New determination of the fine structure constant from the electron *g* value and qed [phys. rev. lett. 97, 030802 (2006)]. *Phys. Rev. Lett.*, 99:039902, Jul 2007.

[3]   C. S. Wu, E. Ambler, R. W. Hayward, D. D. Hoppes, and R. P. Hudson. Experimental test of parity conservation in beta decay. *Phys. Rev.*, 105:1413–1415, Feb 1957.

[4]   T. D. Lee and C. N. Yang. Question of parity conservation in weak interactions. *Phys. Rev.*, 104:254–258, Oct 1956.

[5]   A D Sakharov. Violation of CP in variance, C asymmetry, and baryon asymmetry of the universe. *JETP Letters*, 5(1):24–26, 1967.

[6]   T. E. Chupp, P. Fierlinger, M. J. Ramsey-Musolf, and J. T. Singh. Electric dipole moments of atoms, molecules, nuclei, and particles. *Rev. Mod. Phys.*, 91:015001, Jan 2019.

[7]   J. H. Christenson, J. W. Cronin, V. L. Fitch, and R. Turlay. Evidence for the 2π decay of the k_2^0 meson. *Phys. Rev. Lett.*, 13:138–140, Jul 1964.

[8]   V. Fanti, A. Lai, D. Marras, L. Musa, A.J. Bevan, T.J. Gershon, B. Hay, R.W. Moore, K.N. Moore, D.J. Munday, M.D. Needham, M.A. Parker, S.F. Takach, T.O. White, S.A. Wotton, G. Barr, H. Blümer, et al. A new measurement of direct cp violation in two pion decays of the neutral kaon. *Physics Letters B*, 465(1):335–348, 1999.

[9]   K. Abe, K. Abe, R. Abe, I. Adachi, Byoung Sup Ahn, H. Aihara, M. Akatsu, G. Alimonti, K. Asai, M. Asai, Y. Asano, T. Aso, V. Aulchenko, T. Aushev, A. M. Bakich, E. Banas, et al. Observation of large *CP* violation in the neutral *B* meson system. *Phys. Rev. Lett.*, 87:091802, Aug 2001.

[10]   B. Aubert, D. Boutigny, J.-M. Gaillard, A. Hicheur, Y. Karyotakis, J. P. Lees, P. Robbe, V. Tisserand, A. Palano, G. P. Chen, J. C. Chen, N. D. Qi, G. Rong, P. Wang, Y. S. Zhu, et al. Observation of *CP* violation in the b^0 meson system. *Phys. Rev. Lett.*, 87:091801, Aug 2001.

[11]   B. Aubert, R. Barate, D. Boutigny, F. Couderc, J.-M. Gaillard, A. Hicheur, Y. Karyotakis, J. P. Lees, V. Tisserand, A. Zghiche, A. Palano, A. Pompili, J. C. Chen, N. D. Qi, et al. Direct *cp* violating asymmetry in $B^0 \rightarrow K^+\pi^-$ decays. *Phys. Rev. Lett.*, 93:131801, Sep 2004.

[12] Y. Chao, P. Chang, K. Abe, K. Abe, N. Abe, I. Adachi, H. Aihara, K. Akai, M. Akatsu, M. Akemoto, Y. Asano, T. Aso, V. Aulchenko, T. Aushev, T. Aziz, S. Bahinipati, et al. Evidence for direct cp violation in $B^0 \to K^+\pi^-$ decays. *Phys. Rev. Lett.*, 93:191802, Nov 2004.

[13] Particle Data Group, P A Zyla, R M Barnett, J Beringer, O Dahl, D A Dwyer, D E Groom, C J Lin, K S Lugovsky, E Pianori, D J Robinson, C G Wohl, W M Yao, K Agashe, G Aielli, B C Allanach, C Amsler, M Antonelli, E C Aschenauer, D M Asner, H Baer, Sw Banerjee, L Baudis, C W Bauer, J J Beatty, V I Belousov, S Bethke, A Bettini, O Biebel, K M Black, E Blucher, O Buchmuller, V Burkert, M A Bychkov, R N Cahn, M Carena, A Ceccucci, A Cerri, D Chakraborty, R Sekhar Chivukula, G Cowan, G D'Ambrosio, T Damour, D de Florian, A de Gouvêa, T DeGrand, P de Jong, G Dissertori, B A Dobrescu, M D'Onofrio, M Doser, M Drees, H K Dreiner, P Eerola, U Egede, S Eidelman, J Ellis, J Erler, V V Ezhela, W Fetscher, B D Fields, B Foster, A Freitas, H Gallagher, L Garren, H J Gerber, G Gerbier, T Gershon, Y Gershtein, T Gherghetta, A A Godizov, M C Gonzalez-Garcia, M Goodman, C Grab, A V Gritsan, C Grojean, M Grünewald, A Gurtu, et al. Review of Particle Physics. *Progress of Theoretical and Experimental Physics*, 2020(8), 08 2020. 083C01.

[14] Maxim Pospelov and Adam Ritz. Ckm benchmarks for electron electric dipole moment experiments. *Phys. Rev. D*, 89:056006, Mar 2014.

[15] Andrzej Czarnecki and Bernd Krause. Neutron electric dipole moment in the standard model: Complete three-loop calculation of the valence quark contributions. *Phys. Rev. Lett.*, 78:4339–4342, Jun 1997.

[16] Chien-Yeah Seng. Reexamination of the standard model nucleon electric dipole moment. *Phys. Rev. C*, 91:025502, Feb 2015.

[17] Jonathan Engel, Michael J. Ramsey-Musolf, and U. van Kolck. Electric dipole moments of nucleons, nuclei, and atoms: The standard model and beyond. *Progress in Particle and Nuclear Physics*, 71:21 – 74, 2013. Fundamental Symmetries in the Era of the LHC.

[18] T. Alexopoulos, M. Arenton, R. F. Barbosa, A. R. Barker, L. Bellantoni, A. Bellavance, E. Blucher, G. J. Bock, E. Cheu, S. Childress, R. Coleman, M. D. Corcoran, B. Cox, A. R. Erwin, R. Ford, A. Glazov, A. Golossanov, J. Graham, J. Hamm, K. Hanagaki, Y. B. Hsiung, H. Huang, V. Jejer, D. A. Jensen, R. Kessler, H. G. E. Kobrak, K. Kotera, J. LaDue, A. Ledovskoy, P. L. McBride, E. Monnier, K. S. Nelson, H. Nguyen, R. Niclasen, V. Prasad, X. R. Qi, E. J. Ramberg, R. E. Ray, M. Ronquest, E. Santos, P. Shanahan, J. Shields, W. Slater, D. Smith, N. Solomey, E. C. Swallow, P. A. Toale, R. Tschirhart, Y. W. Wah, J. Wang, H. B. White, J. Whitmore, M. Wilking, B. Winstein, R. Winston, E. T. Worcester, T. Yamanaka, and E. D. Zimmerman. Measurements of K_L branching fractions and the cp violation parameter $|\eta_{+-}|$. *Phys. Rev. D*, 70:092006, Nov 2004.

[19] Giancarlo D'Ambrosio, Gino Isidori, KLOE collaboration, et al. Determination of cp and cpt violation parameters in the neutral kaon system using the bell-steinberger relation and data from the kloe experiment. *Journal of High Energy Physics*, 2006(12):011, 2006.

[20] Adriano Lai, Davide Marras, A Bevan, RS Dosanjh, TJ Gershon, B Hay, GE Kalmus, C Lazzeroni, DJ Munday, E Olaiya, et al. Measurement of the ratio γ (kl $\rightarrow \pi+$ π-)/γ (kl $\rightarrow \pi \pm e \mp \nu$) and extraction of the cp violation parameter $|\eta_{+-}|$. *Physics Letters B*, 645(1):26–35, 2007.

[21] E. Abouzaid, M. Arenton, A. R. Barker, M. Barrio, L. Bellantoni, E. Blucher, G. J. Bock, C. Bown, E. Cheu, R. Coleman, M. D. Corcoran, B. Cox, A. R. Erwin, C. O. Escobar, A. Glazov, A. Golossanov, R. A. Gomes, P. Gouffon, J. Graham, J. Hamm, Y. B. Hsiung, D. A. Jensen, R. Kessler, K. Kotera, J. LaDue, A. Ledovskoy, P. L. McBride, E. Monnier, H. Nguyen, R. Niclasen, D. G. Phillips, V. Prasad, X. R. Qi, E. J. Ramberg, R. E. Ray, M. Ronquest, A. Roodman, E. Santos, P. Shanahan, P. S. Shawhan, W. Slater, D. Smith, N. Solomey, E. C. Swallow, S. A. Taegar, P. A. Toale, R. Tschirhart, Y. W. Wah, J. Wang, H. B. White, J. Whitmore, M. J. Wilking, B. Winstein, R. Winston, E. T. Worcester, T. Yamanaka, E. D. Zimmerman, and R. F. Zukanovich. Precise measurements of direct *cp* violation, *cpt* symmetry, and other parameters in the neutral kaon system. *Phys. Rev. D*, 83:092001, May 2011.

[22] D Babusci, D Badoni, I Balwierz-Pytko, G Bencivenni, C Bini, C Bloise, F Bossi, P Branchini, A Budano, L Caldeira Balkeståhl, et al. A new limit on the cp violating decay ks$\rightarrow 3\pi0$ with the kloe experiment. *Physics Letters B*, 723(1-3):54–60, 2013.

[23] Gary Steigman. Observational tests of antimatter cosmologies. *Annual Review of Astronomy and Astrophysics*, 14(1):339–372, 1976.

[24] O. Adriani, G. C. Barbarino, G. A. Bazilevskaya, R. Bellotti, M. Boezio, E. A. Bogomolov, L. Bonechi, M. Bongi, V. Bonvicini, S. Borisov, S. Bottai, A. Bruno, F. Cafagna, D. Campana, R. Carbone, P. Carlson, M. Casolino, G. Castellini, L. Consiglio, M. P. De Pascale, C. De Santis, N. De Simone, V. Di Felice, A. M. Galper, W. Gillard, L. Grishantseva, P. Hofverberg, G. Jerse, A. V. Karelin, S. V. Koldashov, S. Y. Krutkov, A. N. Kvashnin, A. Leonov, V. Malvezzi, L. Marcelli, A. G. Mayorov, W. Menn, V. V. Mikhailov, E. Mocchiutti, A. Monaco, N. Mori, N. Nikonov, G. Osteria, P. Papini, M. Pearce, P. Picozza, C. Pizzolotto, M. Ricci, S. B. Ricciarini, L. Rossetto, M. Simon, R. Sparvoli, P. Spillantini, Y. I. Stozhkov, A. Vacchi, E. Vannuccini, G. Vasilyev, S. A. Voronov, J. Wu, Y. T. Yurkin, G. Zampa, N. Zampa, and V. G. Zverev. Pamela results on the cosmic-ray antiproton flux from 60 mev to 180 gev in kinetic energy. *Phys. Rev. Lett.*, 105:121101, Sep 2010.

[25] M. Ackermann, M. Ajello, A. Allafort, W. B. Atwood, L. Baldini, G. Barbiellini, D. Bastieri, K. Bechtol, R. Bellazzini, B. Berenji, R. D. Blandford, E. D. Bloom, E. Bonamente, A. W. Borgland, A. Bouvier, J. Bregeon, M. Brigida, P. Bruel, R. Buehler, S. Buson, G. A. Caliandro, R. A. Cameron, P. A. Caraveo, J. M. Casandjian, C. Cecchi, E. Charles, A. Chekhtman, C. C. Cheung, J. Chiang, S. Ciprini,

R. Claus, J. Cohen-Tanugi, J. Conrad, S. Cutini, A. de Angelis, F. de Palma, C. D. Dermer, S. W. Digel, E. do Couto e Silva, P. S. Drell, A. Drlica-Wagner, C. Favuzzi, S. J. Fegan, E. C. Ferrara, W. B. Focke, P. Fortin, Y. Fukazawa, S. Funk, P. Fusco, F. Gargano, D. Gasparrini, S. Germani, N. Giglietto, P. Giommi, F. Giordano, M. Giroletti, T. Glanzman, G. Godfrey, I. A. Grenier, J. E. Grove, S. Guiriec, M. Gustafsson, D. Hadasch, A. K. Harding, M. Hayashida, R. E. Hughes, G. Jóhannesson, A. S. Johnson, T. Kamae, H. Katagiri, J. Kataoka, J. Knödlseder, M. Kuss, J. Lande, L. Latronico, M. Lemoine-Goumard, M. Llena Garde, F. Longo, F. Loparco, M. N. Lovellette, P. Lubrano, G. M. Madejski, M. N. Mazziotta, J. E. McEnery, P. F. Michelson, W. Mitthumsiri, T. Mizuno, A. A. Moiseev, C. Monte, M. E. Monzani, A. Morselli, I. V. Moskalenko, S. Murgia, T. Nakamori, P. L. Nolan, J. P. Norris, E. Nuss, M. Ohno, T. Ohsugi, A. Okumura, N. Omodei, E. Orlando, J. F. Ormes, M. Ozaki, D. Paneque, D. Parent, M. Pesce-Rollins, M. Pierbattista, F. Piron, G. Pivato, T. A. Porter, S. Rainò, R. Rando, M. Razzano, S. Razzaque, A. Reimer, O. Reimer, T. Reposeur, S. Ritz, R. W. Romani, M. Roth, H. F.-W. Sadrozinski, C. Sbarra, T. L. Schalk, C. Sgrò, E. J. Siskind, G. Spandre, P. Spinelli, A. W. Strong, H. Takahashi, T. Takahashi, T. Tanaka, J. G. Thayer, J. B. Thayer, L. Tibaldo, M. Tinivella, D. F. Torres, G. Tosti, E. Troja, Y. Uchiyama, T. L. Usher, J. Vandenbroucke, V. Vasileiou, G. Vianello, V. Vitale, A. P. Waite, B. L. Winer, K. S. Wood, M. Wood, Z. Yang, and S. Zimmer. Measurement of separate cosmic-ray electron and positron spectra with the fermi large area telescope. *Phys. Rev. Lett.*, 108:011103, Jan 2012.

[26] Laurent Canetti, Marco Drewes, and Mikhail Shaposhnikov. Matter and antimatter in the universe. *New Journal of Physics*, 14(9):095012, sep 2012.

[27] Gaëlle Giesen, Mathieu Boudaud, Yoann Génolini, Vivian Poulin, Marco Cirelli, Pierre Salati, and Pasquale D. Serpico. AMS-02 antiprotons, at last! secondary astrophysical component and immediate implications for dark matter. *Journal of Cosmology and Astroparticle Physics*, 2015(09):023–023, sep 2015.

[28] Helen R. Quinn. The asymmetry between matter and antimatter. *Physics Today*, 56(2):30–35, 2003.

[29] David E Morrissey and Michael J Ramsey-Musolf. Electroweak baryogenesis. *New Journal of Physics*, 14(12):125003, dec 2012.

[30] P.A. Zyla et al. Review of Particle Physics. *PTEP*, 2020(8):083C01, 2020.

[31] Patrick Huet and Eric Sather. Electroweak baryogenesis and standard model cp violation. *Phys. Rev. D*, 51:379–394, Jan 1995.

[32] N Yamanaka, BK Sahoo, N Yoshinaga, T Sato, K Asahi, and BP Das. Probing exotic phenomena at the interface of nuclear and particle physics with the electric dipole moments of diamagnetic atoms: A unique window to hadronic and semi-leptonic cp violation. *The European Physical Journal A*, 53(3):1–49, 2017.

[33] Maxim Pospelov and Adam Ritz. Neutron electric dipole moment from electric and chromoelectric dipole moments of quarks. *Physical Review D*, 63(7):073015, 2001.

[34] Maxim Pospelov and Adam Ritz. Electric dipole moments as probes of new physics. *Annals of physics*, 318(1):119–169, 2005.

[35] Jack Dragos, Thomas Luu, Andrea Shindler, Jordy de Vries, and Ahmed Yousif. Confirming the existence of the strong cp problem in lattice qcd with the gradient flow. *Phys. Rev. C*, 103:015202, Jan 2021.

[36] Chien-Yeah Seng and Michael Ramsey-Musolf. Parity-violating and time-reversal-violating pion-nucleon couplings: Higher order chiral matching relations. *Phys. Rev. C*, 96:065204, Dec 2017.

[37] S Aoki, Y Aoki, D Bečirević, T Blum, Gilberto Colangelo, S Collins, M Della Morte, P Dimopoulos, S Dürr, H Fukaya, et al. Flag review 2019. *The European Physical Journal C*, 80(2):1–268, 2020.

[38] R.J. Crewther, P. Di Vecchia, G. Veneziano, and E. Witten. Chiral estimate of the electric dipole moment of the neutron in quantum chromodynamics. *Physics Letters B*, 88(1):123–127, 1979.

[39] Florian Kuchler. *Electric dipole moment searches using the isotope 129-xenon*. PhD thesis, Technische Universität München, 2014.

[40] Maxim Pospelov. Best values for the cp-odd meson–nucleon couplings from supersymmetry. *Physics Letters B*, 530(1):123–128, 2002.

[41] C. Abel, S. Afach, N. J. Ayres, C. A. Baker, G. Ban, G. Bison, K. Bodek, V. Bondar, M. Burghoff, E. Chanel, Z. Chowdhuri, P.-J. Chiu, B. Clement, C. B. Crawford, M. Daum, S. Emmenegger, L. Ferraris-Bouchez, M. Fertl, P. Flaux, B. Franke, A. Fratangelo, P. Geltenbort, K. Green, W. C. Griffith, M. van der Grinten, Z. D. Grujić, P. G. Harris, L. Hayen, W. Heil, R. Henneck, V. Hélaine, N. Hild, Z. Hodge, M. Horras, P. Iaydjiev, S. N. Ivanov, M. Kasprzak, Y. Kermaidic, K. Kirch, A. Knecht, P. Knowles, H.-C. Koch, P. A. Koss, S. Komposch, A. Kozela, A. Kraft, J. Krempel, M. Kuźniak, B. Lauss, T. Lefort, Y. Lemière, A. Leredde, P. Mohanmurthy, A. Mtchedlishvili, M. Musgrave, O. Naviliat-Cuncic, D. Pais, F. M. Piegsa, E. Pierre, G. Pignol, C. Plonka-Spehr, P. N. Prashanth, G. Quéméner, M. Rawlik, D. Rebreyend, I. Rienäcker, D. Ries, S. Roccia, G. Rogel, D. Rozpedzik, A. Schnabel, P. Schmidt-Wellenburg, N. Severijns, D. Shiers, R. Tavakoli Dinani, J. A. Thorne, R. Virot, J. Voigt, A. Weis, E. Wursten, G. Wyszynski, J. Zejma, J. Zenner, and G. Zsigmond. Measurement of the permanent electric dipole moment of the neutron. *Phys. Rev. Lett.*, 124:081803, Feb 2020.

[42] C. A. Baker, D. D. Doyle, P. Geltenbort, K. Green, M. G. D. van der Grinten, P. G. Harris, P. Iaydjiev, S. N. Ivanov, D. J. R. May, J. M. Pendlebury, J. D. Richardson, D. Shiers, and K. F. Smith. Improved experimental limit on the electric dipole moment of the neutron. *Phys. Rev. Lett.*, 97:131801, Sep 2006.

[43] J. M. Pendlebury, S. Afach, N. J. Ayres, C. A. Baker, G. Ban, G. Bison, K. Bodek, M. Burghoff, P. Geltenbort, K. Green, W. C. Griffith, M. van der Grinten, Z. D. Grujić, P. G. Harris, V. Hélaine, P. Iaydjiev, S. N. Ivanov, M. Kasprzak, Y. Kermaidic, K. Kirch, H.-C. Koch, S. Komposch, A. Kozela, J. Krempel, B. Lauss, T. Lefort, Y. Lemière, D. J. R. May, M. Musgrave, O. Naviliat-Cuncic, F. M. Piegsa, G. Pignol, P. N. Prashanth, G. Quéméner, M. Rawlik, D. Rebreyend, J. D. Richardson, D. Ries, S. Roccia, D. Rozpedzik, A. Schnabel, P. Schmidt-Wellenburg, N. Severijns, D. Shiers, J. A. Thorne, A. Weis, O. J. Winston, E. Wursten, J. Zejma, and G. Zsigmond. Revised experimental upper limit on the electric dipole moment of the neutron. *Phys. Rev. D*, 92:092003, Nov 2015.

[44] William B. Cairncross, Daniel N. Gresh, Matt Grau, Kevin C. Cossel, Tanya S. Roussy, Yiqi Ni, Yan Zhou, Jun Ye, and Eric A. Cornell. Precision measurement of the electron's electric dipole moment using trapped molecular ions. *Phys. Rev. Lett.*, 119:153001, Oct 2017.

[45] Vitaly Andreev and NR Hutzler. Improved limit on the electric dipole moment of the electron. *Nature*, 562(7727):355–360, 2018.

[46] B. Graner, Y. Chen, E. G. Lindahl, and B. R. Heckel. Reduced limit on the permanent electric dipole moment of ^{199}Hg. *Phys. Rev. Lett.*, 116:161601, Apr 2016.

[47] N. Sachdeva, I. Fan, E. Babcock, M. Burghoff, T. E. Chupp, S. Degenkolb, P. Fierlinger, S. Haude, E. Kraegeloh, W. Kilian, S. Knappe-Grüneberg, F. Kuchler, T. Liu, M. Marino, J. Meinel, K. Rolfs, Z. Salhi, A. Schnabel, J. T. Singh, S. Stuiber, W. A. Terrano, L. Trahms, and J. Voigt. New limit on the permanent electric dipole moment of ^{129}Xe using ^{3}He comagnetometry and squid detection. *Phys. Rev. Lett.*, 123:143003, Oct 2019.

[48] Michael Bishof, Richard H. Parker, Kevin G. Bailey, John P. Greene, Roy J. Holt, Mukut R. Kalita, Wolfgang Korsch, Nathan D. Lemke, Zheng-Tian Lu, Peter Mueller, Thomas P. O'Connor, Jaideep T. Singh, and Matthew R. Dietrich. Improved limit on the ^{225}Ra electric dipole moment. *Phys. Rev. C*, 94:025501, Aug 2016.

[49] D. Cho, K. Sangster, and E. A. Hinds. Search for time-reversal-symmetry violation in thallium fluoride using a jet source. *Phys. Rev. A*, 44:2783–2799, Sep 1991.

[50] A. N. Petrov, N. S. Mosyagin, T. A. Isaev, A. V. Titov, V. F. Ezhov, E. Eliav, and U. Kaldor. Calculation of P, T-odd effects in ^{205}tlF including electron correlation. *Phys. Rev. Lett.*, 88:073001, Jan 2002.

[51] J. H. Smith, E. M. Purcell, and N. F. Ramsey. Experimental limit to the electric dipole moment of the neutron. *Phys. Rev.*, 108:120–122, Oct 1957.

[52] I.S. Altarev, Yu.V. Borisov, A.B. Brandin, A.I. Egorov, V.F. Ezhov, S.N. Ivanov, V.M. Lobashov, V.A. Nazarenko, G.D. Porsev, V.L. Ryabov, A.P. Serebrov, and R.R. Taldaev. A search for the electric dipole moment of the neutron using ultracold neutrons. *Nuclear Physics A*, 341(2):269–283, 1980.

[53] L I Schiff. Measurability of Nuclear Electric Dipole Moments. *Phys. Rev.*, 132(5):2194–2200, December 1963.

[54] N. Auerbach, V. V. Flambaum, and V. Spevak. Collective t- and p-odd electromagnetic moments in nuclei with octupole deformations. *Phys. Rev. Lett.*, 76:4316–4319, Jun 1996.

[55] V Spevak, N Auerbach, and VV Flambaum. Enhanced t-odd, p-odd electromagnetic moments in reflection asymmetric nuclei. *Physical Review C*, 56(3):1357, 1997.

[56] PGH Sandars. Enhancement factor for the electric dipole moment of the valence electron in an alkali atom. *Physics Letters*, 22(3):290–291, 1966.

[57] Eugene D. Commins, J. D. Jackson, and David P. DeMille. The electric dipole moment of the electron: An intuitive explanation for the evasion of schiff's theorem. *American Journal of Physics*, 75(6):532–536, 2007.

[58] T. G. Vold, F. J. Raab, B. Heckel, and E. N. Fortson. Search for a permanent electric dipole moment on the ^{129}Xe atom. *Phys. Rev. Lett.*, 52:2229–2232, Jun 1984.

[59] Timothy Chupp and Michael Ramsey-Musolf. Electric dipole moments: A global analysis. *Phys. Rev. C*, 91:035502, Mar 2015.

[60] S. A. Murthy, D. Krause, Z. L. Li, and L. R. Hunter. New limits on the electron electric dipole moment from cesium. *Phys. Rev. Lett.*, 63:965–968, Aug 1989.

[61] B. C. Regan, Eugene D. Commins, Christian J. Schmidt, and David DeMille. New limit on the electron electric dipole moment. *Phys. Rev. Lett.*, 88:071805, Feb 2002.

[62] Jonathan J Hudson, Dhiren M Kara, IJ Smallman, Ben E Sauer, Michael R Tarbutt, and Ed A Hinds. Improved measurement of the shape of the electron. *Nature*, 473(7348):493–496, 2011.

[63] J. Baron, W. C. Campbell, D. DeMille, J. M. Doyle, G. Gabrielse, Y. V. Gurevich, P. W. Hess, N. R. Hutzler, E. Kirilov, I. Kozyryev, B. R. O'Leary, C. D. Panda, M. F. Parsons, E. S. Petrik, B. Spaun, A. C. Vutha, and A. D. West. Order of magnitude smaller limit on the electric dipole moment of the electron. *Science*, 343(6168):269–272, 2014.

[64] M. A. Rosenberry and T. E. Chupp. Atomic electric dipole moment measurement using spin exchange pumped masers of ^{129}Xe and ^{3}He. *Phys. Rev. Lett.*, 86:22–25, Jan 2001.

[65] R. H. Parker, M. R. Dietrich, M. R. Kalita, N. D. Lemke, K. G. Bailey, M. Bishof, J. P. Greene, R. J. Holt, W. Korsch, Z.-T. Lu, P. Mueller, T. P. O'Connor, and J. T. Singh. First measurement of the atomic electric dipole moment of ^{225}Ra. *Phys. Rev. Lett.*, 114:233002, Jun 2015.

[66] B. Graner, Y. Chen, E. G. Lindahl, and B. R. Heckel. Erratum: Reduced limit on the permanent electric dipole moment of ^{199}Hg [phys. rev. lett. 116, 161601 (2016)]. *Phys. Rev. Lett.*, 119:119901, Sep 2017.

[67] Tanmoy Bhattacharya, Vincenzo Cirigliano, Saul D. Cohen, Rajan Gupta, Anosh Joseph, Huey-Wen Lin, and Boram Yoon. Isovector and isoscalar tensor charges of the nucleon from lattice qcd. *Phys. Rev. D*, 92:094511, Nov 2015.

[68] Tanmoy Bhattacharya, Vincenzo Cirigliano, Saul D. Cohen, Rajan Gupta, Huey-Wen Lin, and Boram Yoon. Axial, scalar, and tensor charges of the nucleon from $2+1+1$-flavor lattice qcd. *Phys. Rev. D*, 94:054508, Sep 2016.

[69] William B Cairncross and Jun Ye. Atoms and molecules in the search for time-reversal symmetry violation. *Nature Reviews Physics*, 1(8):510–521, 2019.

[70] Iosif B Khriplovich and Steve K Lamoreaux. Cp violation without strangeness: electric dipole moments of particles, atoms, and molecules. 1997.

[71] J. de Vries, E. Mereghetti, and A. Walker-Loud. Baryon mass splittings and strong *CP* violation in su(3) chiral perturbation theory. *Phys. Rev. C*, 92:045201, Oct 2015.

[72] Jacek Dobaczewski, Jonathan Engel, Markus Kortelainen, and Pierre Becker. Correlating schiff moments in the light actinides with octupole moments. *Physical review letters*, 121(23):232501, 2018.

[73] J. Dobaczewski and J. Engel. Nuclear time-reversal violation and the schiff moment of ^{225}Ra. *Phys. Rev. Lett.*, 94:232502, Jun 2005.

[74] Shufang Ban, Jacek Dobaczewski, Jonathan Engel, and A. Shukla. Fully self-consistent calculations of nuclear schiff moments. *Phys. Rev. C*, 82:015501, Jul 2010.

[75] V.V. Flambaum, I.B. Khriplovich, and O.P. Sushkov. On the p- and t-nonconserving nuclear moments. *Nuclear Physics A*, 449(4):750–760, 1986.

[76] V. A. Dzuba, V. V. Flambaum, J. S. M. Ginges, and M. G. Kozlov. Electric dipole moments of hg, xe, rn, ra, pu, and tlf induced by the nuclear schiff moment and limits on time-reversal violating interactions. *Phys. Rev. A*, 66:012111, Jul 2002.

[77] J. H. de Jesus and J. Engel. Time-reversal-violating schiff moment of ^{199}Hg. *Phys. Rev. C*, 72:045503, Oct 2005.

[78] J. de Vries, E. Mereghetti, R.G.E. Timmermans, and U. van Kolck. The effective chiral lagrangian from dimension-six parity and time-reversal violation. *Annals of Physics*, 338:50–96, 2013.

[79] Liam Paul Gaffney, Peter A Butler, Marcus Scheck, Adam B Hayes, Frederik Wenander, Michael Albers, Beyhan Bastin, Christopher Bauer, Andrey Blazhev, Sabine Bönig, et al. Studies of pear-shaped nuclei using accelerated radioactive beams. *Nature*, 497(7448):199–204, 2013.

[80] W. C. Haxton and E. M. Henley. Enhanced t-nonconserving nuclear moments. *Phys. Rev. Lett.*, 51:1937–1940, Nov 1983.

[81] M. V. Romalis and E. N. Fortson. Zeeman frequency shifts in an optical dipole trap used to search for an electric-dipole moment. *Phys. Rev. A*, 59:4547–4558, Jun 1999.

[82] D. H. Potterveld, S. A. Fromm, K. G. Bailey, M. Bishof, D. W. Booth, M. R. Dietrich, J. P. Greene, R. J. Holt, M. R. Kalita, W. Korsch, N. D. Lemke, P. Mueller, T. P. O'Connor, R. H. Parker, T. Rabga, and J. T. Singh. Characterizing the optical trapping of rare isotopes by monte carlo simulation, 2019.

[83] Cheng Chin, Véronique Leiber, Vladan Vuletić, Andrew J Kerman, and Steven Chu. Measurement of an electron's electric dipole moment using cs atoms trapped in optical lattices. *Physical Review A*, 63(3):033401, 2001.

[84] Christopher J Foot et al. *Atomic physics*, volume 7. Oxford University Press, 2005.

[85] William D. Phillips and Harold Metcalf. Laser deceleration of an atomic beam. *Phys. Rev. Lett.*, 48:596–599, Mar 1982.

[86] Richard Parker. *First EDM measurement of radium*. PhD thesis, The University of Chicago, Jan 2015.

[87] Mukut Kalita. *Search for a Permanent Electric Dipole Moment of Ra-225*. PhD thesis, The University of Kentucky, 2015.

[88] Ibrahim Archibald Sulai. *Precision Spectroscopy of Laser Trapped Helium and Radium Atoms*. PhD thesis, The University of Chicago, 2011.

[89] V A Dzuba and V V Flambaum. Calculation of energy levels and transition amplitudes for barium and radium. *Journal of Physics B: Atomic, Molecular and Optical Physics*, 40(1):227–236, dec 2006.

[90] D.W. Booth, T. Rabga, R. Ready, K.G. Bailey, M. Bishof, M.R. Dietrich, J.P. Greene, P. Mueller, T.P. O'Connor, and J.T. Singh. Spectroscopic study and lifetime measurement of the 6d7p 3f2o state of radium. *Spectrochimica Acta Part B: Atomic Spectroscopy*, 172:105967, 2020.

[91] Tenzin Rabga. *Upgrades for an Improved Measurement of the Permanent Electric Dipole Moment of Radium*. PhD thesis, 2020. Copyright - Database copyright ProQuest LLC; ProQuest does not claim copyright in the individual underlying works; Last updated - 2021-01-15.

[92] Emily Paige Abel. *Isotope Harvesting of Aqueous Phase Ions from Heavy-Ion Fragmentation Facilities for the Production of a 47 Ca/47 Sc Generator*. PhD thesis, Michigan State University, 2020.

[93] E Paige Abel, Mikael Avilov, Virginia Ayres, Eva Birnbaum, Georg Bollen, Greg Bonito, Todd Bredeweg, Hannah Clause, Aaron Couture, Joe DeVore, Matt Dietrich, Paul Ellison, Jonathan Engle, Richard Ferrieri, Jonathan Fitzsimmons, Moshe Friedman, Dali Georgobiani, Stephen Graves, John Greene, Suzanne Lapi, C Shaun Loveless, Tara Mastren, Cecilia Martinez-Gomez, Sean McGuinness, Wolfgang Mittig, David Morrissey, Graham Peaslee, Frederique Pellemoine, J David Robertson, Nicholas Scielzo, Matthew Scott, Gregory Severin, Dawn Shaughnessy, Jennifer Shusterman, Jaideep Singh, Mark Stoyer, Logan Sutherlin, Ate Visser, and John Wilkinson. Isotope harvesting at FRIB: additional opportunities for scientific discovery. *Journal of Physics G: Nuclear and Particle Physics*, 46(10):100501, aug 2019.

[94] E. Arnold, W. Borchers, M. Carre, H. T. Duong, P. Juncar, J. Lerme, S. Liberman, W. Neu, R. Neugart, E. W. Otten, M. Pellarin, J. Pinard, G. Ulm, J. L. Vialle, and K. Wendt. Direct measurement of nuclear magnetic moments of radium isotopes. *Phys. Rev. Lett.*, 59:771–774, Aug 1987.

[95] Roy A Ready, Gordon Arrowsmith-Kron, Kevin G Bailey, Dominic Battaglia, Michael Bishof, Daniel Coulter, Matthew R Dietrich, Ruoyu Fang, Brian Hanley, Jake Huneau, et al. Surface processing and discharge-conditioning of high voltage electrodes for the ra edm experiment. *arXiv preprint arXiv:2102.11029*, 2021.

[96] M. R. Dietrich, K. G. Bailey, and T. P. O'Connor. Alignment of a vector magnetometer to an optical prism. *Review of Scientific Instruments*, 88(5):055105, 2017.

[97] S K Lamoreaux. Feeble magnetic fields generated by thermal charge fluctuations in extended metallic conductors: Implications for electric-dipole moment experiments. *Phys. Rev. A*, 60(2):1717–1720, August 1999.

[98] T Varpula and T Poutanen. Magnetic field fluctuations arising from thermal motion of electric charge in conductors. *Journal of Applied Physics*, 55(11):4015–4021, June 1984.

[99] J. Singh. Estimating the size of magnetic fluctuations due to johnson noise currents, 2011.

[100] Rod V Latham. *High voltage vacuum insulation: Basic concepts and technological practice*. Elsevier, 1995.

[101] B Bonin. Field emission and surface conditioning. *Vacuum*, 46(8):907 – 912, 1995.

[102] M. BastaniNejad, Md. Abdullah Mohamed, A. A. Elmustafa, P. Adderley, J. Clark, S. Covert, J. Hansknecht, C. Hernandez-Garcia, M. Poelker, R. Mammei, K. Surles-Law, and P. Williams. Evaluation of niobium as candidate electrode material for dc high voltage photoelectron guns. *Phys. Rev. ST Accel. Beams*, 15:083502, Aug 2012.

[103] Brent Graner. Electric and magnetic field preparation for measurement of the 225ra permanent electric dipole moment. Master's thesis, University of Chicago, 2009.

[104] Herbert B. Michaelson. The work function of the elements and its periodicity. *Journal of Applied Physics*, 48(11):4729–4733, 1977.

[105] R. G. Wilson. Vacuum thermionic work functions of polycrystalline be, ti, cr, fe, ni, cu, pt, and type 304 stainless steel. *Journal of Applied Physics*, 37(6):2261–2267, 1966.

[106] W.M. Haynes. *Handbook of Chemistry and Physics*. Taylor & Francis Group, LLC, Boca Raton, Florida, 2014.

[107] J.R. Davis. *Metals Handbook* . ASM International, Materials Park, OH, 1998.

[108] John R. Rumble. *CRC Handbook of Chemistry and Physics, 101st Edition (Internet Version 2020)*. Taylor & Francis Group, LLC, Boca Raton, Florida, 2020.

[109] D.U. Furrer and S.L. Semiatin. ASM International, 2010.

[110] G. V. Samsonov. *Handbook of the Physicochemical Properties of the Elements*. Plenum Publishing Corporation., New York, New York, 1968.

[111] John F. O'Hanlon. *A User's Guide to Vacuum Technology*. John Wiley & Sons, Inc., Hoboken, New jersey, 2003.

[112] William T. Diamond. New perspectives in vacuum high voltage insulation. ii. gas desorption. *Journal of Vacuum Science & Technology A: Vacuum, Surfaces, and Films*, 16(2):720–735, 1998.

[113] Rod Latham. *High Voltage Vacuum Insulation: A New Perspective*. Authorhouse, Bloomington, Indiana, USA, 2006.

[114] F. Furuta, T. Nakanishi, S. Okumi, T. Gotou, M. Yamamoto, M. Miyamoto, M. Kuwahara, N. Yamamoto, K. Naniwa, K. Yasui, H. Matsumoto, M. Yoshioka, and K. Togawa. Reduction of field emission dark current for high-field gradient electron gun by using a molybdenum cathode and titanium anode. *Nuclear Instruments and Methods in Physics Research Section A: Accelerators, Spectrometers, Detectors and Associated Equipment*, 538(1):33 – 44, 2005.

[115] N. S. Phan, W. Wei, B. Beaumont, N. Bouman, S. M. Clayton, S. A. Currie, T. M. Ito, J. C. Ramsey, and G. M. Seidel. A study of dc electrical breakdown in liquid helium through analysis of the empirical breakdown field distributions, 2020.

[116] J.S. Sheasby. The Oxidation of Niobium in the Temperature Range 450-720 C. *Journal of the Electrochemical Society*, 115:695, 1968.

[117] B.B. Argent and B. Phelps. The oxidation of niobium-titanium and niobium-molybdenum alloys. *Journal of the Less Common Metals*, 2(2):181 – 190, 1960. Conference on Niobium, Tantalum, Molybdenum and Tungsten.

[118] P. Kofstad, P.B. Anderson, and O.J. Krudtaa. Oxidation of titanium in the temperature range 800–1200 c. *Journal of the Less Common Metals*, 3(2):89 – 97, 1961.

[119] E. Gemelli and N.H.A. Camargo. Oxidation kinetics of commercially pure titanium. *Materia (Rio de Janeiro)*, 12:525 – 531, 00 2007.

[120] L. Ogbuji and D.L. Humphrey. Comparison of the oxidation rates of some new copper alloys. *Oxidation of Metals*, 60(3):271–291, Oct 2003.

[121] Mingcheng Sun, Xinqiang Wu, Zhaoen Zhang, and En-Hou Han. Oxidation of 316 stainless steel in supercritical water. *Corrosion Science*, 51(5):1069 – 1072, 2009.

[122] E.A. Gulbransen, K.F. Andrew, and F.A. Brassart. Oxidation of Molybdenum 550 to 1700 C. *Journal of the Electrochemical Society*, 110:952 – 959, 1963.

[123] J. Bailey, K. Borer, F. Combley, H. Drumm, C. Eck, F.J.M. Farley, J.H. Field, W. Flegel, P.M. Hattersley, F. Krienen, F. Lange, G. Lebée, E. McMillan, G. Petrucci, E. Picasso, O. Rúnolfsson, W. von Rüden, R.W. Williams, and S. Wojcicki. Final report on the cern muon storage ring including the anomalous magnetic moment and the electric dipole moment of the muon, and a direct test of relativistic time dilation. *Nuclear Physics B*, 150(Supplement C):1 – 75, 1979.

[124] V. Anastassopoulos, S. Andrianov, R. Baartman, S. Baessler, M. Bai, J. Benante, M. Berz, M. Blaskiewicz, T. Bowcock, K. Brown, B. Casey, M. Conte, J. D. Crnkovic, N. D'Imperio, G. Fanourakis, A. Fedotov, P. Fierlinger, W. Fischer, M. O. Gaisser, Y. Giomataris, M. Grosse-Perdekamp, G. Guidoboni, S. Hacıömeroğlu, G. Hoffstaetter, H. Huang, M. Incagli, A. Ivanov, D. Kawall, Y. I. Kim, B. King, I. A. Koop, D. M. Lazarus, V. Lebedev, M. J. Lee, S. Lee, Y. H. Lee, A. Lehrach, P. Lenisa, P. Levi Sandri, A. U. Luccio, A. Lyapin, W. MacKay, R. Maier, K. Makino, N. Malitsky, W. J. Marciano, W. Meng, F. Meot, E. M. Metodiev, L. Miceli, D. Moricciani, W. M. Morse, S. Nagaitsev, S. K. Nayak, Y. F. Orlov, C. S. Ozben, S. T. Park, A. Pesce, E. Petrakou, P. Pile, B. Podobedov, V. Polychronakos, J. Pretz, V. Ptitsyn, E. Ramberg, D. Raparia, F. Rathmann, S. Rescia, T. Roser, H. Kamal Sayed, Y. K. Semertzidis, Y. Senichev, A. Sidorin, A. Silenko, N. Simos, A. Stahl, E. J. Stephenson, H. Ströher, M. J. Syphers, J. Talman, R. M. Talman, V. Tishchenko, C. Touramanis, N. Tsoupas, G. Venanzoni, K. Vetter, S. Vlassis, E. Won, G. Zavattini, A. Zelenski, and K. Zioutas. A storage ring experiment to detect a proton electric dipole moment. *Review of Scientific Instruments*, 87(11):115116, 2016.

[125] P Adderley, J Clark, J Grames, J Hansknecht, M Poelker, M Stutzman, R Suleiman, K Surles-Law, J McCarter, and M BastaniNejad. Cebaf 200kv inverted electron gun. In *Proceedings of the 2011 Particle Accelerator Conference*, pages 1501–1503, 2011.

[126] Mahzad BastaniNejad, Abdelmageed A. Elmustafa, Eric Forman, Steven Covert, John Hansknecht, Carlos Hernandez-Garcia, Matthew Poelker, Lopa Das, Michael Kelley, and Phillip Williams. Evaluation of electropolished stainless steel electrodes for use in dc high voltage photoelectron guns. *Journal of Vacuum Science & Technology A*, 33(4):041401, 2015.

[127] P. Bernard, D. Bloess, W. Hartung, C. Hauviller, W. Weingarten, P. Bosland, and J. Martignac. Superconducting niobium sputter coated copper cavities at 1500-MHz. *Part. Accel.*, 40:487–496, 1992.

[128] P. Bernard, D. Bloess, T. Flynn, C. Hauviller, W. Weingarten, P. Bosland, and J. Martignac. Superconducting niobium sputter coated copper cavities at 1500-MHz. 1992.

[129] H. Diepers, O. Schmidt, H. Martens, and F.S. Sun. A new method of electropolishing niobium. *Physics Letters A*, 37(2):139 – 140, 1971.

[130] P. Kneisel, K. Nakajima, J. Kirchgessner, J. Mioduszewski, M. Pickup, R. Sundelin, and M. Tigner. Development of Superconducting Cavities of Cylindrical Symmetry at Cornell. *IEEE Transactions on Nuclear Science*, 30(4):3348–3350, 1983.

[131] K. Saito, S. Inoue, E. Kako, T. Fujino, S. Noguchi, M. Ono, and T. Shishido. Superiority of electropolishing over chemical polishing on high gradients. *Particle Accelerators*, 60:193–217, 1998.

[132] L. Lilje, C. Antoine, C. Benvenuti, D. Bloess, J.-P. Charrier, E. Chiaveri, L. Ferreira, R. Losito, A. Matheisen, H. Preis, D. Proch, D. Reschke, H. Safa, P. Schmüser, D. Trines, B. Visentin, and H. Wenninger. Improved surface treatment of the superconducting tesla cavities. *Nuclear Instruments and Methods in Physics Research Section A: Accelerators, Spectrometers, Detectors and Associated Equipment*, 516(2):213 – 227, 2004.

[133] Hasan Padamsee. *RF Superconductivity: Science, Technology, and Applications*. WILEY-VCH Verlag GmbH & Co. KGaA, Weinheim, Germany, 2009.

[134] C. Hernandez-Garcia, D. Bullard, F. Hannon, Y. Wang, and M. Poelker. High voltage performance of a dc photoemission electron gun with centrifugal barrel-polished electrodes. *Review of Scientific Instruments*, 88(9):093303, 2017.

[135] Dmitry Budker, Derek F. Kimball, and David P. DeMille. *Atomic Physics: An Exploration through Problems and Solutions*. Oxford University Press., Great Clarendon Street, Oxford OX2 6DP, United Kingdom, 2008.

[136] Yukikazu Itikawa. Cross sections for electron collisions with oxygen molecules. *Journal of Physical and Chemical Reference Data*, 38(1):1–20, 2009.

[137] N. D. Scielzo, J. R. Guest, E. C. Schulte, I. Ahmad, K. Bailey, D. L. Bowers, R. J. Holt, Z.-T. Lu, T. P. O'Connor, and D. H. Potterveld. Measurement of the lifetimes of the lowest $^3p_1$ state of neutral ba and ra. *Phys. Rev. A*, 73:010501, Jan 2006.

[138] V. A. Dzuba and J. S. M. Ginges. Calculations of energy levels and lifetimes of low-lying states of barium and radium. *Phys. Rev. A*, 73:032503, Mar 2006.

216

[139] J. R. Guest, N. D. Scielzo, I. Ahmad, K. Bailey, J. P. Greene, R. J. Holt, Z.-T. Lu, T. P. O'Connor, and D. H. Potterveld. Laser trapping of ^{225}Ra and ^{226}Ra with repumping by room-temperature blackbody radiation. *Phys. Rev. Lett.*, 98:093001, Feb 2007.

[140] W. L. Trimble, I. A. Sulai, I. Ahmad, K. Bailey, B. Graner, J. P. Greene, R. J. Holt, W. Korsch, Z.-T. Lu, P. Mueller, and T. P. O'Connor. Lifetime of the $7s6d\,^1D_2$ atomic state of radium. *Phys. Rev. A*, 80:054501, Nov 2009.

[141] Jacek Biero, Charlotte Froese Fischer, Stephan Fritzsche, and Krzysztof Pachucki. Lifetime and hyperfine structure of the3d2state of radium. *Journal of Physics B: Atomic, Molecular and Optical Physics*, 37(17):L305–L311, aug 2004.

[142] C_E_ Moore. Atomic energy levels, natl. *Bur. Stand. Circ*, 467, 1971.

[143] Alfred Morgenstern, Christos Apostolidis, Clemens Kratochwil, Mike Sathekge, Leszek Krolicki, and Frank Bruchertseifer. An overview of targeted alpha therapy with 225actinium and 213bismuth. *Current radiopharmaceuticals*, 11(3):200–208, 2018.

[144] Benjamin T. Loseth. *Development of a Single-Atom Microscope for Optical Detection of Atomic Nuclear Reaction Products*. PhD thesis, Michigan State University, 2020.

[145] A.J. Stone and C.P. Wood. Root-rational-fraction package for exact calculation of vector-coupling coefficients. *Computer Physics Communications*, 21(2):195–205, 1980.

[146] Daniel A Steck. Rubidium 85 d line data, 2.2.1, 21 november 2019, 2008.

[147] Dipankar Das, Sachin Barthwal, Ayan Banerjee, and Vasant Natarajan. Absolute frequency measurements in yb with 0.08 ppb uncertainty: Isotope shifts and hyperfine structure in the 399–nm $^1s_0 \rightarrow^1 p_1$ line. *Phys. Rev. A*, 72:032506, Sep 2005.

[148] Daniel A Steck. Rubidium 87 d line data, revision 2.2.1, 21 november 2019, 2001.

[149] A. Andl, K. Bekk, S. Göring, A. Hanser, G. Nowicki, H. Rebel, G. Schatz, and R. C. Thompson. Isotope shifts and hyperfine structure of the $4s^2\,^1s_0-4s4p^1p_1$ transition in calcium isotopes. *Phys. Rev. C*, 26:2194–2202, Nov 1982.

[150] GK Woodgate. Elementary atomic structure, clarendon, 1980.

[151] Donald R. Olander and Valerie Kruger. Molecular beam sources fabricated from multichannel arrays. iii. the exit density problem. *Journal of Applied Physics*, 41(7):2769–2776, 1970.

[152] Wolfgang L Wiese, Melvin William Smith, and BM Miles. Atomic transition probabilities. volume 2. sodium through calcium. Technical report, NATIONAL STANDARD REFERENCE DATA SYSTEM, 1969.

[153] R. F. Gutterres, C. Amiot, A. Fioretti, C. Gabbanini, M. Mazzoni, and O. Dulieu. Determination of the ^{87}Rb $5p$ state dipole matrix element and radiative lifetime from the photoassociation spectroscopy of the rb$_2$ $0_g^-(P_{3/2})$ long-range state. *Phys. Rev. A*, 66:024502, Aug 2002.

[154] R Drozdowski, J Kwela, and M Walkiewicz. Lifetimes of the 4s4p 3 p 1 and 4s3d 1 d 2 states of ca i. *Zeitschrift für Physik D Atoms, Molecules and Clusters*, 27(4):321–324, 1993.

[155] W. Nörtershäuser, N. Trautmann, K. Wendt, and B.A. Bushaw. Isotope shifts and hyperfine structure in the 4s2 1s0 → 4s4p1p1 → 4s4d 1d2 transitions of stable calcium isotopes and calcium-41. *Spectrochimica Acta Part B: Atomic Spectroscopy*, 53(5):709–721, 1998.

[156] E. J. Salumbides, V. Maslinskas, I. M. Dildar, A. L. Wolf, E.-J. van Duijn, K. S. E. Eikema, and W. Ubachs. High-precision frequency measurement of the 423-nm ca i line. *Phys. Rev. A*, 83:012502, Jan 2011.

[157] P. Tremblay, A. Michaud, M. Levesque, S. Thériault, M. Breton, J. Beaubien, and N. Cyr. Absorption profiles of alkali-metal d lines in the presence of a static magnetic field. *Phys. Rev. A*, 42:2766–2773, Sep 1990.

[158] J. Laurec, A. Adam, T. de Bruyne, E. Bauge, T. Granier, J. Aupiais, O. Bersillon, G. Le Petit, N. Authier, and P. Casoli. Fission product yields of 233u, 235u, 238u and 239pu in fields of thermal neutrons, fission neutrons and 14.7-mev neutrons. *Nuclear Data Sheets*, 111(12):2965 – 2980, 2010. Nuclear Reaction Data.

[159] S.K. Basu, G. Mukherjee, and A.A. Sonzogni. Nuclear data sheets for a = 95. *Nuclear Data Sheets*, 111(10):2555 – 2737, 2010.

[160] C.W. Reich. Nuclear data sheets for a = 156. *Nuclear Data Sheets*, 113(11):2537 – 2840, 2012.

[161] N. Nica. Nuclear data sheets for a = 147. *Nuclear Data Sheets*, 110(4):749 – 997, 2009.

[162] AA Sonzogni. Experimental data on ground- and excited-state properties for all nuclei with mass number a=144 have been compiled and evaluated. states populated in radioactive decay as well as in nuclear reactions have been considered. for these nuclei, level and decay schemes have been built, as well as tables of nuclear properties. this work supersedes the 1989 evaluation by j.k. tuli (1989tu02). manuscripts published before december 2000 have been included in this work. *Nuclear Data Sheets*, 93(3):599 – 762, 2001.

[163] C.W. Reich. Nuclear data sheets for a = 161. *Nuclear Data Sheets*, 112(10):2497 – 2713, 2011.

[164] A. Hashizume. Nuclear data sheets for a = 127. *Nuclear Data Sheets*, 112(7):1647 – 1831, 2011.

[165] Jean Blachot. Nuclear data sheets for a = 111. *Nuclear Data Sheets*, 77(2):299 – 432, 1996.

[166] R.G Helmer, J.C Hardy, V.E Iacob, M Sanchez-Vega, R.G Neilson, and J Nelson. The use of monte carlo calculations in the determination of a ge detector efficiency curve. *Nuclear Instruments and Methods in Physics Research Section A: Accelerators, Spectrometers, Detectors and Associated Equipment*, 511(3):360 – 381, 2003.

[167] R.G. Helmer, N. Nica, J.C. Hardy, and V.E. Iacob. Precise efficiency calibration of an hpge detector up to 3.5mev, with measurements and monte carlo calculations. *Applied Radiation and Isotopes*, 60(2):173 – 177, 2004. Proceedings of the 14th International Conference on Radionuclide Metrology and its Applications, ICRM 2003.

[168] K Kolos and ND Scielzo. Determination of gamma-ray branching ratios for 95zr and 147nd. Technical report, Lawrence Livermore National Lab.(LLNL), Livermore, CA (United States), 2020.

[169] K. Kolos, A.M. Hennessy, N.D. Scielzo, V.E. Iacob, J.C. Hardy, M.A. Stoyer, A.P. Tonchev, W.-J. Ong, M.T. Burkey, B. Champine, J.A. Clark, P. Copp, A. Gallant, E.B. Norman, R. Orford, H.I. Park, J. Rohrer, D. Santiago-Gonzalez, G. Savard, A.J. Shaka, B.S. Wang, and S. Zhu. New approach to precisely measure gamma-ray intensities for long-lived fission products, with results for the decay of 95zr. *Nuclear Instruments and Methods in Physics Research Section A: Accelerators, Spectrometers, Detectors and Associated Equipment*, 1000:165240, 2021.

[170] W.R. Leo. *Techniques for Nuclear and Particle Physics Experiments*. Springer-Verlag, Berlin, Germany, 1994.

[171] C. B. Alcock, V. P. Itkin, and M. K. Horrigan. Vapour pressure equations for the metallic elements: 298–2500k. *Canadian Metallurgical Quarterly*, 23(3):309–313, 1984.

[172] A. Kramida. Isotope shifts in neutral and singly-ionized calcium. *Atomic Data and Nuclear Data Tables*, 133-134:101322, 2020.